

Ministry of Science and Higher Education of the Russian Federation  
ITMO University

ISSN 2220-8054

***NANOSYSTEMS:***  
***PHYSICS, CHEMISTRY, MATHEMATICS***

**2022, volume 13(6)**

**Наносистемы: физика, химия, математика**

**2022, том 13, № 6**



# NANOSYSTEMS:

PHYSICS, CHEMISTRY, MATHEMATICS

## ADVISORY BOARD MEMBERS

**Chairman:** V.N. Vasiliev (*St. Petersburg, Russia*),  
V.M. Buznik (*Moscow, Russia*); V.M. Ievlev (*Voronezh, Russia*), P.S. Kop'ev (*St. Petersburg, Russia*), N.F. Morozov (*St. Petersburg, Russia*), V.N. Parmon (*Novosibirsk, Russia*),  
A.I. Rusanov (*St. Petersburg, Russia*),

## EDITORIAL BOARD

**Editor-in-Chief:** I.Yu. Popov (*St. Petersburg, Russia*)

### Section Co-Editors:

Physics – V.M. Uzdin (*St. Petersburg, Russia*),

Material science – V.V. Gusarov (*St. Petersburg, Russia*); O.V. Al'myasheva (*St. Petersburg, Russia*);

Chemistry – V.K. Ivanov (*Moscow, Russia*),

Mathematics – I.Yu. Popov (*St. Petersburg, Russia*).

### Editorial Board Members:

V.M. Adamyan (*Odessa, Ukraine*); A.P. Alodjants (*St. Petersburg, Russia*); S. Bechta (*Stockholm, Sweden*); J. Behrndt (*Graz, Austria*); M.B. Belonenko (*Volgograd, Russia*); A. Chatterjee (*Hyderabad, India*); A.V. Chizhov (*Dubna, Russia*); A.N. Enyashin (*Ekaterinburg, Russia*), P.P. Fedorov (*Moscow, Russia*); E.A. Gudilin (*Moscow, Russia*); H. Jónsson (*Reykjavik, Iceland*); A.A. Kiselev (*Durham, USA*); Yu.S. Kivshar (*Canberra, Australia*); S.A. Kozlov (*St. Petersburg, Russia*); P.A. Kurasov (*Stockholm, Sweden*); A.V. Lukashin (*Moscow, Russia*); I.V. Melikhov (*Moscow, Russia*); G.P. Miroshnichenko (*St. Petersburg, Russia*); I.Ya. Mittova (*Voronezh, Russia*); Nguyen Anh Tien (*Ho Chi Minh, Vietnam*); V.V. Pankov (*Minsk, Belarus*); K. Pankrashkin (*Orsay, France*); A.V. Ragulya (*Kiev, Ukraine*); V. Rajendran (*Tamil Nadu, India*); A.A. Rempel (*Ekaterinburg, Russia*); V.Ya. Rudyak (*Novosibirsk, Russia*); H.M. Sedighi (*Ahvaz, Iran*); D Shoikhet (*Karmiel, Israel*); P Stovicek (*Prague, Czech Republic*); V.M. Talanov (*Novocherkassk, Russia*); A.Ya. Vul' (*St. Petersburg, Russia*); A.V. Yakimansky (*St. Petersburg, Russia*), V.A. Zagrebnov (*Marseille, France*).

### Editors:

I.V. Blinova; A.I. Popov; A.I. Trifanov; E.S. Trifanova (*St. Petersburg, Russia*),  
R. Simoneaux (*Philadelphia, Pennsylvania, USA*).

**Address:** ITMO University, Kronverkskiy pr., 49, St. Petersburg 197101, Russia.

**Phone:** +7(812)607-02-54, **Journal site:** <http://nanojournal.ifmo.ru/>,

**E-mail:** [nanojournal.ifmo@gmail.com](mailto:nanojournal.ifmo@gmail.com)

## AIM AND SCOPE

The scope of the journal includes all areas of nano-sciences. Papers devoted to basic problems of physics, chemistry, material science and mathematics inspired by nanosystems investigations are welcomed. Both theoretical and experimental works concerning the properties and behavior of nanosystems, problems of its creation and application, mathematical methods of nanosystem studies are considered.

The journal publishes scientific reviews (up to 30 journal pages), research papers (up to 15 pages) and letters (up to 5 pages). All manuscripts are peer-reviewed. Authors are informed about the referee opinion and the Editorial decision.

# CONTENT

## MATHEMATICS

- I.S. Lobanov  
**Spin Boltzmann machine** 593

## PHYSICS

- E.S. Sedov, V.A. Lukoshkin, V.K. Kalevich, I.Yu. Chestnov,  
Z. Hatzopoulos, P.G. Savvidis, A.V. Kavokin  
**Double ring polariton condensates with polariton vortices** 608

- G.P. Miroshnichenko, A.N. Arzhanenkova, M.Yu. Plotnikov  
**Investigation of the method of current thermal modulation  
of the wavelength VCSEL** 615

- M.B. Semenov, V.D. Krevchik, D.O. Filatov, D.A. Antonov,  
A.V. Shorokhov, A.P. Shkurinov, I.A. Ozheredov, P.V. Krevchik,  
A.V. Razumov, A.S. Kotov, I.S. Antonov, I.M. Semenov  
**Features of tunneling current-voltage characteristics in dielectric films  
with Ni, Fe and Co nanoparticles, investigated by conductive AFM  
and within the framework of the theory of 1D-dissipative tunneling** 621

- A.D. Vatutin, G.P. Miroshnichenko, A.I. Trifanov  
**Master equation for correlators of normal-ordered field mode  
operators** 628

## CHEMISTRY AND MATERIAL SCIENCE

- E.A. Kozlova, A.A. Valeeva, A.A. Sushnikova,  
A.V. Zhurenok, A.A. Rempel  
**Photocatalytic activity of titanium dioxide produced  
by high-energy milling** 632

- L. Rohmawati, Istiqomah, A. A. Pratama,  
W. Setyarsih, N.P. Putri, Munasir, Darminto  
**The characteristics of TiO<sub>2</sub> anatase from tulungagung sand  
as an antibacterial material** 640

- A.S. Seroglazova, V.I. Popkov  
**Synthesis of highly active and visible-light-driven PrFeO<sub>3</sub>  
photocatalyst using solution combustion approach  
and succinic acid as fuel** 649

D.D. Averkiev, L.L. Larina, O.I. Shevaleevskiy, O.V. Almjasheva <b>Formation of nanocrystalline particles on the basis of La<sub>2</sub>(Ni,Mn,Fe)<sub>2</sub>O<sub>6</sub> variable composition phases having a structure of double perovskite under conditions of solution combustion</b>	<b>655</b>
D.P. Elovikov, O.V. Proskurina, M.V. Tomkovich, V.L. Ugolkov, V.V. Gusarov <b>Thermal stability of the waylandite-structured nanocrystalline BiAl<sub>3</sub>(PO<sub>4</sub>)<sub>2</sub>(OH)<sub>6</sub></b>	<b>662</b>
V.M. Talanov, M.V. Talanov <b>Multi-order and structural mechanism of atom nanocluster formation in rhombohedral Cu-Zr-thiospinels</b>	<b>668</b>
Y.C. Sharma, Snehal D. Patil, Harshal A. Nikam, Padmaja Sharma, Dinesh B. Borse, D.R. Patil <b>Studies on Sn doped cadmium sulfide thin films as highly selective green light photosensors</b>	<b>678</b>
K.Yu. Zhizhin, E.S. Turyshchev, A.V. Kopytin, L.K. Shpigun, N.T. Kuznetsov, N.P. Simonenko, N.N. Zamyatina, M.S. Madraimov, G.I. Betenev <b>Polymer nanocarbon materials as ion-to-electron transducers in solid-contact ion-selective electrodes</b>	<b>688</b>
A.A. Luginina, S.V. Kuznetsov, A.A. Alexandrov, R.V. Gainutdinov, D.I. Petukhov, V.V. Voronov, E.V. Chernova, P.P. Fedorov <b>High lignin content cellulose nanofibrils obtained from thermomechanical pulp</b>	<b>698</b>
<b>Information for authors</b>	<b>709</b>

## Spin Boltzmann machine

Igor S. Lobanov

Faculty of Physics, ITMO University, Saint Petersburg, Russia

[igor.lobanov@metalab.ifmo.ru](mailto:igor.lobanov@metalab.ifmo.ru), [lobanov.igor@gmail.com](mailto:lobanov.igor@gmail.com)

PACS 75.78.-n, 05.65.+b

**ABSTRACT** Boltzmann machine (BM) is a recurrent network, which has a wide range of applications in machine learning (ML) including dimensionality reduction, feature learning and classification. Standard BM is described by the Ising model and can be implemented as a spin ice based device. Such hardware implementation is faster and more energy efficient than a simulation on digital computers. At the moment, a hardware BM is a single purpose device designed on digital computers for a specific task. In the paper we propose a generalized BM capable of fitting parameters by demonstration of training examples, which is done completely inside the spintronic device. Our generalization is based on the Heisenberg model, which is more accurate than the Ising model for spin ice. We show that for some systems minimization of Kullback-Leibler divergence during training of BM is equivalent to minimization of free energy with respect to the biases of the units, hence training of the ML model can be done by energy dissipation. We include the biases as degrees of freedom of the device, whose dynamics is described by the same Landau-Lifschitz-Gilbert equation as for spins representing units of BM. The demonstration of samples from the training set is done by fixing inputs and outputs according to ground truth. The training samples are remembered by the machine becoming minima on the energy landscape implementing a kind of long-term potentiation. The performance of the proposed machine is compared with a single layer perceptron artificial neural network and with a Bernoulli restricted BM on a binary classification problem.

**KEYWORDS** spectral gap, quantum graph, Schrödinger operator, discrete spectrum.

**ACKNOWLEDGEMENTS** The work is supported by Russian Science Foundation grant 22-22-00565: <https://rscf.ru/en/project/22-22-00565/>.

**FOR CITATION** Lobanov I.S. Spin Boltzmann machine. *Nanosystems: Phys. Chem. Math.*, 2022, **13** (6), 593–607.

### 1. Introduction

Advances in machine learning (ML) lead to a breakthrough in the field of artificial intelligence in recent decades. We have seen great progress in previously intractable problems, such as speech recognition, natural language translation, computer vision, motion planning [1] and even in physics itself [2]. The main approaches to ML were inspired by biology, e.g. artificial neural networks (ANN), or physics, e.g. Boltzmann machine (BM). The basic theory of ANN was formulated in the 1940s [3], but soon the research stagnated due to lack of processing power [4]. The rate of development was accelerated dramatically with the appearance of graphical processing units (GPU) offering huge processing power to solve linear algebra problems for a relatively small price. At the moment computers can solve many artificial intelligence (AI) tasks, however the energy efficiency of the organic brain is still much higher. The need to reduce energy consumption leads to the emergence of dedicated AI accelerators [5]. The widespread digital computers are good for precise computations, but analog devices and stochastic computing better suit the needs of ML [6]. For example, linear systems can be solved in constant time by analog computers, which offers a huge speed boost [7].

At the moment, there are many teams trying different approaches to improving ML hardware. It was shown in [8] that almost arbitrary wave dynamics can be considered as a variant of recurrent neural networks. Spintronics devices are one of promising hardware platforms for biologically inspired computing [9]. In [10] nanoscale spintronic oscillators were used to implement the basic block of ANN combining nonlinearity and memory, a successful recognition of spoken digits is reported. The inverse Rashba-Edelstein magnetoelectric neuron was proposed in [11], its effectiveness was demonstrated on handwritten images recognition.  $784 \times 200 \times 10$  deep belief network consisting of p-bit-based neurons was created using spin-orbit-torque magnetic random access memory in [12]. Magnetic skyrmions, stabilized due to topological protection, are prospective novel information carriers [13], which is used in multiple nonclassic computing devices [14, 15]. Artificial synapse was created using magnetic skyrmion in [16]. Spintronic artificial synapse was controlled by ultrashort laser pulses in [17]. Random skyrmion textures were used for reservoir computing [18].

Most approaches to ML distinguish training phase (parameter fitting) and prediction phase. Emerging devices for neuromorphic computing based on new physical principles are devoted to the prediction phase. The prediction is a crucial part of usage of ML algorithms, namely this part is implemented in consumer products, which can benefit from lower

energy usage or faster response of novel devices. However, model training is much more time and energy consuming than prediction. Besides repeated computation of the model, the training includes additional steps such as computation of loss, differentiation of the loss function with respect to the parameters, inference of hidden variables and so on. These actions are not trivially connected with model computation and require additional hardware support. At the current stage of research, the training is rarely made on the device itself, instead it is common to fit the parameters by simulation of the device in a digital computer. In the article we are going to go further and suggest a quite general approach for ML model training directly in the device without digital computers.

The training phase consists in fitting parameters by minimizing loss function (or maximizing likelihood). Energy in dissipative systems naturally decreases, hence an appealing idea is to map the loss function to system energy, thus obtaining automatic training. Quasi-thermodynamics and free energy minimization have been discussed in the context of ML for several decades. Hopfield network [19–21] and BM [22–24] minimize free energy thus converging to memorized states. The energy minimization in BM is used for prediction, training is carried out by a separated procedure, and we are going to unify the processes in our work. In [6] dissipative systems are noted to be popular for simulation of associative memory. In [25] the neuron activity was recognized to be described by pseudo-thermodynamics and the training can be simulated by annealing. In [26] a dissipative quantum model of the brain was shown to match the formation of coherent domains of synchronized neuronal oscillatory activity and phase transitions obtained from neurophysiological data collected from electroencephalograms. In [27] it was observed that the training of ANN can be considered as a dissipative process. In the article [28] an ANN was trained to model energy dissipation, which provides advantages in the reconstruction of magnetic resonance and computed tomography images. In [29] artificial spintronic synapses were designed and shown to be suitable for Hopfield model-based associative memory.

The reversible computing [30] is a topic closely related to ML, where energy minimization is used as the driving force of computation. Quantum mechanics tells us that all computations are reversible, and this is indeed true for quantum gates [31]. The classical computers are not reversible, in particular, due to the loss of information, which leads to an increase in ambient temperature. Elementary steps of classic computation are usually defined as logic gates, which are mappings from inputs to outputs. The symmetry of roles of inputs and outputs can be achieved, if both inputs and outputs are defined by an implicit relation between them. The reversibility in classical computing can be restored, if assumptions of the inverse function theorem are applicable to the relation. There are several physical implementations of reversible computations. In applications it is convenient to define an error function, which represents mismatch between inputs and outputs. If the error can be equated to energy of a physical system, the agreement between inputs and outputs can be achieved by dissipation. The reversible computing devices were created using electrical circuit elements with memory [32]. Invertible boolean logic with BM was described and partially implemented in CMOS-assisted nanomagnet-based hardware in [33]. A magnetic tunnel junctions based device was created in [34], which was able to factorize several numbers (945 is the largest one) using reversible computing in the form of BM. As was demonstrated in [35] by simulation, the digital memcomputing machine is able to solve the boolean satisfiability problem in polynomial time. Reversible elements can be created from nanomagnets as was demonstrated in [36]. Larger magnets permit spin waves, which also can be used for implementation of reversible magnetic logic gates [37]. Large magnetic systems may contain topologically protected solitons, such as skyrmions, which can be used as information carriers for large-scale reversible computation [38].

Lot of new physical devices for ML are variants of BM. Standard BM is described by the Ising model. BM can be naturally implemented in spin-ice [39]. Artificial spin-ice (ASI) systems are constructed from arrays of dipolar coupled monodomain magnets [40,41]. At the moment ASI is used to embody novel functional devices for convenient logic and for neuromorphics [42]. ASI has many metastable-states, they are configured by an external field and are able to store and process temporal input patterns [43]. Thermally driven balanced NAND gate was implemented in kagome spin ice in [44]. Fabrication of computational blocks in spin ice was demonstrated by an experiment in [45].

In the paper we consider a variant of BM based on the Heisenberg model, where orientation of the magnetic moments is not constrained, but can be controlled by anisotropy. We augment the model with additional spins, which generate an effective field playing role of biases in standard BM, thus obtaining a spin Boltzmann machine (SBM). Just like BM, SBM can be implemented as a spin-ice device. The energy dissipation is used for training of SBM, and we describe two schemes of training with spatial or temporal separation of samples. SBM does not rely on external devices for training, it can be retrained on another training set to solve another problem, making SBM reusable.

The paper is organized as follows. In Section 2 we show how minimization of Kullback–Leibler divergence for Boltzmann distribution can be reduced to minimization of energy. In Section 3 we recall the definition and principles of operation of BM. In Section 4 we formulate a binary classification problem and solve the problem using ANN and BM. In Section 5 we introduce SBM and describe how BM can be made flexible by introduction of additional degrees of freedom storing biases. In Section 6 we apply SBM to solve of the binary classification problem and compare the result with the result of ANN and BM.

## 2. Relaxation as distribution learning

Consider problem of estimation of parameters of multivariate normal distribution:

$$\rho(\mathbf{x}|\Sigma, \boldsymbol{\mu}) = \frac{1}{Z} \exp(-E[\mathbf{x}]), \quad E[\mathbf{x}] = \frac{1}{2}(\mathbf{x} - \boldsymbol{\mu}) \cdot \Sigma^{-1}(\mathbf{x} - \boldsymbol{\mu}), \quad \mathbf{x} \in \mathbb{R}^N, \quad (1)$$

with mean  $\boldsymbol{\mu} = \mathbb{E}[\mathbf{x}]$  and covariance matrix  $\Sigma = \mathbb{E}[(\mathbf{x} - \boldsymbol{\mu})(\mathbf{x} - \boldsymbol{\mu})^T] > 0$ . The distribution  $\rho$  is a particular case of Boltzmann distribution for harmonic energy functional  $E$ . The normalization constant  $Z$  in the case is known explicitly:

$$Z = \int_{\mathbb{R}^N} e^{-E[\mathbf{x}]} d\mathbf{x}, \quad \ln Z = \frac{N}{2} \ln(2\pi) + \frac{1}{2} \ln \det \Sigma.$$

In ML the distribution  $\rho$  defines a model. The model can be trained by fitting parameters of the model given some observed samples  $\{\mathbf{x}^m\}_{m=1}^M$  of the distribution  $\rho$ . We follow the maximum likelihood principle, whose goal is to find parameters for which observed samples have highest joint probability. Introduce likelihood function  $\mathcal{L}$ , which expresses probability to obtain the observed samples assuming model parameters are known and the samples are independent:

$$\ln \mathcal{L} = \frac{1}{M} \sum_{m=1}^M \ln \rho(\mathbf{x}^m|\Sigma, \boldsymbol{\mu}) = -\frac{1}{M} \sum_{m=1}^M E[\mathbf{x}^m] - \ln Z.$$

The first addendum is mean value of energy, it can be computed explicitly:

$$\begin{aligned} \frac{1}{M} \sum_{m=1}^M E[\mathbf{x}^m] &= \frac{1}{M} \left[ \frac{1}{2} \mathbf{x}^m \cdot \Sigma^{-1} \mathbf{x}^m - \mathbf{x}^m \cdot \Sigma^{-1} \boldsymbol{\mu} + \frac{1}{2} \boldsymbol{\mu} \cdot \Sigma^{-1} \boldsymbol{\mu} \right] \\ &= \frac{1}{2} \text{Tr}(\Sigma^{-1} V) - \mathbf{a} \cdot \Sigma^{-1} \boldsymbol{\mu} + \frac{1}{2} \boldsymbol{\mu} \cdot \Sigma^{-1} \boldsymbol{\mu}, \end{aligned}$$

where

$$\mathbf{a} = \frac{1}{M} \sum_{m=1}^M \mathbf{x}^m, \quad V = \frac{1}{M} \sum_{m=1}^M \mathbf{x}^m (\mathbf{x}^m)^T.$$

and we have used  $\text{Tr}(ABC) = \text{Tr}(BCA)$ .

According to maximum likelihood principle, the parameters  $\Sigma$  and  $\boldsymbol{\mu}$  can be estimated by maximization of  $\mathcal{L}$  given observed values  $\{\mathbf{x}^m\}$ . Since  $\Sigma$  and  $\boldsymbol{\mu}$  are not subjected to constraints except of  $\Sigma^T = \Sigma$ , the minimum should be a stationary point. Derivative with respect to  $\boldsymbol{\mu}$  can be readily obtained:

$$\frac{\partial \ln \mathcal{L}}{\partial \boldsymbol{\mu}} = -\Sigma^{-1}(\boldsymbol{\mu} - \mathbf{a}) = 0,$$

hence maximum likelihood estimate  $\boldsymbol{\mu} = \mathbf{a}$ . Derivative of the partition function  $Z$  with respect to the covariance matrix  $\Sigma$  coincide with  $\Sigma$  up to a constant:

$$\frac{\partial \ln Z}{\partial \Sigma^{-1}} = \frac{1}{2} \frac{\partial}{\partial \Sigma^{-1}} \ln \det \Sigma^{-1} = \frac{1}{2} \Sigma.$$

Solution of the stationarity condition with respect to the covariance matrix

$$\frac{\partial \ln \mathcal{L}}{\partial \Sigma^{-1}} = -\frac{1}{2} V + \boldsymbol{\mu} \mathbf{a}^T - \frac{1}{2} \boldsymbol{\mu} \boldsymbol{\mu}^T + \frac{1}{2} \Sigma = 0,$$

gives us the estimate of the remaining parameter:

$$\Sigma = V - \boldsymbol{\mu} \boldsymbol{\mu}^T.$$

The same estimate can be obtained from minimization of Kullback–Leibler divergence between distribution  $\rho$  and empirical distribution  $\tilde{\rho}$  of samples  $\mathbf{x}^m$ :

$$D_{KL}(\tilde{\rho}|\rho) = H(\tilde{\rho}, \rho) - H(\tilde{\rho}) = \frac{1}{2} \left\{ \text{Tr}(\tilde{\Sigma}^{-1} \Sigma) + (\tilde{\boldsymbol{\mu}} - \boldsymbol{\mu}) \cdot \tilde{\Sigma}^{-1} (\tilde{\boldsymbol{\mu}} - \boldsymbol{\mu}) - N + \ln \frac{\det \tilde{\Sigma}}{\det \Sigma} \right\},$$

where  $\tilde{\boldsymbol{\mu}}$  and  $\tilde{\Sigma}$  are parameters of distribution  $\tilde{\rho}$ . Entropy is given by

$$H(\tilde{\rho}) = \mathbb{E}_{\tilde{\rho}}[-\ln \tilde{\rho}] = \frac{N}{2} + \frac{N}{2} \ln(2\pi) + \frac{1}{2} \ln \det \tilde{\Sigma} = \frac{N}{2} + \ln \tilde{Z}.$$

Cross-entropy can be estimated by Monte-Carlo method:

$$H(\tilde{\rho}, \rho) = \mathbb{E}_{\tilde{\rho}}[-\ln \rho] \approx -\frac{1}{M} \sum_{m=1}^M \ln \rho(\mathbf{x}^m) = -\ln \mathcal{L}.$$

Hence Kullback–Leibler divergence is equal to minus log-likelihood up to a constant independent of model parameters, which proves equivalence of maximum likelihood estimate and minimization of KL-divergence:

$$D_{KL}(\tilde{\rho}|\rho) = -\ln \mathcal{L} + \text{const.}$$

The training problem (calculation of  $\Sigma$  and  $\boldsymbol{\mu}$  given  $\mathbf{x}^m$ ) can be solved analytically, since the optimization problem is reduced to the solution of the linear system. For more complex ML problems it is convenient to use iterative methods, which increases likelihood function step by step until a local maximum is reached. The simplest iterative method is gradient ascend method with training step  $\eta$ :

$$\Sigma \mapsto \Sigma + \eta \frac{\partial \mathcal{L}}{\partial \Sigma}, \quad \boldsymbol{\mu} \mapsto \boldsymbol{\mu} + \eta \frac{\partial \mathcal{L}}{\partial \boldsymbol{\mu}}.$$

This update rule defines a pseudo-dynamics of the system. Here we are going to demonstrate that the dynamics can be turned to relaxation of the system with respect to control parameters, if we slightly modify the problem to take into account multiple samples in the training set. We consider two approaches: spatial sampling and temporal sampling. Doing spatial sampling we create  $M$  copies (equals to number of samples) of the initial system with the energy  $E$  such that all copies share the same parameters  $\Sigma, \boldsymbol{\mu}$ . Then energy of the training system is given by:

$$\tilde{E} = \frac{1}{M} \sum_{m=1}^M E[\mathbf{x}^m, \boldsymbol{\mu}, \Sigma].$$

We used normalization multiplier  $1/M$  to closely match results of the maximum likelihood principle, but any multiplier leads to the same result. Derivative of the energy:

$$\frac{\partial \tilde{E}}{\partial \boldsymbol{\mu}} = \frac{1}{M} \sum_{m=1}^M \Sigma^{-1}(\boldsymbol{\mu} - \mathbf{x}^m) = \Sigma^{-1}(\boldsymbol{\mu} - \boldsymbol{\alpha}) = -\frac{\partial \ln \mathcal{L}}{\partial \boldsymbol{\mu}},$$

hence indeed maximization of the likelihood with respect to the biases  $\boldsymbol{\mu}$  is equivalent to minimization of energy with respect to the same parameters. This observation opens new possibilities for devices implementing distribution learning in hardware by dissipation of energy. For that purpose the energy should contain exchange  $\boldsymbol{\mu} \cdot \Sigma^{-1} \boldsymbol{\mu}$  between degrees of freedom corresponding to parameters  $\boldsymbol{\mu}$  and observable variables  $\mathbf{x}$ . For any system with continuous dependence of the energy on the state, the energy can be approximated by harmonic potential near metastable states. Hence until perturbations created by training samples stay small, the system can be trained as described above. Moreover, the exchange term of the required form appears in the Ising and the Heisenberg models of spin systems, in the models the perturbations do not have to be small. The BM based on the Ising model will be considered in Section 3, and BM based on the Heisenberg model is studied in Section 5.

The trained distribution sampling can be done by measuring states of the system while it is in thermal equilibrium. Time interval between observations should be large enough to make measurements uncorrelated. The temperature of the system controls variance. It is common in ML to simulate the system numerically by doing Gibbs sampling. Implementation of the system as a physical device can speed up sampling. If parameters  $\boldsymbol{\mu}, \Sigma$  are part of the design of the device, then to change distribution a new device should be designed and fabricated, which can be expensive and is not practical. However, if  $\boldsymbol{\mu}$  are new degrees of freedom of the device, and the degrees of freedom can be controlled by external impulses, then the device is of general purpose and is reusable.

The strength of the physical implementation of the device is most clearly manifested in automatic fitting of the parameters to match an example distribution. The parameters of the system can be fit without usage of any external devices, only training examples should be provided. Sticking to spatial approach to training, let consider new system, which contains multiple copies of the system used for prediction, and let assume that the subsystems do not interact, except that they share degrees of freedom storing parameters  $\boldsymbol{\mu}$ . The training examples are provided by fixing degrees of freedom corresponding to output value  $\mathbf{x}$ , so that the state of  $\mathbf{x}$  equals to  $\mathbf{x}^m$  on copy  $m$  of the system. As was shown above, relaxation of the system with respect to unfixed parameters  $\boldsymbol{\mu}$  is equivalent to maximization of likelihood of sampling the training set from the distribution generated by the system. The parameter  $\boldsymbol{\mu}$  can be measured after relaxation, and the consumer device can have  $\boldsymbol{\mu}$  be fixed by design, if the device is used only for prediction. On the other hand, the system can be used for online training, then training data is updated according to the current situation, and the prediction

is done by some copies of the system, which still share the parameters with other copies, but whose degrees of freedom  $\mathbf{x}$  are not fixed and are subjected to stochastic dynamics.

Creation of multiple copies of the device can be a tricky engineering task, which also leads to increased size of the device. The temporal approach to training allows us to avoid these problems. Suppose we have a single exemplar of the system. At the moment  $t_m$  of time we apply an external control to fix state  $\mathbf{x}^m$  of the system, then after a fixed interval we switch to the next sample  $\mathbf{x}^{m+1}$  at the time  $t_{m+1}$ . The time derivative of state on each step is given by  $\dot{\boldsymbol{\mu}}_m = \partial E[\mathbf{x}^m, \boldsymbol{\mu}] / \partial \boldsymbol{\mu}$ , the mean velocity is obtained by averaging the derivatives over  $M$  steps

$$\frac{1}{M} \sum_{m=1}^M \frac{\partial E[\mathbf{x}^m, \boldsymbol{\mu}]}{\partial \boldsymbol{\mu}}.$$

which coincides with the velocity in the spatial approach. In contrast to the spatial approach, at each moment the dynamics is determined by one term  $\dot{\boldsymbol{\mu}}^m$ . However, if time steps  $t_{m+1} - t_m$  are infinitesimal, the two dynamics coincide. In practice relaxation time over  $\boldsymbol{\mu}$  should be much larger than the time step. The training either can be made once and the results of the training can be measured and used in another device dedicated only for prediction, or the training can be a continuous process with online update of parameters. In the second case, prediction steps are inserted among the training steps, such that the state  $\mathbf{x}$  is allowed to evolve freely. To avoid drift of the parameters during the prediction phase, the relaxation time with respect to  $\boldsymbol{\mu}$  should be significantly larger than relaxation time of  $\mathbf{x}$ .

### 3. Boltzmann machine

BM is an imaginary device, which state is random, and its distribution can be tuned by the training process. The state of BM is described by discrete random variables  $x_j$ , in the classical form only two values  $\{0, 1\}$  are allowed for the variables. Except for the discrete nature of the state  $\mathbf{x} = (x_j)_{j=1}^N$ , all other parts of BM are very similar to the model described in Section 2. The constraints on values of  $\mathbf{x}$  however make the problem harder to analyze and explicit solutions are not known except for very simple connection matrices. The restrictions also create multiple minima, making the model more expressive.

Main characteristic of BM is its energy, which coincides with the energy of the Ising model. It is customary to write energy of BM in the following form

$$E = \frac{1}{2} \mathbf{x} \cdot A \mathbf{x} - \mathbf{x} \cdot \boldsymbol{\mu},$$

which coincides with (1) up to an abandoned term quadratic with respect to  $\boldsymbol{\mu}$ . Since the variables  $x_j$  are discrete, the energy is bounded for all values of parameters  $A$  and  $\boldsymbol{\mu}$ . The joint distribution of the variables is the Boltzmann distribution:

$$p(\mathbf{x}) = \frac{1}{Z} e^{-E[\mathbf{x}]}, \quad Z = \sum_{\mathbf{x}} e^{-E[\mathbf{x}]}.$$

We drop from notation the parameters  $A$  and  $\boldsymbol{\mu}$ , which are assumed constant here. The abandoned term  $\boldsymbol{\mu} \cdot A \boldsymbol{\mu} / 2$  in the energy does affect normalization constant  $Z$ , but otherwise does not change behavior of BM in any way unless we do consider dynamics with respect to the parameters  $A$  and  $\boldsymbol{\mu}$ .

BM can express complex relationship between variables, if it is augmented with hidden units. Then the state vector is divided into two parts  $\mathbf{x} = (\mathbf{v}, \mathbf{h})$ . All the variables  $\mathbf{x} = (\mathbf{v}, \mathbf{h})$  are separated to two classes:  $\mathbf{v}$  are visible variables and  $\mathbf{h}$  are hidden ones. The model should recreate probability distribution of only visible variables  $\mathbf{v}$

$$p(\mathbf{v}) = \sum_{\mathbf{h}} p(\mathbf{v}, \mathbf{h}), \quad p(\mathbf{v}, \mathbf{h}) = p(\mathbf{x}),$$

hence the training data contains only values of visible variables  $\mathbf{v}^m$ . Training of BM is done by maximization of the likelihood  $\mathcal{L}$ , which is probability of observation of samples  $\mathbf{x}^m$  from the training set for given parameters  $A$  and  $\boldsymbol{\mu}$ :

$$\ln \mathcal{L} = \frac{1}{M} \sum_{m=1}^M \ln p(\mathbf{v}^m | A, \boldsymbol{\mu}) \rightarrow \max. \quad (2)$$

In practice BM is simulated by Gibbs sampling, and the likelihood is statistically estimated. For unconstrained BM the estimate is sufficiently good only for very few variables, resulting in a low training rate. The training can be significantly accelerated, if connections between variables in  $A$  are restricted in such a way that visible variables can not interact with themselves, and the same is true for the hidden variables. BM satisfying the condition is called restricted Boltzmann machine (RBM). The energy of RBM has the following form,

$$E = -\mathbf{v} \cdot W\mathbf{h} - \mathbf{c} \cdot \mathbf{h} - \mathbf{d} \cdot \mathbf{v}.$$

where  $W$  is the interaction matrix,  $\mathbf{c}$  and  $\mathbf{d}$  are biases for hidden and visible units respectively. The maximum of the likelihood can be computed by gradient ascend method with some small learning rate  $\eta > 0$ :

$$a \mapsto a + \eta \frac{\partial \ln \mathcal{L}}{\partial a},$$

applied for all parameters  $a = \mathbf{c}, \mathbf{d}, W$ . The derivatives can be computed explicitly:

$$\frac{\partial \ln \mathcal{L}}{\partial a} = G_a^+ - G_a^-, \quad G_a^+ = \frac{1}{M} \sum_{m=1}^M \frac{\partial}{\partial a} \ln \left( \sum_{\mathbf{h}} e^{-E[\mathbf{v}^m, \mathbf{h}]} \right), \quad G_a^- = \frac{\partial}{\partial a} \ln \left( \sum_{\mathbf{v}, \mathbf{h}} e^{-E[\mathbf{v}, \mathbf{h}]} \right).$$

The positive gradient  $G_a^+$  can be expressed as average over all samples from the training set of the expectation value of the  $-\partial E/\partial a$  over the hidden units:

$$G_a^+ = -\frac{1}{M} \sum_{m=1}^M \sum_{\mathbf{h}} p(\mathbf{v}^m | \mathbf{h}) \frac{\partial E[\mathbf{v}^m, \mathbf{h}]}{\partial a} = \frac{1}{M} \sum_{m=1}^M \mathbb{E} \left[ -\frac{\partial E}{\partial a} \middle| \mathbf{v}^m \right].$$

The negative gradient  $G_a^-$  is similar to  $G_a^+$ , but the expectation value is taken with respect the the model distribution of  $\mathbf{v}$ , instead of average over samples from the training set:

$$G_a^- = \mathbb{E}[-\partial E/\partial a].$$

The expectation values can be computed as sum over all outcomes for small BM. For a large number of variables the expectation values are estimated by Monte-Carlo method.

BM has a wide variety of uses, most prominent as associative memory and generative models. When used as an associative memory, BM is provided with partial (or noisy) input, that is only part of visible variables are set to the correct values in the initial state. Running simulation of BM the energy of the state is relaxed and BM is found in one of the remembered states, which is close to the initial state. The final state is a restored state associated with the initial state.

The visible variables can contain arbitrary information, for example we can split the variables into two parts: the first contains features, and the second contains labels. Given features, BM can assign labels by association. Thus BM can be used to solve classification problems.

#### 4. Classification problem

The classification is a problem of assigning labels  $l$  to objects, described by their features  $\phi$ . To take into account disputable cases, it is convenient to compute probability distribution over labels, instead of labels themselves. The probability distribution can be differentiated in contrast to discrete labels, which is necessary for many ML algorithms. Every mapping from the features  $f$  to the probability distributions over the labels  $l$  is called a classifier. We will denote  $f(\phi)_l$  probability of  $\phi$  to belong to the class  $l$ . Doing ML we assume that the classifier belongs to a class of functions parameterized by vectors  $\theta$ ,  $f = f(\phi; \theta)$ . The parameters  $\theta$  can be found by minimizing a loss function  $L$ , used to compare the model prediction and values from the training set  $(\phi^m, l^m)$ . The predicted probability distribution  $p = f(\phi; \theta)$  for fixed  $\phi$  can be compared with correct distribution  $\tilde{p}$  given by its samples  $\{\tilde{l}^k\}_{k=1}^K = \{l^m : \phi^m = \phi\}$  using the following estimate for the cross-entropy:

$$H(\tilde{p}, p) = \mathbb{E}_{\tilde{p}}[-\ln p] \approx -\frac{1}{K} \sum_{k=1}^K \ln p_{l^k}.$$

Averaging the estimate over all inputs  $\phi$  we obtain common definition for loss function:

$$L_{KL}[\theta] = -\frac{1}{M} \sum_{m=1}^M \ln f(\phi^m; \theta)_{l^m}, \quad (3)$$

which coincides with Kullback–Leibler (KL) divergence between model prediction and the distribution of training samples up to a constant. For comparison we also used mean square error (MSE) estimate:

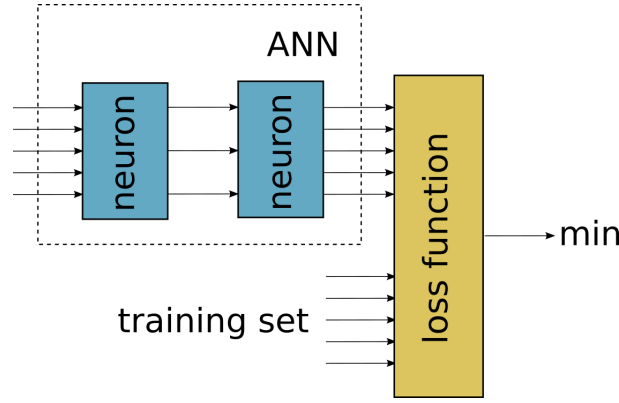


FIG. 1. Schematic of ANN composed of several layers, each representing a simple nonlinear transform with some parameters. Parameters are fitted by minimization of a loss function, which compares prediction of ANN with the training set containing ground truth data

$$L_{MSE}[\theta] = \frac{1}{MZ} \sum_{m=1}^M \sum_{k=1}^Z |f(\phi^m; \theta)_k - \delta_{l^m, k}|^2,$$

where  $Z$  is the number of different labels. The optimal parameters  $\theta$  can be found by minimization of the loss:

$$\operatorname{argmin}_{\theta} L[\theta],$$

which can be done e.g. by gradient descent with the training step size constant  $\eta$ :

$$\theta \mapsto \theta - \eta \frac{\partial L}{\partial \theta}.$$

#### 4.1. Artificial neural network

One of the most popular models in ML is ANN, see Fig. 1 in the case, where  $f = f_1 \circ \dots \circ f_D$  is a composition of functions, called layers, of the form

$$f_d(\phi) = a_d(\psi), \quad \psi_k = \sum_j A_{d, kj} \phi_j + B_{d, k},$$

where  $A_d$  is a matrix,  $B_d$  is a bias, and  $a_d$  is an activation function. Since our ANN should return probability distribution, the activation function of the last layer is the softmax function

$$a_D(\psi)_k = \operatorname{softmax}(\psi)_k = \frac{e^{\psi_k}}{\sum_k e^{\psi_j}}.$$

Common choice for other layers is sigmoid functions, e.g.

$$a_d(\psi)_k = \sigma(\psi)_k = \frac{1}{2} + \frac{1}{\pi} \arctan \psi_k.$$

The parameters  $\theta$  for ANN consists of matrices and biases of linear layers:

$$\theta = (A_1, B_1, \dots, A_D, B_D).$$

The gradient of the loss function with respect to parameters, required for training, is computed using backward propagation:

$$\frac{\partial L}{\partial A_d} = \frac{\partial L}{\partial \mathbf{y}} \frac{\partial f_D}{\partial \mathbf{x}_{D-1}} \dots \frac{\partial f_{d+1}}{\partial \mathbf{x}_{d+1}} \frac{\partial f_d}{\partial A_d},$$

where  $\mathbf{y} = L(\mathbf{x}_D)$ ,  $\mathbf{x}_{d+1} = f_d(\mathbf{x}_d)$ ,  $\mathbf{x}_1 = \phi$ . The expression for  $B_d$  is analogous.

As the most basic benchmark for the classifier, consider binary classification problem that maps single value  $\phi \in [-1, 1]$  to one of two classes  $\{0, 1\}$ . We assume that all values  $\phi$  larger certain threshold  $\phi_0$  belongs to the class 1, and the

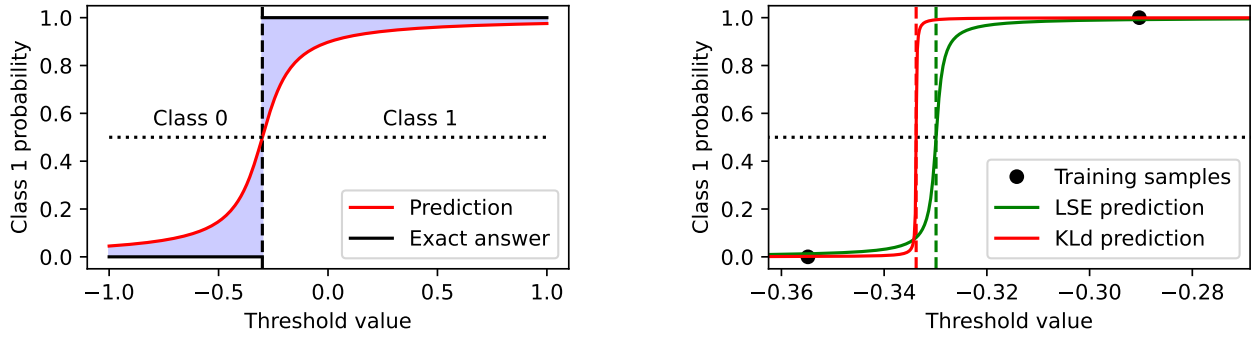


FIG. 2. (left) Binary classification problem with single input. All values smaller than the threshold belong to class 0, all other to class 1. The ML model predicts the probability of a value belonging to class 1. (right) Prediction made by ANN trained on 30 samples using MSE and KL-divergence loss functions. Only a region, where predictions are divergent from the exact answer, is shown

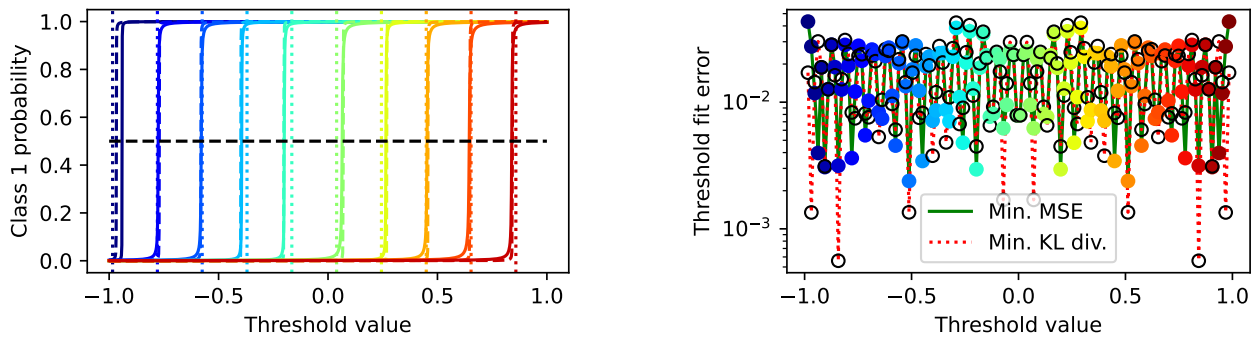


FIG. 3. (left) Predictions of ANN for the benchmark classification problem for different values of the threshold (shown by dotted vertical lines). Solid lines correspond to MSE loss, dashed line, to KL-divergence. (right) Error of fitted threshold values for MSE (filled color circles) and KL divergence losses

smaller values to the class 0. The probability distribution for the binary classifier is completely defined by the probability  $p_1 = f(\phi; \theta)$  of the specimen belonging to the class 0. The ideal classifier in the case is defined by the function

$$f_0(\phi) = \begin{cases} 0, & \phi \leq \phi_0, \\ 1, & \phi > \phi_0. \end{cases}$$

This step function, despite its simplicity, is not suitable for training, since it has zero gradient, except single point, where it is not differentiable. An appropriate model is an approximation of the step function with a sigmoid function  $\sigma$ , we use the following model:

$$f(\phi; \theta_1, \theta_0) = \sigma(\theta_1 \phi + \theta_2).$$

Then the threshold value can be approximated by  $\phi_0 \approx -\theta_2/\theta_1$ . The left panel in Fig. 2 demonstrates both ideal classifier and the model one.

To demonstrate fitting of the threshold parameter, we train our model on a set of samples containing  $M = 32$  uniformly distributed on the interval  $[-1, 1]$  values  $\phi^m$ , and the corresponding labels  $l^m = f_0(\phi^m)$ . The loss function is defined by Equation (3). The output of the trained model is shown on the right pane of Fig. 2. As can be seen, the model does not have enough data to find precise value of the threshold, instead the approximate threshold value is put on the maximum distance from point of both classes, which is not surprising, since our model is also a particular case of a support vector machine.

We repeated the training for different threshold values and estimated accuracy. The result is shown in Fig. 3. The metrics achieves 100% accuracy, except for the point  $\phi_0 = 1$ , where a single point belongs to the class 1. Both KL-divergence and MSE losses demonstrate very similar performance. The error of estimation of the threshold value  $\phi_0$  is within resolution of the training data for all values of  $\phi_0$ .

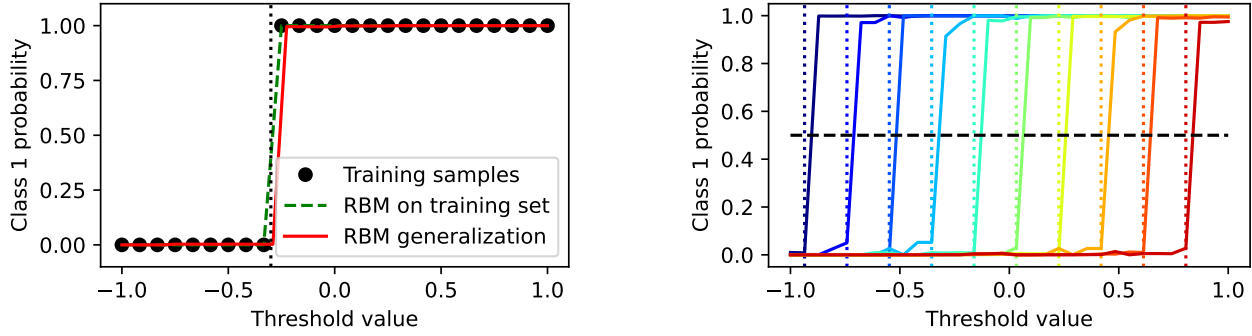


FIG. 4. (left) Prediction of RBM trained on 24 samples shown as black dots. Dotted vertical line represents exact threshold value. Prediction computed on the training set is represented by green dashed lines. Prediction on 32 samples not available in the training set is shown by the red solid line. (right) Prediction of RBM model for different values of threshold indicated by vertical dotted lines

Our trivial problem is solved exceptionally well by the very simple ANN, more complex networks are capable of solving problems of artificial intelligence. Both prediction and training of ANN are done in modern time on GPU or TPU devices, capable of computing arbitrary functions. The digital devices can compute the gradient with a high precision, but the high precision is not important for ANN training, therefore a recent trend is to reduce precision of computing to trade speed and reduce power consumption. Since ANN computation is analog in nature, it would be beneficial to implement it as an analog computer. However, it is hard to find a physical system that implements arbitrary activation functions and linear algebra naturally. Instead BM has natural physical counterparts and can be implemented directly in hardware more effectively than in simulation. The flexibility may be an issue. In the next section we will show, how to adapt BM easily to different problems.

#### 4.2. Restricted Boltzmann machine

There are two common approaches to use RBM for classification. In the first approach RBM is used as a feature extractor, which maps visible variables to the latent variables, which are processed by a simple classifier, such as logistic regression. We will use the second approach, where the classification problem is solved solely by RBM. The visible variables  $v = (\mathbf{f}, l)$  are separated to the vector of features  $\mathbf{f}$  and the label  $l$  (we restrict ourselves to binary classification problems, hence  $l \in \{0, 1\}$ ). To encode the variable  $x \in [-1, 1]$  as a bit string  $\mathbf{f} \in \{0, 1\}^R$ , we map  $x$  to the unit interval by  $y = (x + 1)/2$ , and let  $\mathbf{f}$  be first  $R$  digits in the binary representation of  $y$ :

$$y = \sum_{l=1}^L 2^{-lf_{l-1}} + r, \quad |r| < 2^{-L}.$$

The distribution of the random pairs  $(\mathbf{f}, l)$  generated by RBM can be fitted according to the training set  $(x^m, l^m)$ . In the considered case the samples  $x^m$  are given by their approximated values  $\mathbf{f}^m$  known with the resolution  $R$ . When we solve classification problem, we do not interested in the distribution of  $\mathbf{f}$  itself, instead we are interested in the conditional distribution  $p(l|\mathbf{f})$ , hence the likelihood function (2) should be replaced by the conditional one:

$$\ln \mathcal{L} = \frac{1}{M} \sum_{m=1}^M \ln p(l^m | \mathbf{f}^m, A, \boldsymbol{\mu}) \rightarrow \max.$$

We made tests with RBM for the same binary classification problem as above with the resolution  $L = 5$ , which gives 32 different values of  $x$ . A handmade implementation of RBM in Python+NumPy was used. Total number of visible neurons was 6, namely  $R = 5$  for features plus 1 for the label. We used three hidden units. All the training data were put into one batch. The RBM was trained 1000 iterations with step size 10, which resulted in the loss function value approximately  $10^{-3}$ . The left pane of Fig. 4 demonstrates the result of the training on the dataset containing 25 uniformly distributed values of  $x^m$  out of 32 possible different values. The generalization result is perfect in the case and the threshold value is computed with precision of approximation of  $x$  by  $\mathbf{f}$ . We also tried to decrease the size of the training set, which however results in large errors at random values of  $\mathbf{f}$ . Since RBM initially has no information on the nature of the functions it is approximating, enough information should be provided to the machine to conclude that the function is a step function.

We repeated training of the RBM classifier for different threshold values  $\phi_0$  including all different values of  $\mathbf{f}$  into the training set. The model predictions are shown in the right pane of Fig. 4, one line corresponds one value of  $\phi_0$ , the

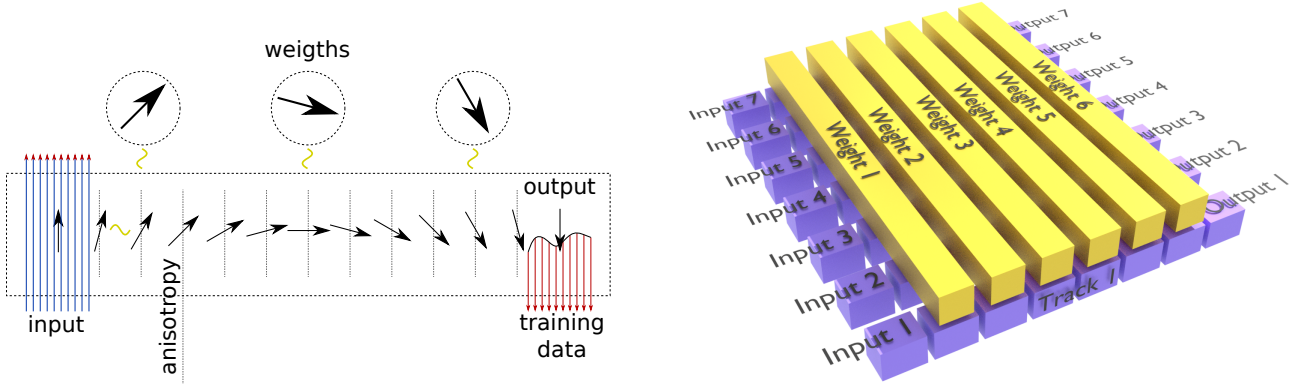


FIG. 5. (left) Schematic diagram of SBM consisting of chain of data spins, and weight spins associated with each data spin. Visible spins are attached to the ends and are controlled by the external magnetic field. Result is read from the rightmost spin. (right) Spatial approach to SBM training. Data spins are multiplied to match the number of training samples. Weight spins are shared by all copies of data spins

values themselves are shown as the vertical dotted lines. The classification was done without mistakes, both precision and recall were 100%.

The considered BM is an analog of the Ising model, hence each spin has one of two possible values  $\{-1, 1\}$ . The Heisenberg model allows the magnetic moment to point in arbitrary direction, hence is applicable for wide range of magnetic systems. In the next section we define a generalized BM based on the Heisenberg model.

## 5. Spin Boltzmann machine

Consider the Heisenberg model of a magnetic substance. The state of the system is defined by vector of magnetic moments  $\mathbf{M}_j \in \mathbb{R}^3$ , which are associated with atoms  $j$  or larger uniformly magnetized clusters. In the considered timescale the length  $M_j$  is constant, hence magnetization can be defined by its direction  $\mathbf{M}_j = M_j \mathbf{S}_j$ ,  $\|\mathbf{S}_j\| = 1$ . The energy of the system includes the Heisenberg exchange energy:

$$E_{ex} = -\frac{1}{2} \sum_{j \neq k} J_{jk} \mathbf{S}_k \cdot \mathbf{S}_j,$$

where the exchange matrix  $J$  is symmetric,  $J_{jk} = J_{kj}$ . We also include easy axis anisotropy with axis  $\hat{z}$  and constant  $K_j > 0$ , which makes states  $\pm \hat{z}$  metastable for isolated spins, these states correspond to states  $\pm 1$  for BM or the Ising model:

$$E_{ani} = -\sum_j K_j S_{j,z}^2.$$

The last necessary contribution to the energy is Zeeman one, that is the energy of interaction with external magnetic field  $\mathbf{B}$ :

$$E_B = -\sum_j M_j \mathbf{B}_j \cdot \mathbf{S}_j.$$

We consider spins  $\mathbf{S}_j$  a generalization of the variables  $x_j$  of BM. The energy  $E = E_{ex} + E_{ani} + E_B$  is a close analog of energy of BM, and the energies coincide up to re-normalization if  $K_j$  and  $B_j$  are infinite. If a strong magnetic field is applied to a spin, the spin tends to rotate along the field, spiraling to the direction of the field due to the damping. Hence the external field  $\mathbf{B}$  allows us to control individual spins or to define inputs of BM. For all other spins the field is set to zero that allows them to rotate freely.

The dynamics of the system is defined by stochastic Landau-Lifshitz-Gilbert equation [46]:

$$\dot{\mathbf{S}}_j = \frac{\gamma}{\mu_j} \mathbf{S}_j \times \left( -\frac{\partial E}{\partial \mathbf{S}_j} + \dot{W}_j \right) + \gamma \alpha \mathbf{S}_j \times \frac{d\mathbf{S}_j}{dt},$$

where  $\gamma$  is the gyromagnetic ratio,  $\alpha > 0$  is the dissipation constant and  $W_j = W_j(t)$  a Wiener process. Assuming the external field is constant, the probability density of states tends to the Boltzmann distribution:

$$\rho(\mathbf{S}) = \frac{1}{Z} e^{-\beta E[\mathbf{S}]}, \quad Z = \int_{\mathbb{S}^2} d\mathbf{S}_1 \cdots \int_{\mathbb{S}^2} d\mathbf{S}_N \cdot e^{-\beta E[\mathbf{S}]},$$

where  $\beta$  is the inverse temperature. Although dynamics of the Heisenberg model is different from BM or Hopfield networks, the final distribution is the same, hence the Heisenberg model can be used in ML in the same way as BM. We call the BM based on the Heisenberg model spin Boltzmann machine (SBM).

We split all spins to three groups: visible  $I_v$ , hidden  $I_h$  and weights  $I_w$ ; restriction of vector field  $S$  to spins from a group  $I_k$  we denote  $S^k$ , e.g.  $S^v = \{\mathbf{S}_j : j \in I_v\}$ . The first two groups are a direct analog of visible and hidden variables in BM, we will call them data spins  $I_d = I_v \cup I_h$ . The last group is an analog of parameters  $\mu$  in the model (1). We include some parameters of BM as degrees of freedom in our system, which allows us to train the model on new data and to reuse the device for new problems.

The visible spins are used as inputs and outputs, therefore the external field is applied only to these spins. If SBM functions in associative memory mode, the external magnetic field is only applied to the spins, which input values are known, all other spins rotate freely to relax the energy of the system. Magnetic field generated by the relaxed state is measured and decoded as an output of the SBM. For the classification problem we split the visible spin  $I_v$  to the group of inputs  $I_{in}$  and outputs  $I_{out}$ . The features are fed to SBM by applying an external field to spins  $I_{in}$ . In the prediction mode the external field is zero on the outputs  $I_{out}$ , and the probability distribution over labels are read from the spins  $I_{out}$ . In the training mode both spins  $I_{in}$  and  $I_{out}$  are constrained by the external field to match a sample from the training set.

Weights spins should interact with data spins, but the interaction can be quite arbitrary. We restrict ourselves to a simple case, where every data spin  $j \in I_d$  is associated with exactly one weight spin  $w(j) \in I_w$ , and the weight spin interacts only with the corresponding data spin. The data spins interact with each other, the interaction matrix defines correlation between the variables. Taking into account specialization of all spins, the energy of the system can be expressed in the form  $E = E_d[\mathbf{S}^d, \mathbf{S}^w] + E_w[\mathbf{S}^w]$ , where energy of data spins is given by:

$$E_d[\mathbf{S}^d, \mathbf{S}^w] = - \sum_{j \in I_v} \mu_j \mathbf{B}_j \cdot \mathbf{S}_j - \sum_{j \in I_d} K_j S_{j,z}^2 - \sum_{j \in I_d} J_j^w \mathbf{S}_j \cdot \mathbf{S}_{w(j)} - \frac{1}{2} \sum_{\substack{j,k \in I_d \\ j \neq k}} J_{ik}^d \mathbf{S}_j \cdot \mathbf{S}_k.$$

The energy of self-interaction of weight spins  $E_w$  will be discussed below.

If dissipation constant is assumed to be large, then the relaxation dominates oscillations, and LLG equation can be approximately written in the following form:

$$\dot{\mathbf{S}}_j = \frac{\gamma\alpha}{\mu_j} \mathbf{S}_j \times \mathbf{S}_j \times \frac{\partial E}{\partial \mathbf{S}_j}. \quad (4)$$

The state of both data spins  $S^d$  and weight spins  $S^w$  are changed by the dynamics. However, we require magnetic moments  $M_j$  to be much larger for weights  $j \in I_w$  than for data  $j \in I_d$  to ensure that variation of weight is much slower than for data spins.

We distinguish two modes of operation of SBM: prediction and training modes. In the prediction mode SBM assigns a label to the object described by its features. In the mode the weight  $\mathbf{S}^w$  are assumed to match the problem before running the algorithm, that is SBM should be trained in advance. The algorithm of usage of SBM in the prediction mode is as follows:

- (1) Apply an external magnetic field to the input spins  $I_{in}$  according to the provided features.
- (2) Let SBM relax.
- (3) Read magnetic field on output spins  $I_{out}$ , statistics of the measurements defines probability distribution over labels.

Computation time must be much shorter than the relaxation time of the weight spins, but the second step must be longer than the relaxation time of the data spins, which can be achieved by appropriate choice of magnetic moments. If SBM is used only for prediction, the self-interaction energy of weights is not important, moreover the weight spins can be completely eliminated, and external magnetic field is substituted for the effective magnetic field produced by the weight spins. Without weights spins SBM coincides with BM generalized to the Heisenberg model.

Another mode of operation of SBM is the training mode. In the training mode we want to minimize average energy of SBM, where minimization is done with respect to the weight spins  $I_w$ , and the average is taken over samples from the training set fed to the visible spins  $I_v$ . The training can be done using spatial or temporal approaches (or mixture of both), introduced at the end of Section 2. In the spatial approach each sample of the training set is fed to its own copy of the data spins, herewith all copies share the same weight spins. Energy of the system for the spatial training

$$E = E_w[\mathbf{S}^w] + \frac{1}{M} \sum_{m=1}^M E_d[\mathbf{S}^{d,m}, \mathbf{S}^w].$$

The data samples are encoded by the external magnetic field on  $m$ -th copy of the visible spins  $\mathbf{S}^{v,m}$ . The external field is set constant, while the relaxation with respect to weight spins  $\mathbf{S}^w$  is going on.

In the temporal approach a single exemplar of the system is enough, but data samples from the training set are fed one by one. In this approach the external magnetic field is not constant, but at each given moment encodes one sample from the dataset. The mean effective field acting on the weight spins is the same as in the spatial approach, hence relaxation dynamics are expected to be the same. The training algorithm for SBM in mixed spatial-temporal approach is as follows:

- (1) Apply training samples to visible spins of all copies of the system. External magnetic field is applied to both inputs  $I_{in}$  and outputs  $I_{out}$  encoding features and labels respectively.
- (2) Wait a period of time sufficient to relax data spins  $I_d$ .
- (3) Repeat from step 1 with new training samples, until convergence of weight spins.

The algorithm resembles stochastic gradient descent commonly used for training on ANN. Recall that relaxation time for weight spins is much larger than for data spin, which is necessary for the convergence of the training iterations.

As was shown in section 2 the minimization of energy with respect to weights is equivalent to minimization of Kullback-Leibler divergence between predicted distribution and distribution of training data, at least if the state is defined by vectors from  $\mathbb{R}^N$ . On the other hand, the training can be considered as a process of memorization of the training data. Consider a simple case of one sample in the training set, and let there be no hidden spins. During the training phase, we find state of the weight spins  $\mathbf{S}^w$  which minimize energy assuming fixed state of visible spins  $\tilde{\mathbf{S}}^v$

$$\tilde{\mathbf{S}}^w = \operatorname{argmin}_{\mathbf{S}^w} E[\tilde{\mathbf{S}}^v, \mathbf{S}^w].$$

In the prediction phase, given weights obtained from the training, we expect that minimum of energy  $E$  with respect to the visible spins should revive training sample  $\tilde{\mathbf{S}}^v$ :

$$\tilde{\mathbf{S}}^v = \operatorname{argmin}_{\mathbf{S}^v} E[\mathbf{S}^v, \tilde{\mathbf{S}}^w]. \quad (5)$$

Thus for every vector  $\tilde{\mathbf{S}}^v$  there should be a vector  $\tilde{\mathbf{S}}^w$  such that  $E$  has minimum at the point  $(\tilde{\mathbf{S}}^v, \tilde{\mathbf{S}}^w)$  with respect to both arguments. The simplest way to ensure the condition is to define energy as a symmetric function with respect to swap of arguments  $\mathbf{S}^d$  and  $\mathbf{S}^w$ . Exchange term between data spins and weights is already symmetric. Since we have freedom of definition of self-interaction of weights  $E_w$ , we can define exchange constants to be equal to exchange constants for data spins:

$$E_w = - \sum_{\substack{j,k \in I_d \\ j \neq k}} J_{d,jk} \mathbf{S}_{w(j)} \cdot \mathbf{S}_{w(j)}.$$

Introduction of interaction between weights is not strictly speaking necessary to satisfy the condition (5). Since magnetic moments directions are subjected to normalization condition  $\mathbf{S}_j^2 = 1$ , the energy functional is always bounded, hence it has at least one minimum. During the training phase, the system is relaxed with respect to both data spins and weight spins, hence the result of the minimization should be minimum with respect to all degrees of freedom, which ensures the condition (5).

## 6. Benchmark

We check the performance of SBM on a simple binary classification problem introduced in Section 4. Internal structure of SBM in this case can be as simple as a chain of  $N$  spins, see the left panel in Fig. 5. Denote  $\mathbf{S}_{0,j}$  the state of the data spin  $j$ , and  $\mathbf{S}_{1,j}$  the state of the corresponding weight. For simplicity we assume interaction constant between data spins to be constant  $J$ . The easy axis anisotropy with axis  $\hat{z}$  and constant  $K$  is applied to the chain. Interaction between data spin and the corresponding weight is set to a constant value  $W$ . The weight spins do not interact with each other. All spins except the first and the last are hidden. The first spin is an input, and the last spin is an output. The control is applied as external magnetic field to the spin 1, and during the training phase to the spin  $N$ . We assume that magnetic moments of all data spins equal to a constant  $\mu_0$ , and all magnetic moments of weight spins equal to a constant  $\mu_1 \gg \mu_0$ . The resulting energy functional is as follows:

$$E[S] = -J \sum_{j=2}^N \mathbf{S}_{0,j-1} \cdot \mathbf{S}_{0,j} - W \sum_{j=1}^N \mathbf{S}_{0,j} \cdot \mathbf{S}_{1,j} - K \sum_{j=1}^N S_{0,j,z}^2 - \mu_0 (\mathbf{B}_0 \cdot \mathbf{S}_{0,0} + \xi \mathbf{B}_N \cdot \mathbf{S}_{0,N}).$$

Input value  $\phi \in [-1, 1]$  is encoded in direction of the magnetic field as

$$\mathbf{B}_0 = B\phi\hat{z} + B\sqrt{1-\phi^2}\hat{x}.$$

The class  $l$  in the training data is mapped to the vector field as follows:

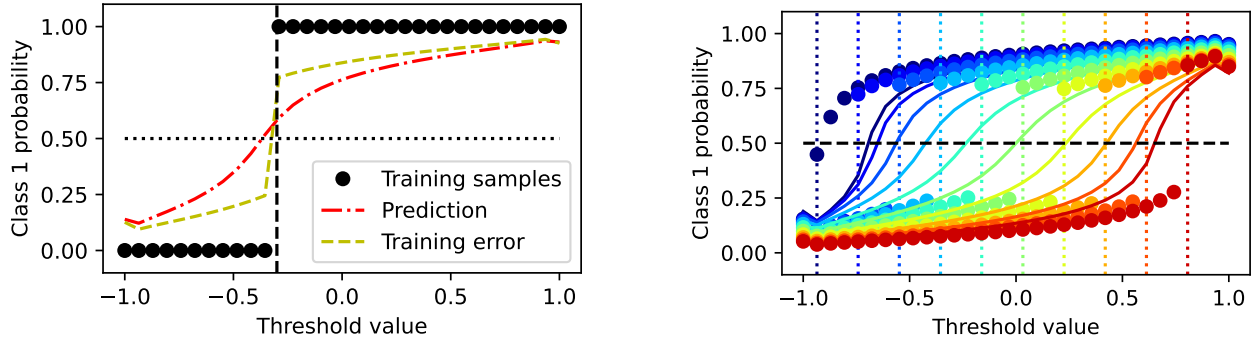


FIG. 6. (left) Output of SBM trained on 32 samples shown by black dots. The threshold value is marked by a vertical dashed line. Red solid line demonstrates model prediction. Yellow dash-dotted line shows output of SBM during the training. (right) SBM prediction (solid lines) for different values of the threshold (vertical dotted lines)

$$\mathbf{B}_N = \begin{cases} B\hat{z}, & l = 1, \\ -B\hat{z}, & l = 0. \end{cases}$$

The output of SBM is given by  $z$  projection of the last spin in the chain. The probability  $p_1$  of class 1 is decoded in the following way, consistent with representation of the training data:

$$p_1 = 2S_{0,N,z} - 1. \quad (6)$$

We use the spatial approach for the training, creating  $M$  copies of the system (by number of samples in the training set), such that all copies share the same weights. One possible organization of the device is shown in the right pane of Fig. 5. The data spins are organized in parallel chains in bottom layer of the system, while weight spins lies in the upper layer. The weights are made of material having high magnetic stiffness to ensure their coherent rotation, each weight can be considered as a single spin having a large magnetic moment. The weights cross all chains containing data spins and interact with all of them with the same exchange constant. The chains of data spins do not interact with each other. We assume the small size of the system, then the demagnetizing field can be neglected. Since there is no special restriction on interaction between spins for general SBM, larger systems with dipole-dipole interaction should probably function as well as SBM, but this is a subject of further research.

We have selected the following parameters of SBM, which give deterministic result for random initial state of spins:

$$J = 3J_0, \quad W = 0.05J_0, \quad K = 0.07J_0, \quad \mu_0 B = J_0,$$

where  $J_0$  is an arbitrary unit of energy. As a training set we use 32 uniformly distributed values  $\phi^m$  on the interval  $[-1, 1]$  and the corresponding label  $l^m = \theta(\phi^m - \phi_0)$ , where  $\theta$  is Heaviside step function. The left panel in Fig. 6 demonstrates the result of the training for a fixed  $\phi_0 = -0.3$ . Each sample was fed to the corresponding copy of the spin chain by applying an external magnetic field both to the first and the last spins. Then the system was relaxed to minimize total energy over all degrees of freedom. The initial state of weight spins is random, hence the final state is also random. However, for the chosen values of parameters only one minimum is possible, hence the result is deterministic. We observed that if too strong magnetic field is applied, the orientation of inputs and outputs match exactly the direction of the field, but when the field is removed the end spin start rotating forgetting its target direction. Hence we used a moderate field  $\xi = 0.08$ .  $z$ -projection of the output spin is labeled as training output in Fig. 6. The output of SBM was computed once again on the same inputs doing prediction. The input  $\phi^m$  was encoded to the first spin in every chain by applying the corresponding external field. No external field is applied to the last spin in the chains. The energy of the system is minimized assuming weights are fixed. The  $z$ -projection of the last spin in every chain is decoded as output, labeled in Figure as the prediction result. The output does not recover the training sample, but the threshold value is determined correctly.

To check performance of SBM for different threshold values, we repeated the training for 32 different values of  $\phi_0 = \phi^m$ . The result is shown in the right pane in Fig. 6. Each line corresponds to one threshold value, the vertical dashed line marks the corresponding  $\phi_0$ . Dots show output of SBM in the training mode, that is orientation of the output spins decoded according to (6). Even when external field is applied to the output spin, its magnetic moment does not align with the magnetic field perfectly. The alignment can be enforced by a stronger training field, but after turning the field off the output spin will rotate to a larger angle, resulting in larger errors in prediction mode.

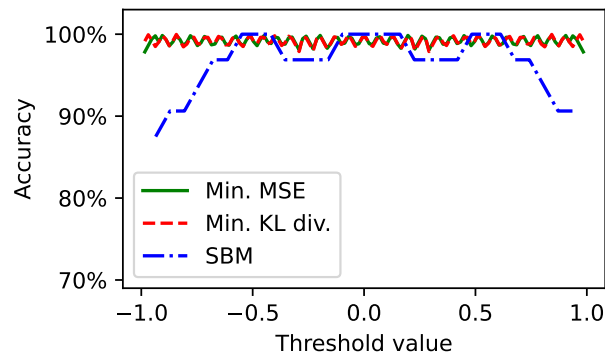


FIG. 7. Accuracy of classification by ANN with MSE loss (solid green line), ANN with KL-divergence loss (dashed red line) and SBM (dash-dotted blue line)

Metrics for the solution of the classification problem for ANN and SBM are shown in Fig. 7 on the left and right panels respectively. Accuracy of ANN is always greater 97%, while accuracy of SBM stays greater than 87%. The largest error occurs for extreme values of the threshold, where small variation of z-projection of the magnetic moment corresponds to large rotation of spin increasing overall error.

## 7. Conclusion

We extended BM by including weight spins, which play the role of biases. The Heisenberg model of a magnetic system is used, which is more accurate than the Ising model. We call the generalization SBM. SBM can be implemented as a device based on artificial spin ice. The weights can be tuned to enable SBM to solve different problems, therefore the device becomes reusable. We proposed a scheme and an algorithm of training of SBM on a given training set, which is in the essence relaxation with respect to weight spins, when inputs and outputs are fixed by the external magnetic field according to the training examples. If state space is a Euclidean space, then the minimization of energy is equivalent to minimization of Kullback-Leibler divergence. For magnetic systems, where magnetic moments are constrained, the exact optimization target is unknown, but SBM nevertheless can function as associative memory. We tested the performance of SBM on a simple binary classification problem and compared the results with the one of an ANN and standard BM. SBM was able to solve the problem, but the accuracy was lesser than the one of ANN and BM, since the exchange matrix in SBM was fixed, while all weights in ANN and BM were optimized. Due to the very simple design of SBM, small sizes and absence of power consumption for computations itself (power is consumed only for input-output), SBM can be an efficient realization of ML devices of the future.

Weight spins of SBM are a tunable analog of biases in BM, but exchange matrix is fixed both in SBM and in BM, that is exchange matrix should be precomputed by a training algorithm using general purpose computers and then fabricated during the manufacturing of the device implementing BM or SBM. The exchange matrix is crucial in determination of correlations between inputs and outputs. The relative poor performance of SBM in the benchmark can be addressed to the fact that the exchange matrix was not tuned. Exchanges between spins in real physical devices are harder to control than biases, however, we believe that this can be done using materials, which demonstrate three or four spins interaction [47]. If spins with large magnetic moments are added to such systems, in a short time scale their state can be considered as constant, but it will affect interaction between other spins.

In the studied benchmark we restricted ourselves to nearest-neighbors interactions. This assumption is valid only for nanoscale systems or near neighbor spin ice [48], where dipolar interactions do not manifest themselves. For larger devices all parts of the systems interact with each other due to the demagnetizing field. The general principles of operation of SBM do not restrict long range interactions between spins, hence the general approach should be applicable to dipolar spin ice, however their performance in this mode is a subject of another study.

In the proposed SBM, relaxation is used both for prediction and for training, but the training process takes orders of magnitude longer than prediction. Relaxation takes much longer than spin waves propagation through the system, hence significant speed up can be achieved, if the relaxation will be used only for training and prediction will be done by wave propagation. Logic devices based on spin-waves were previously demonstrated in [49]. These devices can be augmented with controlled scatterers, which can be fitted by ML methods.

## References

- [1] Alzubaidi L., Zhang J., Humaidi A.J. et al. Review of deep learning: concepts, CNN architectures, challenges, applications, future directions. *J. Big Data*, 2021, **8**(53).
- [2] Karniadakis G.E., Kevrekidis I.G., Lu L. et al. Physics-informed machine learning. *Nat Rev Phys*, 2021, **3**, P. 422–440.
- [3] Hebb D.O. *The Organization of Behavior*. New York: Wiley & Sons.: 1949, 365 p.
- [4] Marvin M., Papert S.A. *Perceptrons: An Introduction to Computational Geometry*. The MIT Press.: 1969, 292 p.

- [5] Reuther A., Michaleas P., Jones M. AI and ML Accelerator Survey and Trends. 2022 IEEE High Performance Extreme Computing Conference (HPEC).
- [6] Siegelmann H.T. *Neural Networks and Analog Computation: Beyond the Turing Limit*. Springer: 1999.
- [7] Sun Z., Pedretti G., Ambrosi E. et al. Solving matrix equations in one step with cross-point resistive arrays. *PNAS*, 2019, **116**(10), P. 4123.
- [8] Hughes T.W., Williamson A.D., Minkov M., Fan Sh. Wave physics as an analog recurrent neural network. *Science Advances*, 2019, **5**(12).
- [9] Grollier J., Querlioz D., Stiles M. D. Spintronic Nanodevices for Bioinspired Computing. *Proc IEEE Inst Electr Electron Eng.*, 2016, **104**(10), P. 2024–2039.
- [10] Torrejon J., Riou M., Araujo F. et al. Neuromorphic computing with nanoscale spintronic oscillators. *Nature*, 2017, **547**, P. 428–431.
- [11] Stephan A.W., Lou Q., Niemier M.T., Hu X.S., Koester S.J. Nonvolatile Spintronic Memory Cells for Neural Networks. *IEEE Journal on Exploratory Solid-State Computational Devices and Circuits*, 2019, **5**(2), P. 67–73.
- [12] Ostwal V., Zand R., De Mara R. A Novel Compound Synapse Using Probabilistic Spin–Orbit–Torque Switching for MTJ-Based Deep Neural Networks. *IEEE Journal on Exploratory Solid-State Computational Devices and Circuits*, 2019, **5**(2), P. 182–187.
- [13] Bläsing R., Khan A.A., Filippou P.Ch. Magnetic Racetrack Memory: From Physics to the Cusp of Applications Within a Decade *Proceedings of the IEEE*, 2020, **108**(8), P. 1303–1321.
- [14] Sai L., Wang K., Xichao Zh. Magnetic skyrmions for unconventional computing. *Materials Horizons*, 2021, **8**(3), P. 854–868.
- [15] Vakili H., Xu J-W., Zhou W. Skyrmionics—Computing and memory technologies based on topological excitations in magnets. *Journal of Applied Physics*, 2021, **130**, 070908.
- [16] Song K. M., Jeong J-S., Pan B, et al. Skyrmion-based artificial synapses for neuromorphic computing. *Nature Electronics*, 2020., **3**, P. 148–155.
- [17] Chakravarty A., Mentinka J.H., Davies C.S., Yamada K.T., Kimel A.V., Rasinga Th. Supervised learning of an opto-magnetic neural network with ultrashort laser pulses. *Appl. Phys. Lett.*, 2019, **114**, 192407.
- [18] Pinna D., Bourianoff G., Everschor-Sitte K. Reservoir Computing with Random Skyrmion Textures. *Phys. Rev. Applied*, 2020, **14**, 054020.
- [19] Hopfield J.J. Neural networks and physical systems with emergent collective computational abilities. *PNAS*, 1982, **79**(8), P. 2554–2558.
- [20] Hopfield J.J. Neurons With Graded Response Have Collective Computational Properties Like Those of Two-State Neurons. *Proceedings of the National Academy of Sciences*, 1984, **81**(10), P. 3088–3092.
- [21] Hopfield J.J. Searching for memories, Sudoku, implicit check bits, and the iterative use of not-always-correct rapid neural computation *Neural Comput*, 2008, **20**(5), P. 1119–64.
- [22] Sherrington D., Kirkpatrick S. Solvable Model of a Spin-Glass. *Physical Review Letters*, 1975, **35**(26), P. 1792.
- [23] Hinton G., Sejnowsk T.J. Analyzing Cooperative Computation. 5th Annual Congress of the Cognitive Science Society. Rochester, New York, 1983.
- [24] MacKay D. *Information Theory, Inference, and Learning Algorithms*. University of Cambridge, 2003.
- [25] Neelakanta P., De Groff D.F. *Neural Network Modeling: Statistical Mechanics and Cybernetic Perspectives*. CRC Press, Boca Raton.: 1994. 256 p.
- [26] Freeman W.J., Vitiello G. Dissipation and spontaneous symmetry breaking in brain dynamics. *J. Phys. A: Math. Theor*, 2008, **41**(30), P. 304042.
- [27] Gori M., Maggini M., Rossi A. Neural network training as a dissipative process *Neural Networks*, 2016, **81**, P. 72–80.
- [28] Möller M., Möllenhoff T., Cremers D. Controlling Neural Networks via Energy Dissipation. International Conference on Computer Vision (ICCV), 2019, P. 3255–3264.
- [29] Fukami S., Ohno H. Perspective: Spintronic synapse for artificial neural network featured. *Journal of Applied Physics*, 2018, **124**, P. 151904.
- [30] Saeedi M., Markov I.L. Synthesis and optimization of reversible circuits — a survey. *ACM Computing Surveys*, 2013, **45**(2), P. 1–34.
- [31] Nielsen M.A., Chuang I.L. *Quantum Computation and Quantum Information*. Cambridge University Press. 2011.
- [32] Ventra M.D., Traversa F.L. Perspective: Memcomputing: Leveraging memory and physics to compute efficiently. *Journal of Applied Physics*, 2018, **123**, P. 180901.
- [33] Camsari K.Y., Faria R., Sutton B.M., Datta S. Stochastic p-Bits for Invertible Logic. *Phys. Rev. X*, 2017, **7**, P. 031014.
- [34] Borders W.A., Pervaiz A.Z., Fukami S., Camsari K.Y., Ohno H., Datta S. Integer factorization using stochastic magnetic tunnel junctions. *Nature*, 2019, **573**, P. 390–393.
- [35] Bearden S.R.B., Pei Y.R., Di Ventra M. Efficient solution of Boolean satisfiability problems with digital memcomputing. *Sci Rep*, 2020, **10**, P. 19741.
- [36] Gypens P., Waeyenberge B.V., Di Ventra M., Leliaert J., Pinna D. Nanomagnetic Self-Organizing Logic Gates. *Phys. Rev. Applied*, 2021, **16**(2), P. 024055.
- [37] Balynskiy M., Chiang H., Gutierrez D., Kozhevnikov A., Filimonov Yu., Khitun A. Reversible magnetic logic gates based on spin wave interference *Journal of Applied Physics*, 2018, **123**, P. 144501.
- [38] Chauwin M., Hu X., Garcia-Sanchez F., Betrabet N., Paler A., Moutafis C., Friedman J.S. Skyrmion Logic System for Large-Scale Reversible Computation *Phys. Rev. Applied*, 2019, **12**(6), P. 064053.
- [39] Amit D.J., Gutfreund H., Sompolinsky H. Spin-glass models of neural networks. *Phys. Rev. A*, 1985, **32**, P. 1007.
- [40] Bramwell S.T., Harris M.J. The history of spin ice. *Journal of Physics: Condensed Matter*, 2020, **32**(37), P. 374010.
- [41] Farhan A., Derlet P., Kleibert A., Balan A., Chopdekar R. V., Wyss M., Anghinolfi L., Nolting F., Heyderman L.J. Exploring hyper-cubic energy landscapes in thermally active finite artificial spin-ice systems. *Nature Phys*, 2013, **9**, P. 375–382.
- [42] Kaffash M.T., Lendinez S., Jungfleisch M.B. Nanomagnonics with artificial spin ice. *Physics Letters A*, 2021, **402**, P. 127364.
- [43] Jensen J.H., Folven E., Tuft G. Computation in artificial spin ice. Proceedings of the ALIFE 2018: Tokyo, Japan. July 23–27, 2018. (P. 15–22).
- [44] Gypens P., Leliaert J., Van Waeyenberge B. Balanced Magnetic Logic Gates in a Kagome Spin Ice. *Phys. Rev. Applied*, 2018, **9**, P. 034004.
- [45] Arava H., Leo N., Schildknecht D., Cui J., Vijayakumar J., Derlet P. M., Kleibert A., Heyderman L.J. Engineering Relaxation Pathways in Building Blocks of Artificial Spin Ice for Computation. *Phys. Rev. Applied*, 2019, **11**, P. 054086.
- [46] Banas L., Brzezniak Z., Neklyudov M., Prohl A. *Stochastic Ferromagnetism: Analysis and Numerics*. De Gruyter. 2014.
- [47] Hoffmann M., Blügel S. Systematic derivation of realistic spin models for beyond-Heisenberg solids. *Phys. Rev. B*, 2020, **101**, P. 024418.
- [48] Bramwell S.T., Gingras M.J.P. Spin Ice State in Frustrated Magnetic Pyrochlore Materials. *Science*, 2001, **294**(5546), P. 1495–1501.
- [49] Klingler S., Pirrob P., Brächer T., Leven B., Hillebrands B., Chumak A.V. Spin-wave logic devices based on isotropic forward volume magneto-static waves. *Appl. Phys. Lett*, 2015, **106**, P. 212406.

---

Submitted 26 October 2022; revised 17 November 2022; accepted 30 November 2022

Information about the author:

Igor S. Lobanov – Faculty of Physics, ITMO University, Lomonosova Str. 9, Saint Petersburg, 191002 Russia;  
ORCID 0000-0001-8789-3267; igor.lobanov@metalab.ifmo.ru, lobanov.igor@gmail.com

## Double ring polariton condensates with polariton vortices

Evgeny S. Sedov<sup>1,2,3,5,a</sup>, Vladimir A. Lukoshkin<sup>3,6,b</sup>, Vladimir K. Kalevich<sup>3,6,c</sup>, Igor Yu. Chestnov<sup>4,5,d</sup>, Zacharias Hatzopoulos<sup>7,e</sup>, Pavlos G. Savvidis<sup>1,2,7,8,f</sup>, Alexey V. Kavokin<sup>1,2,3,9,g</sup>

<sup>1</sup>Key Laboratory for Quantum Materials of Zhejiang Province, School of Science, Westlake University, Zhejiang, China

<sup>2</sup>Institute of Natural Sciences, Westlake Institute for Advanced Study, Hangzhou, Zhejiang Province, China

<sup>3</sup>Spin Optics Laboratory, St. Petersburg State University, St. Petersburg, Russia

<sup>4</sup>ITMO University, St. Petersburg, 197101, Russia

<sup>5</sup>Vladimir State University, Vladimir, Russia

<sup>6</sup>Ioffe Institute, Russian Academy of Sciences, St. Petersburg, Russia

<sup>7</sup>FORTH-IESL, Heraklion, Crete, Greece

<sup>8</sup>Department of Materials Science and Technology, University of Crete, Heraklion, Crete, Greece

<sup>9</sup>Moscow Institute of Physics and Technology, Moscow Region, Russia

<sup>a</sup>[evgeny\\_sedov@mail.ru](mailto:evgeny_sedov@mail.ru), <sup>b</sup>[v.lukosh@mail.ioffe.ru](mailto:v.lukosh@mail.ioffe.ru), <sup>c</sup>[kalevich.solid@mail.ioffe.ru](mailto:kalevich.solid@mail.ioffe.ru), <sup>d</sup>[igor\\_chestnov@mail.ru](mailto:igor_chestnov@mail.ru)

<sup>e</sup>[chatzop@physics.uoc.gr](mailto:chatzop@physics.uoc.gr), <sup>f</sup>[p.savvidis@westlake.edu.cn](mailto:p.savvidis@westlake.edu.cn), <sup>g</sup>[a.kavokin@westlake.edu.cn](mailto:a.kavokin@westlake.edu.cn)

Corresponding author: Evgeny S. Sedov, [evgeny\\_sedov@mail.ru](mailto:evgeny_sedov@mail.ru)

PACS 71.36.+c, 03.75.Lm

**ABSTRACT** We study formation of persistent currents of exciton polaritons in annular polariton condensates in a cylindrical micropillar cavity under the spatially localised nonresonant optical pumping. Since polariton condensates are strongly nonequilibrium systems, the trapping potential for polaritons, formed by the pillar edge and the reservoir of optically induced incoherent excitons, is not real in general case. Its imaginary part includes the spatially distributed gain from the pump and losses of polaritons in the condensate. We show that engineering the gain-loss balance in the micropillar plane gives one an access to the excited states of the polariton condensate. We demonstrate, both theoretically and experimentally, the formation of vortices in double concentric ring polariton condensates in the case of complex annular trap potential.

**KEYWORDS** polariton, exciton-polariton condensate, persistent current, micropillar, vortex.

**ACKNOWLEDGEMENTS** This work was done under the support of the Saint Petersburg State University (Grant No. 91182694). A. K. and P. S. acknowledge the support of Westlake University, Project 041020100118 and Program 2018R01002 funded by Leading Innovative and Entrepreneur Team Introduction Program of Zhejiang Province of China. A. K. acknowledges support from the Moscow Institute of Physics and Technology under the Priority 2030 Strategic Academic Leadership Program. Numerical simulations were supported by the RF Ministry of Science and Higher Education under Agreement No. 0635-2020-0013 and by the RF Presidential Grant for state support of young scientists No. MK-4729.2021.1.2 and No. MK-5318.2021.1.2.

**FOR CITATION** Sedov E.S., Lukoshkin V.A., Kalevich V.K., Chestnov I.Yu., Hatzopoulos Z., Savvidis P.G., Kavokin A.V. Double ring polariton condensates with polariton vortices. *Nanosystems: Phys. Chem. Math.*, 2022, **13** (6), 608–614.

### 1. Introduction

Exciton polaritons are hybrid bosonic quasiparticles emerging under the strong coupling of photons and excitons. The coupling can be provided in specially designed stratified structures, semiconductor optical microcavities with embedded quantum wells [1]. Microcavities provide localization of light along one spatial direction, reducing the problem to two dimensions. Quantum wells are holders of excitons close to the resonance with the microcavity photons.

Cavity polaritons are able to form Bose-Einstein condensates. Such states are known for their superfluid properties [2, 3]. Superfluidity implies the existence of persistent polariton currents in the system [4]. The configuration of the current field considerably depends on the geometry of the localizing potential for polaritons. Azimuthal persistent currents have been predicted and observed in polariton condensates trapped in annular potentials [5–9]. Such currents can exhibit both vortex and non-vortex nature. To distinguish them, one needs to pay attention to their phase. For vortices, phase rotates around the trap by  $2\pi m$ , where the integer number  $m$  is known as the winding number, which plays the role of the

topological charge of the vortex [10]. The second distinctive feature of vortices, which is known as the vanishing density of the superfluid at the core, is not relevant for the annular geometry of the potential.

In the above mentioned papers [5–8], the polariton condensates supporting circular polariton currents have been characterized by a single ring shape occupying the ground radial state of the annular trap. As one has shown [11, 12], due to the nonequilibrium nature of the polariton condensates, which can exist only under the external (optical) pumping, they are able to occupy the excited states, including those in the form of concentric rings. Herewith circular polariton currents are also allowed in such condensates [13].

In this manuscript, we consider the system of a cylindrical micropillar cavity excited by a non-resonant laser pump focused close to its center. The pump creates a reservoir of incoherent excitons, which feeds the exciton polariton condensate through stimulated scattering processes. We study the conditions needed for exciting condensates in the form of concentric rings in the annular trapping potential by analysing the balance of gain of the condensate from the optical pump and losses of polaritons. We predict formation of double concentric ring polariton vortices and confirm our predictions by experimental observations. We note that double ring polariton condensates may be used as building blocks in polariton quantum networks [14].

## 2. Exciton polariton condensates in an annular trap

### 2.1. Gross–Pitaevskii equation for describing polariton condensates

The traditional approach to characterizing the exciton polariton condensate is based on using the generalized Gross–Pitaevskii equation for the polariton wave function (WF)  $\Psi(t, \mathbf{r})$  [13, 15–17]:

$$i\hbar\partial_t\Psi = \left\{ [i\eta n_R - 1] \frac{\hbar^2}{2M} \nabla^2 + V(r) + \alpha|\Psi|^2 + \alpha_R n_R + \frac{i\hbar}{2} [Rn_R - \gamma] \right\} \Psi, \quad (1)$$

where  $M$  is the effective polariton mass in the microcavity plane,  $V(r) = V_0\delta(r - d/2)$  is the stationary potential of the micropillar, taken in the form of cylinder of diameter  $d$  and height  $V_0$ .  $\alpha$  and  $\alpha_R$  are the polariton-polariton and polariton-exciton interaction constants, respectively. The rightmost imaginary term in Eq. (1) characterizes non-conservative processes of polariton losses and gain from the incoherent reservoir of optically induced excitons.  $n_R(t, \mathbf{r})$  is the density of the reservoir,  $R$  is the stimulated scattering rate from the reservoir to the condensate,  $\gamma$  and  $\gamma_R$  are the decay rates of polaritons and excitons, respectively. In Eq. (1), we also take into account the energy relaxation of polaritons during their propagation [15, 16].  $\eta$  is the energy relaxation constant. This latter term distinguishes our model from one proposed in [7].

Due to larger effective masses and higher losses of excitons, the reservoir dynamics is significantly faster than one of polaritons. This allows us to treat the change of the reservoir as the adiabatic adjustment to the evolution of the condensate:

$$n_R \simeq \frac{P(\mathbf{r})}{\gamma_R + R|\Psi|^2} \approx \frac{P(\mathbf{r})}{\gamma_R} - \frac{P(\mathbf{r})R|\Psi|^2}{\gamma_R^2}. \quad (2)$$

The reservoir is excited by the optical pump of the intensity  $P(\mathbf{r}) = P_s(r) + \delta P(\mathbf{r})$ , where  $P_s(r) \propto \exp[-r^2/2w^2]$  is the Gaussian function of width  $w$  centered in the micropillar, and  $\delta P(\mathbf{r})$  describes perturbation due to the displacement of the pump spot or deformation of its shape.

### 2.2. Gain-loss balance for emergence of the polariton condensate

Let us start our consideration with the rotationally symmetric ( $\delta P(\mathbf{r}) \rightarrow 0$ ) linear ( $\alpha|\Psi|^2 \rightarrow 0$ ) system. The polariton WF then can be factorized as follows:  $\Psi_{m,n} = \Upsilon_n(r) \exp[-i(E_{m,n}t/\hbar - m\theta)]$ , where  $\Upsilon_n(r)$  is the radial component of WF with the quantum number  $n$ .  $m$  is the azimuthal quantum number, that is also the winding number characterizing circulation of polaritons around the trap.  $E_{n,m}$  is the complex eigenvalue of the problem, obeying the equation

$$\left( E_{n,m} + i\frac{\hbar}{2}\gamma \right) \Upsilon_n = \left\{ \frac{\hbar^2}{2M} \left( i\frac{\eta P_s(r)}{\gamma_R} - 1 \right) \left( \frac{\partial^2}{\partial r^2} + \frac{1}{r} \frac{\partial}{\partial r} - \frac{m^2}{r^2} \right) V(r) + \frac{P_s(r)}{\gamma_R} \left[ \alpha_R + i\frac{\hbar R}{2} \right] \right\} \Upsilon_n. \quad (3)$$

The emergence of the condensate is determined by the overall balance of gain and loss in the system. The gain-loss balance for the state  $\Psi_{n,m}$  at a given pump power is determined by the imaginary part of the eigenvalue  $E_{n,m}$ . The pump power, for which the condition  $\text{Im}[E_{n,m}] = 0$  is satisfied, is the threshold power for the state  $\Psi_{n,m}$  [18]. Those states, for which gain exceeds losses ( $\text{Im}[E_{n,m}] > 0$ ), are supported by the system, and they can be occupied by the polariton condensate.

The gain and loss terms can be included in the effective potential of polaritons, which then acquires a complex form. Tuning the parameters of the complex potential, one can manipulate by the emerging polariton condensate modes. We have numerically studied the effect of the width of the annular potential and the pump power on the condition of emergence of excited polariton condensate states, see illustrations in Fig. 1. For numerical simulations, we take the following values of the parameters. The effective mass of polaritons is  $M = 3 \cdot 10^{-5}m_e$ , where  $m_e$  is the free electron mass. The height of the stationary potential is  $V_0 = 1$  meV. The polariton and exciton decay rates are  $\gamma = 0.1$  ps<sup>-1</sup> and  $\gamma_R = 0.33$  ps<sup>-1</sup>, respectively. The stimulated scattering rate is  $\hbar R = 0.1$  meV  $\mu\text{m}^2$ . The nonlinearity coefficients are

$\alpha = \alpha_R/2 = 3 \mu\text{eV} \mu\text{m}^2$ . The fitting parameter of the energy relaxation is  $\eta = 0.01 \mu\text{m}^2$ . The pump width is  $w = 3 \mu\text{m}$ . The pump power simultaneously contributes both the real part of the trapping potential, affecting height of the potential hill from the exciton reservoir, and the imaginary part, affecting gain of polaritons in the condensate. We would also like to note that although in this manuscript we consider the effective trapping potential which includes the stationary potential of the micropillar, our discussion can be expanded to the case of a fully optically induced potential [19, 20].

The dependence of the imaginary parts of the eigenvalues  $E_{n,0}$  on the width  $d$  of the potential ring at the fixed pump power is shown in Fig. 1(a). One can see that at small radius, the system supports only the ground polariton condensate state with  $n = 1$  (see Fig. 1(c)), characterized by a single ring shape. This is implemented, e.g., in  $25 \mu\text{m}$  wide micropillars (solid vertical line on the panel) studied in Refs. [6–8]. At some  $d$  the eigenspectrum of the trap is supplemented with the first excited state with  $n = 2$  (see Fig. 1(d)), which, however, remains the only eigenstate of the system with further increase in  $d$  (when  $\text{Im}[E_{1,0}]$  becomes negative). These states characterized by a double concentric ring shape in a  $30 \mu\text{m}$  wide micropillar (dashed vertical line in the panel (a)) are in the focus of our present consideration. The further increase in  $d$  brings states with larger  $n$  into play, while the states with smaller  $n$  are eliminated. Similar turnover of the eigenstates takes place with the change of the pump power. In Fig. 1(b) the dependencies of  $E_{n,0}$  on the pump power for  $d = 25 \mu\text{m}$  and  $30 \mu\text{m}$  wide micropillars are shown.

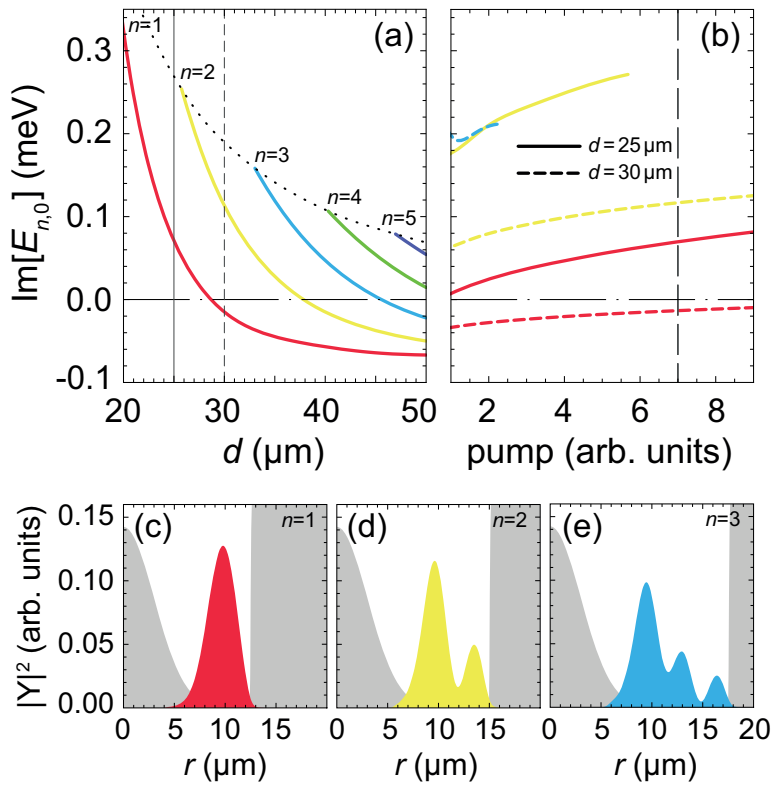


FIG. 1. The dependence of the imaginary part of the eigenvalues  $E_{n,0}$  for several lower states on the diameter of the pillar,  $d$ , at the fixed pump power (a) and on the pump power at the fixed diameter (b). (c–e) Examples of the density distribution of the three lowest eigenstates with  $n = 1, 2, 3$ . The vertical solid and dashed lines in (a) as well as the solid and dashed curves in (b) correspond to  $d = 25 \mu\text{m}$  and  $30 \mu\text{m}$ , respectively. The vertical dashed line in (b) indicates the pump power used for (a). The gray shaded regions in (c–e) indicate the effective trapping potential for polaritons. The colors in all panels indicate the number  $n$  of the energy level

### 2.3. Polariton vortices in concentric ring condensates

We now return to the general case of the system and bring the pump perturbation,  $\delta P(\mathbf{r})$ , and polariton-polariton interactions,  $\alpha|\Psi|^2$ , back into consideration. We use the approach developed in [7] and consider the projection of Eq. (1) onto the solution  $\Upsilon_2(r)$  of Eq. (3). We substitute the decomposition  $\Psi(t, \mathbf{r}) = \Upsilon_2(r)\Phi(t, \theta)$  in Eq. (1). After averaging over  $r$ , we obtain the following equation for the azimuthal WF component  $\Phi(t, \theta)$ :

$$i\partial_t\Phi = \left\{ [A_1(\theta) - A_2(\theta)|\Phi|^2] \frac{\partial^2}{\partial\theta^2} + U_1(\theta) + U_2(\theta)|\Phi|^2 \right\} \Phi, \quad (4)$$

where

$$A_1(\theta) = -\frac{\hbar}{2M} \left\langle \frac{1}{r^2} \left( 1 - i \frac{\eta P(\mathbf{r})}{\gamma_R} \right) \right\rangle, \quad (5a)$$

$$A_2(\theta) = -i \frac{\hbar \eta R}{2M \gamma_R^2} \left\langle \frac{1}{r^2} P(\mathbf{r}) |\Upsilon|^2 \right\rangle, \quad (5b)$$

$$U_1(\theta) = \frac{i \hbar \eta}{2M \gamma_R} \left\langle \delta P(\mathbf{r}) \left( \frac{\partial^2}{\partial r^2} + \frac{1}{r} \frac{\partial}{\partial r} \right) \right\rangle + \frac{1}{\gamma_R} \left( \frac{\alpha_R}{\hbar} + i \frac{R}{2} \right) \langle \delta P(\mathbf{r}) \rangle, \quad (5c)$$

$$U_2(\theta) = -\frac{i \hbar \eta R}{2M \gamma_R^2} \left\langle P(\mathbf{r}) |\Upsilon|^2 \left( \frac{\partial^2}{\partial r^2} + \frac{1}{r} \frac{\partial}{\partial r} \right) \right\rangle - \frac{R}{\gamma_R^2} \left( \frac{\alpha_R}{\hbar} + i \frac{R}{2} \right) \langle P(\mathbf{r}) |\Upsilon|^2 \rangle + \frac{1}{\hbar} \alpha \langle |\Upsilon|^2 \rangle. \quad (5d)$$

In (5), the following notation is used:  $\langle \dots \rangle = \int_0^\infty \dots |\Upsilon|^2 r dr$ . We omitted the subscript “2” at  $\Upsilon$  for brevity. The functions of angle  $U_1(\theta)$  and  $U_2(\theta)$  contribute to the symmetry breaking due to the pump perturbation and interaction-induced nonlinearity, respectively.

As one has shown in [7], breaking the rotational symmetry of a single ring polariton condensate, e. g., due to weak ellipticity of the pump spot and its small displacement from the center of the micropillar, can lead to the emergence of azimuthal polariton currents. We apply similar approach to the concentric ring geometry of the condensate. We take the pump in the form  $P(\mathbf{r}) \propto \exp[-(\mathbf{r} - \mathbf{r}_p)^2 / (1 + s \cos^2 \theta) w^2]$ , where  $s$  is responsible for the deformation of the pump spot,  $\mathbf{r}_p$  describes the displacement of the pump spot. Keeping  $s$  fixed and solving Eqs. (3)–(4) with different  $\mathbf{r}_p$ , we simulate concentric ring polariton condensates with and without azimuthal polariton currents.

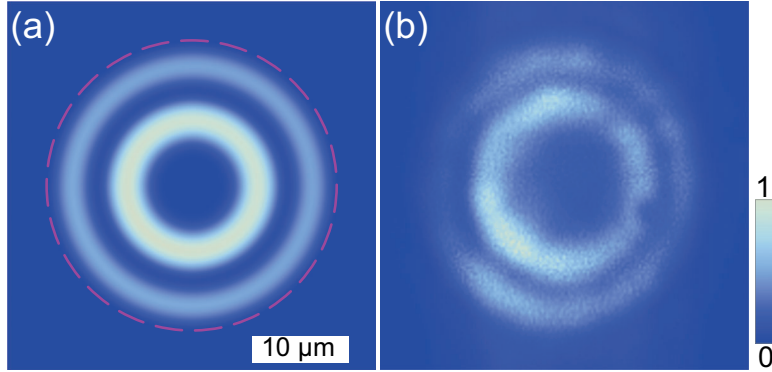


FIG. 2. Simulated (a) and experimentally observed (b) density distribution of the polariton condensate in the shape of double concentric rings. The magenta dashed circle in (a) indicates the edge of the micropillar

Fig. 2(a) shows the simulated density distribution of the double ring polariton condensate. Weak submicrometer displacement of the pump spot hardly affects its shape, so it remains the same in all simulations discussed below. We can judge the emergence of azimuthal polariton currents by the phase variation of the condensate around the micropillar. In the upper panels in Fig. 3, we show three examples of the phase distribution of the simulated concentric ring polariton condensates. In panel (c), the phase does not vary in the azimuthal direction, while in (a) and (e) the phases change by  $2\pi$  with one turn around the pillar in the counterclockwise and clockwise directions in both condensate rings, respectively. For quantifying polariton vortices, we use the winding number  $m$ . Following the definition, given in the Introduction, we obtain  $m = +1, 0$  and  $-1$  for panels (a), (b) and (c), respectively. The lower panels in Fig. 3 show the phases of the condensates relative to the phase of the spherical wave. These figures are helpful for comparing the simulation results with the experimental observations discussed below.

### 3. Experimental observation of double ring polariton vortices.

Vortex and non-vortex states of double concentric ring polariton condensates have been observed by us in the experiment. We excited the polariton condensates in a cylindrical pillar of diameter of  $30 \mu\text{m}$ , etched in the GaAs microcavity with a set of embedded quantum wells. The excitation was performed at temperature of 4 K by a nonresonant laser pump beam focused close to the center of the micropillar. We measured photoluminescence from the condensate to reveal the density distribution of polaritons in the micropillar. To get access to the phase of the polariton condensate, we measured

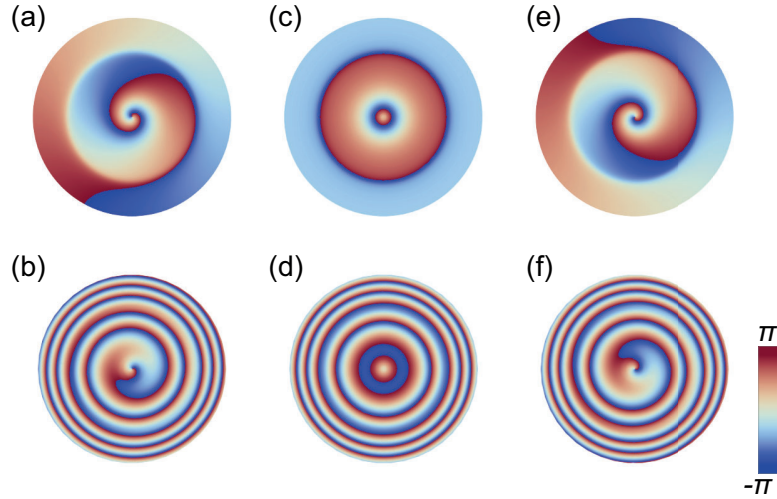


FIG. 3. Examples of the phase components of the simulated polariton condensates with ( $m = \pm 1$ ) and without ( $m = 0$ ) azimuthal polariton currents. Upper panels show phases of the concentric ring polariton condensates, lower panels show corresponding phases relative to the phase of the reference spherical wave

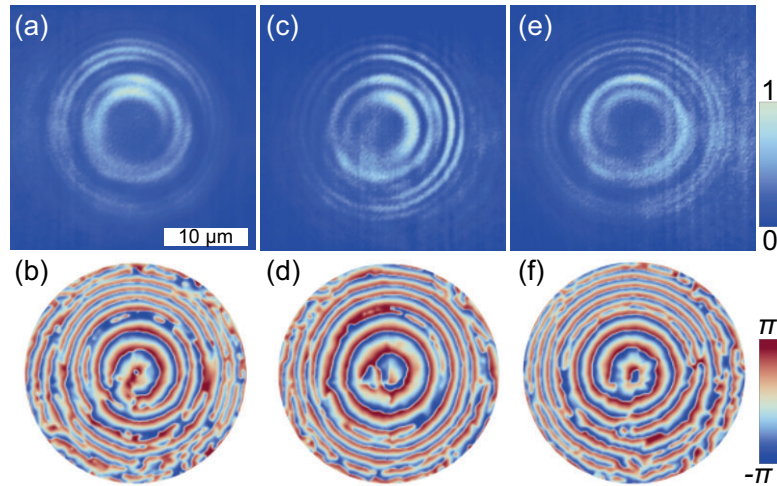


FIG. 4. Observation of concentric ring polariton condensates with azimuthal polariton currents. Upper panels show images of interference of the polariton condensates with the reference spherical wave. Lower panels show corresponding distribution of the phases of the condensates relative to the phase of the reference wave

interference of the condensate photoluminescence with the spherical reference wave using the Mach–Zehnder interferometer. The spherical wave was obtained by magnifying a small peripheral area of the condensate image. More details on the experimental setup and the sample are given in [5, 13].

Fig. 2(b) shows the photoluminescence from the double ring exciton polariton condensate in the micropillar. Upper panels in Fig. 4 show interferometry images of three observed double ring condensates. The interference fringes in (a) and (e) have the shape of spirals, diverging in counterclockwise and clockwise directions, respectively. The fringes in (c) represent concentric rings. Brightness of the fringes fades beyond the condensate, including the slit between the condensate rings.

We use the Fourier-transform method adapted for closed interference fringes [5] for extracting phase of the condensate from the interferograms. The lower panels in Fig. 4 show the phases of the observed polariton condensates relative to the phase of the spherical reference wave. One can see that the phase patterns repeat the spiral or concentric ring shape of the interferometry images. The comparison of the restored relative phases with the results of numerical simulations (lower panels in Fig. 3) allows us to conclude that among the observed condensates, the two of them, (a,b) and (e,f), are in the vortex states with  $m = +1$  and  $m = -1$ , respectively, while the remaining state (c,d) is in the non-vortex state with  $m = 0$ .

The observed condensates with differing vorticity were obtained by slight displacing the pump spot near the center of the micropillar. Along with the inevitable inhomogeneities of the localizing potential landscape, the displacement led to breaking the rotational symmetry of the system and selection of the preferred direction for azimuthal polariton currents. We also would like to note that at the chosen pump power in the micropillar under consideration we hadn't observed the polariton condensates with the radial quantum number other than  $n = 2$ . The vortex states were highly stable and existed as long as the optical excitation was presented. The double concentric ring shape of the condensates also did not change during their observation.

#### 4. Conclusion

In the manuscript, we have analyzed the conditions for exciting concentric ring exciton polariton condensates in cylindrical micropillars under the nonresonant optical pumping. We have shown that manipulating by the imaginary part of the trapping potential, responsible for the spatial distribution of gain and loss in the micropillar, one can select the radial quantization states of the polariton condensate. Based on numerical analysis, we have predicted excitation of azimuthal polariton current states in concentric ring polariton condensates. Our predictions have been supported by experimental observation of stable double ring polariton vortices. The results of our study have prospects for application in developing new interferometric devices and in coding and transferring optical information using the orbital degree of freedom of light, as well as for implementation of double-qubit logic gates.

#### References

- [1] Kavokin A., Baumberg J., Malpuech G., Laussy F. *Microcavities*, 2nd ed., Series on Semiconductor Science and Technology, Oxford University Press, Oxford, 2017, xxx+592 p.
- [2] Sanvitto D., Marchetti F.M., Szymańska M.H., et al. Persistent currents and quantized vortices in a polariton superfluid. *Nature Physics*, 2010, **6**(7), P. 527–533.
- [3] Carusotto I., Ciuti C. Quantum fluids of light. *Review of Modern Physics*, 2013, **85**(1), P. 299–366.
- [4] Nalitov A.V., Liew T.C.H., Kavokin A.V., Altshuler B.L., Rubo Y.G. Spontaneous Polariton Currents in Periodic Lateral Chains. *Physical Review Letters*, 2017, **119**(6), P. 067406.
- [5] Lukoshkin V.A., Kalevich V.K., Afanasiev M.M., et al. Persistent circular currents of exciton-polaritons in cylindrical pillar microcavities. *Physical Review B*, 2018, **97**(19), P. 195149.
- [6] Sedov E., Lukoshkin V., Kalevich V., et al. Persistent Currents in Half-Moon Polariton Condensates. *ACS Photonics*, 2020, **7**, P. 1163–1170.
- [7] Sedov E.S., Lukoshkin V.A., Kalevich V.K., et al. Circular polariton currents with integer and fractional orbital angular momenta. *Physical Review Research*, 2021, **3**(1), P. 013072.
- [8] Sedov E., Arakelian S., Kavokin A. Spontaneous symmetry breaking in persistent currents of spinor polaritons. *Scientific Reports*, 2021, **11**, P. 22382.
- [9] Xue Y., Chestnov I., Sedov E., et al. Split-ring polariton condensates as macroscopic two-level quantum systems. *Physical Review Research*, 2021, **3**(1), P. 013099.
- [10] Lagoudakis K.G., Wouters M., Richard M., et al. Quantized Vortices in an Exciton-Polariton Condensate. *Nature Physics*, 2008, **4**, P. 706–710.
- [11] Kalevich V.K., Afanasiev M.M., Lukoshkin V.A., et al. Controllable structuring of exciton-polariton condensates in cylindrical pillar microcavities. *Physical Review B*, 2015, **91**(4), P. 045305.
- [12] Dreismann A., Cristofolini P., Balili R., et al. Coupled counterrotating polariton condensates in optically defined annular potentials. *PNAS*, 2014, **111**(24), P. 8770–8775.
- [13] Lukoshkin V.A., Sedov E.S., Kalevich V.K., et al., *Steady state oscillations of circular currents in concentric polariton condensates*, 2022.
- [14] Kavokin A., Liew T.C.H., Schneider C., et al. Polariton condensates for classical and quantum computing. *Nature Reviews Physics*, 2022, **4**, P. 435–451.
- [15] Wouters M. Energy relaxation in the mean-field description of polariton condensates. *New Journal of Physics*, 2012, **14**, P. 075020.
- [16] Wertz E., Amo A., Solnyshkov D.D., et al. Propagation and Amplification Dynamics of 1D Polariton Condensates. *Physical Review Letters*, 2012, **109**(21), P. 216404.
- [17] Barrat J., Cherbunin R., Sedov E., et al. *Stochastic circular persistent currents of exciton polaritons*, 2022.
- [18] Cherotchenko E.D., Sigurdsson H., Askitopoulos A., Nalitov A.V. Optically controlled polariton condensate molecules. *Physical Review B*, 2021, **103**(11), P. 115309.
- [19] Schmutzler J., Lewandowski P., Aßmann M., et al. All-optical flow control of a polariton condensate using nonresonant excitation. *Physical Review B*, 2015, **91**(19), P. 195308.
- [20] Askitopoulos A., Nalitov A.V., Sedov E.S., et al. All-optical quantum fluid spin beam splitter. *Physical Review B*, 2018, **97**(23), P. 235303.

---

*Submitted 31 October 2022; revised 6 November 2022; accepted 7 November 2022*

#### Information about the authors:

*Evgeny S. Sedov* – Key Laboratory for Quantum Materials of Zhejiang Province, School of Science, Westlake University, 18 Shilongshan Rd, Hangzhou 310024, Zhejiang, China; Institute of Natural Sciences, Westlake Institute for Advanced Study, 18 Shilongshan Road, Hangzhou, Zhejiang Province 310024, China; Spin Optics Laboratory, St. Petersburg State University, Ulyanovskaya 1, St. Petersburg 198504, Russia; Vladimir State University, 87 Gorky str. 600000, Vladimir, Russia; ORCID 0000-0001-5684-151X; [evgeny\\_sedov@mail.ru](mailto:evgeny_sedov@mail.ru)

*Vladimir A. Lukoshkin* – Spin Optics Laboratory, St. Petersburg State University, Ulyanovskaya 1, St. Petersburg 198504, Russia; Ioffe Institute, Russian Academy of Sciences, 26 Politechnicheskaya, 194021 St-Petersburg, Russia; ORCID 0000-0002-6565-916X; v.lukosh@mail.ioffe.ru

*Vladimir K. Kalevich* – Spin Optics Laboratory, St. Petersburg State University, Ulyanovskaya 1, St. Petersburg 198504, Russia; Ioffe Institute, Russian Academy of Sciences, 26 Politechnicheskaya, 194021 St-Petersburg, Russia; ORCID 0000-0002-8010-2714; kalevich.solid@mail.ioffe.ru

*Igor Yu. Chestnov* – Department of Physics and Technology, ITMO University, St. Petersburg, 197101, Russia; Vladimir State University, 87 Gorky str. 600000, Vladimir, Russia; ORCID 0000-0002-3949-5421; igor.chestnov@mail.ru

*Zacharias Hatzopoulos* – FORTH-IESL, P.O. Box 1527, 71110 Heraklion, Crete, Greece; chatzop@physics.uoc.gr

*Pavlos G. Savvidis* – Key Laboratory for Quantum Materials of Zhejiang Province, School of Science, Westlake University, 18 Shilongshan Rd, Hangzhou 310024, Zhejiang, China; Institute of Natural Sciences, Westlake Institute for Advanced Study, 18 Shilongshan Road, Hangzhou, Zhejiang Province 310024, China; FORTH-IESL, P.O. Box 1527, 71110 Heraklion, Crete, Greece; Department of Materials Science and Technology, University of Crete, P.O. Box 2208, 71003 Heraklion, Crete, Greece; ORCID 0000-0002-8186-6679; p.savvidis@westlake.edu.cn

*Alexey V. Kavokin* – Key Laboratory for Quantum Materials of Zhejiang Province, School of Science, Westlake University, 18 Shilongshan Rd, Hangzhou 310024, Zhejiang, China; Institute of Natural Sciences, Westlake Institute for Advanced Study, 18 Shilongshan Road, Hangzhou, Zhejiang Province 310024, China; Spin Optics Laboratory, St. Petersburg State University, Ulyanovskaya 1, St. Petersburg 198504, Russia; Moscow Institute of Physics and Technology, Institutskiy per., 9, Dolgoprudnyi, Moscow Region, 141701, Russia; ORCID 0000-0003-2713-1062; a.kavokin@westlake.edu.cn

*Conflict of interest:* the authors declare no conflict of interest.

## Investigation of the method of current thermal modulation of the wavelength VCSEL

George P. Miroshnichenko<sup>a</sup>, Alina N. Arzhanenkova<sup>b</sup>, Michail Yu. Plotnikov<sup>c</sup>

ITMO University, St. Petersburg, Russia

<sup>a</sup>gpmirosh@gmail.com, <sup>b</sup>11arzh11@gmail.com, <sup>c</sup>plotnikov-michael@yandex.ru

Corresponding author: G. P. Miroshnichenko, gpmirosh@gmail.com

**ABSTRACT Subject of investigation.** In this paper, we analyzed in detail the thermal mode of the operation of a vertical-cavity surface-emitting laser (VCSEL) used in the experiment. **Method.** As a part of the work, we carried out a theoretical study of the recurrence relation describing the change in the VCSEL wavelength under the action of specially selected modulation current pulses. The high speed of the device working is determined by the optical demodulation scheme, which is based on using a phase-modulated carrier (the demodulation method used is arctangent demodulation: Phase Generated Carrier (PGC-ATAN)). **Main results.** Formulas were obtained that determine the frequency, phase, and modulation depth which leads to calculation of the principle of change in the modulated VCSEL wavelength at sampling points. Comparison with experimental data showed that the obtained formulas allow one to choose the optimal thermal mode of VCSEL operation and reliably calculate the characteristics of the modulation process in terms of the carrier phase. **Practical significance.** The obtained formulas make it possible to calculate the exact characteristics of the modulation process, and the precisely calculated phase of the modulation source. As a result, one can compensate it more effectively when demodulating phase of the interferometer.

**KEYWORDS** VCSEL, modulation, interferometric measurements, PGC- demodulation, PGC-ATAN.

**FOR CITATION** Miroshnichenko G.P., Arzhanenkova A.N., Plotnikov M.Yu. Investigation of the method of current thermal modulation of the wavelength VCSEL. *Nanosystems: Phys. Chem. Math.*, 2022, **13** (6), 615–620.

### 1. Introduction

Surface-emitting lasers with a vertical cavity (VCSEL) at a wavelength of 1550 nm is used not only in the telecommunications field, but also in constructing various fiber-optic sensor systems, in particular, based on Bragg gratings. Important problems in the development of such systems are as follows: the choice of the laser source of optical radiation, analysis of the noise of the measuring system, and the choice of the modulation method for the optical carrier. Reliable operation of fiber-optic interferometric measuring systems requires a small-sized source of optical radiation with the possibility of direct frequency modulation and the formation of optical pulses without external modulators. The aim of this work is to explore the thermal characteristics of VCSEL and analytically derive the parameters of the radiation source modulation principle. To select optimal method for modulating frequency of the radiation source, it is necessary to research principles of VCSEL operation when modulating current pulses of various shapes, with different durations and periods, and the possibility of controlling central wavelength. Source wavelength modulation is used to measure the phase produced in fiber optic interferometers. The construction of interferometers requires various metamaterials used in the parts of the interferometer. Particularly, one can mention mirrors in fiber-optic Fabry-Perot interferometer with certain metamaterials, the composition and properties of which can be found in article [1].

### 2. Review of previous studies

Surface-emitting lasers with vertical cavity form a separate type of semiconductor laser sources. The idea of creating such devices was proposed by the Japanese researcher Kenichi Iga in 1977 [2]. Due to a number of advantages, VCSEL finds application in modern radio-photonic devices designed for radio-electronic and combined systems of telecommunication and radar purposes, as well as in the development of various fiber-optic sensor systems. Modern VCSELs can operate in the wavelength range from 410 nm to 1000 nm. One observes the great interest to the sources in the telecom range – 850, 1300, 1550 nm. With rapid development of wireless communication networks, there is also an increasing need for simple, power-efficient and cost-effective transmission and distribution of radio frequency signals over optical fibers [2]. A theoretical analysis of VCSEL laser generation process at 1550 nm was carried out in [2–10]. For this purpose, the non-linear Statz-DeMars equations have been studied. These equations describe the dynamics and interaction of the carrier density and generation photon density under the action of the pump current for a set of VCSEL parameters at a wavelength of 1550 nm at a fixed temperature. Here parameters and combinations of parameters are defined that can be directly related to the experiment. Steady-state solutions and threshold values for the carrier density are found.

The frequency response of a laser transmitter when modulating a small signal is determined under the usual assumption of harmonic current modulation superimposed on a DC offset above the threshold value. The transfer function is found in frequency domain in the low-signal and the strong-signal approximations for modulation frequencies in the high-frequency GHz range. The FM response in the domain of high modulation frequencies from 10 MHz to 5.2 GHz is due to the carrier effect.

The theory of VCSEL modulation characteristics in the low frequency domain (up to several megahertz) is more complex. VCSEL allows one to tune the wavelength using the laser pump current. Up to a few megahertz, wavelength tuning is mostly a thermal effect: the current causes the VCSEL chip to heat up, and, as a result, the increasing of the refractive index of the material leads to the increase of the laser wavelength. To construct a theory for the dynamic processes under these conditions, it is necessary to improve the system of Statz-DeMars rate equations by adding the heat conduction equation with heat sources. The temperature model of VCSEL was described in works [2–7]. This model takes into account the effect of temperature increase in active domain depending on the injection current and the ambient temperature, and takes into account the temperature dependence of the gain, the pump current, and the barrier transparency. On the other hand, the frequency modulation at low modulation frequency exists due to the temperature modulation effect, which is successfully described by the dynamic thermal equation.

Studies of the thermal characteristics of VCSEL, as well as the principles of its operation, were done in works [2–4]. The coherent properties of the VCSEL radiation were also studied here. The experimental method for obtaining the coherence function of a laser diode with a vertical cavity is also used to obtain the dependences of the change in the central radiation wavelength and the width of the spectral components with direct current modulation of the laser at various frequencies and with various inverse duty cycles.

The method of homodyne demodulation based on the calculation of the values of arctangent function (PGC-ATAN) is one of the methods for processing the interference signals of fiber optic systems, where signal that enters the demodulation circuit has the following form:

$$I_{in} = A + B \cdot \cos [C \cdot \cos (2 \cdot \pi \cdot \nu_0 \cdot t + \varphi_{gen}) + \varphi(t)]. \quad (1)$$

Here  $A$  and  $B$  are constants that are proportional to the power of the optical radiation,  $C$  is the depth of phase modulation,  $\nu_0$  is the frequency of the signal from the reference oscillator,  $\varphi(t)$  is the measured phase signal,  $\varphi_{gen}$  is the phase shift of the reference oscillator signal, which plays the role of the VCSEL modulation parameter. We need to determine  $\varphi_{gen}$  analytically, since inaccurate phase determination leads to unwanted demodulation errors, such as, for example, incorrect determination of the amplitude of the measured phase signal [11]. Articles [11–13] describe ways of finding the exact value  $\varphi_{gen}$ . It is proposed to look for the time delay between the signal from the reference oscillator and the carrier component of the interference signal after the bandpass filter [12]. In [13], it is suggested to replace the main carrier and the second harmonic with the meander of the carrier and the second harmonic, respectively.

### 3. The principle of VCSEL wavelength modulation using a train of pump pulses

For the operation of the fiber-optic interferometric measuring systems that do not use an external modulator, it is necessary to know the principle of the change in the VCSEL wavelength with time due to the internal modulation. As has been noted above, such formula can be obtained by solving the coupled Statz-De Mars equations and the heat conduction equations [14–20]. These equations are parametrized by several source parameters, some of which are taken from the experimental data. Instead of this method, in the patent [21], a phenomenological approach is proposed. The authors used the experimentally obtained speed characteristics of the change in wavelength due to heating and cooling. The recurrent relations were derived that relate changes in the wavelength in the adjacent time intervals. In our work, these relations were solved explicitly. Let's divide the time axis into intervals  $k = 0, 1, \dots$ , with the length of the time discretization  $T_d = \nu^{-1} = 10^{-6}$  sec, where  $\nu$  is the discretization frequency. In each interval  $k$ , one can observe two processes: 1 – VCSEL heating using a modulation current pulse with a duration  $T_k$ , 2 – VCSEL cooling after switching off the pulse for time  $T_d - T_k$ . The duration of the heating is adjustable and depends on the number of the interval according to the law of changing the duty cycle of the pulses:

$$T_k = T_{in} + T_a \cdot \sin (2 \cdot \pi \cdot \nu_0 \cdot T_d \cdot k) \quad (2)$$

Figure 1 is a plot of VCSEL wavelength during heating for various modulation currents [22–24].

These experimental curves make it possible to obtain the dynamic characteristics of thermal processes in the laser. Wavelength change by  $\Delta\lambda$  nm in the heating process can be described by the formula:

$$\Delta\lambda = a_1 \cdot (1 - \exp(-b_1 \cdot t)) \quad (3)$$

Here the parameters obtained from the experiment are introduced: the heating rate  $b_1 \text{ sec}^{-1}$  and the frequency shift due to heating  $a_1$  nm. The wavelength shift  $\Delta\lambda_k$  at the  $k$ -th interval (at the end of heating) is described by the following formula

$$\Delta\lambda_k = a_1 \cdot (1 - \exp(-b_1 \cdot T_k)) \quad (4)$$

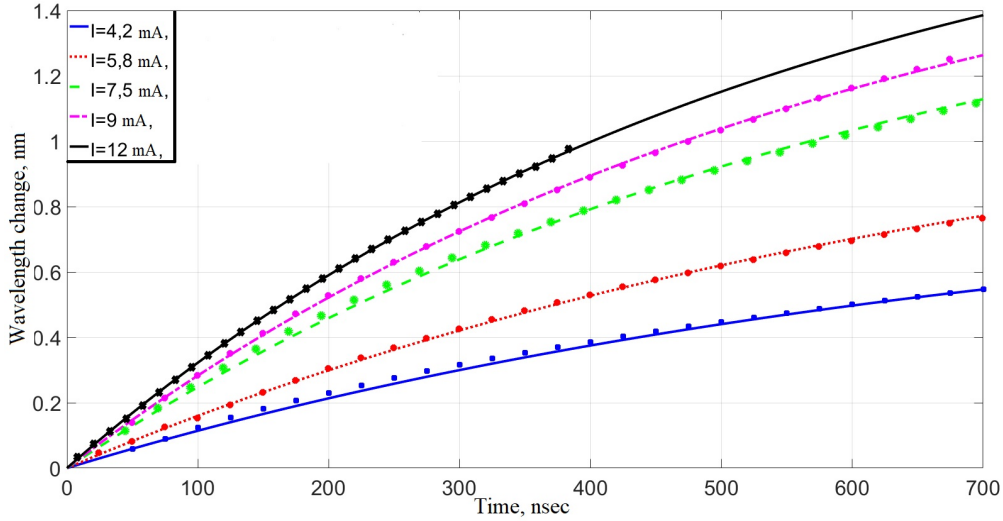


FIG. 1. VCSEL wavelength changes for different modulation amperages

The maximum wavelength shift  $\Delta\lambda_k^{\max}$  at the  $k$ -th interval is as follows

$$\Delta\lambda_k^{\max} = \Delta\lambda_k^{\min} + \Delta\lambda_k \quad (5)$$

The VCSEL law of cooling at the  $k$ -th interval (after the heating stage) is determined by the speed parameter  $b_2 \text{ sec}^{-1}$ .

$$\varepsilon = \exp(-b_2 \cdot t) \quad (6)$$

Parameter  $\varepsilon$  at the end of the  $k$ -th interval of the cooling stage is as follows:

$$\varepsilon_k = \exp(-b_2 \cdot (T_d - T_k)) \quad (7)$$

At the end of the  $k$ -th interval (at the beginning of the  $(k+1)$ -th interval) the minimal wavelength shift  $\Delta\lambda_{k+1}^{\min}$  is as follows:

$$\Delta\lambda_{k+1}^{\min} = \Delta\lambda_k^{\max} \cdot \varepsilon_k \quad (8)$$

Figure 2 shows a plot with VCSEL cooling parameters [22–24].

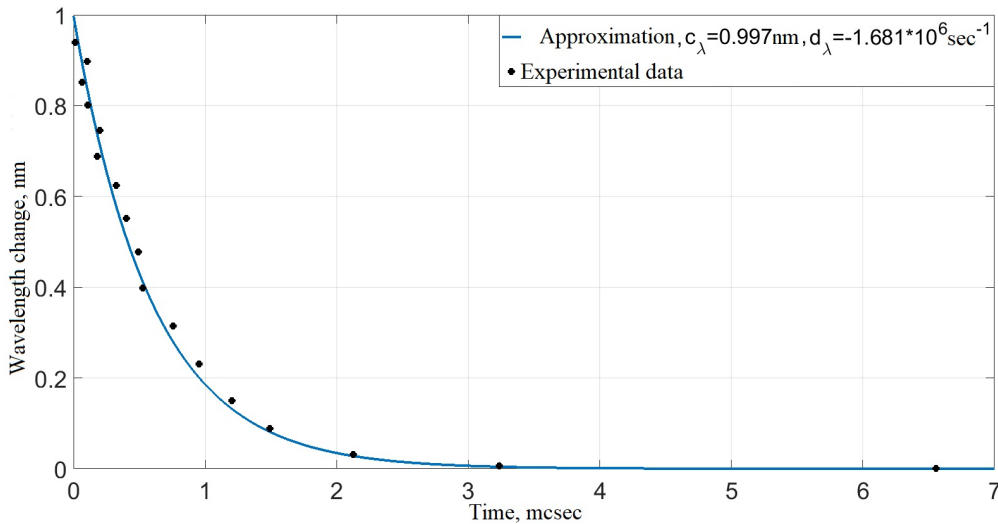


FIG. 2. Graph of VCSEL wavelength change during the cooling process

Figure 3 shows the plot of VCSEL wavelength change, calculated by recurrence relations with parameters selected from the experiment to study the process of the thermal modulation:

$$a_1 = 1.641 \text{ nm}, \quad b_1 = 5.434 \cdot 10^5 \text{ sec}^{-1}, \quad b_2 = 1.177 \cdot 10^6 \text{ sec}^{-1}, \quad T_{in} = 10^{-8} \text{ sec}, \quad T_a = 5 \cdot 10^{-9} \text{ sec}, \quad \nu_0 = 5 \cdot 10^4 \text{ sec}^{-1}$$

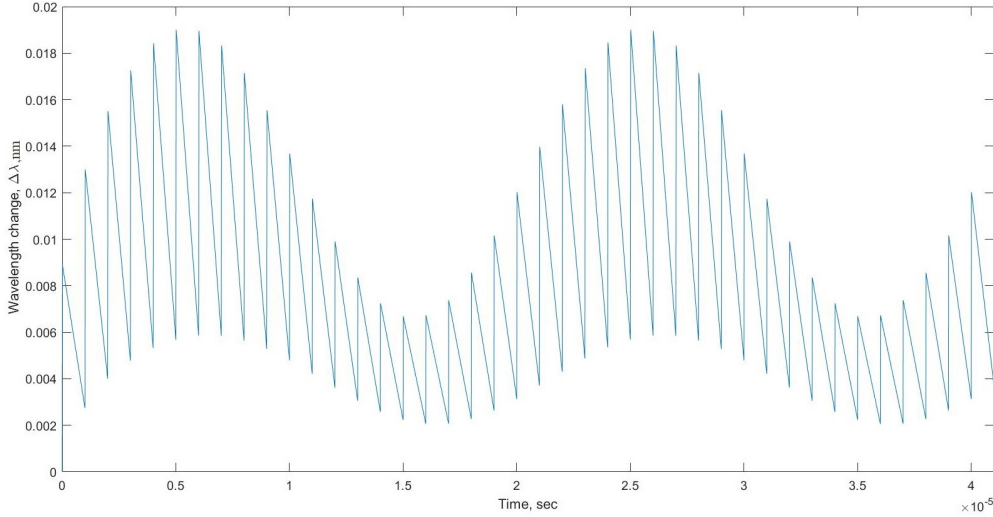


FIG. 3. VCSEL wavelength change with modulation amperage pulses

#### 4. Analytical derivation of formulas for calculating the principle of change of VCSEL modulated wavelength

Let us denote by  $\lambda_V = 1540$  nm the VCSEL generation wavelength in the absence of modulation pulses. Under the action of modulation pulses, the wavelength in each interval changes continuously, according to Fig. 3. The measuring system captures the VCSEL wavelength only at the sampling points  $t_k = T_d \cdot k$ , in which this length takes the values:

$$\lambda_V^{(k)} = \lambda_V + \Delta\lambda_k^{\min} \quad (9)$$

At the  $k$ -th wavelength sampling interval the wavelength takes the maximum value  $\lambda_V + \Delta\lambda_k^{\max}$ . Here  $\Delta\lambda_k^{\min}$  is the wavelength  $\lambda_V$  correction at the  $k$ -th sampling point,  $\Delta\lambda_k^{\max}$  is the maximum wavelength shift at the  $k$ -th sampling point. Under the action of modulation pulses, a periodic process of changing the wavelength is established. Using these parameters, we obtain a recursive relation describing the modulation process:

$$\begin{cases} \Delta\lambda_k^{\max} = \Delta\lambda_k^{\min} + \Delta\lambda_k \\ \Delta\lambda_{k+1}^{\min} = \Delta\lambda_k^{\max} \cdot \varepsilon_k \end{cases} \quad (10)$$

The recurrence relation for the desired correction  $\Delta\lambda_k^{\min}$  has the following form:

$$\Delta\lambda_{k+1}^{\min} = (\Delta\lambda_k^{\min} + \Delta\lambda_k) \cdot \varepsilon_k \quad (11)$$

The initial condition is as follows:  $\Delta\lambda_0^{\min} = 0$ . The solution of the recurrence relation takes the form:

$$\begin{cases} \Delta\lambda_{k+1}^{\min} = \sum_{q=0}^k \left( \Delta\lambda_q \cdot \prod_{s=q}^k \varepsilon_s \right), & k = 0, 1, 2, \dots \\ \Delta\lambda_0^{\min} = 0 \end{cases} \quad (12)$$

In order to evaluate the product

$$\prod_{s=q}^k \varepsilon_s = \exp(-b_2 (T_d - T_{in}) (k - q + 1)) \exp\left(b_2 T_a \sum_{s=q}^k \sin(2\pi\nu_0 T_d s)\right) \quad (13)$$

one can use the well-known formula:

$$\sum_{s=0}^k \sin(\varphi \cdot s) = \frac{\sin\left(\frac{k}{2} \cdot \varphi\right) \cdot \sin\left(\frac{k+1}{2} \cdot \varphi\right)}{\sin\left(\frac{\varphi}{2}\right)}, \quad \varphi = 2\pi\nu_0 T_d. \quad (14)$$

Keeping in mind that  $|b_1 \cdot T_k| \ll 1$ ,  $|b_2 \cdot T_a| \ll 1$  and assuming that  $\Delta\lambda_q \approx a_1 \cdot b_1 \cdot T_q$ , one simplifies the product as follows:

$$\prod_{s=q}^k \varepsilon_s \approx \exp(-b_2 \cdot (T_d - T_{in}) \cdot (k + 1 - q)) \quad (15)$$

Hence, relation (12) is simplified as follows:

$$\Delta\lambda_{k+1}^{\min} \approx a_1 b_1 e^{-b_2(T_d - T_{in})(k+1)} \sum_{q=0}^k (T_q e^{b_2(T_d - T_{in})q}) \quad (16)$$

For large  $k$  ( $k \rightarrow \infty$ ) one can deal with asymptotics (the asymptotic behavior is observed quite quickly, at about a hundredth step):

$$\Delta\lambda_k^{\min} = \alpha - \beta \cos(2\pi\nu_0 T_d k + \Delta), \quad \Delta\lambda_0^{\min} = 0, \quad \alpha = \frac{a_1 b_1 T_{in}}{\exp(b_2(T_d - T_{in})) - 1}, \quad \beta = \frac{a_1 b_1 T_a}{Z}, \quad (17)$$

$$Z = \sqrt{1 + \exp(2b_2(T_d - T_{in})) - 2 \cos(2\pi\nu_0 T_d) \exp(b_2(T_d - T_{in}))}.$$

Here the phase shift  $\Delta$  is the solution of the following system of equations:

$$\begin{cases} \sin(\Delta) = \frac{1}{Z} (\cos(2\pi\nu_0 T_d) \exp(b_2(T_d - T_{in})) - 1), \\ \cos(\Delta) = \frac{1}{Z} \sin(2\pi\nu_0 T_d) \exp(b_2(T_d - T_{in})). \end{cases} \quad (18)$$

Finally, we calculate the time-dependent source wavelength modulated by the frequency  $\nu_0$ :

$$\lambda(t) = \lambda_V + \alpha - \beta \cos(2\pi\nu_0 t + \Delta). \quad (19)$$

## 5. Results

In Fig. 4, we can see a comparison of the exact wavelength, measured at the sampling points  $\lambda_V^{(k)} = \lambda_V + \Delta\lambda_k^{\min}$  with an asymptotic solution  $\lambda(t)$ . In general, despite a slight discrepancy at the beginning, the asymptotic solution is in agreement with the exact values.

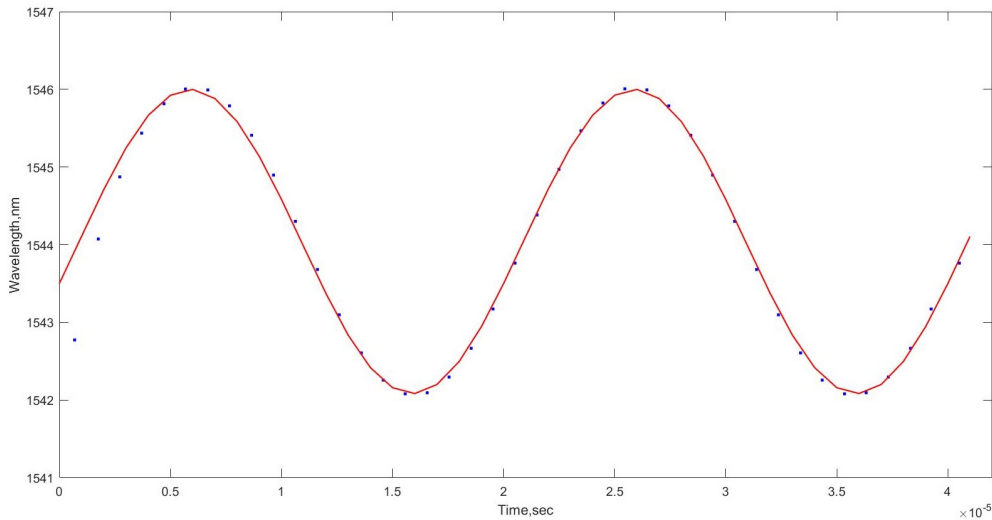


FIG. 4. Comparison of the exact wavelength (blue dots) with the asymptotic solution (red curve)

It follows from formulas (17) that the wavelength modulation law is determined by four parameters: the central wavelength  $\lambda_V + \alpha$ , where  $\alpha$  is the central wavelength shift due to the heating procedure,  $\beta$  is the modulation depth,  $\varphi_{gen} = \Delta - \pi$  is the modulation phase principle (desired phase shift of the reference oscillator signal),  $\nu_0$  is the modulation frequency. According to formulas (3), these parameters are calculated through the thermal parameters of VCSEL.

## 6. Conclusion

In this work, we explored the thermal regime of the VCSEL radiation source. With the help of the experimental data, four parameters were analytically obtained for the optimal calculation of the VCSEL modulation principle: the central wavelength, the modulation depth, the phase and the frequency of modulation. In Fig. 4, we can see that precisely calculated wavelength  $\lambda(t)$  practically coincides with the asymptotic solution having a small discrepancy at the beginning only. In the previous researches, the thermal parameters of VCSEL were not calculated, although it was pointed out that unreliably calculated characteristics of signal from the reference generator can lead to errors in the interference signal, which is necessary for further processing. Attempts have been made to calculate the exact value of  $\varphi_{gen}$ , in order to improve the quality of the interference signal entering the demodulation circuit, but the analytical solution hasn't been considered. The obtained formulas for exact calculation of VCSEL source parameters will improve the quality of

phase demodulation from the interferometer signal and will allow one to avoid errors from the source in determining the interference signal.

## References

- [1] Kivshar Yu.S. From metamaterials to metasurfaces and metadevices. *Nanosystems: physics, chemistry, mathematics*, 2015, **6**(3), P. 346–352.
- [2] Iga K. Surface-Emitting Laser—Its Birth and Generation of New Optoelectronics Field. *IEEE J. Sel. Top. In Qu. El.*, 2000, **6**(6), P. 1201.
- [3] Rashidul Hasan R., Basak R. Characteristics of a Designed 1550 nm AlGaInAs/InP MQW VCSEL. *Int. J. Multidis. Scien. Eng.*, 2013, **4**(1), P. 5–9.
- [4] Jungo M., Monti di Sopra F., Erni D., Baechtold W. Scaling effects on vertical-cavity surface-emitting lasers static and dynamic behavior. *Journal of Applied Physics*, 2002, **91**(9), P. 5550–5557.
- [5] Bjerkan L., Royset A., Hafskjaer L., and Myhre D. Measurement of Laser Parameters for Simulation of High-speed Fiberoptic Systems. *J. Lightwave Technol.*, 1996, **15**, P. 839.
- [6] Tucker R.S. High-speed Modulation of Semiconductor Lasers. *IEEE Trans. El. Dev.*, 1985, **ED-32**(1)2, P. 2572.
- [7] Chen J., Hangauer A., Strzoda-Markus-Christian Amann R. Experimental characterization of the frequency modulation behavior of vertical cavity surface emitting lasers. *Appl. Phys. Lett.*, 2007, **91**, P. 141105.
- [8] Dutta N.K., Tayahi M. and Choquette K.D. Transmission experiments using oxide confined vertical cavity surface emitting lasers. *Electronics Letters*, 1997, **33**(13), P. 1147–1148.
- [9] Meng Xun, Guanzhong Pan, Zhuangzhuang Zhao, Yun Sun, Chengyue Yang, Qiang Kan, Jingtao Zhou, and Dexin Wu. Analysis of Thermal Properties of 940-nm Vertical Cavity Surface Emitting Laser Arrays. *IEEE Trans. El. Devices*, 2021, **68**(1), P. 158–163.
- [10] Larsson A., Carlsson C., Gustavsson J., Haglund E., Modh P., Bengtsson J. Direct high-frequency modulation of VCSELs and applications in fibre optic RF and microwave links. *New J. Phys.*, 2004, **6**, P. 176.
- [11] Nikitenko A., Plotnikov M., Volkov A. PGC-ATAN demodulation scheme with the Carrier Phase Delay Compensation for Fiber-Optic Interferometric sensors. *IEEE Sensors Journal*, 2018, **18**(5), P. 1985–1992.
- [12] Volkov A.V., Oskolkova E.S., Plotnikov M.Yu., Mekhregin M.V., Shuklin P.A. Phase shift influence research of the reference oscillator signal on the output signal in homodyne demodulation scheme. *Scientific and Technical Journal of Information Technologies, Mechanics and Optics*, 2015, **15**(4), P. 608–614.
- [13] Huang S.-C., Lin H. Modified phase-generated carrier demodulation compensated for the propagation delay of the fiber. *Applied Optics*, 2007, **46**(31), P. 7594–7603.
- [14] Carlsson C., Martinsson H., Schatz R., Halonen J., Larsson A. Analog Modulation Properties of Oxide Confined VCSELs at Microwave Frequencies. *J. Light. Tech.*, 2002, **20**(9), P. 1740–1749.
- [15] Yang Yi, Ruan Yu, Li Zhengjia. Rate-equation-based Thermal VCSEL Model and its Equivalent Circuit Application in Transceiver Module Design. *J. Opt. Commun.*, 2002, **236**, P. 205–208.
- [16] Mena P.V., Morikuni J.J., Kang S.-M., Harton A.V., and Wyatt K.W. A Simple Rate-Equation-Based Thermal VCSEL Model. *J. Light. Tech.*, 1999, **17**(5), P. 865–872.
- [17] Garciaand V.G., Farzane M. Transient thermal imaging of a vertical cavity surface-emitting laser using thermoreflectance microscopy. *Journal of Applied Physics*, 2016, **119**, P. 045105.
- [18] Chen G., Tien C.L., Wu X., Smith J.S. Thermal Diffusivity Measurement of GaAs/AlGaAs Thin-Film Structures. *Journal of Heat Transfer, Transactions ASME*, 1994, **116**(2), P. 325–331.
- [19] Zhao Y.-G. and McNemey J.G. Transient Temperature Response of Vertical-Cavity Surface-Emitting Semiconductor Lasers. *IEEE J. Quant. El.*, 1995, **31**(9), P. 1668–1673.
- [20] Kobayashi S., Yamamoto Y., Ito M., Kimura T. Direct Frequency Modulation in AlGaAs Semiconductor Lasers. *IEEE Transactions on Microwave Theory and Techniques*, 1982, **MTT-30**(4), P. 428.
- [21] Kireenkov A.Yu., Aleinik A.S., Plotnikov M.Yu., Mekhregin M.V. Patent No. 2646420. Method for frequency-pulse modulation of a semiconductor laser source of optical radiation for interrogating optical interferometric sensors. Russian Federation, IPC: H01S 5/042, G01B 9/02, G02F1/00. Priority from 11/23/2016.
- [22] Belikin M.N., Kulikov A.V., Strigalev V.E., Aleinik A.S., and Kireenkov A.Yu. Study of a compact radiation source for fiber-optic interferometric phase sensors. *J. Opt. Technol.*, 2015, **82**(12), P. 805–809.
- [23] Belikin M.N. Small-sized high-speed spectral response recorder for fiber-optical Bragg-gratings sensors. PhD dissertation in technical sciences, Saint Petersburg, 2016, P. 95–104.
- [24] Kireenkov A.Yu. Fiber-optic interferometric methods for constructing measuring systems based on a surface-emitting laser. PhD dissertation in physical sciences, Saint Petersburg, 2017, P. 90–108.

---

*Submitted 20 October 2022; revised 29 November 2022; accepted 30 November 2022*

### Information about the authors:

*George P. Miroshnichenko* – ITMO University, Kronverkskiy, 49, St. Petersburg, 197101, Russia; ORCID 0000-0002-4265-8818; gpmirosh@gmail.com

*Alina N. Arzhanenkova* – ITMO University, Kronverkskiy, 49, St. Petersburg, 197101, Russia; ORCID 0000-0003-4869-2838; 11arzh11@gmail.com

*Michail Yu. Plotnikov* – ITMO University, Kronverkskiy, 49, St. Petersburg, 197101, Russia; ORCID 0000-0003-2506-0379; plotnikov-michael@yandex.ru

*Conflict of interest:* the authors declare no conflict of interest.

## Features of tunneling current-voltage characteristics in dielectric films with Ni, Fe and Co nanoparticles, investigated by conductive AFM and within the framework of the theory of 1D-dissipative tunneling

Mikhail B. Semenov<sup>1,a</sup>, Vladimir D. Krevchik<sup>1</sup>, Dmitry O. Filatov<sup>2</sup>, Dmitry A. Antonov<sup>2</sup>, Alexey V. Shorokhov<sup>1,b</sup>, Alexander P. Shkurinov<sup>3</sup>, Ilya A. Ozheredov<sup>3</sup>, Pavel V. Krevchik<sup>1</sup>, Alexey V. Razumov<sup>1</sup>, Alexey S. Kotov<sup>2</sup>, Ilya S. Antonov<sup>1</sup>, Ivan M. Semenov<sup>1</sup>

<sup>1</sup>Penza State University, Penza, Russia

<sup>2</sup>Lobachevsky State University of Nizhni Novgorod, Nizhni Novgorod, Russia

<sup>3</sup>Institute for Problems of Laser and Information Technologies RAS, Moscow reg., Russia

<sup>a</sup>misha29.02.1@gmail.com, <sup>b</sup>alex.shorokhov@gmail.com

Corresponding author: Mikhail B. Semenov, misha29.02.1@gmail.com

PACS 73.63-b, 68.37 Ps, 68.37 Ef

**ABSTRACT** In this work, we have experimentally investigated the features of tunneling current-voltage (I–V) curves in the case of 1D-dissipative tunneling in the limit of weak dissipation for various both synthesized (and in the process of synthesis) metallic nanoparticles (NPs) (Ni, Co, Fe) in a combined atomic force microscope/scanning tunneling microscope (AFM/STM) system in an external electric field. It is shown that for individual tunneling I–V curves, a single peak is observed at one of the polarities. In the process of synthesizing metallic nanoparticles with a change in polarity, instead of nanoclusters, it is possible to synthesize toroidal structures (shown by the example of “growing” Ni-NPs). The investigated effects of 1D-dissipative tunneling made it possible to develop the author’s method of controlled growth of quantum dots in a combined AFM/STM system. A qualitative agreement was obtained between the experimental and theoretical results, which allows us to assume the possibility of experimental observation of the macroscopic dissipative tunneling effects and thereby confirm the hypothesis expressed in the pioneering works of A. J. Leggett, A. I. Larkin, Yu. N. Ovchinnikov and other authors.

**KEYWORDS** metal nanoparticles, dissipative tunneling, conductive AFM

**ACKNOWLEDGEMENTS** The authors thank prof. A. J. Leggett for helpful discussions, as well as IPLIT RAS, Collective Use Center of Moscow State University, named by M. V. Lomonosov and SEC “Physics of Solid-State Nanostructures” UNN named after N. I. Lobachevsky for help with the experimental part of this work. This work was supported by grant from the Ministry of Science and Higher Education of the Russian Federation 0748-2020-0012. The part of this work was supported by RFBR (project 20-02-00830).

**FOR CITATION** Semenov M.B., Krevchik V.D., Filatov D.O., Antonov D.A., Shorokhov A.V., Shkurinov A.P., Ozheredov I.A., Krevchik P.V., Razumov A.V., Kotov A.S., Antonov I.S., Semenov I.M. Features of tunneling current-voltage characteristics in dielectric films with Ni, Fe and Co nanoparticles, investigated by conductive AFM and within the framework of the theory of 1D-dissipative tunneling. *Nanosystems: Phys. Chem. Math.*, 2022, **13** (6), 621–627.

### 1. Introduction

Experimental observation of theoretically predicted macroscopic quantum effects of dissipative tunneling in low-dimensional systems (see, for example, [1–3]) is one of the current interest problems of modern condensed matter physics [1, 4, 5], since it allows both to study fundamental observable macroscopically realizable quantum effects and to develop the innovative nanoelectronics and nanophotonics devices with controlled characteristics (optical THz-IR converters, tunneling photodiodes, etc.). In the last decade, the authors of this work have experimentally observed effects due to dissipative tunneling of electrons in a number of artificial nanoscale systems. The results achieved to date are summarized in Table. 1.

In this paper, the authors provide experimental evidence for the presence of one-dimensional dissipative tunneling effects in the limit of weak dissipation in an external electric field for metal nanoparticles (Ni, Co, Fe), including those synthesized using a probe AFM. Experimentally observed features of the tunneling I–V curves are interpreted on the basis of the one-dimensional dissipative theory of tunneling in the limit of weak dissipation [1, 4, 6–8]. A qualitative comparison was carried out between the experimental (individual tunneling I–V curves) and theoretical results obtained in the

TABLE 1. Experimentally observed effects of dissipative tunneling.

1D	1D	2D	2D
The weak dissipation limit	The strong dissipation limit	The weak dissipation limit	The strong dissipation limit
The maximum on tunneling I–V curves for Au nanoparticles in SiO <sub>2</sub> films [1]	A series of non-equidistant peaks in the tunneling I–V curve of InAs/GaAs(001) quantum dots [1, 2]	2D-bifurcations on the tunnel I–V curves of the Au nanoparticles-arrays in SiO <sub>2</sub> films [1]	2D bifurcations on the field dependence of the photocurrent of a p-i-n diode with double asymmetric InAs/GaAs(001) quantum dots [3]

one-instanton semiclassical approximation in a model double-well oscillatory potential in the framework of the science of quantum tunneling with dissipation [1, 2, 4–7, 9–20] under conditions of an external electric field, and experimentally (by the method of conducting AFM). The experimental results are interpreted on the basis of the one-dimensional dissipative theory of tunneling in the limit of weak dissipation [1, 4, 6–8], and a qualitative comparison is made between the experimental and theoretical results (individual tunneling I–V curves and the field dependence of the probability of 1D dissipative tunneling). The experimental studies, presented in our work, based on the theoretical results most part of that was obtained in our previous papers mentioned above.

The essential advantage of the theory of quantum tunneling with dissipation is the possibility to obtain the main results for the tunneling probability in an analytical form (using the one-instanton semiclassical approximation). To date there are two main models which allows to obtain results in the exact analytical form within the framework of this theory: (1) “cubic parabola potential” simulating Josephson junctions [1, 4, 6]; (2) “double-well oscillatory potential”, which makes it possible to simulate tunnel transport through single nanoparticles in the system of a combined AFM/STM under conditions of an external electric field. The last approach was used by authors in this paper to theoretically describe the dissipative transport.

For the first time, the idea of using the double-well potential model in describing tunnel transport in a combined AFM/STM system under conditions of an external electric field was formulated in [21]. This approach was developed, in particular, in [8] (see, also, [1]) where authors used ideas and results of the theory of quantum tunneling with dissipation [1, 4, 6] to describe tunnel transport in this system. Note that Yu. N. Ovchinnikov have shown [10] that it is possible to qualitatively compare the experimental tunneling current (more precisely, the I–V curves) for planar structures of individual metal nanoparticles in a combined AFM/STM system with the probability of tunneling from the cantilever tip into the nearest nanoparticle.

In the considered double-well potential model, the positions of the minima of the double-well oscillatory potential, which depend on the strength of the external electric field, are mainly related to the “geometry” of the experiment. The left well simulates the AFM/STM cantilever needle (in our experiment, it is the platinum cantilever needle with an average radius of about 40 nm), while the right well models the metal nanoparticle closest to the cantilever needle (with a characteristic size of 2-5 nm in our experiment) separated from the cantilever needle by dielectric barrier. The real potential turns out to be much more complicated but our model potential makes it possible to obtain accurate analytical results that are in good qualitative agreement with the experiment. In our model the control parameters (in addition to geometric factors) are the strength of the external electric field and the temperature. Also this model takes into account (as theoretical parameters) the frequency of the oscillators of the model potential, the frequencies of phonon modes and the coefficients of interaction with these modes (in the linear approximation).

In this paper, we use the following formula for the probability of the dissipative tunneling (up to a pre-exponential factor  $B$ ):

$$\Gamma = B \exp(-S), \quad (1)$$

where  $S$  is the one-instanton quasi-classical action in the one-instanton quasi-classical approximation in a model double-well oscillatory potential. We refer readers to the author’s theoretical paper [22] (see, also Appendix in [23]) where one can find our theoretical results for the probability of dissipative tunneling in the considered system using this formula.

Let us make some remarks about formula (1). This main theoretical formula for the probability of 1D-dissipative tunneling was obtained for the double-well oscillatory potential for the first time in the work [8] (see, also, [1]). Readers can find comments to Formula (1) in the pioneering works of A. I. Larkin, E. J. Leggett, Yu .N. Ovchinnikov and other authors [1, 4, 6].

The field dependence of the probability of 1D-dissipative tunneling was presented in the paper [16]. In this paper, the first qualitative comparison of the experimental tunneling I–V curves for individual zirconium nanoparticles (I–V curves have a single peak at one of the polarities) with a theoretical field dependence of the probability of 1D-dissipative tunneling

in the model of a double-well oscillatory potential was carried out. It has been shown that the initially asymmetric double-well oscillatory potential becomes symmetrical one at a certain value of the external electric field strength and at one of the polarities. In this case the pre-exponential factor  $B$  of the probability of 1D-dissipative tunneling (1) gives a single (thermo-dependent) peak.

It should be mentioned here about the contribution of above-barrier transitions at a finite temperature (the real experiment was performed at room temperature). It is well-known that the de Broglie wavelength of the particle should be much smaller than the characteristic linear scale of the potential in the semiclassical approximation. As the temperature increases, the sub-barrier length in the double-well oscillatory potential decreases, and the standard semiclassical approximation is violated. It was shown by Larkin et al., in the papers mentioned above, that the value of the pre-exponential factor  $B$  in the tunneling probability increases with increasing temperature and it can become comparable with the value of the exponential contribution  $\exp(-S)$  in the formula (1) obtained analytically in the one-instanton semiclassical approximation. In this case, taking into account the pre-exponential factor makes it possible, with a certain accuracy, not to include in the consideration above-barrier transitions, which were studied in the works of A. I. Larkin in detail. In addition, it should be mentioned again that the appearance of a single peak in the field dependence of the probability of 1D-dissipative tunneling in the model of a double-well oscillatory potential is due to taking into account the pre-exponential factor at a finite temperature.

## 2. Experimental part

Films of  $ZrO_2(Y)$  and  $HfO_2(Y)$  (12 mol. % Y) 10 nm thick were deposited on conductive TiN(25 nm)/Ti(25 nm)/ $SiO_2(500\text{ nm})/Si(001)$  substrates with preliminarily deposited metallic sublayer (Ni, Co or Fe) 10 nm thick by high-frequency magnetron sputtering using a Torr International MSS-3GS vacuum setup for thin film deposition at a substrate temperature of  $300^\circ\text{C}$ . AFM studies were carried out using AFM NT-MDT Solver Pro at  $300^\circ\text{K}$  in atmospheric conditions in the contact mode. NT MDT NSG-11 DCP probes with a DLC conductive coating were used.

Synthesis of Ni, Co, and Fe NPs in the thickness of  $ZrO_2(Y)$  and  $HfO_2(Y)$  films was carried out as follows: The AFM probe was brought into contact with the surface of the dielectric film, and sawtooth electric voltage pulses with an amplitude of  $\sim 8\text{ V}$  and a duration of 6 s have been applied. When a positive electric potential is applied to the substrate, due to the drift of metal ions from the metal sublayer, where they are formed as a result of the electrochemical oxidation reaction, a conductive thread (filament) consisting of metal atoms is formed to the AFM probe, which closes the conductive substrate and the AFM probe. When an electric potential of reverse polarity is applied, the filament is partially destroyed, and a metallic NP is formed in the thickness of the dielectric. Methods for the formation of dielectric films and metal NPs in them using an AFM probe are described in detail in [24, 25].

## 3. Experimental results and discussion

### 3.1. Features of dissipative tunneling in Ni, Fe and Co nanoclusters, comparison of experiment and theory

In the tunnel current-voltage characteristics of the contact of the AFM probe to the surface of dielectric films, peaks are observed at the locations of metal nanoparticles associated with dissipative tunneling of electrons between the AFM probe and the conductive substrate. During the synthesis of metallic NPs with a change in polarity, instead of NPs, synthesis of toroidal structures is possible (shown on the example of Ni NPs (see Subsection 4.2, Fig. 2)). A qualitative agreement between the experimental and theoretical results was obtained (see Fig.1(a-c)), which suggests the possibility of experimental observation of the effects of macroscopic dissipative tunneling [1, 4].

Figures 1(a-c) (theoretical curve 2) of the text of this paper have curves containing a single peak for the case of a symmetric double-well potential at a certain value of the external electric field strength, obtained as the field dependence of the probability of dissipative tunneling  $\Gamma = B \exp(-S)$ , ([1, 8], Appendix to [23]). This peak, obtained theoretically, qualitatively coincides with individual experimental tunneling  $I - V$  characteristics for single NPs in the combined AFM/STM system (see Fig. 1).

### 3.2. Formation of ring-shaped metal nanostructures using an AFM probe

It was found that when the polarity of the applied voltage was changed after the completion of the NPs formation (i.e., when a negative voltage pulse was applied to the metal sublayer after a positive one), the formation of toroidal structures was observed (Fig. 2)). The formation of such structures is associated with local anodic oxidation of the central parts of metal NPs, followed by the drift of metal ions towards the conductive substrate (Fig.3)

These observations open up prospects for the development of an original technique for the controlled formation of ring-shaped metal nanostructures in thin dielectric films for use in nanoelectronics, nanophotonics, plasmonics, etc.

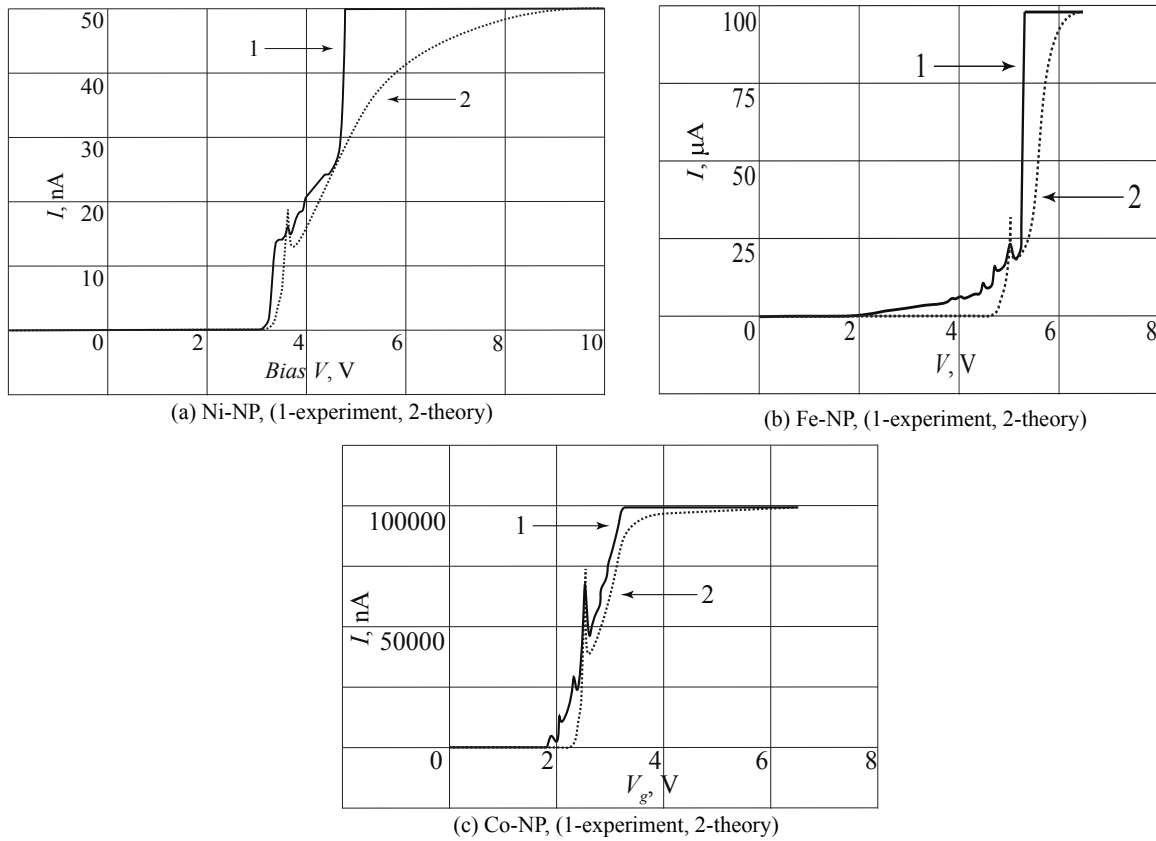


FIG. 1. Comparison of experimental I–V characteristics for NPs: (a) Ni, (b) Fe, (c) Co, with the theoretical field dependence of the probability of 1D dissipative tunneling

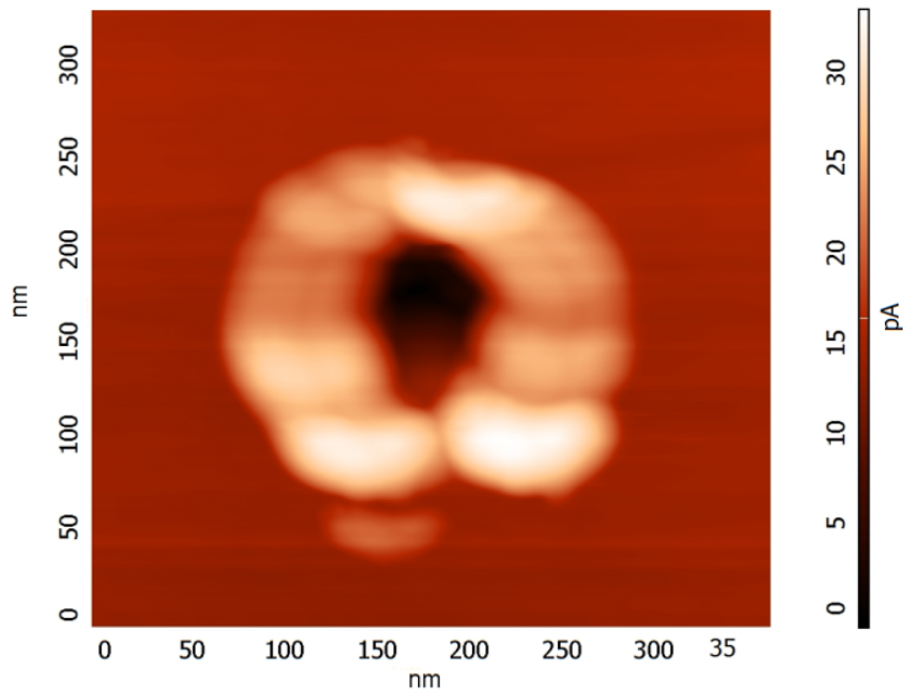


FIG. 2. Current image (map of the current flowing through the CAFM probe) of a toroidal Ni nanostructure formed inside a  $\text{ZrO}_2(\text{Y})/\text{Ni}/\text{Si}(001)$  film by local reduction/oxidation with a CAFM probe. Offset voltage 0.5 V.

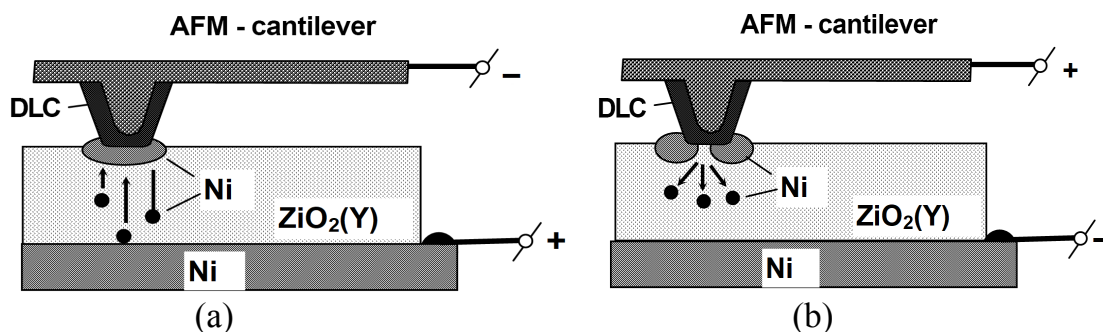


FIG. 3. Scheme of the formation of Ni-NPs during local reduction of Ni ions in a ZrO<sub>2</sub>(Y) film using an AFM probe at (a) negative and (b) positive voltages on the Ni sublayer relative to the AFM probe.

#### 4. Conclusion

In this work, the peculiarities of tunneling volt-ampere characteristics (CVC) in the case of one-dimensional dissipative tunneling in the limit of weak dissipation for various metal nanoclusters (Ni, Co, Fe) in a combined system of an atomic force and scanning tunneling microscope in an external electric field are studied experimentally and theoretically. It is shown that for individual tunneling I–V characteristics, a single peak is observed at one of the polarities. In the process of synthesizing metal nanoclusters with a change in polarity, instead of nanoclusters, toroidal structures can be synthesized (shown on the example of “growing” Ni-NPs). The studied effects of one-dimensional dissipative tunneling made it possible to develop an author’s method for the controlled growth of quantum dots in a combined AFM/STM system. Qualitative agreement between the experimental and theoretical results is obtained, which makes it possible to assume the possibility of experimental observation of macroscopic dissipative tunneling effects and thereby confirm the hypothesis expressed in the “pioneer” works of A. J. Leggett, A. I. Larkin, Yu. N. Ovchinnikov and other authors [1, 4, 6].

Note that the temperature dependence of a single peak was experimentally studied recently by co-authors of this paper from the Probe Microscopy Laboratory of the Lobachevsky State University of Nizhni Novgorod in an experiment with cobalt nanoparticles. This experiment has confirmed the theoretical prediction that “the amplitude of a single peak increases weakly non-linear with decreasing temperature”. These results will form the basis of a separate joint work.

Let us discuss here the interesting question about the relation between resonant and dissipative tunneling. Our experimental results with synthesized Fe, Co, and Ni nanoparticles (first, filamentous structures were formed, and then the “thread” was destroyed by a sawtooth voltage to get a nanoparticle) showed that additional peaks could be observed next to a single (usually larger amplitude) peak. These additional peaks are most likely resonant in nature. At small sizes of metal nanoparticles, a quantum size effect arises (in this case, metal differs slightly from semiconductor) and we see additional oscillations, in addition to a single thermo-dependent peak (due to the effect of dissipative tunneling). These oscillations are related with the participation of these levels in the nanocluster in resonant tunneling and with the fine tuning of energy levels in an external electric field.

Note also that in our first joint paper [16], it was shown that tunneling I–V curves (experiment with zirconium nanoparticles) with various features are also actually observed (for example, the “Coulomb ladder”, the case of several peaks of a resonant nature). Also the clear single peaks were observed at one (positive) polarity in a number of experimental tunneling I–V curves. In later experiments with gold nanoparticles, some I–V curves exhibited a single peak at one negative polarity (due to the influence of the nanometer protrusions on a non-ideal cantilever needle). Therefore, it should be noted that the observed effect of a single peak is realized only on separate I–V curves.

Our experiments showed that additional peaks formed due to resonant tunneling smear out with increasing temperature. Whereas a single temperature-dependent peak (higher amplitude) due to dissipative tunneling does not smear out with increasing temperature, but only decreases in amplitude. As a result, we can make an assumption about a possible new physical effect. Two tunneling mechanisms are realized on the observed tunneling I–V curves: resonant and dissipative with different behavior of the corresponding peaks with temperature change. As the temperature rises, the resonance peaks are smeared out, while the “dissipative” peak is retained.

The results of this work show that the development of nanotechnology has made it possible to experimentally observe the effects of dissipative electron tunneling in artificial size-quantized nanostructures.

## References

- [1] Bendersky V.A., Leggett A.J., Ovchinnikov Yu.N., Krevchik V.D., Semenov M.B., Dahnovsky Yu.I., Gorshkov O.N., Filatov D.O., et al. *Controlled dissipative tunneling. Tunnel transport in low-dimensional systems*. Ed. A.J. Leggett. Fizmatlit, Moscow, 2011–2012, 496 pp.
- [2] Kusmartsev F.V., Krevchik V.D., Semenov M.B., Filatov D.O., Shorokhov A.V., Krevchik P.V., et al. Phonon assisted resonant tunnelling and its phonons control. *JETP Letters*, 2016, **104**, P. 392–397.
- [3] Semenov M.B., Krevchik V.D., Filatov D.O., Shorokhov A.V., Shkurinov A.P., Ozheredov I.A., Krevchik P.V., Wang Y.H., Lie T.R., Malik A.K., Marychev M.O., Baidus N.V., and Semenov I.M. Dissipative tunneling of electrons in vertically coupled double asymmetric InAs/GaAs(001) quantum dots. *Tech. Phys.*, 2022, **67**, P. 115–125.
- [4] Caldeira A.O., Leggett A.J. Quantum tunnelling in a dissipative system. *Ann. of Phys.*, 1983, **149** (2), P. 374–456.
- [5] Benderskii V.A., Vetoshkin E.V., Kats E.I., Trommsdorff H.P. Competing tunneling trajectories in a two-dimensional potential with variable topology as a model for quantum bifurcations, *Phys. Rev. E*, 2003, **67**, 026102.
- [6] Larkin A.I., Ovchinnikov Yu.N. Decay of supercurrent in tunnel junctions. *Phys. Rev. B*, 1983, **28**, P. 6281–6285.
- [7] Ivlev B.I., Ovchinnikov Yu.N. Decay of metastable states in a situation with close-lying tunneling trajectories. *Sov. Phys. JETP*, 1987, **66** (2), P. 378–383.
- [8] Dakhnovsky Yu.I., Ovchinnikov A.A., Semenov M.B. Low-temperature chemical reactions considered as dissipative tunnel systems. *Sov. Phys. JETP*, 1987, **65** (3), P. 541–547.
- [9] Aringazin A.K., Dahnovsky Yuri, Krevchik V.D., Semenov M.B., Ovchinnikov A.A., Yamamoto K. Two-dimensional tunnel correlations with dissipation. *Phys. Rev. B*, 2003, **68**, 155426.
- [10] Ovchinnikov Yu.N. Conductivity of granular metallic film. *JETP*, 2007, **104**, P. 254–257.
- [11] Dahnovsky Yu., Krevchik V.D., Krivnov V.Ya., Semenov M.B., Yamamoto K., Shorokhov A.V., et al. *Transfer processes in low-dimensional systems*. UT Research Institute Press, Tokyo: 2005, 690 pp.
- [12] Caldeira A.O., Leggett A.J. Influence of dissipation on quantum tunneling in macroscopic systems. *Phys. Rev. Lett.*, 1981, **46** (4), P. 211–214.
- [13] Larkin A.I., Ovchinnikov Yu.N. Quantum tunneling with dissipation. *JETP Letters*, 1983, **37** (7), P. 382–385.
- [14] Dakhnovskii Yu.I., Horia M. Absolute negative resistance in double-barrier heterostructures in a strong laser field. *Phys. Rev. B*, 1995, **51**, P. 4193–4199.
- [15] Zhukovsky V.Ch., Dakhnovskii Yu.I., Gorshkov O.N., Krevchik V.D., Semenov M.B., Smirnov Yu.G., Chuprunov E.V., Rudin V.A., Skibitskaya N.Yu., Krevchik P.V., Filatov D.O., Antonov D.A., Lapshina M.A., Yamamoto K., Shenina M.E. Observed two-dimensional tunnel bifurcations in an external electric field. *Moscow University Physics Bulletin*, 2009, **64**, P. 475–480.
- [16] Zhukovsky V.Ch., Gorshkov O.N., Krevchik V.D., Semenov M.B., Groznaya E.V., Filatov D.O., Antonov D.A. Controllable dissipative tunneling in an external electric field. *Moscow University Physics Bulletin*, 2009, **64**, P. 27–32.
- [17] Filatov D., Guseinov D., Antonov I., Kasatkin A., Gorshkov O. Imaging and spectroscopy of Au nanoclusters in yttria-stabilized zirconia films using ballistic electron/hole emission microscopy. *RSC Adv.*, 2014, **4**, P. 57337–57342.
- [18] Ledentsov N.N., Ustinov V.M., Shchukin V.A., Kop'ev P.S., Alferov Zh.I., Bimberg D. Quantum dot heterostructures: fabrication, properties, lasers (Review). *Semiconductors*, 1998, **32** (4), P. 343–455.
- [19] Stier O., Grundmann M., Bimberg D. Electronic and optical properties of strained quantum dots modeled by 8-band k-p theory. *Phys. Rev. B*, 1999, **59**, P. 5688–5703.
- [20] Karpovich I.A., Zvonkov B.N., Baidus' N.V., Tikhov S.V., Filatov D.O. Tuning the energy spectrum of the InAs/GaAs quantum dot structures by varying the thickness and composition of a thin double GaAs/InGaAs cladding layer. *Trends in Nanotechnology Research*, Ed. by Dirote E.V. Nova Science Publishers, New York, 2004. P. 173–208.
- [21] Louis A.A., Sethna J.P. Atomic tunneling from a scanning-tunneling or atomiforce microscope tip: Dissipative quantum effects from phonons. *Phys. Rev. Lett.*, 1995, **74** (8), P. 1363–1366.
- [22] Ovchinnikov A.A., Dakhnovsky Yu.I., Krevchik V.D., Semenov M.B., Aringazin A.K. *Principles of controlled modulation of low-dimensional structures*. UNTsDO, Moscow, 2003, 510 pp. (in Russian)
- [23] Krevchik V.D., Razumov A.V., Semenov M.B., Uvaysov S.U., Kulagin V.P., Komada P., Smailova S., Mussabekova A. Influence of an external electric field and dissipative tunneling on recombination radiation in quantum dots. *Sensors*, 2022, **22**, 1300.
- [24] Antonov D.A., Novikov A.S., Filatov D.O., Kruglov A.V., Antonov I.N., Zdoroveishchev A.V., Gorshkov O.N. Formation of nanosized Ni ferromagnetic filaments in ZrO<sub>2</sub>(Y) films. *Tech. Phys. Lett.*, 2021, **47**, P. 539–541.
- [25] Antonov D.A., Filatov D.O., Novikov A.S., Kruglov A.V., Antonov I.N., Zdoroveyshchev A.V., Gorshkov O.N. An atomic force microscopics study of resistive switching resonance activation in ZrO<sub>2</sub>(Y) films. *Tech. Phys.*, 2020, **65**, P. 1744–1747.

---

*Submitted 23 August 2022; revised 12 October 2022; accepted 2 December 2022*

*Information about the authors:*

*Mikhail B. Semenov* – Penza State University, Krasnaya, 40, Penza, 440026, Russia; ORCID 0000-0003-4348-0000; misha29.02.1@gmail.com

*Vladimir D. Krevchik* – Penza State University, Krasnaya, 40, Penza, 440026, Russia; ORCID 0000-0002-3522-8326; physics@pnzgu.ru

*Dmitry O. Filatov* – Lobachevsky State University of Nizhni Novgorod, Prospect Gagarina, 23, bldg. 2, 603950, Nizhniy Novgorod, Russia; ORCID 0000-0001-5231-5037; Dmitry\_filatov@inbox.ru

*Dmitry A. Antonov* – Lobachevsky State University of Nizhni Novgorod, Prospect Gagarina, 23, bldg. 2, 603950, Nizhniy Novgorod, Russia; ORCID 0000-0002-3247-8178; antonov@phys.unn.ru

*Alexey V. Shorokhov* – Penza State University, Krasnaya, 40, Penza, 440026, Russia; ORCID 0000-0001-6007-5598; alex.shorokhov@gmail.com

*Alexander P. Shkurinov* – Institute for Problems of Laser and Information Technologies RAS, Moscow reg., 140700, Russia; ORCID 0000-0002-6309-4732; ashkurinov@gmail.com

*Ilya A. Ozheredov* – Institute for Problems of Laser and Information Technologies RAS, Moscow reg., 140700, Russia; ORCID 0000-0002-3620-6903; ozheredov@physics.msu.ru

*Pavel V. Krevchik* – Penza State University, Krasnaya, 40, Penza, 440026, Russia; physics@pnzgu.ru

*Alexey V. Razumov* – Penza State University, Krasnaya, 40, Penza, 440026, Russia; razumov\_alex@mail.ru

*Alexey S. Kotov* – Lobachevsky State University of Nizhni Novgorod, Prospect Gagarina, 23, bldg. 2, 603950, Nizhnij Novgorod, Russia; Alexey\_600sl@mail.ru

*Ilya S. Antonov* – Penza State University, Krasnaya, 40, Penza, 440026, Russia; physics@pnzgu.ru

*Ivan M. Semenov* – Penza State University, Krasnaya, 40, Penza, 440026, Russia; semenovivm@gmail.com

*Conflict of interest:* the authors declare no conflict of interest.

## Master equation for correlators of normal-ordered field mode operators

Alexander D. Vatutin<sup>a</sup>, George P. Miroshnichenko<sup>b</sup>, Alexander I. Trifanov<sup>c</sup>

ITMO University, Kronverkskiy, 49, St. Petersburg, 197101, Russia

<sup>a</sup>advatutin@yandex.ru, <sup>b</sup>gpmirosh@gmail.com, <sup>c</sup>alextrifanov@gmail.com

Corresponding author: Alexander D. Vatutin, advatutin@yandex.ru

PACS 03.65.Yz, 03.65.Ca

**ABSTRACT** We study the master equation for open quantum systems in the alternative form, preserving the normal form of the averaged normal-ordered operators. We give an example of using this equation for the correlators of normal-ordered field mode operators. We explore the properties of the system of linear equations for the higher-order field operators based on the example of a two-mode bosonic system.

**KEYWORDS** master equation, normal-ordered correlators, two-mode bosonic system

**FOR CITATION** Vatutin A.D., Miroshnichenko G.P., Trifanov A.I. Master equation for correlators of normal-ordered field mode operators. *Nanosystems: Phys. Chem. Math.*, 2022, **13** (6), 628–631.

### 1. Introduction

Quantum information processing is transfer, storage, and conversion of quantum information. It is essential for quantum protocols like quantum teleportation [1], quantum computing [2], quantum key distribution [3], dense coding, and quantum memory [4]. There are plenty of approaches to various problems for these protocols, but there is no general model that describes all kinds of them.

Models of open quantum systems are intended for solving problems of transport and storage of quantum information. This approach can be described in terms of completely positive trace-preserving (CPTP), or trace-non-increasing linear mappings known as quantum channels. The quantum master equation is the most effective way to determine the dynamics of open systems. More precisely, we use the Lindblad-type master equation [5, 6]. This equation was studied using physical methods [7–9] and mathematical techniques for the case of the single-mode Lindblad equation [6, 10–17]. In the case of multi-mode bosonic systems, the mathematical approach was used to construct the Fock-like eigenstates of the Lindblad superoperators using the Lie algebras [18].

This approach simplifies the determination of the dynamics of the averaged moments of the Stokes operator and the polarization of light [19]. These parameters are sufficient for a fairly accurate description of many physical processes. However, these averaged moments of the Stokes operator are inadequate in cases when other statistical parameters than the wave average intensity are recorded [20]. Hence, the investigation of the higher-order moment correlators is required for a more detailed description of these quantum processes. We offer a more convenient representation of the Lindblad equation for the calculation of higher-order moments. The equation saves the normal form of the operators: if the original averaged operator was represented in the normal form, then each term in the equation has the form of the average of the operator in the normal form.

### 2. Model

The starting point is the Gorini–Kossakowski–Sudarshan–Lindblad (GKSL) form of the master equation for polarized light in the two-mode bosonic system in optical fibers:

$$\frac{\partial \rho}{\partial t} = -i \sum_{n,m} \frac{1}{2} \Omega_{n,m} [a_n^\dagger a_m, \rho] - \sum_{n,m} \frac{1}{2} \Gamma_{n,m} \left( (n_T + 1) (a_n^\dagger a_m \rho + \rho a_n^\dagger a_m - 2a_m \rho a_n^\dagger) + n_T (a_m a_n^\dagger \rho + \rho a_m a_n^\dagger - 2a_n^\dagger \rho a_m) \right), \quad (1)$$

where indexes  $n, m \in \{1, 2\}$ , dagger denotes the Hermitian conjugation,  $\rho$  is the density matrix of a quantum state,  $a_n^\dagger$  and  $a_n$  are the creation and the annihilation operators of the  $n$ -th mode,  $\Omega$  and  $\Gamma$  are the frequency and the relaxation matrices [21], and  $n_T$  is the mean number of thermal photons:

$$n_T = \frac{1}{\exp\left(\frac{\hbar\Omega_0}{k_B T}\right) - 1},$$

where  $\Omega_0$  is the free-space frequency,  $\hbar$  is the reduced Planck constant,  $T$  is the environment temperature.  $k_B$  is the Boltzmann constant. The frequency ( $\Omega$ ) and the relaxation ( $\Gamma$ ) matrices are Hermitian:  $\Omega = \Omega^\dagger, \Gamma = \Gamma^\dagger$ . The positivity condition for the relaxation matrix has the following (conventional) form:  $z^* \Gamma z \geq 0, z \in \mathbb{C}^2$ .

### 3. Alternative form for the Lindblad equation

Let us apply some operator  $\hat{A}$  to the both parts of equation (1) and calculate the trace of the obtained operators. Note that the average  $A$  of the operator  $\hat{A}$  is given by the following formula  $A = \langle \hat{A} \rangle = \text{Tr}(\hat{A}\rho)$ . Keeping in mind that the trace is invariant under cyclic permutations, we obtain the following relation:

$$\begin{aligned} \frac{\partial A}{\partial t} = \text{Tr} \left( -\frac{i}{2} \sum_{n,m} \Omega_{n,m} (\hat{A} a_n^\dagger a_m \rho - a_n^\dagger a_m \hat{A} \rho) - \right. \\ \left. -\frac{1}{2} \sum_{n,m} \Gamma_{n,m} (n_T + 1) (\hat{A} a_n^\dagger a_m \rho + a_n^\dagger a_m \hat{A} \rho - 2a_n^\dagger A a_m \rho) - \right. \\ \left. -\frac{1}{2} \sum_{n,m} \Gamma_{n,m} n_T (\hat{A} a_m a_n^\dagger \rho + a_m a_n^\dagger \hat{A} \rho - 2a_m \hat{A} a_n^\dagger \rho) \right). \quad (2) \end{aligned}$$

Our goal is to bring the equation to such a form that if the operator  $A$  is in the normal form then the equation contains operators in the normal form only. Consider each of the sums in (2), starting with the first one:

$$\begin{aligned} \text{Tr} \left( -\frac{i}{2} \sum_{n,m} \Omega_{n,m} (\hat{A} a_n^\dagger a_m \rho - a_n^\dagger a_m \hat{A} \rho) \right) = \\ \text{Tr} \left( -\frac{i}{2} \sum_{n,m} \Omega_{n,m} (\hat{A} a_n^\dagger a_m - a_n^\dagger \hat{A} a_m + a_n^\dagger \hat{A} a_m - a_n^\dagger a_m \hat{A}) \rho \right) = \\ \text{Tr} \left( -\frac{1}{2} \sum_{n,m} (i\Omega_{n,m} [\hat{A}, a_n^\dagger] a_m - i\Omega_{n,m} a_n^\dagger [a_m, \hat{A}]) \rho \right). \quad (3) \end{aligned}$$

As for the second sum, one subtracts and adds  $a_n^\dagger a_m \hat{A} \rho$  to obtain commutators:

$$\begin{aligned} -\frac{1}{2} \sum_{n,m} \Gamma_{n,m} (n_T + 1) (\hat{A} a_n^\dagger a_m \rho + a_n^\dagger a_m \hat{A} \rho - 2a_n^\dagger \hat{A} a_m \rho) = \\ -\frac{1}{2} \sum_{n,m} (n_T + 1) \Gamma_{n,m} ([\hat{A}, a_n^\dagger] a_m + a_n^\dagger [a_m, \hat{A}]) \rho. \quad (4) \end{aligned}$$

Let us consider the third sum in more details following the procedure used above:

$$\begin{aligned} \text{Tr} \left( -\frac{1}{2} \sum_{n,m} \Gamma_{n,m} n_T (\hat{A} a_m a_n^\dagger \rho + a_m a_n^\dagger \hat{A} \rho - 2a_m \hat{A} a_n^\dagger \rho) \right) = \\ \text{Tr} \left( -\frac{1}{2} \sum_{n,m} \Gamma_{n,m} n_T (\hat{A} a_m a_n^\dagger - a_m a_n^\dagger \hat{A} + 2[a_m, [a_n^\dagger, \hat{A}]] + 2[a_n^\dagger, A] a_m) \rho \right) = \\ \text{Tr} \left( -\sum_{n,m} \Gamma_{n,m} n_T ([a_m, [a_n^\dagger, A]]) \rho - \frac{1}{2} \sum_{n,m} \Gamma_{n,m} n_T (A a_n^\dagger a_m - a_n^\dagger a_m A + 2[a_n^\dagger, A] a_m) \rho \right) = \\ \text{Tr} \left( -\sum_{n,m} \Gamma_{n,m} n_T [[\hat{A}, a_n^\dagger], a_m] \rho \right) + \text{Tr} \left( \frac{1}{2} \sum_{n,m} \Gamma_{n,m} n_T ([\hat{A}, a_n^\dagger] a_m + a_n^\dagger [a_m, \hat{A}]) \rho \right). \quad (5) \end{aligned}$$

Substituting (3), (4) and (5) in (2), we obtain the following relation for averaging of any operator  $\hat{A}$ :

$$\begin{aligned} \frac{\partial A}{\partial t} = \\ \frac{1}{2} \sum_{n,m} \left( \langle [\hat{A}, a_n^\dagger] a_m \rangle (-i\Omega_{n,m} - \Gamma_{n,m}) + \langle a_n^\dagger [a_m, \hat{A}] \rangle (i\Omega_{n,m} - \Gamma_{n,m}) \right) - n_T \sum_{n,m} \Gamma_{n,m} \langle [[\hat{A}, a_n^\dagger], a_m] \rangle. \quad (6) \end{aligned}$$

One can note that this form of the master equation saves the normal form of the operators. An example showing this property is presented below.

#### 4. Second normal-ordered moments

Let us assume the operator  $\hat{A} = a_p^\dagger a_q$  has the form of a field operator. Hence, the commutators in the expression (6) can be rewritten as follows:

$$\begin{aligned} [a_p^\dagger a_q, a_n^\dagger] &= \delta_{qn} a_p^\dagger, \\ [[a_p^\dagger a_q, a_n^\dagger], a_m] &= -\delta_{qn} \delta_{pm}, \\ [a_m, a_p^\dagger a_q] &= \delta_{pm} a_q \end{aligned}$$

and equation (6) takes the form:

$$\frac{\partial \langle a_p^\dagger a_q \rangle}{\partial t} = \frac{1}{2} \sum_m \langle a_p^\dagger a_m \rangle (-i\Omega_{q,m} - \Gamma_{q,m}) + \frac{1}{2} \sum_n \langle a_n^\dagger a_q \rangle (i\Omega_{n,p} - \Gamma_{n,p}) + n_i \Gamma_{q,p}. \quad (7)$$

Note that all operations in (6) are very simple. All transformations are reduced to counting of three simple commutators. The commutators in the first and the second sums preserve the order of the operators, and the double commutator in the third sum lowers the order by 2. This property takes place for any field operator. Furthermore, it is valid for any operator, if we expand it in respect to the basis of the field operators.

Let the set of operators  $\hat{A}_i(\hat{B}_i)$  consist of the normal-ordered operators. Let any operator  $\hat{A}_i$  be a product of  $\alpha$  operators of annihilation and  $\beta$  operators of creations in any possible variants of modes; any operator  $\hat{B}_i$  is a product of  $\alpha - 1$  operators of annihilation and  $\beta - 1$  operators of creations in any possible variants of modes. Then the system of differential equations for the set  $\hat{A}_i$  derived from equation (6) gives one the expression containing two sets of operators  $\hat{A}_i$  and  $\hat{B}_i$ . This means that the equations of higher orders depend on the lower ones recursively. Example (7) shows this property in the simplest case ( $\alpha = \beta = 1$ ).

We can mention the amount of non-recurring expressions in the system. Only an amount of possible variations of operators of the creation (annihilation) in the first mode affects the quantity of all variants, because of  $[a_p^\dagger, a_q^\dagger] = [a_p, a_q] = 0$ . Hence, the amount of equations is equal to  $(\alpha + 1)(\beta + 1)$ .

#### 5. Conclusion

In this paper, we presented the equation for the normal-ordered moments and its property of saving the normal order. We started with the master equation in the GKSL form, converted it to the convenient form for the normal-ordered moments (6), and gave the example for the two-mode bosonic system. This is a logical continuation for the description of open quantum systems. We will try to continue the idea in terms of hidden polarization of light.

#### References

- [1] Pirandola S., Eisert J., Weedbrook C., Furusawa A., Braunstein S.L. Advances in quantum teleportation. *Nat. Photon.*, 2015, **9**, P. 641–652.
- [2] Gyongyosi L., Imre S. A survey on quantum computing technology. *Comput. Sci. Rev.*, 2019, **31**, P. 51–71.
- [3] Pirandola S., Andersen U., Banchi L., Berta M., Bunandar D., Colbeck R., Englund D., Gehring T., Lupo C., Ottaviani C., Pereira J. Advances in quantum cryptography. *Adv. Opt. Photon.*, 2020, **12**, P. 1012–1236.
- [4] Lvovsky A.I., Sanders B.C., Tittel W. Optical quantum memory. *Nat. Photon.*, 2009, **3**, P. 706–714.
- [5] Gaidash A., Kozubov A., Miroshnichenko G. Dissipative dynamics of quantum states in the fiber channel. *Phys. Rev. A*, 2020, **102**, 023711.
- [6] Bonetti J., Hernandez S.M., Grosz D.F. Master equation approach to propagation in nonlinear fibers. *Opt. Lett.*, 2021, **46**, P. 665–668.
- [7] Pearle P. Simple derivation of the Lindblad equation. *Eur. J. Phys.*, 2012, **33**, P. 805–822.
- [8] Albash T., Boixo S., Lidar D.A., Zanardi P. Quantum adiabatic Markovian master equations. *New J. Phys.*, 2012, **14**, 123016.
- [9] McCauley G., Cruikshank B., Bondar D.I., Jacobs K. Accurate Lindblad-form master equation for weakly damped quantum systems across all regimes. *npj Quantum Inf.*, 2020, **6**, 74.
- [10] Miroshnichenko G. Decoherence of a one-photon packet in an imperfect optical fiber. *Bull. Russ. Acad. Sci.*, 2018, **82**, P. 1550–1555.
- [11] Kozubov A., Gaidash A., Miroshnichenko G. Quantum model of decoherence in the polarization domain for the fiber channel. *Phys. Rev. A*, 2019, **99**, 053842.
- [12] Miroshnichenko G.P. Hamiltonian of photons in a single-mode optical fiber for quantum communications protocols. *Opt. Spectrosc.*, 2012, **112**, P. 777–786.
- [13] Lu H.-X., Yang J., Zhang Y.-D., Chen Z.-B. Algebraic approach to master equations with superoperator generators of  $su(1,1)$  and  $su(2)$  Lie algebras. *Phys. Rev. A*, 2003, **67**, 024101.
- [14] Tay B.A., Petrosky T. Biorthonormal eigenbasis of a Markovian master equation for the quantum Brownian motion. *J. Math. Phys.*, 2008, **49**, 113301.
- [15] Honda D., Nakazato H., Yoshida M. Spectral resolution of the Liouvillian of the Lindblad master equation for a harmonic oscillator. *J. Math. Phys.*, 2010, **51**, 072107.
- [16] Tay B.A. Eigenvalues of the Liouvillians of quantum master equation for a harmonic oscillator. *Physica A*, 2020, **556**, 124768.
- [17] Shishkov V.Y., Andrianov E.S., Pukhov A.A., Vinogradov A.P., Lisyansky A.A. Perturbation theory for Lindblad superoperators for interacting open quantum systems. *Phys. Rev. A*, 2020, **102**, 032207.
- [18] Teuber L., Scheel S. Solving the quantum master equation of coupled harmonic oscillators with Lie-algebra methods. *Phys. Rev. A*, 2020, **101**, 042124.

- [19] Gaidash A., Kozubov A., Miroshnichenko G., Kiselev A.D. Quantum dynamics of mixed polarization states: effects of environment-mediated intermode coupling. *JOSA B*, 2021, **38** (9), 425226.
- [20] Klyshko D.M. Polarization of light: fourth-order effects and polarization-squeezed states. *Zh. Eksp. Teor. Fiz.*, 1997, **111**, P. 1955–1983.
- [21] Miroshnichenko G.P. Parameterization of an interaction operator of optical modes in a single-mode optical fiber. *Nanosystems: Physics, Chemistry, Mathematics*, 2015, **6** (6), P. 857–865.

---

Submitted 24 October 2022; revised 31 October 2022; accepted 13 November 2022

*Information about the authors:*

Alexander D. Vatutin – ITMO University, Kronverkskiy, 49, St. Petersburg, 197101, Russia;  
ORCID 0000-0003-1853-2171; advatutin@yandex.ru,

George P. Miroshnichenko – ITMO University, Kronverkskiy, 49, St. Petersburg, 197101, Russia;  
ORCID 0000-0002-4265-8818; gpmirosh@gmail.com

Alexander I. Trifanov – ITMO University, Kronverkskiy, 49, St. Petersburg, 197101, Russia;  
ORCID 0000-0002-5109-2086; alextrifanov@gmail.com

*Conflict of interest:* the authors declare no conflict of interest.

## Photocatalytic activity of titanium dioxide produced by high-energy milling

Ekaterina A. Kozlova<sup>1,2,a</sup>, Albina A. Valeeva<sup>3,b</sup>, Anna A. Sushnikova<sup>1,c</sup>, Angelina V. Zhurenok<sup>2,d</sup>,  
Andrey A. Rempel<sup>1,e</sup>

<sup>1</sup>Institute of Metallurgy, UB RAS, Yekaterinburg, 620016, Russia

<sup>2</sup>Boreskov Institute of Catalysis, SB RAS, Novosibirsk, 630090, Russia

<sup>3</sup>Institute of Solid State Chemistry, UB RAS, Yekaterinburg, 620108, Russia

<sup>a</sup>kozlova@catalysis.ru, <sup>b</sup>anibla\_v@mail.ru, <sup>c</sup>sushnikova.ann@gmail.com, <sup>d</sup>angelinazhurenok@gmail.com,  
<sup>e</sup>rempe.imet@mail.ru

Corresponding author: Ekaterina A. Kozlova, kozlova@catalysis.ru

PACS 82.65.+r, 68.43.-h

**ABSTRACT** In this work, photocatalysts based on titanium dioxide were synthesized by high-energy ball milling of commercial titanium dioxide in the anatase modification. Using a complex of physicochemical methods, including XRD, low-temperature nitrogen adsorption, XPS and TEM, it was shown that the milling of commercial anatase leads to phase transformations and the formation of several phases of titanium dioxide, namely the high-pressure phase, the monoclinic phase of anatase and rutile, except for in addition, there is a change in the crystalline size and the value of the specific surface area grows from 8 to 31 m<sup>2</sup>/g. It was found that defects are introduced into the system during ball milling. The photocatalysts obtained by milling showed an activity comparable to the commercial standard TiO<sub>2</sub> Degussa P25 in the destruction of the methylene blue dye under the action of UV light, while the adsorption properties of the synthesized samples exceeded those of commercial P25.

**KEYWORDS** Titanium dioxide, high-energy ball milling, photocatalytic oxidation

**ACKNOWLEDGEMENTS** This work was supported by the Russian Science Foundation, project no. 21-73-20039. XPS and HRTEM investigations was performed using the facilities of the shared research center “National Center for the Investigation of Catalysts” at the Boreskov Institute of Catalysis. Authors thanks to I. D. Popov, A. A. Saraev, E. Yu. Gerasimov for DRS, XPS, and TEM experiments, respectively.

**FOR CITATION** Kozlova E.A., Valeeva A.A., Sushnikova A.A., Zhurenok A.V., Rempel A.A. Photocatalytic activity of titanium dioxide produced by high-energy milling. *Nanosystems: Phys. Chem. Math.*, 2022, **13** (6), 632–639.

### 1. Introduction

Currently, the problem of water and air purification from various contaminants is very urgent [1]. The recent rapid growth of the industry led to worldwide environmental problems [2]. It is well known that dyes play an important role in various branches of textile industry. Nowadays over 100 000 commercially available synthetic dyes are usually used in industries. These dyes are mainly derived from coal tar and petroleum intermediates, with a total annual production of more than  $7 \cdot 10^5$  tons [3–6].

Advanced oxidation processes (AOPs) are the most widely used technology for dye degradation. Recently, there has been a great amount of works that has been done and various kinds of AOPs have been developed [7]. At present, for the oxidation of various pollutants, including dyes, photocatalysis on semiconductors is widely used [8]. Of great interest is the photocatalytic oxidation of pesticides and detergents [9]. Photocatalytic reactions for the oxidation of pesticides such as acrinathrine, methamidophos, malathion, diazion, carbetamide, and the insecticide fenitration have already been described [9–13]. A large number of works are devoted to the photocatalytic oxidation of various dyes [14, 15].

In the photocatalytic method of water purification, titanium dioxide is used in most cases. Titanium dioxide TiO<sub>2</sub> is one of the most common photocatalysts due to its stability, relatively high activity, and environmental safety [16, 17]. This compound occurs in three phases: anatase (tetragonal), rutile (tetragonal), and brookite (orthorhombic). The anatase phase is considered to be the most photocatalytically active than the rutile phase due to the higher (by 0.1 eV) position of the Fermi level, due to which the electrons have a higher reduction potential [18]. On the other hand, rutile has a smaller band gap (3.0 eV) compared to anatase (3.2 eV) [19], which contributes to the absorption of light with a longer wavelength [20]. Previously, in our works, a strong influence of the phase composition of titanium dioxide on its photocatalytic activity was shown [21, 22]. An affordable way to modify titanium dioxide is high-energy ball milling. During high-energy milling,

various processes can occur, including the formation of structural defects, phase transformations, morphology changes, and particle fragmentation [23].

In this work, photocatalysts based on titanium dioxide with improved physicochemical properties were synthesized by a simple and cost-effective method of high-energy milling of commercially available anatase. These samples were successfully tested in the photocatalytic oxidation of methylene blue dye under the action of UV irradiation. The influence of milling parameters on the photocatalytic and adsorption properties of the samples was revealed.

## 2. Experimental

### 2.1. Photocatalyst synthesis

Anatase titanium dioxide (Sigma Aldrich, composition: anatase – 98 wt.% rutile – 2 wt.%, 99.8% purity) was used as the initial powders (A0 sample). To modify the initial titanium dioxide powders, high-energy ball milling was used in Retsch PM 200 planetary ball mill. The high-strength ceramics, namely zirconium dioxide  $ZrO_2$  stabilized with yttrium oxide  $Y_2O_3$  was chosen as the material for the milling bowls and balls to minimize sample contamination during milling. The optimal mass ratio of milling balls and powders, namely 10:1, was chosen to effectively obtain the smallest nanoparticle size. Isopropyl alcohol was used as the milling liquid. To prevent the formation of rutile during milling, a special mode was chosen in this experiment: rotation speed of support disks 500 rpm at milling duration of 4 and 8 h with direction reversal every 10 minutes and a pause of 15 minutes. The obtained samples of anatase after mechanical activation for different milling times are designated A4 and A8, respectively.

### 2.2. Photocatalyst characterization

X-ray phase analysis of the initial and milled powders was performed in  $CuK_{\alpha 1,2}$  radiation using XRD-7000 (Shimadzu, Japan) autodiffractometer in the Bragg–Brentano geometry in the step-by-step scanning mode with  $\Delta(2\theta) = 0.02^\circ$  in the angle range  $2\theta$  from  $10$  to  $120^\circ$  with high statistics. The “Powder Standards Database – ICDD, USA, Release 2016” was used to identify the phases. Phase analysis was carried out using the Powder Cell 2.4 program. The dimensional and deformation contributions to the reflection broadening were determined by the Williamson–Hall method.

The specific surface area of all samples was measured using a Nova 1200e analyzer (Quantachrome Instruments, USA) implementing the Brunauer–Emmett–Teller (BET) method with preliminary degassing at  $150^\circ C$  for 60 min.

Optical properties were studied by using FS-5 spectrofluorometer (Edinburgh Instruments) equipped by arc Xe-lamp (450 W), photomultiplier and integrating sphere. Spectroscopic measurements were done in the range of 250 – 850 nm at ambient temperature. Optical polytetrafluoroethylene was used as a white standard for diffuse reflectance. Processing of experimental spectra was performed using the Kubelka–Munch function.

X-ray photoelectron spectroscopy (XPS) was used to study the chemical composition of the surface of the photocatalysts with the use of photoelectron spectrometer SPECS Surface Nano Analysis GmbH (Berlin, Germany) using non-monochromatized  $AlK_{\alpha}$  radiation ( $h\nu = 1486.61$  eV). Data processing was carried out using the CasaXPS software package. Transmission electron microscopy (TEM) was used to study the structure and microstructure of the catalysts using a ThemisZ electron microscope (Thermo Fisher Scientific, Waltham, MO, USA).

The structure and microstructure of the samples were studied by high-resolution transmission electron microscopy (HRTEM) on a ThemisZ dual-corrector transmission electron microscope (Thermo Fisher Scientific, USA). Images were recorded using a Ceta 16 CCD array (Thermo Fisher Scientific, USA). The instrument is equipped with a SuperX (Thermo Fisher Scientific, USA) energy-dispersive characteristic X-ray spectrometer (EDX) with a semiconductor Si detector with an energy resolution of 128 eV.

### 2.3. Photocatalytic experiments

The photocatalytic reactor and emission spectra of the light source are shown in Fig. 1.

An aqueous solution of methylene blue with a concentration of  $2 \cdot 10^{-4}$  M for carrying out photocatalytic oxidation was diluted 10 times and adjusted to  $pH = 7$  with a NaOH solution with a concentration of 0.01 M. The  $pH$  of the stock solution was measured with an Ohaus Starter ST3100  $pH$  meter. A suspension consisting of an aqueous solution of methylene blue with a volume of 100 ml and a photocatalyst with a mass of 50 mg was placed in a photocatalytic reactor and processed in an ultrasonic bath “Sapphire” UZV-1.3/2. Next, the reactor was removed for 60 minutes in a dark place for efficient adsorption of methylene blue on the catalyst. After adsorption, the photocatalytic reactor was illuminated by a LED with a wavelength of 365 nm ( $2 \text{ mW cm}^{-2}$ ) for 3 hours. Samples of methylene blue with a volume of 3 ml were taken before and after adsorption, as well as every hour during illumination. To obtain a pure solution without catalyst impurities, the samples were filtered using hydrophobic membrane filters. Samples were analyzed by UV-Vis spectroscopy on Shimadzu UV-2501 PC spectrophotometer.

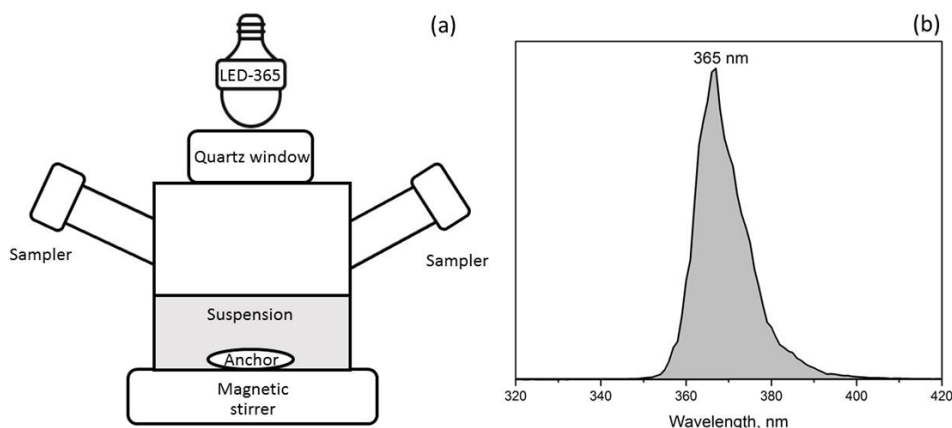


FIG. 1. Photocatalytic reactor (a), emission spectra of the light source (b)

### 3. Results and discussion

#### 3.1. Characterization of photocatalyst samples

A sample of commercial anatase before milling and photocatalysts synthesized by ball milling the original  $\text{TiO}_2$  were examined by XRD (Fig. 2a). The phase composition and textural properties of photocatalysts are presented in Table 1.

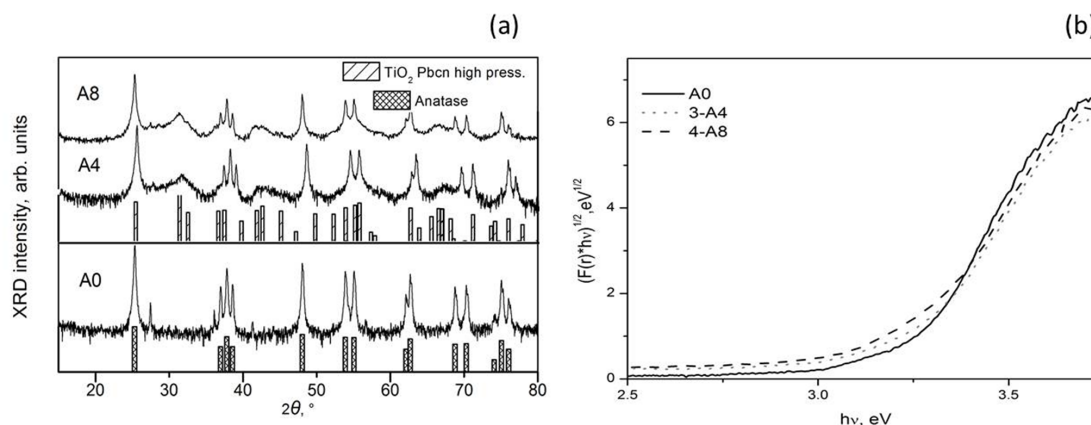


FIG. 2. XRD (a), diffuse reflectance spectra in Tauc's plot (b) of the samples

The original sample A0 is a standard anatase (I41/amd) with rutile impurities. Analysis by XRD shows that the ball milling of anatase proceeds with the formation of several modifications of  $\text{TiO}_2$ . After 4 hours of anatase milling, in addition to the standard anatase phase (I41/amd), the formation of a high-pressure phase (Pbcn) – 27 wt.%, anatase monoclinic phase (C2/m) – 3 wt.% and a standard rutile phase (P42/ mnm) – 1 wt.% were observed. Milling up to 8 hours leads to an increase in the content of the high-pressure phase up to 24 wt. %, a decrease in the average particle size and an increase in the specific surface area from 8 to 31  $\text{m}^2/\text{g}$ .

To analyze the optical properties of the samples, diffuse reflectance spectra of photocatalysts were obtained. The band gap of the studied catalysts was determined using the Kubelka–Munk function, the calculation was performed for an indirect ( $n = 2$ ) allowed transition (Fig. 2b). An analysis of the dependences showed that anatase milling does not lead to significant changes in the band gap of the catalysts; band gap energy is about 3.2 eV, which is typical for the anatase modification of titanium dioxide [24].

The surface properties of photocatalysts A0, A4, and A8 were studied by XPS. The relative concentrations (atomic ratios) of the elements in the surface layer of the samples, as well as the values of the Ti2p, O1s, and C1s binding energies, determined on the basis of XPS data, are presented in Table 2.

The Ti2p spectra of the studied samples are shown in Fig. 3a. As is known, the 2p level of titanium is split into two sublevels  $\text{Ti}2p_{3/2}$  and  $\text{Ti}2p_{1/2}$  due to the spin-orbit interaction; the spin-orbit splitting is 5.66 eV. The  $\text{Ti}2p_{3/2}$  peak has a symmetrical shape, and the  $\text{Ti}2p_{3/2}$  binding energy is 459.0 eV, which corresponds to Ti in the  $\text{Ti}^{4+}$  state in the  $\text{TiO}_2$  structure. In the literature,  $\text{Ti}2p_{3/2}$  binding energies are given for  $\text{TiO}_2$  in the range of 458.7 – 459.2 eV, while for Ti in the  $\text{Ti}^{3+}$  state, in the range of 456.2 – 457.4 eV [25–29]. Also, in the Ti2p spectra of titanium of all samples, except for A0,

TABLE 1. Phase composition and textural, adsorption, and photocatalytic characteristics of the tested catalysts

Sample	Phase composition		wt. %	CSR, nm	$S_{BET}$ , m <sup>2</sup> /g	$E_g$ , eV	$(C_0 - C)/C_0$ , % after adsorption	$(C_0 - C)/C_0$ , % after photocatalysis
A0	Anatase	<i>I41/amd</i>	98	100	8	3.22	32	89
	Rutile	<i>P42/mnm</i>	2	>100				
A4	Anatase	<i>I41/amd</i>	69	81	16	3.22	79	87
	Anatase	<i>Pbcn</i>	27	—				
	Anatase	<i>C2/m</i>	3	—				
	Rutile	<i>P42/mnm</i>	1	53				
A8	Anatase	<i>I41/amd</i>	72	80	31	3.21	58	84
	Anatase	<i>Pbcn</i>	24	8				
	Anatase	<i>C2/m</i>	2	—				
	Rutile	<i>P42/mnm</i>	2	—				
Evonik P25	Anatase	<i>I41/amd</i>	85	19	55	3.14	9	96
	Rutile	<i>P42/mnm</i>	15	30				

TABLE 2. Relative atomic concentrations of elements<sup>1</sup> in the surface layer of the studied samples, as well as the Ti2p, O1s, and C1s binding energies (eV)

No.	Sample	[Ti <sup>3+</sup> ]	[O <sub>x</sub> ]	[C]	[O]	Binding energy, eV		
						Ti <sup>3+</sup> Ti2p <sub>3/2</sub>	O1s	C1s
1	A0	0.01	2.56	2.38	3.25	—	530.3	285.3
2	A4	0.08	2.55	4.81	3.35	457.8	530.3	285.2
3	A8	0.11	2.47	6.18	3.56	457.8	530.3	285.2

<sup>1</sup>All correlations are normalized to [Ti]

a low-intensity doublet is observed in the region of lower binding energies (the binding energy of Ti2p<sub>3/2</sub> is 457.8 eV), which, according to the literature data, can be attributed to Ti in the Ti<sup>3+</sup> state.

The O1s spectra are shown in Fig. 3b. The spectra are described by several peaks corresponding to oxygen in different environments, so the O1s peak in the region of 530.3 eV undoubtedly refers to oxygen in the TiO<sub>2</sub> structure [25–29]. The peak in the O1s spectra in the region of 531.9 eV for samples of series A refers to the surface OH-, sulfate/sulfite, and phosphate groups; the peak in the region and 533.6 eV refers to adsorbed water.

In order to show the transformation of the properties of the samples during milling, HRTEM images of all photocatalysts were obtained.

According to the HRTEM data, sample A0 consists of rounded particles with sizes on the order of 100 nm. On the surface of the particles, lamellar particles with sizes of 5 – 10 nm, also related to TiO<sub>2</sub>, are observed. The analysis of interplanar distances showed the presence of the anatase phase and did not reveal defects or impurities in the composition of rounded particles, however, it should be noted that an amorphous layer is observed on the surface, this type can be attributed to contamination with carbonaceous deposits (Fig. 4a–b). HRTEM images of sample A4 are shown in Fig. 4c–d. In this sample, a large number of TiO<sub>2</sub> particles with sizes of about 10 nm appear on the surface of large agglomerates, while some of the fine particles also form agglomerates with sizes of about 100 nm. The study of interplanar distances showed that the nanoparticles of the main phase can be attributed to the anatase modification, and the precipitated phase to the rutile modification. This is displayed in the figures as distances of 3.3 Å for rutile and 3.5 Å for anatase. According to HRTEM data (Fig. 5), in sample A8, the content of the rutile phase increases, some of these particles agglomerate with the formation of lamellar disordered defective particles with a microdomain structure. An analysis of the interplanar

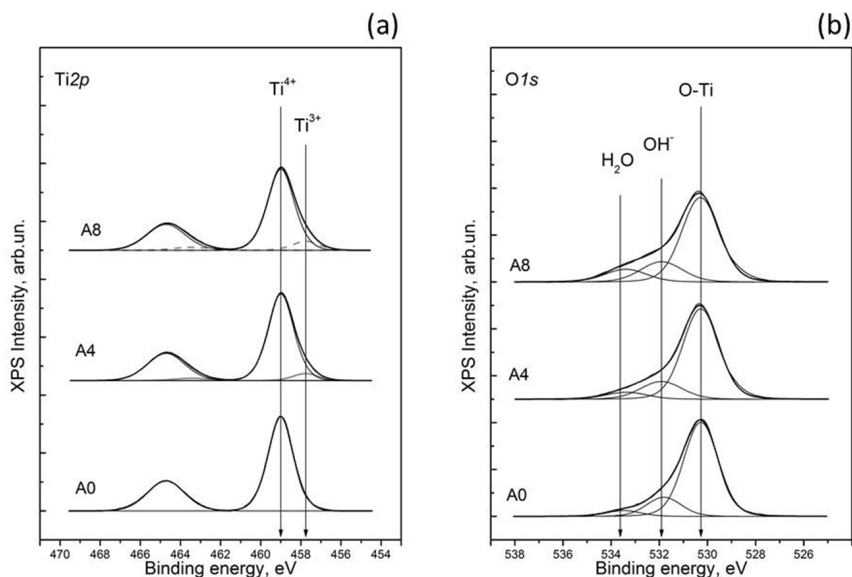


FIG. 3. XPS Ti2p (a), O1s (b) spectra of the samples

distances did not reveal the formation of new phases. Elemental mapping also shows that the sample is composed of titanium dioxide.

In general, according to the characterization by a complex of physicochemical methods of samples A0, A4, A8, the following conclusion can be made that the milling of commercial anatase leads to phase transformations and the formation of several phases of titanium dioxide, namely the high-pressure phase, the monoclinic phase of anatase and rutile, in addition there is a change in the crystalline size and the value of the specific surface area from 8 to 31 m<sup>2</sup>/g. It has been established that defects are introduced into the system during grinding, which is confirmed by XPS and HRTEM data. It is believed that this defective structure improves the adsorption and catalytic properties of materials.

### 3.2. Photocatalytic activity

The activity of all the studied samples was investigated in the photocatalytic oxidation of the methylene blue dye under the action of UV radiation with a wavelength of 365 nm. Optical densities of the dye solutions before and after irradiation at a wavelength of 666 nm were used to calculate the decoloration degree of the dye. For comparison, photocatalytic oxidation was carried out using the most commonly used commercial photocatalyst TiO<sub>2</sub> Degussa P25 (anatase/rutile).

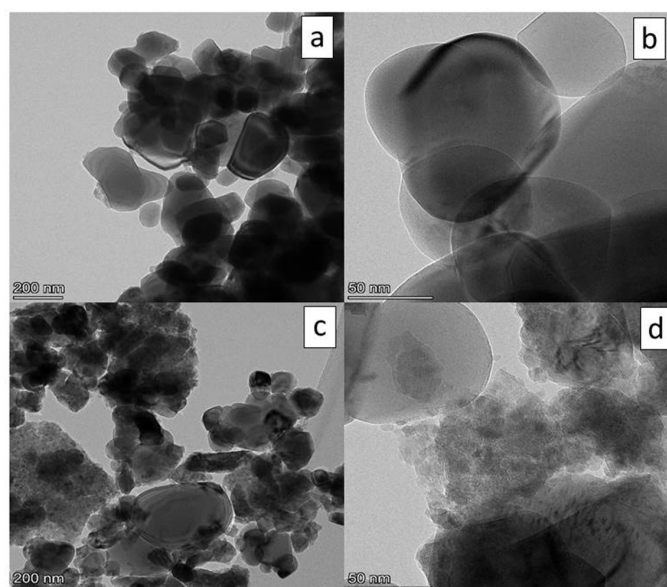


FIG. 4. HRTEM images of sample A0 (a–b top) and A4 (c–d bottom)

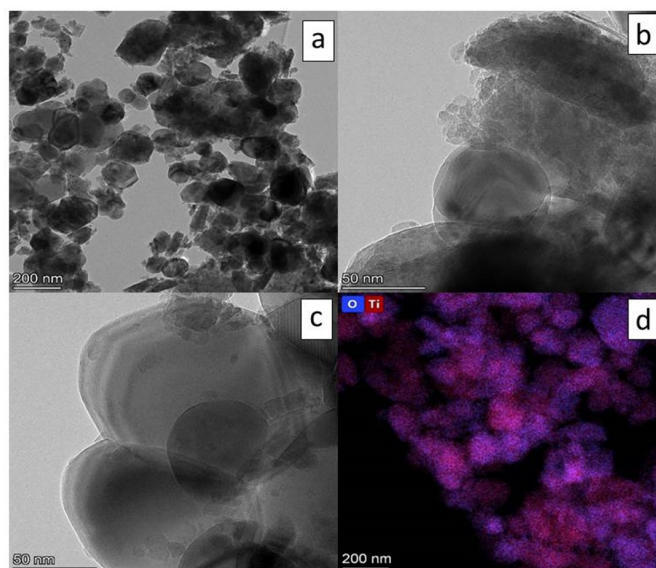


FIG. 5. HRTEM images (a–c) and EDX mapping (d) of sample A8

Substrate adsorption and photocatalytic oxidation data are presented in Table 1; kinetic dependences of photocatalytic oxidation are presented in Fig. 6.

It can be seen that in the blank experiment without a photocatalyst, no degradation of the dye under the action of UV-irradiation is observed. At the same time, with all samples of titanium dioxide, including Degussa P25, almost complete degradation of the MB dye occurred in an hour of irradiation. A significant difference is the much stronger adsorption occurring both in the presence of sample A0, and especially in the presence of samples A4 and A8. Thus, almost 80 % of the dye was degraded during an hour of dark adsorption on sample A4. It is worth paying attention to the UV-vis spectra of the reaction suspension obtained during experiments with the A8 photocatalyst. It can be seen that after the stage of dark adsorption and at the first stages of oxidation, adsorption in the 400 – 600 nm region increases, which can be explained by the rapid formation of intermediate oxidation products. According to the literature, high performance liquid chromatography revealed the formation of some dyes of the thiazine series, such as azures and thionine, during irradiation of methylene blue solutions in the presence of modified titania [30,31].

It can be concluded that the milling of anatase A0 significantly increases its adsorption properties, which, of course, is associated with an increase in the specific surface area of the samples and a decrease in the size of titanium dioxide crystallites. In addition, the defectiveness of the synthesized samples is also a beneficial for its adsorption and photocatalytic properties. It should be noted that from a practical point of view, fast adsorption with further oxidation of the pollutant, as occurs in the case of samples A4 and A8, is more advantageous than slow adsorption with further faster photocatalytic oxidation, as in the case of commercial Degussa P25, because the main task is to quickly neutralize the release of harmful substances.

#### 4. Conclusions

In conclusion, in this work, a new method for the formation of active photocatalysts based on high-energy ball milling of commercial anatase was proposed. It has been shown that milling leads to a complication of the phase composition of anatase with the formation of new high-pressure phases; the dispersion of particles and the specific surface of the material increase, and defects also appear. It was shown that the materials synthesized in this work have unique properties and phase composition. The samples obtained by grinding showed high activity in the photocatalytic oxidation of the dye, methylene blue, under the UV irradiation. The adsorption properties of the obtained materials significantly exceed those of the commercial TiO<sub>2</sub> Degussa P25, which leads to good prospects for the use of these materials for environmentally friendly water purification from pollution of various classes.

#### References

- [1] Reddy N.R., Reddy P.M., Jyothi N., Kumar A.S., Jung J.H., Joo S.W. Versatile TiO<sub>2</sub> bandgap modification with metal, non-metal, noble metal, carbon material, and semiconductor for the photoelectrochemical water splitting and photocatalytic dye degradation performance. *J. of Alloys and Compounds*, 2023, **935**, 167713.
- [2] Jo W.K., Tayade R.J. Recent developments in photocatalytic dye degradation upon irradiation with energy-efficient light emitting diodes. *Chinese J. of Catalysis*, 2014, **35** (11), P. 1781–1792.
- [3] Ajmal A., Majeed I., Malik R.N., Idriss H., Nadeem M.A. Principles and mechanisms of photocatalytic dye degradation on TiO<sub>2</sub> based photocatalysts: A comparative overview. *RSC Advances*, 2014, **4** (70), P. 37003–37026.

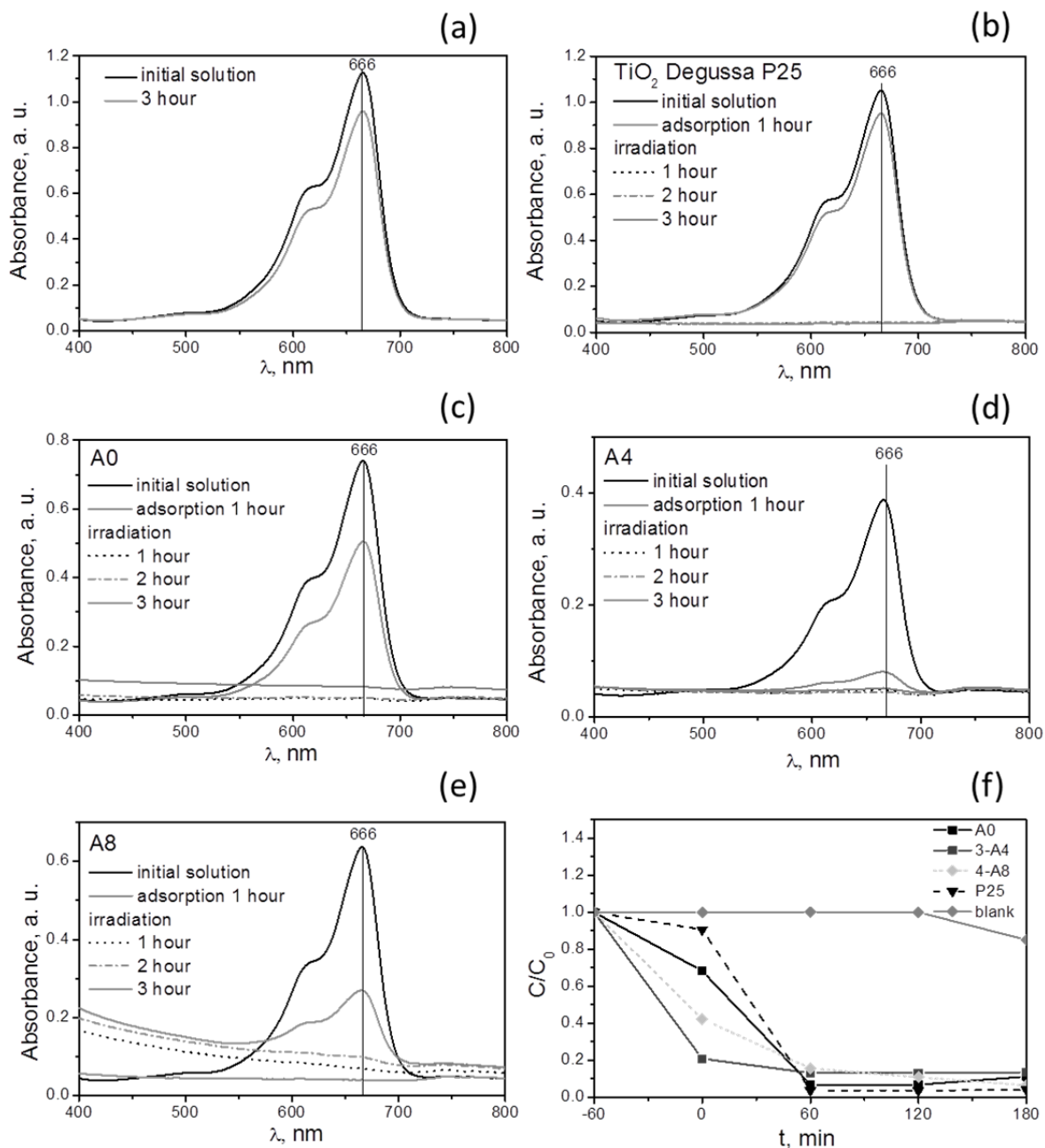


FIG. 6. Absorption spectra of methylene blue before and after the photocatalytic reaction without photocatalyst (a), with photocatalyst: P25 (b), A0 (c), A4 (d), A8 (e), kinetic dependences of photocatalytic oxidation of the samples (f)

- [4] Bensalah N., Alfaro M.A.Q., Martínez-Huitle C.A. Electrochemical treatment of synthetic wastewaters containing Alphazurine A dye. *Chemical Engineering J.*, 2009, **149** (1–3), P. 348–352.
- [5] Turhan K., Turgut Z. Decolorization of direct dye in textile wastewater by ozonization in a semi-batch bubble column reactor. *Desalination*, 2009, **242** (1–3), P. 256–263.
- [6] Gosetti F., Gianotti V., Angioi S., Polati S., Marengo E., Gennaro M.C. Oxidative degradation of food dye E133 Brilliant Blue FCF: Liquid chromatography-electrospray mass spectrometry identification of the degradation pathway. *J. of Chromatogr. A*, 2004, **1054** (1–2), P. 379–387.
- [7] Rauf M.A., Ashraf S.S. Fundamental principles and application of heterogeneous photocatalytic degradation of dyes in solution. *Chemical Engineering J.*, 2009, **151** (1–3), P. 10–18.
- [8] Adhikari S., Sarkar D. Metal oxide semiconductors for dye degradation. *Materials Research Bulletin*, 2015, **72**, P. 220–228.
- [9] Mohibbul M., Bahnemann D., Muneer M. Photocatalytic Degradation of Organic Pollutants: Mechanisms and Kinetics. In: *Organic Pollutants Ten Years After the Stockholm Convention – Environmental and Analytical Update*, Ed. T. Puzyn, A. Mostrag-Szlichtyng, 2012.
- [10] Malato S., Blanco J., Fernández-Alba A.R., Agüera A. Solar photocatalytic mineralization of commercial pesticides: Acrinathrin. *Chemosphere*, 2000, **40** (4), P. 403–409.
- [11] Percherancier J.P., Chapelon R., Pouyet B. Semiconductor-sensitized photodegradation of pesticides in water: the case of carbetamide. *J. of Photochemistry and Photobiology, A: Chemistry*, 1995, **87** (3), P. 261–266.

- [12] Doong R.A., Chang W.H. Photoassisted titanium dioxide mediated degradation of organophosphorus pesticides by hydrogen peroxide. *J. of Photochemistry and Photobiology A: Chemistry*, 1997, **107** (1–3), P. 239–244.
- [13] Kerzhentsev M., Guillard C., Herrmann J.M., Pichat P. Photocatalytic pollutant removal in water at room temperature: Case study of the total degradation of the insecticide fenitrothion (phosphorothioic acid O,O-dimethyl-O-(3-methyl-4-nitro-phenyl) ester). *Catalysis Today*, 1996, **27** (1–2), P. 215–220.
- [14] Akpan U.G., Hameed B.H. Parameters affecting the photocatalytic degradation of dyes using TiO<sub>2</sub>-based photocatalysts: A review. *J. of Hazardous Materials*, 2009, **170** (2–3), P. 520–529.
- [15] Bachina A.K., Popkov V.I., Seroglazova A.S., Enikeeva M.O., Kurenkova A.Yu., Kozlova E.A., Gerasimov E.Yu., Valeeva A.A., Rempel A.A. Synthesis, Characterization and Photocatalytic Activity of Spherulite-like r-TiO<sub>2</sub> in Hydrogen Evolution Reaction and Methyl Violet Photodegradation. *Catalysts*, 2022, **12** (12), 1546.
- [16] Rempel A.A., Valeeva A.A. Nanostructural titanium dioxide for medical chemistry. *Russ. Chem. Bull.*, 2019, **68**, P. 2163–2171.
- [17] Postnova I., Kozlova E., Cherepanova S., Tsybulya S., Rempel A., Shchipunov Y. Titania synthesized through regulated mineralization of cellulose and its photocatalytic activity. *RSC Advances*, 2015, **5** (12), P. 8544–8551.
- [18] Bickley R.I., Gonzalez-Carreno T., Lees J.S., Palmisano L., Tilley R.J.D. A structural investigation of titanium dioxide photocatalysts. *J. of Solid State Chemistry*, 1991, **92** (1), P. 178–190.
- [19] Rempel A.A., Valeeva A.A., Vokhmintsev A.S., Weinstein I.A. Titanium dioxide nanotubes: synthesis, structure, properties and applications. *Russ. Chem. Rev.*, 2021, **90** (11), P. 1397–1414.
- [20] Hurum D.C., Agrios A.G., Gray K.A., Rajh T., Thurnauer M.C. Explaining the enhanced photocatalytic activity of Degussa P25 mixed-phase TiO<sub>2</sub> using EPR. *J. of Physical Chemistry B*, 2003, **107** (19), P. 4545–4549.
- [21] Saraev A.A., Kurenkova A.Y., Gerasimov E.Y., Kozlova E.A. Broadening the Action Spectrum of TiO<sub>2</sub>-Based Photocatalysts to Visible Region by Substituting Platinum with Copper. *Nanomaterials*, 2022, **12** (9), 1584.
- [22] Kurenkova A.Y., Kremneva A.M., Saraev A.A., Murzin V., Kozlova E.A., Kaichev V.V. Influence of Thermal Activation of Titania on Photoreactivity of Pt/TiO<sub>2</sub> in Hydrogen Production. *Catalysis Letters*, 2021, **151** (3), P. 748–754.
- [23] Ordinatsev D.P., Pechishcheva N.V., Valeeva A.A., Zaitseva P.V., Korobitsyna A.D., Belozerova A.A., Sushnikova A.A., Petrova S.A., Shunyaev K.Yu., Rempel A.A. Nanosized Titania for Removing Cr(VI) and As(III) from Aqueous Solutions. *Russian J. of Physical Chemistry A*, 2022, **96** (11), P. 2408–2416.
- [24] Reddy K.M., Manorama S.V., Reddy A.R. Bandgap studies on anatase titanium dioxide nanoparticles. *Materials Chemistry and Physics*, 2003, **78** (1), P. 239–245.
- [25] Luan Z., Maes E.M., Van Der Heide P.A.W., Zhao D., Czernuszewicz R.S., Kevan L. Incorporation of titanium, into mesoporous silica molecular sieve SBA-15. *Chemistry of Materials*, 1999, **11** (12), P. 3680–3686.
- [26] Hasegawa Y., Ayame A. Investigation of oxidation states of titanium in titanium silicalite-1 by X-ray photoelectron spectroscopy. *Catalysis Today*, 2001, **71** (1–2), P. 177–187.
- [27] Agnoli S., Barolo A., Finetti P., Sedona F., Sambì M., Granozzi G. Core and valence band photoemission study of highly strained ultrathin NiO films on Pd(100). *J. of Physical Chemistry C*, 2007, **111** (9), P. 3736–3743.
- [28] Kaichev V.V., Popova G.Ya., Chesalov Yu.A., Saraev A.A., Zemlyanov D.Y., Beloshapkin S.A., Knop-Gericke A., Schlögl R., Andrushkevich T.V., Bukhtiyarov V.I. Selective oxidation of methanol to form dimethoxymethane and methyl formate over a monolayer V<sub>2</sub>O<sub>5</sub>/TiO<sub>2</sub> catalyst. *J. of Catalysis*, 2014, **311**, P. 59–70.
- [29] Kaichev V.V., Chesalov Yu.A., Saraev A.A., Klyushin A.Yu., Knop-Gericke A., Andrushkevich T.V., Bukhtiyarov V.I. Redox mechanism for selective oxidation of ethanol over monolayer V<sub>2</sub>O<sub>5</sub>/TiO<sub>2</sub> catalysts. *J. of Catalysis*, 2016, **338**, P. 82–93.
- [30] Rauf, M.A., Meetani, M.A., Khaleel A., Ahmed, A. Photocatalytic degradation of methylene blue using a mixed catalyst and product analysis by LC/MS. *Chemical Engineering J.*, 2010, **157**, P. 373–378.
- [31] Markovskaya, D.V., Zhurenok, A.V., Kurenkova, A.Y., Kremneva, A.M., Saraev, A.A., Zharkov, S.M., Kozlova, E.A., Kaichev, V.V. New Titania-Based Photocatalysts for Hydrogen Production from Aqueous-Alcoholic Solutions of Methylene Blue. *RSC Advances*, 2020, **10**, P. 34137–34148.

---

Submitted 1 November 2022; revised 24 November 2022; accepted 26 November 2022

#### Information about the authors:

**Ekaterina A. Kozlova** – Institute of Metallurgy, Ural Branch of the Russian Academy of Sciences, 620016 Amundsena St., 101, Ekaterinburg, Russia; Borekov Institute of Catalysis, Siberian Branch of the Russian Academy of Sciences, 630090, pr. Ak. Lavrentieva, 5, Novosibirs, Russia; ORCID 0000-0001-8944-7666; kozlova@catalysis.ru

**Albina A. Valeeva** – Institute of Solid State Chemistry, Ural Branch of the Russian Academy of Sciences, 620108, Pervomayskaya 91, Ekaterinburg, Russia; ORCID 0000-0003-1656-732X; anibla.v@mail.ru

**Anna A. Sushnikova** – Institute of Metallurgy, Ural Branch of the Russian Academy of Sciences, 620016 Amundsena St., 101, Ekaterinburg, Russia; ORCID 0000-0002-7604-5673; sushnikova.ann@gmail.com

**Angelina V. Zhurenok** – Borekov Institute of Catalysis, Siberian Branch of the Russian Academy of Sciences, 630090, pr. Ak. Lavrentieva, 5, Novosibirs, Russia; ORCID 0000-0003-3908-1963; angelinazhurenok@gmail.com

**Andrey A. Rempel** – Institute of Metallurgy, Ural Branch of the Russian Academy of Sciences, 620016 Amundsena St., 101, Ekaterinburg, Russia; ORCID 0000-0002-0543-9982; rempel.imet@mail.ru

**Conflict of interest:** the authors declare no conflict of interest.

## The characteristics of TiO<sub>2</sub> anatase from tulungagung sand as an antibacterial material

L. Rohmawati<sup>1</sup>, Istiqomah<sup>2</sup>, A. A. Pratama<sup>1</sup>, W. Setyarsih<sup>1</sup>, N. P. Putri<sup>1</sup>, Munasir<sup>1</sup>, Darminto<sup>3</sup>

<sup>1</sup>Physics Department, Faculty of Mathematics and Natural Science, Universitas Negeri Surabaya, Ketintang, Gayungan, Surabaya 60231, Indonesia

<sup>2</sup>Physics Department, Faculty of Mathematics and Natural Science, Universitas Negeri Malang, Semarang 5, Malang 65145, Indonesia

<sup>3</sup>Physics Department, Faculty of Science and Data Analytics, Institut Teknologi Sepuluh Nopember (ITS), Keputih, Sukolilo, Surabaya 60111, Indonesia

Corresponding author: L. Rohmawati, [lydiarohmawati@unesa.ac.id](mailto:lydiarohmawati@unesa.ac.id)

**ABSTRACT** TiO<sub>2</sub> anatase is a material that has good photocatalytic properties. The synthesis of TiO<sub>2</sub> anatase from Tulungagung natural sand used the leaching method. The synthesized samples were characterized by TGA, XRD, FTIR, BET, SEM, UV-DRS and tested for antibacterial effect. In this study, the TiO<sub>2</sub> anatase phase was already formed and experiencing three stages of weight loss. It had stretching vibration of the OH group, had a bending mode of water Ti–OH, and Ti–O–Ti at wavenumbers 4000 to 400 cm<sup>-1</sup>. It also had a mesoporous size, was spherical with a grain size of 58 nm and had an energy gap of 3.42 eV. TiO<sub>2</sub> anatase with a 600 μg/mL concentration could reduce *Escherichia coli*, *Staphylococcus aureus*, and *Pseudomonas aeruginosa* bacteria. Therefore, TiO<sub>2</sub> anatase has the potential in an antibacterial agent.

**KEYWORDS** TiO<sub>2</sub> anatase, natural sand, antibacterial

**FOR CITATION** Rohmawati L., Istiqomah, Pratama A.A., Setyarsih W., Putri N.P., Munasir, Darminto The characteristics of TiO<sub>2</sub> anatase from tulungagung sand as an antibacterial material. *Nanosystems: Phys. Chem. Math.*, 2022, **13** (6), 640–648.

### 1. Introduction

The rapid development of nanotechnology has increased the number of nanoparticle-based materials. Due to their unique physical properties, nanomaterials have changed their functions in commercial product applications, including food packaging, drug delivery, biosensors and antibacterial agents [1]. One of them is titanium dioxide (TiO<sub>2</sub>) nanomaterial, widely studied in the last two decades [2]. TiO<sub>2</sub> nanoparticles are considered as an option in biological and environmental remediation applications compared to other semiconductor materials. TiO<sub>2</sub> is available in nature, low cost, and non-toxic, has high surface area and has unique physiochemical properties. In addition, this material has also photocatalytic activity, biocompatibility and reasonable thermal stability [3]. TiO<sub>2</sub> anatase has a tetragonal structure and is formed at lower temperatures [4]. Anatase has the best photocatalytic properties among the three phases than rutile and brookite [5]. Research of TiO<sub>2</sub> in antibacterial agents has been ongoing for the past 20 years. Antibacterial refers to substances that do away or obstruct the growth of microorganisms [6]. Although gram-positive bacteria can form spores and are difficult to inactivate, TiO<sub>2</sub> with photocatalytic properties can kill gram-positive and gram-negative bacteria [7]. The antibacterial effect of TiO<sub>2</sub> plays an essential role in the medical world because it can kill pathogenic bacteria, such as *Escherichia coli*, *Staphylococcus aureus* and *Pseudomonas aeruginosa* [8]. The antibacterial properties of TiO<sub>2</sub> depend on the size of particles and concentration of particles, thus affecting the length of retention time of bacteria [9, 10]. Indonesia, especially the Tulungagung region in East Java, has a natural wealth of mineral sand, where the main content in mineral sand is Fe and Ti elements, which are bound to other elements. The elements of Fe and Ti bind to each other to form ilmenite (FeTiO<sub>3</sub>), hematite (Fe<sub>2</sub>O<sub>3</sub>) and magnetite (Fe<sub>3</sub>O<sub>4</sub>) compounds [11]. One is the ilmenite compound of the three compounds extracted into titanium dioxide (TiO<sub>2</sub>) [12]. The anatase compound (TiO<sub>2</sub>) obtained from the extraction of ilmenite (FeTiO<sub>3</sub>) is a content of coastal sand that can be used as an antibacterial agent [13].

Several researchers have extracted TiO<sub>2</sub> from the Ilmenite sands of the Indonesian island of Bangka with specific methods. Lalasari et al. [14] synthesized TiO<sub>2</sub> using the hydrothermal method using NaOH, but as for the results of their research, there were two phases, namely rutile TiO<sub>2</sub> and ilmenite (FeTiO<sub>3</sub>). Aristanti et al. [15] reported that TiO<sub>2</sub> could be synthesized using a caustic fusion process using NaOH and a leaching process with H<sub>2</sub>SO<sub>4</sub>. As a result, he produced anatase and rutile phases of TiO<sub>2</sub> with impurities in the form of α-Fe<sub>2</sub>O<sub>3</sub>. Likewise, in Wahyuningsih et al.'s research [16], anatase TiO<sub>2</sub> can be synthesized using a dissolution roasted ilmenite process with Na<sub>2</sub>S followed by a leaching process with H<sub>2</sub>SO<sub>4</sub>. The roasted ilmenite process requires a high temperature of 900 °C for 6 hours. Supriyatna et al. [17] also carried out the same process, but the leaching process used HCl solvent, and the products obtained were rutile TiO<sub>2</sub> (94.6 %) and ilmenite impurities.

Each sand in Indonesia has different characteristics, such as in the Tulungagung area, where it is known that the TiO<sub>2</sub> and Fe<sub>2</sub>O<sub>3</sub> contents in the Tulungagung mineral sand are 12.2 and 83.35 %, correspondingly [13]. So far, Tulungagung sand has only been used as a building material, and there has been no further use. Thus, to increase the usefulness of Tulungagung sand, innovation is needed to explore the sand's content. As explained above, TiO<sub>2</sub> can be applied as an antibacterial material. Based on the literacy results from previous studies, the antibacterial characteristics of the anatase TiO<sub>2</sub> compound from Tulungagung sand have never been reported. The novelty of this research is the analysis of the antibacterial aspect of TiO<sub>2</sub> anatase from Tulungagung sand. In addition, anatase TiO<sub>2</sub> nanoparticles were synthesized using the leaching method with the chemical solvent 8 M H<sub>2</sub>SO<sub>4</sub> and low temperature in this study. High concentrations of sulfuric acid in the leaching process can produce TiO<sub>2</sub> anatase [16]. In this study, Tulungagung mineral sand was not roasted like some of the studies above but was carried out with a simple method, namely taking ilmenite sand from the Tulungagung sand using a magnetic rod carried out by the leaching process. Therefore, the results expect that TiO<sub>2</sub> anatase from these natural ingredients can be excellent antibacterial material.

## 2. Materials and method

### 2.1. Materials

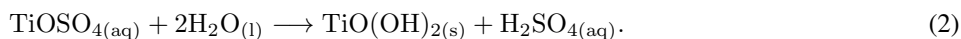
The materials needed in this research include mineral sand in Tulungagung, East Java, Indonesia, H<sub>2</sub>SO<sub>4</sub> (Sigma Aldrich 99 %), and demineralized water. Equipment needed for the synthesis process includes bar magnet, mortar pestle, 200 mesh sieve, vacuum pump, hot plate stirrer, pH meter, glass beaker, and furnace.

### 2.2. Experimental methods and data analysis

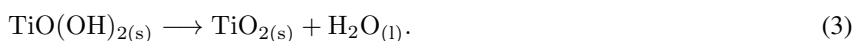
In the first stage, Tulungagung mineral sand was washed first and dried. The next stage was to separate magnetic and non-magnetic sand using a magnetic rod. After that, the magnetic sand is sieved using a 200 mesh strainer to obtain a fine homogeneous powder. Next was the leaching process, where the powder was dissolved with H<sub>2</sub>SO<sub>4</sub> 8 M and heated using a hot plate stirrer at a temperature of 110 °C for 30 minutes until it formed a slurry solution. After that, it was vacuum pumped to separate the TiOSO<sub>4</sub> filtrate and FeSO<sub>4</sub> precipitate, with reaction presented below:



TiOSO<sub>4</sub> filtrate was added with distilled water and heated using a hot plate stirrer at 100 °C until forming sediment, with the following hydrolysis reaction:



Furthermore, the sediment was washed with demineralized water to obtain a pH of 7, then filtered and calcined at 600 °C during 2 hours, with condensation reaction as:



The calcined samples were then characterized by TGA, XRD, FTIR, BET, SEM, UV-DRS, and antibacterial activity test. Thermo Gravimetric Analyzer (TGA) Linseis model STA PT 1000 was used to observe the mass change from the sample thermal decomposition. The phase identification of the sample used data from X-ray Diffraction (XRD) type Phillips X'Pert MPD (multi-purpose diffraction) with monochromatic wavelength CuK $\alpha$ , voltage 40 kV/40 mA and scattering angle of 10 to 90°. The data from the XRD were analyzed qualitatively using the QualX Software. The sample's Ti–O–Ti, Ti–OH, and OH functional groups could be identified by characterization using the Fourier transform infrared (FTIR) brand Shimadzu type IRPrestige 21 with 4000 – 400 cm<sup>-1</sup> of wavenumber. The data obtained from the Brunauer–Emmett–Teller (BET) characterization of Quantachrome TouchWin 1.2 type were analyzed using the Barret–Joyner–Halenda (BJH) method to determine the sample pore size and surface area. Characterization Scanning Electron Microscopy (SEM), the Inspect-S50 type FEO, operated at 20 kV, 60 A, magnifying 150,000 times equipped with EDX (Energy Dispersive X-ray), was used to observe the samples' morphology. The grain diameter distribution in the sample was analyzed using ImageJ software. The Ultra Violet-Visible Diffuse Reflectance Spectroscopic (UV-Vis DRS) characterization of the Analytical Jena type Specord 200 Plus was carried out to observe the UV-visible absorbance spectrum in samples with 190 – 800 nm of wavelength. The data from UV-DRS could also be identified as the sample bandgap using Tauc plot analysis.

### 2.3. Preparation of antibacterial test

Antibacterial testing on samples was carried out using the International Normative ASTM E2149-10 standard on gram-positive (*Staphylococcus aureus*) and gram-negative (*Escherichia coli* and *Pseudomonas aeruginosa*) bacteria. The first stage was to perform cell culture of each bacterium in a stationary phase and measure it using a spectrometer of 600 nm. After that, it was stored in liquid medium and incubated at 37 °C until it reached bacterial concentration 108 CFU/mL. To obtain the concentration of bacteria about 105 CFU/mL, it was carried out three times dilute from 1/10. In the second stage, sample TiO<sub>2</sub> powder was dissolved with water demineralized until it formed suspension. The sample TiO<sub>2</sub> with concentrations of 100, 200, 300, 400, 500, and 600  $\mu\text{g/mL}$  were each given a bacterial solution with a

105 CFU/mL concentration and irradiated using a UVA lamp for 3 hours. Then each 10  $\mu$ L of the test solution was grown in a petri dish at 37 °C for 24 hours, and observations were made.

### 3. Results and discussion

#### 3.1. Thermo gravimetric analysis (TGA)

Thermogravimetric analysis allows one to study the magnitude of the reduction in sample weight due to thermal treatment, with the test starting at room temperature up to 850 °C. Based on the TGA curve (Fig. 1), one concludes that there were three stages of sample weight loss with increasing temperature, and significant weight loss occurred at temperatures less than 580 °C. After 580 °C, the thermogravimetric curve was almost flat, indicating that the sample did not lose weight up to 680 °C. The sample weight loss was easier to observe using a weight derivative of thermogravimetric curve. In the first stage, the sample lost weight at a temperature of 200 to 330 °C by 8.1 % because the absorbed water was dehydrated. At a temperature of 330 to 580 °C in the second stage, the sample experienced a weight loss of 10.53 % due to the decomposition of hydroxyl compounds and changes due to the crystallization process from the amorphous phase to anatase transformation. The product was utterly transformed into the anatase TiO<sub>2</sub> phase at 580 °C. The same observation at this temperature had also been reported by Zablotsky et al. [18] where TiO<sub>2</sub> anatase was fully formed at 560 °C. There was no weight loss at a temperature of 580 to 640 °C, so there was no phase change. The third stage was a phase change from the anatase to rutile phase at 680 to 810 °C followed by 9.5 % sample weight loss because of removal of impurity. At last, at the temperature of 810 until 850 °C, the curve was almost flat.

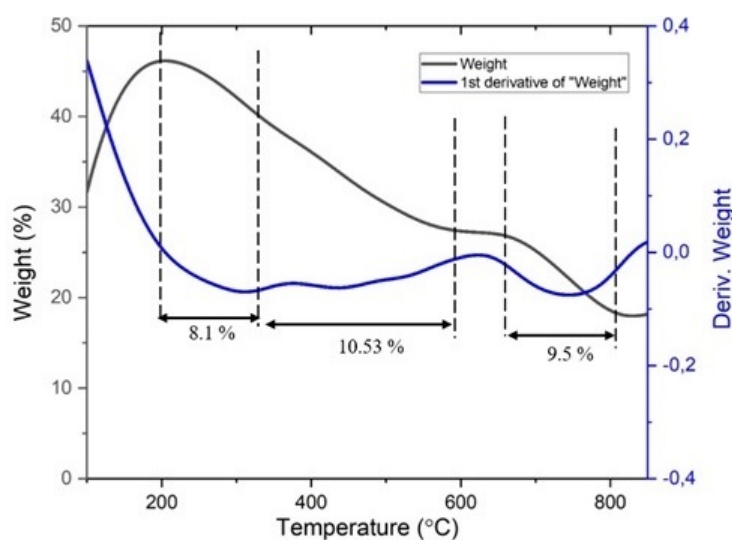


FIG. 1. TGA and the first derivative weight of sample

#### 3.2. X-ray diffraction (XRD)

The diffraction pattern of the synthesized sample is shown in Fig. 2. The data obtained from XRD were analyzed using QualX software to identify the TiO<sub>2</sub> anatase phase. The diffractogram in Fig. 2 shows that the anatase phase TiO<sub>2</sub> has been completely formed in the sample. The anatase phase is formed at a diffraction angle of 25.35°. It is the highest diffraction intensity with crystal orientation (101). Other diffraction peaks which show the anatase phase is 37.03, 37.86, 38.6, 48.11, 53.94, 55.09, 62.13, 62.76, 68.80, 70.32, 75.08, 75.35, and 82.73 ° with miller indices (013), (004), (112), (200), (105), (211), (213), (204), (116), (220), (215), (301), and (224), which are appropriate with Joint Committee on Powder Diffraction Standard (JCPDS) data number 9015929. The results are similar to those reported by several researchers [19–21].

#### 3.3. Fourier transform infrared (FTIR)

The chemical bonding functional group of a sample can be determined by FTIR characterization. This characterization was carried out using infrared spectroscopy in the wavenumber of 4000 – 400 cm<sup>-1</sup>. The results of the FTIR characterization can be seen in Fig. 3. In this study, the synthesized samples had absorption peaks at wave numbers of 3423.76, 1641.48, 1087.89, 669.32, 551.15 cm<sup>-1</sup>. Firm absorption peaks at wave numbers 551.15 and 669.32 cm<sup>-1</sup> indicated Ti–O–Ti bonds in the TiO<sub>2</sub> lattice and were characteristic of TiO<sub>2</sub> anatase [21]. Al-Taweel and Saud [22] also observed this type of bond and Dicastillo et al. [23], namely, the absorption peak occurred at 700 – 400 cm<sup>-1</sup> of wavenumber. The absorption peak at a wavenumber of 1087.89 cm<sup>-1</sup> was a stretching or deviational vibration of the Ti–O–Ti bond in TiO<sub>2</sub> [24]. The peak of 1641.48 cm<sup>-1</sup> showed a bending mode of water Ti–OH which indicated the presence of some

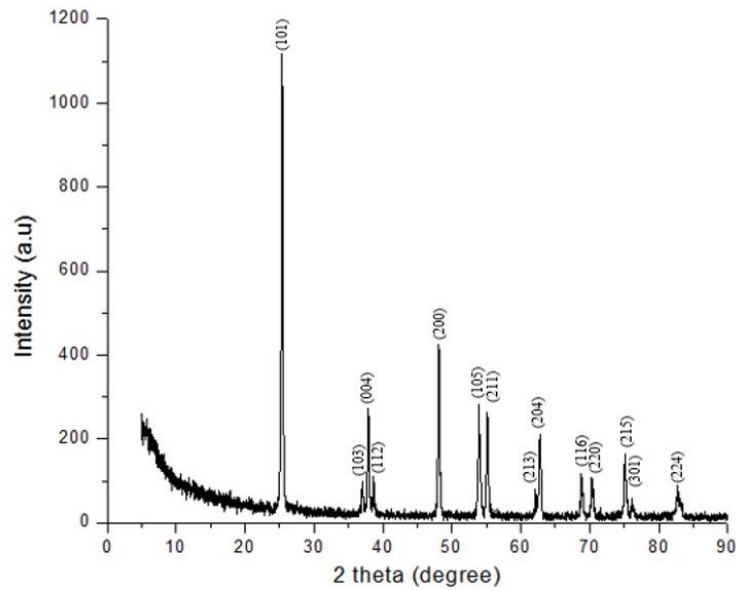


FIG. 2. XRD pattern of sample

H<sub>2</sub>O [23, 25] and was a type of scissors deformation of adsorbed water protonation [26, 27]. The functional groups at  $3423.76\text{ cm}^{-1}$  of wavenumber indicated stretching vibration of the OH group [23] and adsorbed water molecules [28]. The same results were also observed by several researchers, Al-Taweel and Saud [22], who reported that the absorption peak at  $3600 - 3400\text{ cm}^{-1}$  indicated an intermolecular connection in the hydroxyl group for water molecules with TiO<sub>2</sub> surfaces. The functional group hydroxyl group had an essential role in the microbicidal mechanism [29, 30].

### 3.4. Brunauer–Emmett–Teller (BET)

Pore size, pore structure and pore surface area in the sample can be investigated using BET characterization. Fig. 4 shows that the isotherm curve forms a hysteresis loop in the relative pressure range ( $0.9 - 1.0 P/P_0$ ). The TiO<sub>2</sub> isotherm curve formed belongs to the V type with the H<sub>1</sub> type hysteresis loop in the form of a cylindrical pore, which shows the characteristics of mesoporous materials [31]. The adsorption-desorption isotherm curve has an open end, wherein the adsorption process nitrogen gas will be absorbed and enter the pores; thus, the volume of nitrogen gas absorbed will be greater than that released. When used as antibacterial material, it has the potential to inhibit bacteria well. Several researchers have revealed that the mesoporous material in TiO<sub>2</sub> is very efficient as an antimicrobial agent [32, 33].

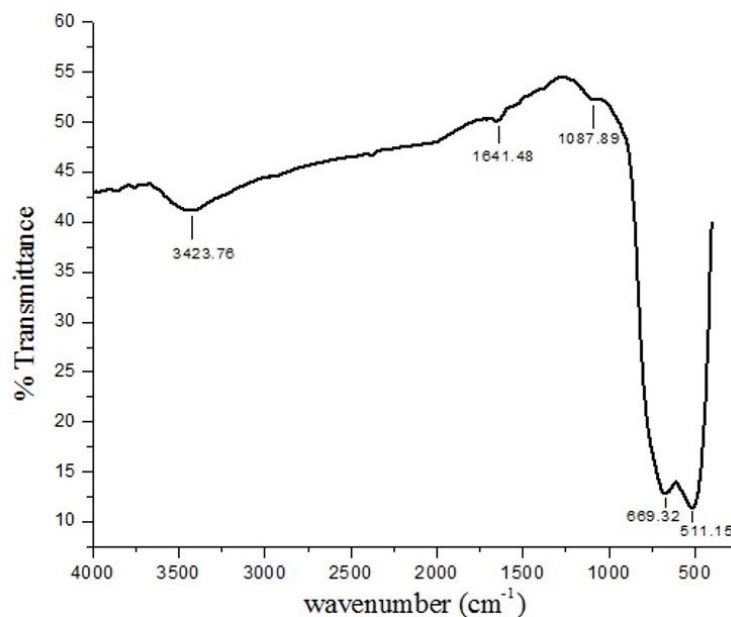


FIG. 3. FTIR spectra of sample

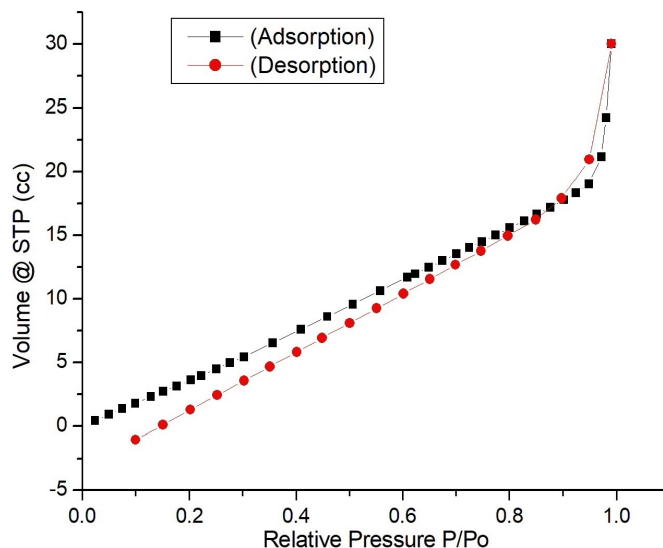


FIG. 4. The isotherms of sample

Based on the analysis of Barret Joyner Hallenda (BJH), it is known that the pore size distribution of the synthesized sample from the desorption curve (Fig. 5) is 3.06 nm (pore radius 15.31 Å). The size belongs to the mesoporous category ( $2 \text{ nm} < d < 50 \text{ nm}$ ). The BET analysis represents that the  $\text{TiO}_2$  sample had  $727,590 \text{ m}^2/\text{g}$  of surface area. This value is greater than the results of several researchers, including  $266 \text{ m}^2/\text{g}$  [33],  $65.65 \text{ m}^2/\text{g}$  [34],  $124 \text{ m}^2/\text{g}$  [35]. The large pore surface area possessed by the synthesized  $\text{TiO}_2$  sample can be the main determining factor in increasing antimicrobial activity because it provides good contact between nanoparticles and microorganisms [36].

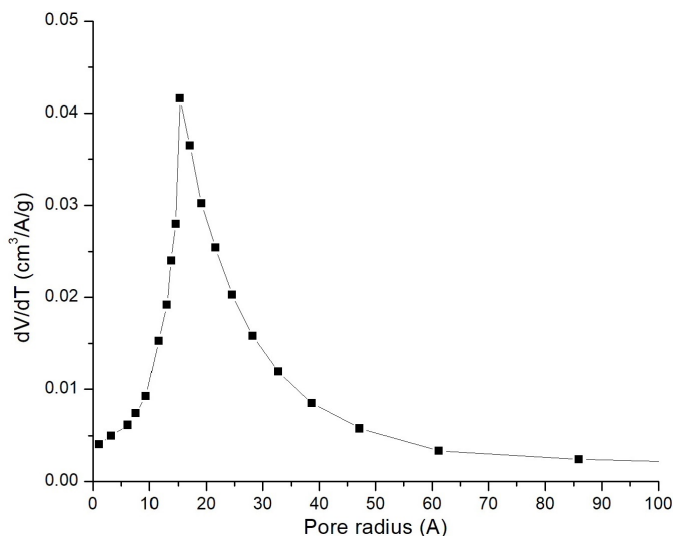


FIG. 5. Desorption curve on the sample

### 3.5. Scanning electron microscopy (SEM)

Figure 6 depicts the surface morphology of the anatase  $\text{TiO}_2$  sample. The figure shows that the sample's morphology is spherical, although there is still agglomeration at some points. Based on the Energy Dispersive X-ray (EDX) results, 100 % anatase  $\text{TiO}_2$  samples were formed from Ti and O elements without any other elements.

Analysis of the grain size distribution of the anatase  $\text{TiO}_2$  sample using ImageJ software, the results of which are shown in Fig. 7. The grain size of the anatase  $\text{TiO}_2$  sample is 58 nm, which results from considering about 100 grains, indicating a size smaller than 100 nm, and includes nanoparticles.

### 3.6. Ultra violet-visible diffuse reflectance spectroscopic analysis (UV-Vis DRS)

The absorbance of the sample at a specific wavelength of light can be determined using UV-DRS analysis. In Fig. 8(a), it appears that the sample has a strong UV absorption with a wavelength of less than 400 nm. However, at a wavelength

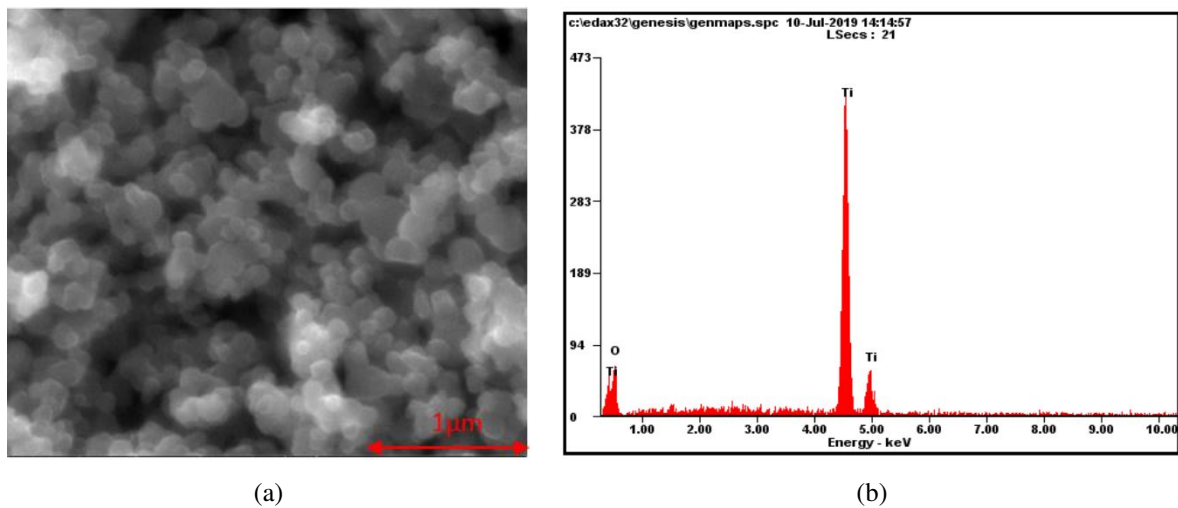


FIG. 6. Characterization results (a) SEM (b) EDX on samples

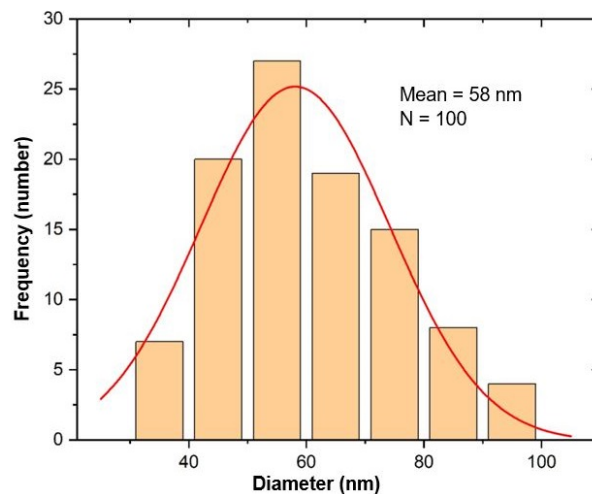


FIG. 7. Distribution of sample grain sizes from SEM image

in visible light, no absorption is observed by the sample in this region. It means that the photon energy at that wavelength does not stimulate electrons to move to a higher energy level [37]. The energy gap of the sample can be determined using the Tauc plot analysis, the results of which can be seen in Fig. 8(b). The sample has an energy gap of 3.42 eV and includes TiO<sub>2</sub> anatase [38, 39].

### 3.7. Antibacterial behaviour

In this study, the bacteria used were *E. coli*, *E. aureus*, and *P. aeruginosa*, with concentrations of TiO<sub>2</sub> 200, 300, 400, 500, and 600 μg/ml. Table 1 displays the antibacterial behaviour of TiO<sub>2</sub> with several cell concentrations and log reduction. Bacteria dissolved in demineralized water without UV radiation were used as a control. When irradiated with UV light, TiO<sub>2</sub> showed antibacterial activity characterized by wane in the number of bacteria as the concentration of TiO<sub>2</sub> increased. It shows that UV radiation can obstruct the growth of bacteria. The 600 μg/mL concentration of TiO<sub>2</sub> has the highest inhibitory ability for both gram-positive and gram-negative bacteria which is characterized by the number of live bacteria around  $3.7 \cdot 10^3$  CFU/mL. At concentrations of 400 to 600 μg/mL, it was found that there was a slight decrease in the number of live bacterial colonies for *E. coli*, *S. aureus*, and *P. aeruginosa* bacteria, as shown in Fig. 9, where it was inhibited the number of bacterial growth although slowly. It is because the dilution factor affects the diffusion process, where a high concentration of TiO<sub>2</sub> allows low solubility, causing limited diffusion rates. It influences the ability of TiO<sub>2</sub> to inhibit the growth of bacteria such as *E. coli*, *S. aureus*, and *P. aeruginosa*. Valgas et al. [40] stated that the deposition of antibacterial compounds could cause a limited diffusion rate. This study was limited to a concentration of 600 μg/mL. It is because the data at that concentration is already sufficient to show the ability of TiO<sub>2</sub> as an antibacterial in both gram-positive and gram-negative bacteria.

The antibacterial behaviour of TiO<sub>2</sub> can be explained by an oxidation reaction when exposed to UV radiation [41]. TiO<sub>2</sub> surface exposed to UV radiation will produce hydroxyl and superoxide, reactive oxygen species (ROS). The surface

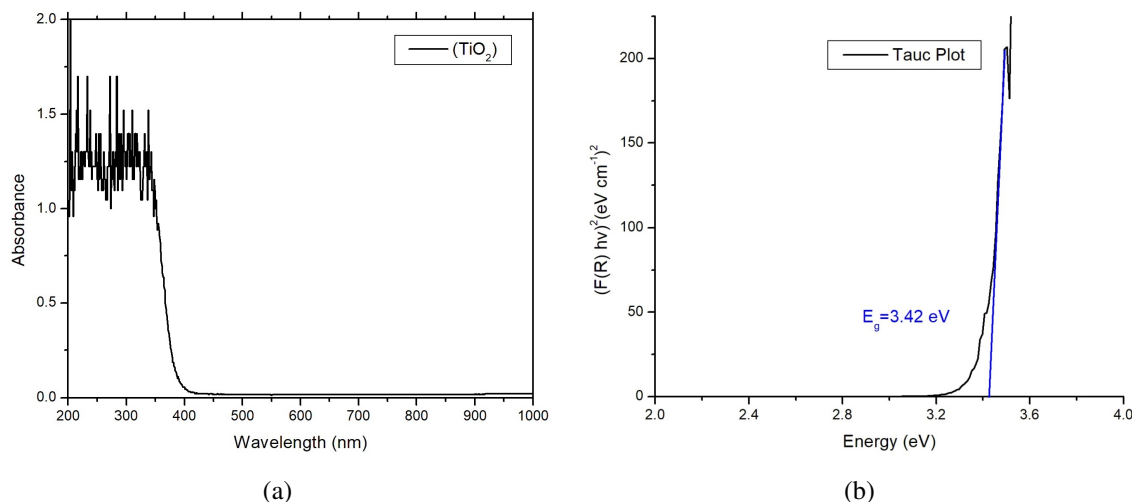
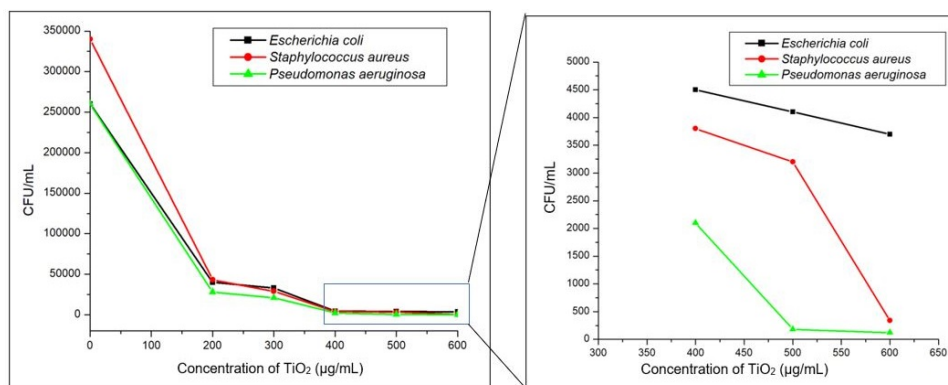


FIG. 8. (a) UV-vis spectra of sample, (b) UV-Tauc plot of sample

TABLE 1. Antibacterial behaviour of  $\text{TiO}_2$  at different concentrations

Bacteria $\text{TiO}_2$ ( $\mu\text{g}/\text{mL}$ )	<i>Escherichia coli</i>		<i>Staphylococcus aureus</i>		<i>Pseudomonas aeruginosa</i>	
	Cell conc. (CFU/mL)	Log Reduction	Cell conc. (CFU/mL)	Log Reduction	Cell conc. (CFU/mL)	Log Reduction
0	$2.6 \cdot 10^5$	$5.41 \pm 0.03$	$3.4 \cdot 10^5$	$5.54 \pm 0.04$	$2.6 \cdot 10^5$	$5.41 \pm 0.11$
200	$4.0 \cdot 10^4$	$4.60 \pm 0.02$	$4.3 \cdot 10^4$	$4.63 \pm 0.09$	$2.8 \cdot 10^4$	$4.44 \pm 0.15$
300	$3.3 \cdot 10^4$	$4.51 \pm 0.05$	$2.9 \cdot 10^4$	$4.46 \pm 0.02$	$2.1 \cdot 10^4$	$4.32 \pm 0.12$
400	$4.5 \cdot 10^3$	$3.65 \pm 0.11$	$3.8 \cdot 10^3$	$3.57 \pm 0.04$	$2.1 \cdot 10^3$	$3.32 \pm 0.08$
500	$4.1 \cdot 10^3$	$3.61 \pm 0.09$	$3.2 \cdot 10^3$	$3.50 \pm 0.03$	$1.8 \cdot 10^2$	$2.25 \pm 0.06$
600	$3.7 \cdot 10^3$	$3.50 \pm 0.07$	$3.4 \cdot 10^2$	$2.53 \pm 0.03$	$1.2 \cdot 10^2$	$2.07 \pm 0.09$

FIG. 9. Antibacterial activity with the concentration of  $\text{TiO}_2$ 

of the bacteria will come into contact with  $\text{TiO}_2$  particles, which are oxidized when exposed to UV radiation. Makowski and Wardas [42] stated that the generation of reactive oxygen compounds could destroy bacteria through damage to bacterial cell walls. Observation of the  $\text{TiO}_2$  antibacterial activity for 24 hours showed that  $\text{TiO}_2$  was effective in obstructing the accretion of *S. aureus*, *P. aeruginosa*, and *E. coli*. The antibacterial activity of *S. aureus* and *P. aeruginosa* as gram-positive bacteria was higher than that of *E. coli* as gram-negative bacteria. It is because the three bacteria have different cell wall structures and thicknesses [41]. Cell wall helpfulness is to protect bacteria from antibacterial compounds that can enter and kill bacteria. The cell wall structure of gram-negative bacteria is more complex and has a layer of peptidoglycan, and a layer of lipopolysaccharide, which acts as a barrier to the entry of antibacterial compounds into bacterial cells. Gram-negative bacteria are more resistant to antibacterial from  $\text{TiO}_2$  when compared to gram-positive bacteria.

In contrast, gram-positive bacteria have no lipopolysaccharide layer, allowing antibacterial compounds to enter the cell and cause lysis. The single-layered gram-positive cell wall structure is relatively simple, making it easier for antibacterial compounds to enter cells and inhibit bacterial growth. In addition to cell wall thickness, the duration of UV radiation also affects the antibacterial activity of TiO<sub>2</sub>. TiO<sub>2</sub> concentration of 600 µg/mL was able to reduce bacteria *E. coli*, *S. aureus* and *P. aeruginosa*, respectively  $3.7 \cdot 10^3$ ;  $3.4 \cdot 10^2$  and  $1.2 \cdot 10^2$  CFU/mL. The longer the UV radiation, the more ROS produced and can obstruct the growth of more bacteria. The size of TiO<sub>2</sub> nanoparticles also inhibited bacterial growth [39].

#### 4. Conclusion

TiO<sub>2</sub> anatase has been successfully synthesized from mineral sands of Tulungagung using the hydrothermal leaching method in this study. The characteristics of TiO<sub>2</sub> anatase can be seen from the results of XRD, TGA, FTIR, BET, SEM, UV-DRS, and antibacterial tests on *E. coli*, *S. aureus*, and *P. aeruginosa* bacteria. The results of the characterization include: TiO<sub>2</sub> anatase phase has been formed, has 3 stages of weight loss, has Ti–O–Ti, Ti–OH, and OH functional groups. It also had a pore size of 3.06 nm with a surface area of 727.590 m<sup>2</sup>/g and mesoporous category. The synthesized TiO<sub>2</sub> had a spherical morphology with a grain size of 58 nm. TiO<sub>2</sub> had strong absorption of UV light with a wavelength of less than 400 nm and had an energy gap of 3.42 eV. TiO<sub>2</sub> with a 600 g/mL concentration had the most optimum reducing ability on *E. coli*, *S. aureus* and *P. aeruginosa* bacteria, respectively  $3.7 \cdot 10^3$ ;  $3.4 \cdot 10^2$  and  $1.2 \cdot 10^2$  CFU/mL for 24 hours.

#### References

- [1] Lu P., Huang S., Chen Y., Chiueh L., Shih D.Y. Analysis of Titanium Dioxide and Zinc Oxide Nanoparticles in Cosmetics. *J. Food Drug Anal.*, 2015, **23** (3), P. 587–594.
- [2] Hayle S.T. Synthesis and Characterization of Titanium Oxide Nanomaterials Using Sol-Gel Method. *J. Nanosci. Nanotechnol.*, 2014, **2** (1), P. 1–7.
- [3] Khashan K.S., Sulaiman G.M., Abdulameer F.A., Albukhaty S., Ibrahim M.A., Al-Muhimeed T., Alobaid A.A. Antibacterial Activity of TiO<sub>2</sub> Nanoparticles Prepared by One-Step Laser Ablation in Liquid. *Appl. Sci.*, 2021, **11** (4623): P. 2–12.
- [4] Al-Dhahir T.A. Quantitative Phase Analysis for Titanium Dioxide from X-ray Powder Diffraction Data Using the Rietveld Method. *Diyala J. for Pure Science*, 2013, **9** (2), P. 108–119.
- [5] Luís A.M., Neves M.C., Mendonça M.H., Monteiro O.C. Influence of Calcination Parameters on The TiO<sub>2</sub> Photocatalytic Properties. *Mater. Chem. Phys.*, 2011, **125** (2), P. 20–25.
- [6] Piskin S., Palantöken A., Yilmaz M.S. Antimicrobial Activity of Synthesized TiO<sub>2</sub> Nanoparticles. *Int. Conf. on Emerging Trends in Engineering and Technology (ICETET'2013)*. Patong Beach, Dec. 7–8, Phuket (Thailand), 2013.
- [7] Kongsong P., Sikong L., Niyomwas S., Rachpech V. Photocatalytic Antibacterial Performance of Glass Fibers Thin Film Coated with N-Doped SnO<sub>2</sub>/TiO<sub>2</sub>. *Sci. World J.*, 2014, 869706.
- [8] Mahdy S.A., Mohammed W.H., Kareem H.A. The Antibacterial Activity of TiO<sub>2</sub> Nanoparticles. *J. Univ. Babylon*, 2017, **25** (3), P. 955–961.
- [9] Sánchez-López E., Gomes D., Esteruelas G., Bonilla L., Lopez-Machado A.L., Cano A., Espina M., Etechecho M., Camins A., Silva A.M. Metal-based nanoparticles as antimicrobial agents: An overview. *Nanomaterials*, 2020, **10** (2), 292.
- [10] Han C., Lalley J., Namboodiri D., Cromer K., Nadagouda M.N. Titanium dioxide-based antibacterial surfaces for water treatment. *Curr. Opin. Chem. Eng.*, 2016, **11**, P. 46–51.
- [11] Setiawati L.D., Rahman T.P., Nugroho D.W., Nofrizal, Ikono R., Suryandaru, Yuswono, Siswanto, Rochman N.T. Ekstraksi Titanium Dioksida (TiO<sub>2</sub>) Dari Pasir Besi Dengan Metode Hidrometalurgi. *Proceeding Seminar Semirata FMIPA*, 2013, **1** (1), P. 465–468.
- [12] Mahdi E.M., Shukor M.H.A., Yusoff M.M.S., Wilfred P. XRD and EDXRF analysis of anatase Nano-TiO<sub>2</sub> synthesized from mineral precursors. *Adv. Mat. Res.*, 2013, **620**, P. 179–185.
- [13] Istiqomah, Putri A.N., Patmawati T., Rohmawati L., Setyarsih, W. Ekstraksi Titanium Dioksida (TiO<sub>2</sub>) Anatase Menggunakan Metode Leaching dari Pasir Mineral Tulungagung. *Akta Kimia Indonesia*, 2019, **4** (2), P. 145–151.
- [14] Lalasari L.H., Firdiyono F., Yuwono A.H., Harjanto S., Suharno. Preparation, Decomposition and Characterizations of Bangka-Indonesia Ilmenite (FeTiO<sub>3</sub>) derived by Hydrothermal Method using Concentrated NaOH Solution. *Adv. Mat. Res.*, 2012, **535–537**, P. 750–756.
- [15] Aristanti Y., Supriyatna Y.I., Masduki N.P., Soepriyanto S. Effect of calcination temperature on the characteristics of TiO<sub>2</sub> synthesized from ilmenite and its applications for photocatalysis. *IOP Conf. Ser.: Mater. Sci. Eng.*, 2019, **478**, P. 1–8.
- [16] Wahyuningsih S., Ramelan A.H., Pramono E., Sulistya A.D., Argawan P.R., Dharmawan F.D. Synthesis of Anatase and Rutile TiO<sub>2</sub> Nanostructures from Natural Ilmenite. *AIP Conf. Proc.*, 2016, 1710.
- [17] Supriyatna Y.I., Astuti W., Sumardi S., Sudibyo, Prasetya A., Ginting L.I.B., Irmawati Y., Asri N.S., Bayu H.T., Petrus M. Correlation of Nano Titanium Dioxide Synthesis and the Mineralogical Characterization of Ilmenite Ore as Raw Material. *Int. J. Technol.*, 2021, **12** (4), P. 749–759.
- [18] Zablotsky D., Maiorov M.A., Krumina A., Romanova M., Blums E. Role of precursor composition in the polymorph transformations, morphology control and ferromagnetic properties of nanosized TiO<sub>2</sub>. *Condensed Matter – Materials Science*, 2021, arXiv:2102.03058.
- [19] Suliman A.A.M., Isha R., Seman M.N.A., Ahmad A.A., Roslan J. Mesoporous Ce-doped Ti: Ash Photocatalyst Investigation in Visible Light Photocatalytic Water Pretreatment Process. *Bull. Chem. React. Eng. Catal.*, 2020, **15** (2), P. 367–378.
- [20] Johari N.D., Rosli Z.M., Juoi J. M., Yazid S.A. Comparison on the TiO<sub>2</sub> crystalline phases deposited via dip and spin coating using green sol-gel route. *J. Mater. Res. Technol.*, 2019, **8** (2), P. 2350–2358.
- [21] Bagheri S., Shameli K., Hamid S.B.A. Synthesis and Characterization of Anatase Titanium Dioxide Nanoparticles Using Egg White Solution via Sol-Gel Method. *J. Chem.*, 2013, **2013**.
- [22] Al-Taweel S.S., Saud H.R. New route for synthesis of pure anatase TiO<sub>2</sub> nanoparticles via ultrasound assisted sol-gel method. *J. Chem. Pharm. Res.*, 2016, **8** (2), P. 620–626.
- [23] Dicastillo, Patiño C., Palma J.L., Alburquenque D., Escrig J. Novel Antimicrobial Titanium Dioxide Nanotubes Obtained Through a Combination of Atomic Layer Deposition and Electrospinning Technologies. *J. Nanomater.*, 2018, **8** (128), P. 1–17.
- [24] Chen N., Deng D., Li Y., Xing X., Xiao X., Wang Y. TiO<sub>2</sub> nanoparticles functionalized by Pd nanoparticles for gas-sensing application with enhanced butane response performances. *Sci. Rep.*, 2017, **7** (7692), P. 1–11.
- [25] Kil H., Jung Y., Moon J., Song J., Lim D., Cho S. Glycothermal Synthesis and Photocatalytic Properties of Highly Crystallized Anatase TiO<sub>2</sub> Nanoparticles. *J. Nanosci. Nanotechnol.*, 2015, **15** (8), P. 6193–6200.

- [26] Mosquera-Pretelt J., Mejia M.I., Marin J.M. Synthesis and Characterization of Photoactive S-TiO<sub>2</sub> from TiOSO<sub>4</sub> Precursor Using an Integrated Sol-Gel and Solvothermal Method at Low Temperatures. *J. Adv. Oxid. Technol.*, 2018, **21** (1).
- [27] Mendoza-Anaya D., Salas P., Chavez C.A., Pérez-Hernández R. Microstructural characterization and morphology of TiO<sub>2</sub> for thermoluminescent applications. *Rev. Mex. Fis.*, 2003, **1** (50), P. 12–16.
- [28] Dadoo-Arhin D., Buabeng F.P., Mwabora J.M., Amaniampong P.N., Agbe H., Nyankson E., Obada D.O., Asiedu N.Y. The effect of titanium dioxide synthesis technique and its photocatalytic degradation of organic dye pollutants. *Heliyon*, 2018, **4** (7).
- [29] Dong F., Zhao W., Wu Z., Guo S. Band structure and visible light photocatalytic activity of multi-type nitrogen doped TiO<sub>2</sub> nanoparticles prepared by thermal decomposition. *J. Hazard. Mater.*, 2009, **162** (2–3), P. 763–770.
- [30] Huang M., Xu C., Wu Z., Huang Y., Lin J., Wu J. Photocatalytic discolorization of methyl orange solution by Pt modified TiO<sub>2</sub> loaded on natural zeolite. *Dyes Pigm.*, 2008, **77** (2008), P. 327–334.
- [31] Sing K.S.W., Everett D.H., Haul R.A.W., Moscou L., Pierotti R.A., Rouquerol J., Siemieniwska T. Reporting Physisorption Data for Gas/Solid Systems with Special Reference to the Determination of Surface Area and Porosity. *Pure & Appl. Chem.*, 1985, **57** (4), P. 603–619.
- [32] Liu Y., Wang X., Yang F., Yang X. Excellent antimicrobial properties of mesoporous anatase TiO<sub>2</sub> and Ag/TiO<sub>2</sub> composite films. *Microporous Mesoporous Mater.*, 2008, **114** (1–3), P. 431–439.
- [33] Naik K., Chatterjee A., Prakash H., Kowshik M. Mesoporous TiO<sub>2</sub> Nanoparticles Containing Ag Ion with Excellent Antimicrobial Activity at Remarkable Low Silver Concentrations. *J. Biomed. Nanotechnol.*, 2013, **9** (4), P. 664–673.
- [34] Budi C.S., Kartini I., Rusdiarso B. Synthesis of mesoporous titania by potato starch templated sol-gel reactions and its characterization. *Indo. J. Chem.*, 2010, **10** (1), P. 26–31.
- [35] Lan K., Wang R., Zhang W., Zhao Z., Elzatahry A., Zhang X., Liu Y., Al-Dhayan D., Xia Y., Zhao D. Mesoporous TiO<sub>2</sub> microspheres with precisely controlled crystallites and architectures. *Chem.*, 2018, **4** (10), P. 2436–2450.
- [36] Pal A., Pehkonen S.O., Yu L.E., Ray M.B. Photocatalytic inactivation of Gram-positive and Gram-negative bacteria using fluorescent light. *J. Photochem. Photobiol. A*, 2007, **186** (2–3), P. 335–341.
- [37] Liu Y., Zhu X., Yuan D., Wang W., Gao L. Preparation and characterization of TiO<sub>2</sub> based on wood templates. *Scientific Report*, 2020, **10**, 12444.
- [38] Fu G., Vary P.S., Lin C.T. Anatase TiO<sub>2</sub> Nanocomposites for antimicrobial coatings. *J. Phys. Chem. B*, 2005, **109** (18), P. 8889–8898.
- [39] Alhadrami H.A., Baqasi A., Iqbal J., Shoudri R.A.M., Ashshi A.M., Azhar E.I., Al-Hazmi F., Al-Ghamdi A., Wageh S. Antibacterial Applications of Anatase TiO<sub>2</sub> Nanoparticle. *Am. J. Nanomater. (Print)*, 2017, **5** (1), P. 31–42.
- [40] Valgas C., Machado de Souza S., Smânia E.F.A., Smânia Jr. A. Screening methods to determine antibacterial activity of natural products. *Braz. J. Microbiol.*, 2007, **38**, P. 369–380.
- [41] Xing Y., Li X., Xu Q., Che Z., Li W., Bai Y., Li K. Effect of TiO<sub>2</sub> nanoparticles on the antibacterial and physical properties of polyethylene-based film. *Prog. Org. Coat.*, 2012, **73** (2–3), P. 219–224.
- [42] Makowski A., Wardas W. Photocatalytic degradation of toxins secreted to water by cyanobacteria and unicellular algae and photocatalytic degradation of the cells of elected microorganisms. *Current Topics in Biophysics*, 2001, **25** (1), P. 19–25.

---

Submitted 15 November 2021; revised 14 June 2022; accepted 16 October 2022

*Information about the authors:*

*L. Rohmawati* – Physics Department, Faculty of Mathematics and Natural Science, Universitas Negeri Surabaya, Ketintang, Gayungan, Surabaya 60231, Indonesia; lydiarohmawati@unesa.ac.id

*Istiqomah* – Physics Department, Faculty of Mathematics and Natural Science, Universitas Negeri Malang, Semarang 5, Malang 65145, Indonesia; istiqomahistiqomah1999@gmail.com

*A. A. Pratama* – Physics Department, Faculty of Mathematics and Natural Science, Universitas Negeri Surabaya, Ketintang, Gayungan, Surabaya 60231, Indonesia; angela.17030224011@mhs.unesa.ac.id

*W. Setyarsih* – Physics Department, Faculty of Mathematics and Natural Science, Universitas Negeri Surabaya, Ketintang, Gayungan, Surabaya 60231, Indonesia; worosetyarsih@unesa.ac.id

*N. P. Putri* – Physics Department, Faculty of Mathematics and Natural Science, Universitas Negeri Surabaya, Ketintang, Gayungan, Surabaya 60231, Indonesia; nugrahaniprimary@unesa.ac.id

*Munasir* – Physics Department, Faculty of Mathematics and Natural Science, Universitas Negeri Surabaya, Ketintang, Gayungan, Surabaya 60231, Indonesia; munasir\_physics@unesa.ac.id

*Darminto* – Physics Department, Faculty of Science and Data Analytics, Institut Teknologi Sepuluh Nopember (ITS), Keputih, Sukolilo, Surabaya 60111, Indonesia; darminto@physics.its.ac.id

*Conflict of interest:* the authors declare no conflict of interest.

## Synthesis of highly active and visible-light-driven PrFeO<sub>3</sub> photocatalyst using solution combustion approach and succinic acid as fuel

Anna S. Seroglazova<sup>1,2,a</sup>, Vadim I. Popkov<sup>2,b</sup>

<sup>1</sup>Saint Petersburg State Institute of Technology, St. Petersburg, Russia

<sup>2</sup>Ioffe Institute, St. Petersburg, Russia

<sup>a</sup>[annaseroglazova@yandex.ru](mailto:annaseroglazova@yandex.ru), <sup>b</sup>[vadim.i.popkov@mail.ioffe.ru](mailto:vadim.i.popkov@mail.ioffe.ru)

Corresponding author: Anna S. Seroglazova, [annaseroglazova@yandex.ru](mailto:annaseroglazova@yandex.ru)

PACS 61.46.+w

**ABSTRACT** In this work, nanocrystalline powder of praseodymium orthoferrite was obtained by the solution combustion synthesis using succinic acid as organic fuel. The obtained sample is characterized by techniques of powder x-ray diffraction, scanning and transmission electron microscopy, and UV-Vis diffuse reflectance spectroscopy. The sample was discovered to have a porous, foamy morphology with an average crystallite size of 36.1 nm and a band gap value of 2.1 eV. The study of Fenton-like photocatalytic activity was carried out on the example of the decomposition of the methyl violet dye in the presence of hydrogen peroxide under visible light. The maximum value of the degradation rate constant is 0.0325 min<sup>-1</sup>. The results were compared to the available data obtained for similar systems.

**KEYWORDS** praseodymium orthoferrite, solution combustion method, succinic acid, nanoparticles, photo-Fenton-like reactions, photocatalysis.

**ACKNOWLEDGEMENTS** This work was carried out in accordance with the Grant of the President of the Russian Federation MK-795.2021.1.3. The Authors acknowledge V. N. Nevedomskiy for the help with TEM investigations.

**FOR CITATION** Seroglazova A.S., Popkov V.I. Synthesis of highly active and visible-light-driven PrFeO<sub>3</sub> photocatalyst using solution combustion approach and succinic acid as fuel. *Nanosystems: Phys. Chem. Math.*, 2022, **13** (6), 649–654.

### 1. Introduction

In recent years, a large number of studies have been directed toward the development and study of new functional materials with a wide range of applications. The most interesting ones among such materials are ferrites with different structures and compositions, in particular ferrites, of rare earth elements (REE).

Rare earth orthoferrites belong to a class of complex oxides with the general chemical formula RFeO<sub>3</sub> (R = rare earth element: Ce, La, Gd, or Pr). The enhanced interest in this class of compounds is due to their unusual distorted perovskite-like structure with a space group of *Pbnm/Pnma* [1–3], which provides them with unique chemical and physical properties: electrical, magnetic, and optical. The combination of the unique properties allows the use of REE orthoferrites in the production of ceramic materials, electronic devices, gas sensors, magnetic materials, MRI contrast agents, and catalytic materials [4–6]. The use of REE orthoferrites as photocatalytic materials in the visible region is identified as the most promising area due to the low value of the band gap (2–3 eV), semiconductor properties, and chemical stability [7, 8].

Among the varieties of orthoferrites of rare earth elements, PrFeO<sub>3</sub> praseodymium orthoferrite is known to have good electromagnetic properties, but it also stands out due to its distinguished photocatalytic properties under visible light [9–11]. However, one of the problems associated with the development of catalytic materials is the production of catalysts with a developed surface and a porous structure. To date, a large number of studies devoted to the preparation of PrFeO<sub>3</sub> nanoparticles using synthesis routes such as sol-gel, co-precipitation, the template method, and the solution combustion method have been published [12–17]. The listed methods of synthesis make it possible to obtain nanostructured materials with tuned particle sizes, morphology, and structure, but most of them are power-consuming and do not always allow one to obtain a structure with a developed porous surface, with the exception of synthesis by solution combustion [18–20]. Distinctive features of the method are its versatility, speed, and the possibility of varying synthesis parameters that allow tuning of the structural, morphological, and functional characteristics of the materials, as well as the possibility of transforming it into large-scale industrial production with the manufacturing of high-purity products. The most important synthesis parameter is the type of organic fuel, which provides the process of self-ignition for the reaction mixture and acts as a chelating agent for metal ions. Glycine and metal nitrates are conventionally chosen as reagents for the combustion

solution synthesis. However, this type of fuel does not allow for the formation of particles with a small average size and a developed porous surface [21–24].

The present study aims to produce pure nanopowders based on  $\text{PrFeO}_3$  by solution combustion synthesis with succinic acid as an organic fuel, followed by a mild heat treatment at  $500^\circ\text{C}$ , and to characterize the synthesized sample by a set of methods of physicochemical analysis. The photo-Fenton-like catalytic activity was then investigated using the model reaction of photodegradation of methyl violet in the presence of  $\text{PrFeO}_3$  as a catalyst and hydrogen peroxide.

## 2. Materials and methods

The starting reagents used for the synthesis of  $\text{PrFeO}_3$  praseodymium orthoferrite were praseodymium nitrate hexahydrate ( $\text{Pr}(\text{NO}_3)_3 \cdot 6\text{H}_2\text{O}$ ), iron nitrate nonahydrate ( $\text{Fe}(\text{NO}_3)_3 \cdot 9\text{H}_2\text{O}$ ), succinic acid ( $\text{C}_4\text{H}_6\text{O}_4$ ), as well as distilled water. All the reagents were chemically pure and used as purchased from Neva-Reactiv (Saint Petersburg, Russia). The reaction solution was prepared by dissolving metal nitrate and succinic acid, taken according to the stoichiometric ratio, in 40 ml of distilled water under constant mixing until all components were completely dissolved. The resulting solution was placed in a glassy carbon dish and heated on an electric stove until complete water removal was achieved, followed by self-ignition of the reaction mixture and the formation of the final solid product, which was ground in a mortar until a homogeneous bright brown powder was formed. The powder was then subjected to heat treatment at  $500^\circ\text{C}$  for 1 hour in an air atmosphere to remove unreacted residues of nitrates and organics.

The elemental composition and morphology of the synthesized  $\text{PrFeO}_3$  particles were studied by scanning electron microscopy using a Tescan Vega 3 SBH microscope equipped with an Oxford INCA 200 electron probe microanalyzer. Analysis of structure and phase composition was performed via powder x-ray diffraction on a Rigaku Smart Lab 3 diffractometer using  $\text{Cu}_{K\alpha 1}$  irradiation ( $\lambda=0.154056$  nm). For a more detailed assessment of the morphology and microstructure, transmission electron microscopy was performed on a JEOL TEM-100CX microscope. Diffuse reflectance spectra were measured with an Avaspec-ULS2048 spectrometer equipped with an AvaSphere-30-Refl integrating sphere.

Methyl violet (MV) was chosen as a model dye for studying photocatalytic activity. The photodegradation process was carried out in an insulated box equipped with a light source with a wavelength of  $\lambda \geq 420$  nm, a magnetic stirrer for constant stirring of the reaction solution, and a 50-ml graduated cylinder.

The experiment included the preparation of a reaction solution containing a dye, a catalyst ( $\text{PrFeO}_3$ ), and hydrogen peroxide ( $\text{H}_2\text{O}_2$ ) with a concentration of 0.0232 g/L, 0.25 g/L, and 0.24 mol/L, respectively. The volume of the solution was 30 mL. Before the start of the experiment, the solution was stirred in the dark for 30 minutes to establish adsorption equilibrium. After that, it was irradiated with a visible light source for 60 minutes with sampling of 5 ml every 10 minutes to determine the MF concentration. Changes in the dye concentration were recorded using an Avaspec-ULS208 spectrometer.

## 3. Results and discussion

Elemental analysis of the combustion products and X-ray diffraction data collected on the initial and heat-treated samples are shown in Fig. 1.

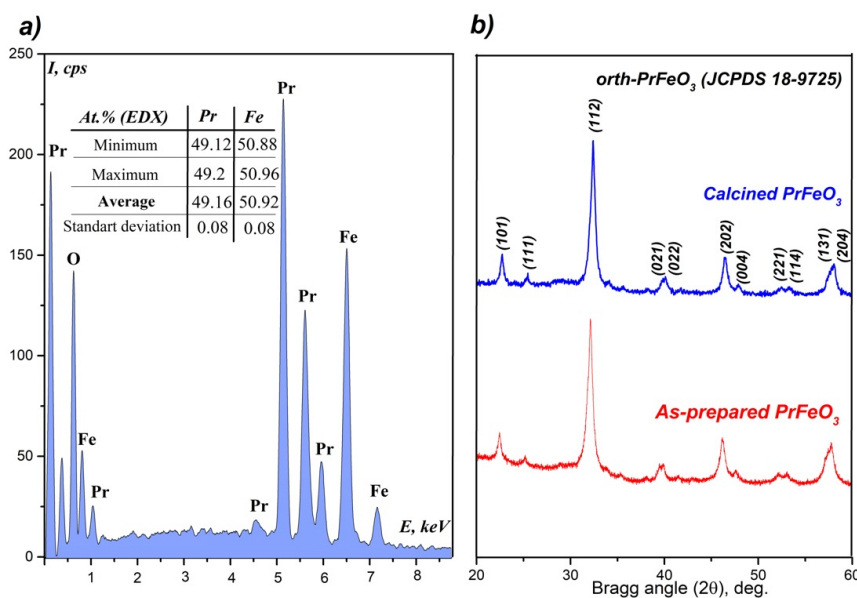


FIG. 1. The energy dispersive X-ray spectroscopy (a) and powder X-ray diffraction patterns (b) of the as-prepared and heat-treated  $\text{PrFeO}_3$  samples

According to the presented results (Fig. 1a), the elemental composition of the synthesis product corresponds to  $\text{PrFeO}_3$ , as evidenced by the presence of three main spectral lines belonging to the key elements: praseodymium (Pr), iron (Fe), and oxygen (O). Within the method's error, the quantitative ratio Pr:Fe in the obtained sample was 49.16 and 50.92 at.%, which is very close to praseodymium orthoferrite in terms of stoichiometry. Detailed results of EDX measurements in terms of Fe and Pr are presented in the table in Fig. 1a.

The X-ray powder diffraction patterns shown in Fig. 1b indicate the formation of only one crystalline phase of praseodymium orthoferrite before and after the heat treatment of the combustion products of the mixture. The crystal structure of the heat-treated product was refined by the Rietveld method. According to the refinement results, the unit cell parameters are in good agreement with the data of JCPDS card No. 18-9725 and are as follows:  $a=5.4858(4)$ ,  $b=5.5756(2)$ ,  $c=7.7898(7)$  Å which corresponds to the space group  $Pbnm$ . The data obtained are also consistent with the results of other studies on the production of  $\text{PrFeO}_3$  by the methods of glycine-nitrate synthesis, microwave, and hydrothermal synthesis [9, 13, 25]. The average crystallite size calculated from the broadening of X-ray diffraction lines for the initial sample was 27.9 nm. After the heat treatment, a slight increase in size up to 36.1 nm is observed, which indicates the process of recrystallization into larger crystals upon moderate heating. It should be noted that  $\text{PrFeO}_3$  synthesized by solution combustion using succinic acid at a stoichiometric ratio has smaller crystallite sizes than  $\text{PrFeO}_3$  synthesized by a similar method, but using glycine as a fuel (57.9 nm) [13].

According to SEM and TEM analysis (Fig. 2b), the morphology of the combustion product after finishing heat treatment is spongy with a developed system of micron and submicron pores, which is typical for many substances, particularly simple and complex oxides obtained by a similar synthesis method [26–28]. The formation of agglomerates consisting of individual  $\text{PrFeO}_3$  particles is also observed, which is associated both with high temperatures in the reaction zone during combustion and with the thermal treatment of the product, which leads to an increase in mass transfer processes. A more detailed study of these processes was previously studied using the examples of the  $\text{YFeO}_3$  [24] and  $\text{NiO}$  [29] systems.

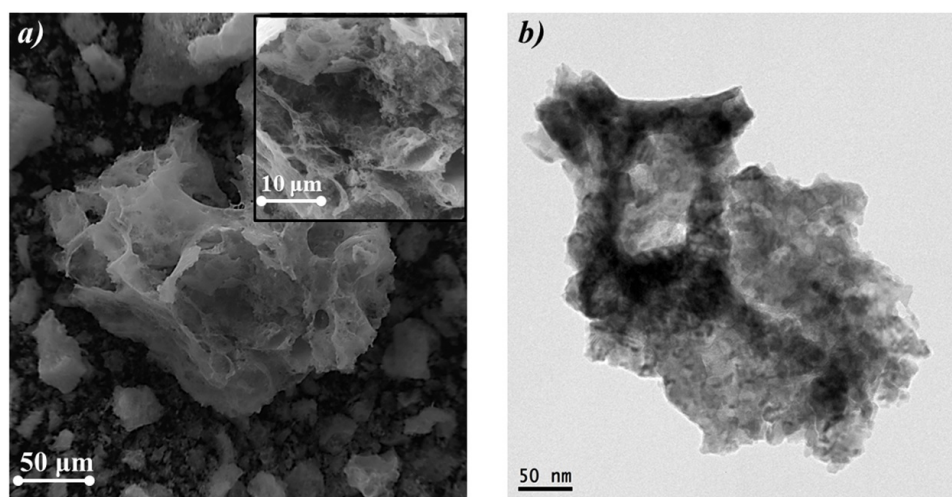


FIG. 2. SEM (a) and TEM (b) images of calcined  $\text{PrFeO}_3$  nanopowder

To describe the optical characteristics of the sample, diffuse reflectance spectroscopy in the UV-Vis region was carried out, the results of which are shown in Fig. 3.

The spectrum shown in Fig. 3a shows a wide absorption band in the wavelength range from 500 nm to 700 nm, corresponding to the visible region of light. The value of the band gap, recalculated in accordance with the Kubelka-Munk transformation and presented in the Tauc coordinates, is shown in Fig. 3b and is 2.1 eV, which is consistent with the literature data [12, 13, 17].

The combination of the research results from powder X-ray diffraction, SEM analysis, and diffuse reflection spectroscopy makes it possible to assume that the synthesized sample can act as a promising photocatalyst in the visible region. It is possible due to its porous structure and small crystallite sizes, which provide greater access for reagents to the catalyst surface area, as well as due to the small value of the band gap, which, when irradiated with visible light, allows for an electron to pass from the valence band to the conduction band with the subsequent formation of a powerful oxidizing hydroxyl radical [13, 30, 31].

The study of the functional properties of  $\text{PrFeO}_3$  in a photocatalytic Fenton-like oxidation process was carried out on the example of the decomposition of the model methyl violet (MV) dye under the action of visible light. The results of the study are shown in Fig. 4.

Fig. 4a shows the typical absorption spectra of methyl violet during photo-Fenton-like degradation. According to the obtained data, in all spectra, there is a single absorption peak corresponding to 550 nm, which naturally decreases

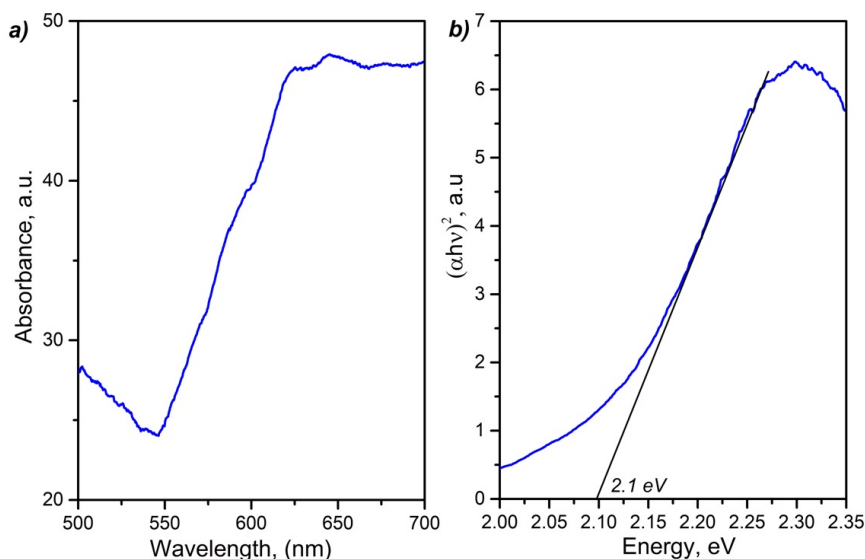


FIG. 3. UV-Vis spectrum of  $\text{PrFeO}_3$  (a) and the corresponding Tauc plot (b)

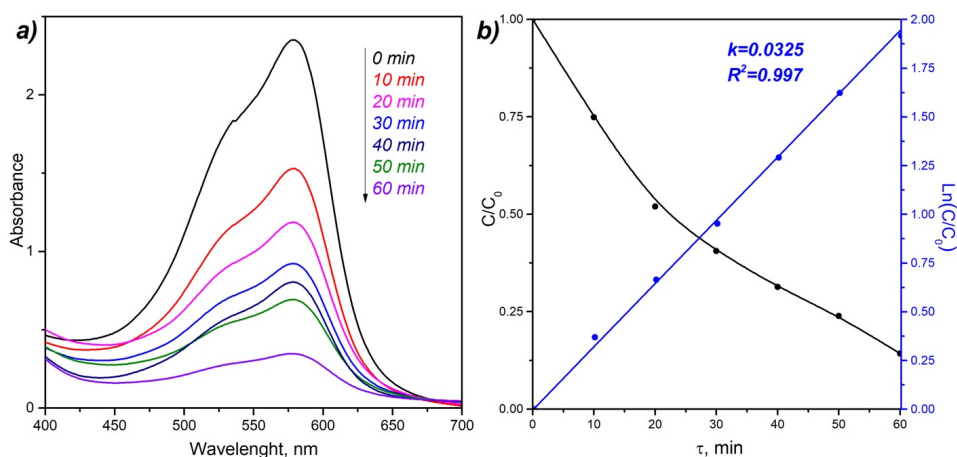


FIG. 4. UV-Vis absorption spectra of methyl violet during photo-Fenton-like degradation (a) and corresponding kinetic curves (b)

with time during prolonged irradiation with a light source, which confirms the photocatalytic activity of the synthesized sample. The most intense decrease in the dye concentration is observed in the first 10 minutes of irradiation, then the intensity of discoloration decreases, which is associated with a gradual decrease in the generation of hydroxyl radicals caused by the processes of recombination of electron-hole pairs [13, 32] and the peculiarity of the filling of catalytically active centers on the catalyst surface.

Based on the experimental data, kinetic studies were also carried out, the results of which are shown in Fig. 4b. As noted earlier, the relative concentration of the dye decreases regularly with the course of irradiation, and in accordance with the shape of the kinetic dependence, it refers to the pseudo-first order of the reaction. The rate constant was calculated by linearizing the kinetic dependence in logarithmic coordinates. The obtained value was  $0.0325 \text{ min}^{-1}$ , which is higher compared to other rare-earth ferrites and orthoferrites (Table 1).

#### 4. Conclusion

Thus, within the framework of this work, the possibility of obtaining pure nanocrystalline praseodymium orthoferrite by combustion in solution using succinic acid as a fuel was shown. According to the results of comparison with the literature data, the obtained particles have a smaller crystallite size (36.1 nm) than in similar synthesis using a standard fuel, glycine (57.9 nm), which makes it possible to vary the particle size, morphology, and specific surface area using different types of fuel. Analysis of photocatalytic activity showed high efficiency in the photo-Fenton-like degradation of methyl violet with a rate constant of  $0.0325 \text{ min}^{-1}$ .

TABLE 1. Comparison of rare earth orthoferrites as visible-light-driven photocatalysts depending on rare earth element, synthesis method and crystallite size

No	Photocatalyst	Synthesis method	Crystallite size, nm	Dye	k, min <sup>-1</sup>	Reference
1	YbFeO <sub>3</sub>	Solution combustion synthesis	54.6	Methyl Violet	0.0040	[33]
2	EuFeO <sub>3</sub>	Sol-gel synthesis	25.2	Rhodamine B	0.0020	[31]
3	NiFe <sub>2</sub> O <sub>4</sub>	Solution combustion synthesis	27.0	Methylene blue	0.0080	[34]
4	PrFeO <sub>3</sub>	Solution combustion synthesis	36.1	Methyl Violet	0.0325	This work

## References

- [1] Lone I.H., Aslam J., Radwan N.R.E., Bashal A.H., Ajlouni A.F.A., Akhter A. Multiferroic ABO<sub>3</sub> Transition Metal Oxides: a Rare Interaction of Ferroelectricity and Magnetism. *Nanoscale Research Letters*, 2019, **14**, P. 1–12.
- [2] Popkov V.I., Tugova E.A., Bachina A.K., Almyasheva O.V. The formation of nanocrystalline orthoferrites of rare-earth elements XFeO<sub>3</sub> (X = Y, La, Gd) via heat treatment of coprecipitated hydroxides. *Russian Journal of General Chemistry*, 2017, **87**, P. 2516–2524.
- [3] Akbashev A.R., Semisalova A.S., Perov N.S., Kaul A.R. Weak ferromagnetism in hexagonal orthoferrites RFeO<sub>3</sub> (R = Lu, Er-Tb). *Applied Physics Letters*, 2011, **99**, P. 2011–2014.
- [4] Xu H, Hu X, Zhang L. Generalized low-temperature synthesis of nanocrystalline rare-earth orthoferrites LnFeO<sub>3</sub> (Ln = La, Pr, Nd, Sm, Eu, Gd). *Crystal Growth and Design*, 2008, **8**, P. 2061.
- [5] Li M., Tan H., Duan W. Hexagonal rare-earth manganites and ferrites: A review of improper ferroelectricity, magnetoelectric coupling, and unusual domain walls. *Physical Chemistry Chemical Physics. Royal Society of Chemistry*, 2020, **22**, P. 14415–14432.
- [6] Mir F.A., Sharma S.K., Kumar R. Magnetizations and magneto-transport properties of Ni-doped PrFeO<sub>3</sub> thin films. *Chinese Physics B*, 2014, **23**.
- [7] Kondrashkova I.S., Martinson K.D., Zakharova N.V., Popkov V.I. Synthesis of Nanocrystalline HoFeO<sub>3</sub> Photocatalyst via Heat Treatment of Products of Glycine-Nitrate Combustion. *Russian Journal of General Chemistry*, 2018, **88**, P. 2465–2471.
- [8] Maity R., Sheikh M.S., Dutta A., Sinha T.P. Visible Light Driven Photocatalytic Activity of Granular Pr Doped LaFeO<sub>3</sub>. *Journal of Electronic Materials*, 2019, **48**, P. 4856–4865.
- [9] Qin C., Li Z., Chen G., Zhao Y., Lin T. Fabrication and visible-light photocatalytic behavior of perovskite praseodymium ferrite porous nanotubes. *Journal of Power Sources*, 2015, **285**, P. 178–184.
- [10] Arakawa T., Tsuchi-Ya S.I., Shiohara J. Catalytic properties and activity of rare-earth orthoferrites in oxidation of methanol. *Journal of Catalysis*, 1982, **74**, P. 317–322.
- [11] Megarajan S.K., Rayalu S., Nishibori M., Labhsetwar N. Improved catalytic activity of PrMO<sub>3</sub> (M = Co and Fe) perovskites: Synthesis of thermally stable nanoparticles by a novel hydrothermal method. *New Journal of Chemistry*, 2015, **39**, P. 2342–2348.
- [12] Wang X., Cao S., Wang Y., Yuan S., Kang B., Wu A., et al. Crystal growth and characterization of the rare earth orthoferrite PrFeO<sub>3</sub>. *Journal of Crystal Growth*, 2013, **362**, P. 216–219.
- [13] Seroglazova A.S., Lebedev L.A., Chebanenko M.I., Sklyarova A.S., Buryanenko I.V., Semenov V.G., et al. Ox/Red-controllable combustion synthesis of foam-like PrFeO<sub>3</sub> nanopowders for effective photo-Fenton degradation of methyl violet. *Advanced Powder Technology*, 2022, **33**, P. 103398.
- [14] Nguyen A.T., Nguyen V.Y., Mittova I.Y., Mittova V.O., Viryutina E.L., Hoang C.C.T., et al. Synthesis and magnetic properties of PrFeO<sub>3</sub> nanopowders by the co-precipitation method using ethanol. *Nanosystems: Physics, Chemistry, Mathematics*, 2020, **11**, P. 468–473.
- [15] Abdellahi M., Abhari A.S., Bahmanpour M. Preparation and characterization of orthoferrite PrFeO<sub>3</sub> nanoceramic. *Ceramics International*, 2016, **42**, P. 4637–4641.
- [16] Freeman E., Kumar S., Thomas S.R., Pickering H., Fermin D.J., Eslava S. PrFeO<sub>3</sub> Photocathodes Prepared Through Spray Pyrolysis. *ChemElectroChem*, 2020, **7**, P. 1365–1372.
- [17] Tang P., Xie X., Chen H., Lv C., Ding Y. Synthesis of Nanoparticulate PrFeO<sub>3</sub> by Sol–Gel Method and its Visible-Light Photocatalytic Activity. *Ferroelectrics*, 2019, **546**, P. 181–187.
- [18] Wen W., Wu J.M. Nanomaterials via solution combustion synthesis: A step nearer to controllability. *RSC Advances*, 2014, **4**, P. 58090–58100.
- [19] Zhu C., Akiyama T. Optimized conditions for glycine-nitrate-based solution combustion synthesis of LiNi<sub>0.5</sub>Mn<sub>1.5</sub>O<sub>4</sub> as a high-voltage cathode material for lithium-ion batteries. *Electrochimica Acta*, 2014, **127**, P. 290–298.
- [20] Mukasyan A.S., Epstein P., Dinka P. Solution combustion synthesis of nanomaterials. *Proceedings of the Combustion Institute*, 2007, **31**, P. 1789–1795.
- [21] Tugova E., Yastrebov S., Karpov O., Smith R. NdFeO<sub>3</sub> nanocrystals under glycine nitrate combustion formation. *Journal of Crystal Growth*, 2017, **467**, P. 88–92.
- [22] Bachina A., Ivanov V.A., Popkov V.I. Peculiarities of LaFeO<sub>3</sub> nanocrystals formation via glycine-nitrate combustion. *Nanosystems: Physics, Chemistry, Mathematics*, 2017, **8**, P. 647–653.
- [23] Komova O.V., Simagina V.I., Mukha S.A., Netskina O.V., Odegova G.V., Bulavchenko O.A., et al. A modified glycine-nitrate combustion method for one-step synthesis of LaFeO<sub>3</sub>. *Advanced Powder Technology*, 2016, **27**, P. 496–503.
- [24] Popkov V.I., Almyasheva O.V., Nevedomskiy V.N., Sokolov V.V., Gusarov V.V. Crystallization behavior and morphological features of YFeO<sub>3</sub> nanocrystallites obtained by glycine-nitrate combustion. *Nanosystems: Physics, Chemistry, Mathematics*, 2015, **6**, P. 866–874.
- [25] Tijare S.N., Bakardjieva S., Subrt J., Joshi M.V., Rayalu S.S., Hishita S., et al. Synthesis and visible light photocatalytic activity of nanocrystalline PrFeO<sub>3</sub> perovskite for hydrogen generation in ethanol-water system. *Journal of Chemical Sciences*, 2014, **126**, P. 517–525.
- [26] Mukasyan A.S., Dinka P. Novel approaches to solution-combustion synthesis of nanomaterials. *International Journal of Self-Propagating High-Temperature Synthesis*, 2007, **16**, P. 23–35.
- [27] Popkov V.I., Martinson K.D., Kondrashkova I.S., Enikeeva M.O., Nevedomskiy V.N., Panchuk V.V., et al. SCS-assisted production of EuFeO<sub>3</sub> core-shell nanoparticles: formation process, structural features and magnetic behavior. *Journal of Alloys and Compounds*, 2021, **859**, P. 157812.
- [28] Petschnig L.L., Fuhrmann G., Schildhammer D., Tribus M., Schottenberger H., Huppertz H. Solution combustion synthesis of CeFeO<sub>3</sub> under ambient atmosphere. *Ceramics International*, 2016, **42**, P. 4262–4267.

- [29] Wolf E.E., Manukyan K.V., Cross A., Roslyakov S., Rouvimov S., Rogachev A.S., et al. Solution Combustion Synthesis of Nano-Crystalline Metallic Materials: Mechanistic Studies. *The Journal of Physical Chemistry C*, 2013, **117**, P. 24217–24227.
- [30] Sarikhani F., Zabardasti A., Reza A., Mahmoud S. Enhanced visible light activity of – EuFeO<sub>3</sub>/TiO<sub>2</sub> nanocomposites prepared by thermal treatment – hydrolysis precipitation method. *Applied Physics*, 2020, **126**, P. 476.
- [31] Ju L., Chen Z., Fang L., Dong W., Zheng F., Shen M. Sol-gel synthesis and photo-Fenton-like catalytic activity of EuFeO<sub>3</sub> nanoparticles. *Journal of the American Ceramic Society*, 2011, **94**, P. 3418–3424.
- [32] Tikhanova S.M., Lebedev L.A., Kirillova S.A., Tomkovich M.V., Popkov V.I. Synthesis, structure, and visible-light-driven activity of o-YbFeO<sub>3</sub>/h-YbFeO<sub>3</sub>/CeO<sub>2</sub> photocatalysts. *Chimica Techno Acta*, 2021, **8**, P. 20218407.
- [33] Tikhanova S.M., Lebedev L.A., Martinson K.D., Chebanenko M.I., Burianenko I.V., Semenov V.G., Nevedomskiy V.N., Popkov V.I. Synthesis of novel heterojunction h-YbFeO<sub>3</sub>/o-YbFeO<sub>3</sub> photocatalyst with enhanced Fenton-like activity under visible-light. *New Journal Chemistry*, 2020, **45**, P. 1541–1550.
- [34] Martinson K.D., Belyak V.E., Sakhno D.D., Kiryanov N.V., Chebanenko M.I., Popkov V.I. Effect of fuel type on solution combustion synthesis and photocatalytic activity of NiFe<sub>2</sub>O<sub>4</sub> nanopowders. *Nanosystems: Physics, Chemistry, Mathematics*, 2021, **12**, P. 792–798.

---

*Submitted 28 August 2022; accepted 1 December 2022*

*Information about the authors:*

*Anna S. Seroglazova* – Saint Petersburg State Institute of Technology, 26 Moskovsky prospect, St. Petersburg, 190013 Russia; Ioffe Institute, St. Petersburg, 194021 Russia; ORCID 0000-0002-3304-9068; annaseroglazova@yandex.ru

*Vadim I. Popkov* – Ioffe Institute, St. Petersburg, 194021 Russia; ORCID 0000-0002-8450-4278; vadim.i.popkov@mail.ioffe.ru

*Conflict of interest:* the authors declare no conflict of interest.

## Formation of nanocrystalline particles on the basis of $\text{La}_2(\text{Ni,Mn,Fe})_2\text{O}_6$ variable composition phases having a structure of double perovskite under conditions of solution combustion

Denis D. Averkiev<sup>1,2,a</sup>, Lyudmila L. Larina<sup>3</sup>, Oleg I. Shevaleevskiy<sup>3,b</sup>, Oksana V. Almjasheva<sup>1,2,c</sup>

<sup>1</sup>Ioffe Institute, St. Petersburg, Russia

<sup>2</sup>St. Petersburg State Electrotechnical University “LETI”, St. Petersburg, Russia

<sup>3</sup>Solar Photovoltaic Laboratory, Emanuel Institute of Biochemical Physics, Moscow, Russia

<sup>a</sup>swnesli2019@gmail.com, <sup>b</sup>shevale2006@yahoo.com, <sup>c</sup>almjasheva@mail.ru

Corresponding author: Oksana V. Almjasheva, almjasheva@mail.ru

**ABSTRACT** Nanocrystalline particles on the basis of  $\text{La}_2(\text{Ni,Mn,Fe})_2\text{O}_6$  variable composition phases of a double perovskite structure have been produced by glycine-nitrate combustion. The size of crystallites grows from 5 to 45 nm with an increase in iron content of synthesized particles. It is demonstrated that iron unevenly builds into octahedral sites of nickel and manganese ions substituting mainly manganese ions. At the same time, the dependence of double perovskite unit cell volume on the iron ions concentration is well described by Retgers' law.

**KEYWORDS** double perovskite, nanocrystals, solution combustion, photovoltaics.

**ACKNOWLEDGEMENTS** The authors express their gratitude to V. V. Gusarov for the attention he paid to the work. X-ray diffraction and SEM was performed using the equipment of the Engineering Center of Saint Petersburg State Institute of Technology.

This study was financially supported by the Russian Science Foundation (project no. 20-63-47016).

**FOR CITATION** Averkiev D.D., Larina L.L., Shevaleevskiy O.I., Almjasheva O.V. Formation of nanocrystalline particles on the basis of  $\text{La}_2(\text{Ni,Mn,Fe})_2\text{O}_6$  variable composition phases having a structure of double perovskite under conditions of solution combustion. *Nanosystems: Phys. Chem. Math.*, 2022, **13** (6), 655–661.

### 1. Introduction

Double perovskites of general formula  $A_2BB'O_6$  with  $d$ -elements ions in octahedral sites ( $B$ ,  $B'$ ) are well known for their electronic, transport and magnetic properties [1–10]. In these compounds, cation sublattices of  $d$ -elements –  $B$  and  $B'$ , as a rule, have the capability of ferromagnetic or antiferromagnetic ordering [11], which determines, to a great extent, the formation of physical properties of materials based on them.  $B$  and  $B'$  elements variation or their partial substitution for other elements may significantly affect the properties of materials [12–14]. Changing the properties by the partial substitution of ions in octahedral sublattices may also be defined by the peculiarities of the electronic structure of substituting cations and by their impact on the redistribution of major cations –  $B$  and  $B'$  – to octahedral sites, as, for example, in the case of phases having a chrysoberyl structure  $\text{BeMeMe}'\text{O}_4$  described in [15].

Currently,  $\text{La}_2\text{NiMnO}_6$  seems to be one of the most in-demand compounds with the double perovskite structure. The interest in this compound is due primarily to its high interrelated magnetic and electrophysical properties [16–24]. Owing to such range of properties, materials on the basis of  $\text{La}_2\text{NiMnO}_6$  are considered as promising for the use in spintronics [16–18]. Furthermore,  $\text{La}_2\text{NiMnO}_6$  has been extensively studied recently with regard to the use of this compound in photovoltaics [25–30].

In order to obtain  $\text{La}_2\text{NiMnO}_6$ , solid-phase synthesis is usually used. Depending on the conditions of the synthesis,  $\text{La}_2\text{NiMnO}_6$  may be formed as three different crystal structures – rhombohedral (R-3c), monoclinic ( $P2_1/n$ ) or orthorhombic (Pbnm) [16, 19, 22, 31]. In [31], it is noted that exactly the temperature mode of the synthesis defines the formation of one or other structure. However, the analysis of findings from a great number of researches published by now [13, 16, 19, 22, 28, 31–35] does not allow tracing clear correlation of  $\text{La}_2\text{NiMnO}_6$  structure with the temperature at which the compound was produced.

It is known that the temperature of the synthesis can greatly affect the extent of elements ordering during their distribution to various sites in crystals [36, 37]. The temperature impact is particularly significant for the redistribution of ions to various structural sites in cases where they take positions with similar values of coordination numbers [15, 38]. However, it is far from being the only factor defining the distribution of ions by sites [39–43]. Papers [42, 43] have shown that the ordering of  $d$ -element cations in octahedral sites depends on the  $\text{La}_2\text{NiMnO}_6$  production method. There are

also discrepancies in respect of the impact of synthesis conditions on the oxidation rate of nickel and manganese ions in  $\text{La}_2\text{NiMnO}_6$  compound and, therefore, on the properties of double perovskite [21, 22, 35, 44–46].

A profound effect on properties of materials may be exerted by the size of particles and crystallites of phases that form them, especially with the transition into nano-scale range of their values [47–53]. It should be noted that, as shown in [31–35, 42–46, 50, 51, 54], the influence of synthesis methods and conditions on properties is specifically great for nanocrystalline materials. In this regard, a typical example is the effect of crystallite sizes and conditions of synthesis of  $\text{BiFeO}_3$  nano-powders on their magnetic properties [50].

One of the promising methods of synthesis of complex oxides is the method of glycine-nitrate combustion [50–65]. At the same time, this method not always guarantees the possibility of one-stage synthesis of complex oxide phases [22, 28, 32, 33, 46, 58]. Another problem of producing the compounds by the glycine-nitrate combustion method is associated with the chance of evaporation in the combustion front under conditions of high temperatures of the most volatile ingredients of the synthesized phases and, therefore, disturbance of stoichiometry of the compounds produced. It is also difficult to adjust the size of crystallites of forming phases when using this method.

The above-listed considerations initiated the research in  $\text{La}_2(\text{Ni}, \text{Mn}, \text{Fe})_2\text{O}_6$  peculiarities of variable composition nanocrystalline double perovskite formation under conditions of glycine-nitrate combustion and the analysis of the impact of iron nitrate introduction into source reagents on the composition, structural parameters and crystallite size of the synthesized complex oxide phase.

## 2. Experimental

The synthesis of  $\text{La}_2(\text{Ni}, \text{Mn}, \text{Fe})_2\text{O}_6$  variable composition nanocrystalline phase, in which the iron content, according to the given formula, varies from 0 to 1, was performed by glycine-nitrate combustion in accordance with the procedure described in detail in [65]. Water solution containing manganese (II) sulphate, lanthanum nitrate, nickel (II) nitrate and iron (III) nitrate in accordance with the set ratio of cations in the synthesized phase, were mixed with glycine in the proportion complying with the stoichiometry of the glycine-nitrate combustion reaction. The mixture was brought to the boil. Once most of the water has evaporated, a gel-like mixture was produced, which self-ignited and burnt generating a porous powder product.

The nominal iron content introduced into the system was calculated on the assumption of even substitution of *d*-element atoms in octahedral sites of nickel and manganese –  $\text{La}_2\text{Ni}_{1-x}\text{Fe}_x\text{Mn}_{1-x}\text{Fe}_x\text{O}_6$ , where *x* value varied in the range of 0–1 at 0.2 intervals.

The elemental composition of the materials obtained was determined by the X-ray fluorescence analysis (XRF) using Spectroscan GF-2 device.

The study of sample phase composition was performed by X-ray powder diffraction by means of Rigaku SmartLab 3 diffractometer ( $\text{CuK}\alpha$ ). The identification of peaks in the diffraction pattern was performed using PDWin 4.0 software suite and Crystallographica Search-Match package. The average size of crystallites was calculated on the basis of data on X-ray diffraction line profile broadening using Scherrer equation and a software package (SmartLabStudio III).

The morphology of the produced materials was determined by means of scanning electron microscopy (Vega3 Tescan microscope).

## 3. Findings and discussions

A powder material the morphology of which changed with an increase in iron amount in the system was obtained by the glycine-nitrate combustion method (Fig. 1). For an iron-free sample, it is typical to have a sponge-like structure (Fig. 1). In iron-containing samples, the structure of particles with interpenetrating solid phase and pores is consistently changing with an increase in iron content of the reaction system. At a nominal value of  $x = 0.2$  in  $\text{La}_2\text{Ni}_{1-x}\text{Fe}_x\text{Mn}_{1-x}\text{Fe}_x\text{O}_6$  synthesized phase, pores of sizes varying from 0.3 to 2.0 microns are observed in photomicrographs of particles. At  $x = 0.4$ , the pore size falls in the range of 0.5–2.5 microns. At  $x = 0.6$ , the pore size varies generally in the range of 0.5–5 microns. A further increase in the nominal values of *x* in  $\text{La}_2\text{Ni}_{1-x}\text{Fe}_x\text{Mn}_{1-x}\text{Fe}_x\text{O}_6$  synthesized double perovskite to  $x = 0.8$  leads to a decrease in both the pore quantity and the minimum size, and at  $x = 1$ , the sample comprises solid aggregates consisting of almost pore-free plate-like particles.

Elemental composition of the materials produced presented in Table 1 shows significant differences in the nominal and actual compositions of synthesized phases of  $\text{La}_2(\text{Ni}, \text{Mn}, \text{Fe})_2\text{O}_6$  containing all the three elements in octahedral sites. As distinct from these cases, the nominal and actual compositions of  $\text{La}_2\text{NiMnO}_6$  double perovskite and  $\text{LaFeO}_3$  lanthanum ferrite having the perovskite structure are practically identical. The analysis of the data given in Table 1 shows that iron ions chiefly substitute manganese ions in their octahedral sites. This may be related with the fact that in the process of glycine-nitrate combustion in the combustion wave at high temperatures and low values of gas atmosphere oxygen potential, manganese ions exist mainly in the state of  $\text{Mn}^{3+}$  oxidation [67], and at the moment of entry into the structure of double perovskite, due to the proximity of  $\text{Mn}^{3+}$  and  $\text{Fe}^{3+}$  ionic radius values [68], manganese ions are substituted for iron with ease. It should be noted that in such case, owing to the local charge neutralization effect [69], one can expect nickel stabilization in the state of Ni (III) in  $\text{La}_2(\text{Ni}, \text{Mn}, \text{Fe})_2\text{O}_6$  double perovskite. In publications, the chance of finding  $\text{Ni}^{3+}$  and  $\text{Mn}^{3+}$  ions in double perovskite in octahedral sites was mentioned in [21, 22, 44]. A significantly greater

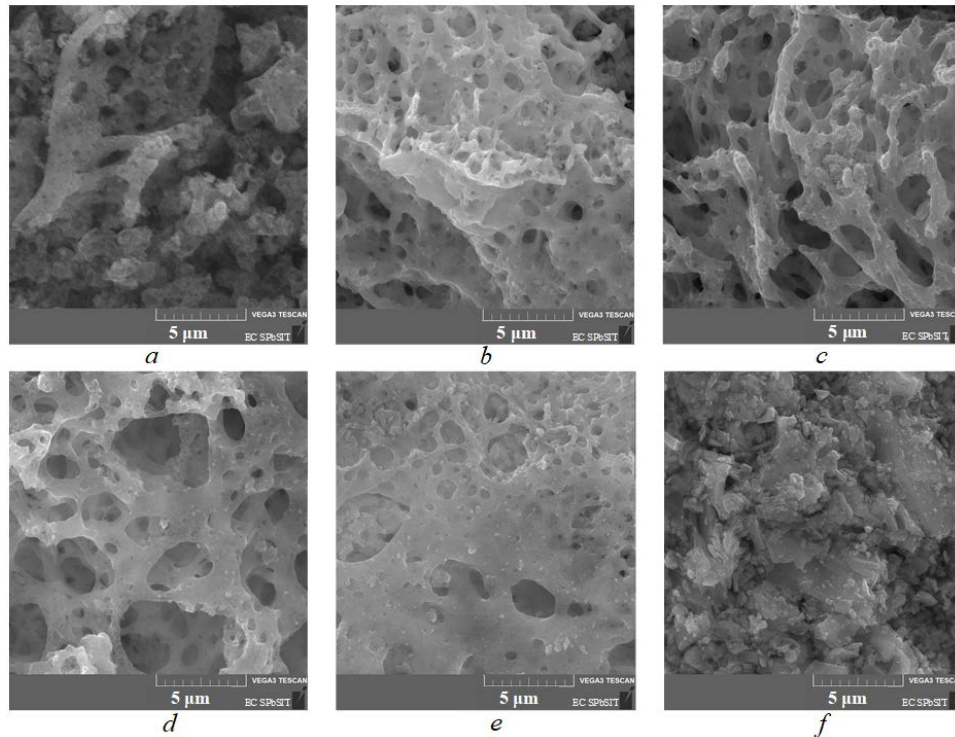


FIG. 1. Photomicrographs of samples with nominal composition of  $\text{La}_2\text{Ni}_{1-x}\text{Fe}_x\text{Mn}_{1-x}\text{Fe}_x\text{O}_6$ .  
 $a - x = 0$ ;  $b - x = 0.2$ ;  $c - x = 0.4$ ;  $d - x = 0.6$ ;  $e - x = 0.8$ ;  $f - x = 1$

TABLE 1. Elemental composition of samples with regard to distribution of  $d$ -elements over octahedral sites

Nominal composition of samples $\text{La}_2\text{Ni}_{1-x}\text{Fe}_x\text{Mn}_{1-x}\text{Fe}_x\text{O}_6$	Sample composition according to X-ray fluorescence analysis						
	Recalculation to the double perovskite formula $\text{La}_2\text{Ni}_{1-x}\text{Fe}_x\text{Mn}_{1-y}\text{Fe}_y\text{O}_6$						Total
	La	$(1-x)\text{Ni}$	$x\text{Fe}$	$(1-y)\text{Mn}$	$y\text{Fe}$	$(x+y)\text{Fe}$	Fe
$x(2x)\text{Fe}$	2	1.00	0.00	1.00	0.00	0.00	0.00
0.0 (0.0)	2	1.00	0.00	0.74	0.26	0.26	0.43
0.2 (0.4)	2	0.79	0.21	0.43	0.57	0.78	0.88
0.4 (0.8)	2	0.59	0.41	0.31	0.69	1.10	1.47
0.6 (1.2)	2	0.28	0.72	0.15	0.85	1.57	1.81
0.8 (1.6)	2	0.00	1.00	0.00	1.00	2.00	2.00
1.0 (2.0)	2	0.00	1.00	0.00	1.00	2.00	2.00

difference in ionic radii of  $\text{Ni}^{3+}$  and  $\text{Fe}^{3+}$  as compared to  $\text{Mn}^{3+}$  and  $\text{Fe}^{3+}$  in this case, apparently, is the main cause of the predominant substitution of manganese ion octahedral sites for iron ions. It should be noted that the result obtained contradicts to some extent to the conclusion made in [13,14] where the authors concluded that doping  $\text{La}_2\text{NiMnO}_6$  double perovskite with  $d$ -elements takes place as a result of Ni substitution in octahedral sites. The explanation of this discrepancy may be the fact that in the given papers the substitution of ions in octahedral sites of  $\text{La}_2\text{NiMnO}_6$  double perovskite was performed by other methods and for other  $d$ -elements.

As shown by the analysis of the data given in Table 1, the fraction of iron required for substitution of nickel and manganese in octahedral sites of double perovskite is less than the total iron content of the sample. This can be associated with both the non-stoichiometry of double perovskite, the possibility of which it was noted in [23], and with the localization of a part of iron-containing component in the non-autonomous (intergranular) phase, which occurs especially frequently in nanocrystalline materials [70–74].

According to the X-ray diffractometry data (Fig. 2), iron-containing samples are single-phase and comprise double perovskite having an orthorhombic structure. In case of complete substitution of nickel and manganese ions in double

perovskite for iron, peaks corresponding to the phase of  $\text{LaFeO}_3$  (card 37-1493) and having the structure of perovskite with an orthorhombic crystal lattice are recorded in the X-ray diffractogram. Low-intensity reflexes corresponding to the phases of  $\text{La}_2\text{NiO}_4$  and  $\text{MnO}_2$  (Fig. 2), which are missing in all other samples containing iron even in small amounts, are recorded in the X-ray diffractogram of an iron-free sample. This may be associated with a higher temperature in the glycine-nitrate combustion front in the presence of iron oxide being a glycine oxidation catalyst, which was also noted in some other papers on glycine-nitrate synthesis of iron-containing oxide phases [57, 58, 65, 66]. The increase in temperature of the synthesis, in turn, intensifies the double perovskite formation process. The assumption that, during the synthesis of double perovskite with the composition  $\text{La}_2\text{NiMnO}_6$ , the temperature in the combustion front is insufficient to fully complete the process of the target product formation may be confirmed by the fact that, according to the data of papers [28, 32, 33, 46], the authors carried out additional heat treatment of combustion products. Another indirect proof of more intense running of the glycine-nitrate synthesis of double perovskite as its composition includes iron oxide is an increase in the size of crystallites of  $\text{La}_2(\text{Ni,Mn,Fe})_2\text{O}_6$  variable composition phase with an increasing iron content of the phase (Fig. 3).

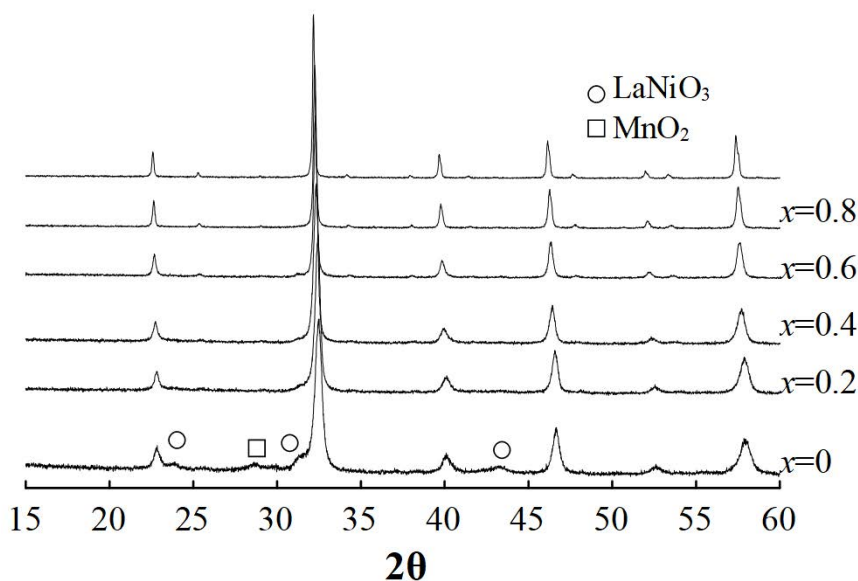


FIG. 2. X-ray diffractograms of samples produced by the glycine-nitrate combustion method

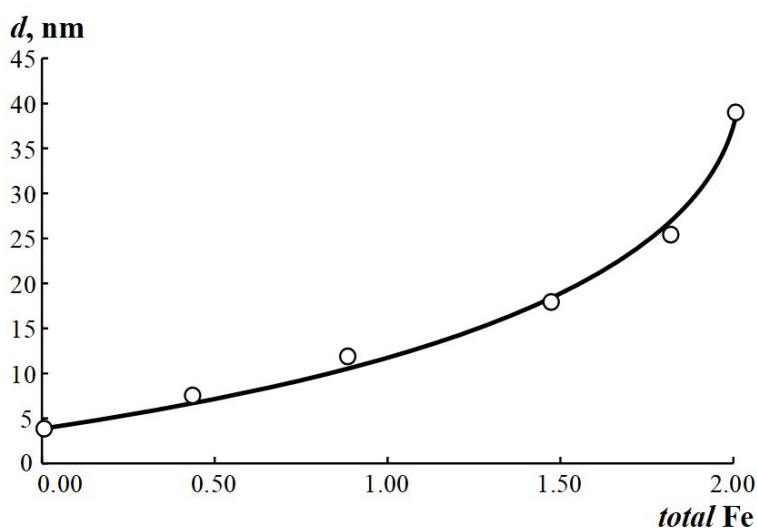


FIG. 3. Sizes of phase  $\text{La}_2(\text{Ni,Mn,Fe})_2\text{O}_6$  crystallites versus actual total iron content of the system (Table 1)

A higher iron content of the samples leads to the displacement of reflexes to the field of smaller angles, i.e., to an increase in unit cell parameters. The analysis of the character of dependence of the unit cell volume on the iron amount  $-(x + y)$ , in phase  $\text{La}_2\text{Ni}_{1-x}\text{Fe}_x\text{Mn}_{1-y}\text{Fe}_y\text{O}_6$ , according to the data of Table 1 (Fig. 4), testifies that this dependence

complies with Retgers' law. Comparison of the data on the dependence of double perovskite unit cell volume on its  $\text{Fe}^{3+}$  ions content with the data on ionic radii of  $\text{Ni}^{2+}$ ,  $\text{Ni}^{3+}$ ,  $\text{Mn}^{3+}$ ,  $\text{Mn}^{4+}$  and  $\text{Fe}^{3+}$  in octahedral coordination may serve as an indirect proof that iron ions entering the structure of double perovskite facilitate stabilization of Ni and Mn cations in charge states of  $\text{Ni}^{3+}$  and  $\text{Mn}^{3+}$  since exactly in this case an increase in double perovskite unit cell volume in accordance with the dependence shown in Fig. 4 may be expected.

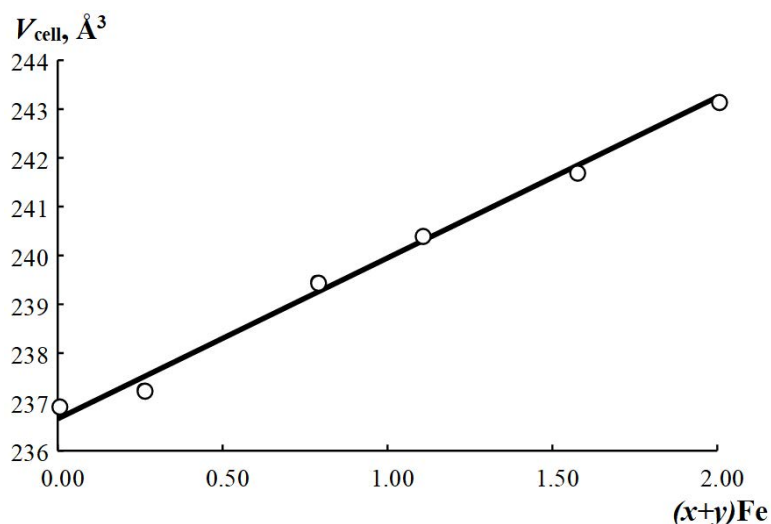


FIG. 4. Dependence of  $\text{La}_2(\text{Ni}_{1-x}\text{Fe}_x)(\text{Mn}_{1-y}\text{Fe}_y)\text{O}_6$  unit cell volume on the amount of iron in the system (iron amount is given according to the data of Table 1)

#### 4. Conclusion

Thus, it may be concluded that  $\text{La}_2(\text{Ni,Mn,Fe})\text{O}_6$  nanocrystalline phases of variable composition on the basis of double perovskite with an orthorhombic structure can be obtained by the glycine-nitrate combustion method without any additional heat treatment. Iron ions predominantly occupy octahedral sites of manganese and stabilize nickel and manganese in the states  $\text{Ni}^{3+}$ ,  $\text{Mn}^{3+}$ . The size of crystallites in the formed phases grows from 5 to 45 nm with an increase in iron amount in the system.

#### References

- [1] Blasse G. Ferromagnetic interactions in non-metallic perovskites. *J. Phys. Chem. Solids*, 1965, **26**, P. 1969–1971.
- [2] Goodenough J.B., Wold A., Arnett R.J., Menyuk N. Relationship between crystal symmetry and magnetic properties of ionic compounds containing  $\text{Mn}^{3+}$ . *Phys. Rev.*, 1961, **124**, P. 373–384.
- [3] Kojima A., Teshima K., Shirai Y., Miyasaka T. Organometal halide perovskites as visible-light sensitizers for photovoltaic cells. *J. Am. Chem. Soc.*, 2009, **131**(17), P. 6050–6051.
- [4] Grinberg I., West D.V., Torres M., Gou G., Stein D.M., Wu L., Chen C., Gallo E.M., Akbashev A.R., Davies P.K., Spanier J.E., Rappe A.M. Perovskite oxides for visiblelight-absorbing ferroelectric and photovoltaic materials. *Nature*, 2013, **503**, P. 509–512.
- [5] Wang F., Grinberg I., Rappe A.M. Semiconducting ferroelectric photovoltaics through  $\text{Zn}^{2+}$  doping into  $\text{KNbO}_3$  and polarization rotation. *Phys. Rev.*, 2014, **89**(23), P. 235105.
- [6] Nechache R., Harnagea C., Li S., Cardenas L., Huang W., Chakrabarty J., Rosei F. Bandgap tuning of multiservice oxide solar cells. *Nat. Photonics*, 2015, **9**, P. 61–67.
- [7] Liu Y.P., Chen S.H., Tung J.C., Wang Y.K. Investigation of possible half-metal material on double perovskites  $\text{Sr}_2\text{BBO}_6$  (B, B=3d transition metal) using firstprinciple calculations. *Solid State Commun.*, 2012, **152**(11), P. 968–973.
- [8] Berger R.F., Neaton J.B. Computational design of low-band-gap double perovskites. *Physical Review B*, 2012, **86**(16), P. 165211.
- [9] Troullier N., Martins J.L. Efficient Pseudopotentials for plane wave calculations. *Physical Review B*, 1991, **43**(3), P. 1993–2006.
- [10] Giannozzi P., Baroni S., Bonini N. Quantum Espresso: a modular and open-source software project for quantum simulations of materials. *J. Phys. Condens. Matter*, 2009, **21**, P. 395502.
- [11] Kobayashi K.I., Kimura T., Sawada H., Terakura K., Tokura Y. Room-temperature magnetoresistance in an oxide material with an ordered double-perovskite structure. *Nature*, 1998, **395**, P. 677–680.
- [12] Najjar F.A., Abass S., Sultan K., Kharadi M. A., Malik G.F.A., Samad R. Comparative study of optical properties of substitutionally doped  $\text{La}_2\text{NiMnO}_6$  double perovskite ceramic: A potential candidate for solar cells and dielectrics. *Physica B: Condensed Matter*, 2021, **621**, P. 413311.
- [13] Tirmali P.M., Mane S.M., Kadam S.L., Kulkarni S.B. Effect of substitutions on dielectric behavior of  $\text{La}_2\text{NiMnO}_6$ . *Chinese Journal of Physics*, 2018, **56**(2), P. 525–537.
- [14] Gan H., Wang C., Shen Q. Improved magnetic performance of Co-doped  $\text{La}_2\text{NiMnO}_6$  ceramics prepared at low temperature. *Journal of the European Ceramic Society*, 2020, **40**(5), P. 1909–1916.
- [15] Gusarov V.V., Matrosov V.N., Semin E.G., Suvorov S.A. Theoretical analysis of thermodynamic parameters of mixing during intracrystalline exchange in chrysoberyl. *Catalytic processes and catalysts*. LTI im. Lensovet, Leningrad, 1983, P. 76–81. In Russian

- [16] Rogado N.S., Li J., Sleight A.W., Subramanian M.A. Magnetocapacitance and magnetoresistance near room temperature in a ferromagnetic semiconductor:  $\text{La}_2\text{NiMnO}_6$ . *Adv. Mater.*, 2005, **17**(18), P. 2225–2227.
- [17] Spurgeon S.R., Du Y., Droubay T., Devaraj A., Sang X., Longo P., Yan P., Kotula P.G., Shutthanandan V., Bowden M.E., LeBeau J.M., Wang C., Sushko P.V., Chambers S.A. Competing pathways for nucleation of the double perovskite structure in the epitaxial synthesis of  $\text{La}_2\text{MnNiO}_6$ . *Chem. Mater.*, 2016, **28**(11), P. 3814–3822.
- [18] Choudhury D., Mandal P., Mathieu R., Hazarika A., Rajan S., Sundaresan A., Waghmare U.V., Knut R., Karis O., Nordblad P., Sarma D.D. Near-room-temperature colossal magnetodielectricity and multiglass properties in partially disordered  $\text{La}_2\text{NiMnO}_6$ . *Phys. Rev. Lett.*, 2012, **108**(12), P. 127201.
- [19] Iliev M.N., Guo H., Gupta A. Raman spectroscopy evidence of strong spin-phonon coupling in epitaxial thin films of the double perovskite  $\text{La}_2\text{NiMnO}_6$ . *Appl. Phys. Lett.*, 2007, **90**, P. 151914.
- [20] Bull C.L., Gleeson D., Knight K.S. Determination of B-site ordering and structural transformations in the mixed transition metal perovskites  $\text{La}_2\text{CoMnO}_6$  and  $\text{La}_2\text{NiMnO}_6$ . *J. Phys. Condens. Matter.*, 2003, **15**(29), P. 4927–4936.
- [21] Joly V.L.J., Joy P.A., Date S.K., Gopinath C.S. Two ferromagnetic phases with different spin states of Mn and Ni in  $\text{LaMn}_{0.5}\text{Ni}_{0.5}\text{O}_3$ . *Phys. Rev. B.*, 2002, **65**(18), P. 184416.
- [22] Dass R.I., Yan J.Q., Goodenough J.B. Oxygen stoichiometry, ferromagnetism, and transport properties of  $\text{La}_{2-x}\text{NiMnO}_{6+\delta}$ . *Phys. Rev. B.*, 2003, **68**(6), P. 64415.
- [23] Chandrasekhar K.D., Das A.K., Mitra C., Venimadhav A. The extrinsic origin of the magnetodielectric effect in the double perovskite  $\text{La}_2\text{NiMnO}_6$ . *J. Phys. Condens. Matter.*, 2012, **24**(49), P. 495901.
- [24] Blanco J., García J., Sanchez M.C., Campo J., Subías G., P'erez-Cacho J. Magnetic properties of  $\text{LaNi}_{1-x}\text{Mn}_x\text{O}^{3+\delta}$  perovskites. *Eur. Phys. J. B.*, 2002, **30**, P. 469–479.
- [25] Kozlov S.S., Alexeeva O.V., Nikolskaia A.B., Shevaleevskiy O.I., Averkiev D.D., Kozhuhovskaya P.V., Almjasheva O.V., Larina L.L. Double perovskite oxides  $\text{La}_2\text{NiMnO}_6$  and  $\text{La}_2\text{Ni}_{0.8}\text{Fe}_{0.2}\text{MnO}_6$  for inorganic perovskite solar cells. *Nanosystems: Phys. Chem. Math.*, 2022, **13**(3), P. 314–319.
- [26] Nikolskaia A.B., Kozlov S.S., Karyagina O.K. Alexeeva O.V., Almjasheva O.V., Averkiev D.D., Kozhuhovskaya P.V., Shevaleevskiy O.I. Cation Doping of  $\text{La}_2\text{NiMnO}_6$  complex oxide with the double perovskite structure for photovoltaic applications. *Russ. J. Inorg. Chem.*, 2022, **67**(6), P. 921–925.
- [27] Nikolskaia A.B., Vildanova M.F., Kozlov S.S., Almjasheva O.V., Gusarov V.V., Shevaleevskiy O.I. High performance tandem perovskite-silicon solar cells with very large bandgap photoelectrodes. *Nanosystems: Phys. Chem. Math.*, 2021, **12**(2), P. 246–251.
- [28] Lan C., Zhao S., Xu T., Ma J., Hayase S., Ma T. Investigation on structures, band gaps, and electronic structures of lead free  $\text{La}_2\text{NiMnO}_6$  double perovskite materials for potential application of solar cell. *J. Alloys Compd.*, 2016, **655**, P. 208–214.
- [29] Dixit H., Punetha D., Pandey S.K. Improvement in performance of leadfree inverted perovskite solar cell by optimization of solar parameters. *Optik*, 2019, **179**, P. 969–976.
- [30] Kumar M., Prajapati B., Raj A., Anshul A., Sati P.C., Sahni M., Kumar A. Progresses and challenges in the structural and magnetic properties of double perovskite  $\text{La}_2\text{NiMnO}_6$  with their applications in solar energy. *Materials Today: Proceedings*, 2022, **49**(8), P. 3088–3092.
- [31] de Azevedo Filho J.B., Souza R.F., Queiroz J.C.A., Costa T.H.C., Sena C.P.S., Fonseca S.G.C., da Silva A.O., Oliveira J.B.L. Theoretical and experimental investigation of the structural and magnetic properties of  $\text{La}_2\text{NiMnO}_6$ . *Journal of Magnetism and Magnetic Materials*, 2021, **527**, P. 167770.
- [32] Nasir M., Kumar S., Patra N., Bhattacharya D., Jha S.N., Basaula D.R., Bhatt S., Khan M., Liu S.-W., Biring S., Sen S. Role of antisite disorder, rare-earth size, and superexchange angle on band gap, Curie temperature, and magnetization of  $\text{R}_2\text{NiMnO}_6$  double perovskites. *ACS Appl. Electron. Mater.*, 2019, **1**(1), P. 141–153.
- [33] Kumar M., Prajapati B., Singh A., Kumar S., Kumar A., Mittal S., Aditya. Structural, optical and magneto-electric coupling analysis in 'Y' doped double perovskite  $\text{La}_2\text{NiMnO}_6$  nanoparticles. *Chemical Physics*, 2020, **532**, P. 110688.
- [34] Gaikwad V.M., Yadav K.K., Lofland S.E., Ramanujachary K.V., Chakraverty S., Ganguli A.K., Jha M. New low temperature process for stabilization of nanostructured  $\text{La}_2\text{NiMnO}_6$  and their magnetic properties. *Journal of Magnetism and Magnetic Materials*, 2019, **471**, P. 8–13.
- [35] Singh M.P., Truong K.D., Jandl S., Fournier P. Long-range Ni/Mn structural order in epitaxial double perovskite  $\text{La}_2\text{NiMnO}_6$  thin films. *Phys. Rev. B.*, 2009, **79**, P. 224421.
- [36] Reznitsky L.A. *Solid state calorimetry (structural, magnetic, electronic transformations)*. Moscow State University, Moscow, 1981, 184 p. In Russian
- [37] Reznitsky L.A. *Chemical bonding and transformations of oxides*. Moscow State University, Moscow, 1991, 168 p. In Russian
- [38] Gusarov V.V., Semin E.G. State diagram of the subsolidus region of the quasi-binary system  $\text{BeAl}_2\text{O}_4$ – $[\text{BeFe}_2\text{O}_4]$ . *Rus. J. Inorg. Chem.*, 1992, **37**(9), P. 2092–2096. In Russian
- [39] Reznitsky L.A. *Crystal energetics of oxides*. Dialog – Moscow State University, Moscow, 1998, 146 p. In Russian
- [40] Krasilin A.A., Gusarov V.V. Redistribution of Mg and Ni cations in crystal lattice of conical nanotube with chrysotile structure. *Nanosystems: Phys., Chem., Math.*, 2017, **8**(5), P. 620–627.
- [41] Saxena S.K. *Thermodynamics of rock-forming crystalline solutions*. Springer, Berlin, Heidelberg, 1973, 188 p.
- [42] Sayed F.N., Achary S.N., Jayakumar O.D. Role of annealing conditions on the ferromagnetic and dielectric properties of  $\text{La}_2\text{NiMnO}_6$ . *J. Mater. Res.*, 2011, **26**, P. 567–577.
- [43] Balcells L., Navarro J., Bibes M., Roig A., Martinez B., Fontcuberta J. Cationic ordering control of magnetization in  $\text{Sr}_2\text{FeMoO}_6$  double perovskite. *Appl. Phys. Lett.*, 2001, **78**, P. 781–783.
- [44] Pal S., Sharada G., Goyal M., Mukherjee S., Pal B., Saha R., Sundaresan A., Jana S., Karis O., Freeland J.W., Sarma D.D. Effect of anti-site disorder on magnetism in  $\text{La}_2\text{NiMnO}_6$ . *Phys. Rev. B.*, 2018, **97**, P. 165137.
- [45] Wang X., Sui Y., Li Y., Li L., Zhang X., Wang Y., Liu Z., Su W., Tang J. The influence of the antiferromagnetic boundary on the magnetic property of  $\text{La}_2\text{NiMnO}_6$ . *Appl. Phys. Lett.*, 2009, **95**, P. 252502.
- [46] Nasir M., Khan M., Kumar S., Bhatt S., Patra N., Bhattacharya D., Jha S.N., Biring S., Sen S. The effect of high temperature annealing on the antisite defects in ferromagnetic  $\text{La}_2\text{NiMnO}_6$  double perovskite. *Journal of Magnetism and Magnetic Materials*, 2019, **483**, P. 114–123.
- [47] Gusarov V.V., Ishutina Z.N., Malkov A.A., Malygin A.A. Peculiarities of the solid-phase chemical reaction in formation of mullite in the nanosize film composition. *Doklady Akademii Nauk*, 1997, **357**(2), P. 203–205. In Russian
- [48] Fokin B.S., Belenkiy M.Ya., Almjashev V.I., Khabensky V.B., Almjasheva O.V., Gusarov V.V. Critical heat flux in a boiling aqueous dispersion of nanoparticles. *Tech. Phys. Lett.*, 2009, **35**(5), P. 440–442.
- [49] Yudin V.E., Otaigbe J.U., Svetlichnyi V.M., Korytkova E.N., Almjasheva O.V., Gusarov V.V. Effects of nanofiller morphology and aspect ratio on the rheo-mechanical properties of polyimide nanocomposites. *EXP. Pol. Lett.*, 2008, **2**(7), P. 485–493.

- [50] Lomanova N.A., Panchuk V.V., Semenov V.G., Pleshakov I.V., Volkov M.P., Gusarov V.V. Bismuth orthoferrite nanocrystals: magnetic characteristics and size effects. *Ferroelectrics*, 2020, **569**, P. 240–250.
- [51] Popkov V.I., Almjasheva O.V., Semenova A.S., Kellerman D.G., Nevedomskiy V.N., Gusarov V.V. Magnetic properties of  $\text{YFeO}_3$  nanocrystals obtained by different soft-chemical methods. *Journal of Materials Science: Materials in Electronics*, 2017, **28**(10), P. 7163–7170.
- [52] Prylypko, S.Y., Akimov, G.Y., Revenko, Y.F. et al. Crystallite size and magnetic properties of  $\text{La}_{0.7}\text{Mn}_{1.3}\text{O}_{3\pm\Delta}$ . *Tech. Phys.*, 2010, **55**(7), P. 1056–1057.
- [53] Nag A., Bose R.S.C., Venu K.S., Singh H. Influence of particle size on magnetic and electromagnetic properties of hexaferrite synthesised by sol-gel auto combustion route. *Ceramics International*, 2022, **48**(11), P. 15303–15313.
- [54] Proskurina O.V., Sokolova A.N., Sirotkin A.A., Abiev R.Sh., Gusarov V.V. Role of Hydroxide Precipitation Conditions in the Formation of Nanocrystalline  $\text{BiFeO}_3$ . *Russ. J. Inorg. Chem.*, 2021, **66**(2), P. 163–169.
- [55] Rogachev A.S., Mukasyan A.S. *Combustion for the synthesis of materials: an introduction to structural macrokinetics*. FIZMATLIT, Moscow, 2013, 400 p.
- [56] Ostroushko A.A., Russkikh O.V. Oxide material synthesis by combustion of organic-inorganic compositions. *Nanosystems: Phys., Chem., Math.*, 2017, **8**(4), P. 476–502.
- [57] Komlev A.A., Gusarov V.V. Glycine-nitrate combustion synthesis of nonstoichiometric Mg-Fe spinel nanopowders. *Inorg Mater.*, 2014, **50**(12), P. 1247–1251.
- [58] Popkov V.I., Almjasheva O.V., Schmidt M.P., Izotova S.G., Gusarov V.V. Features of nanosized  $\text{YFeO}_3$  formation under heat treatment of glycine-nitrate combustion products. *Russ. J. Inorg. Chem.*, 2015, **60**(10), P. 1193–1198.
- [59] Popkov V.I., Almjasheva O.V., Nevedomskiy V.N., Sokolov V.V., Gusarov V.V. Crystallization behavior and morphological features of  $\text{YFeO}_3$  nanocrystallites obtained by glycine-nitrate combustion. *Nanosystems: Phys., Chem., Math.*, 2015, **6**(6), P. 866–874.
- [60] Lomanova N.A., Tomkovich M.V., Sokolov V.V., Gusarov V.V. Special features of formation of nanocrystalline  $\text{BiFeO}_3$  via the glycine-nitrate combustion method. *Russ. J. Gen. Chem.*, 2016, **86**(10), P. 2256–2262.
- [61] Lomanova N. A., Tomkovich M. V., Danilovich D. P., Osipov A. V., Panchuk V. V., Semenov V. G., Pleshakov I. V., Volkov M. P., Gusarov V. V. Magnetic characteristics of nanocrystalline  $\text{BiFeO}_3$ -based materials prepared by solution combustion synthesis. *Inorg. Mater.*, 2020, **56**(12), P. 1271–1277.
- [62] Lomanova N.A., Tomkovich M.V., Sokolov V.V., Ugolkov V.L., Panchuk V.V., Semenov V.G., Pleshakov I.V., Volkov M.P., Gusarov V.V. Thermal and magnetic behavior of  $\text{BiFeO}_3$  nanoparticles prepared by glycine-nitrate combustion. *Journal of Nanoparticle Research*, 2018, **20**, Art.No 17.
- [63] Martinson K.D., Sakhno D.D., Belyak V.E., Kondrashkova I.S.  $\text{Ni}_{0.4}\text{Zn}_{0.6}\text{Fe}_2\text{O}_4$  nanopowders by solution-combustion synthesis: influence of Red/Ox ratio on their morphology, structure, and magnetic properties. *International Journal of Self-Propagating High-Temperature Synthesis*, 2020, **29**, P. 202–207.
- [64] Martinson K.D., Kondrashkova I.S., Popkov V.I. Synthesis of  $\text{EuFeO}_3$  nanocrystals by glycine-nitrate combustion method. *Russ. J. Appl. Chem.*, 2017, **90**(8), P. 1214–1218.
- [65] Dyachenko S.V., Martinson K.D., Cherepkova I.A., Zhernovoi A.I. Particle size, morphology, and properties of transition metal ferrosinels of the  $\text{MFe}_2\text{O}_4$  (M = Co, Ni, Zn) type, produced by glycine-nitrate combustion. *Russ. J. Appl. Chem.*, 2016, **89**(4), P. 535–539.
- [66] Popkov V.I., Almjasheva O.V. Yttrium orthoferrite  $\text{YFeO}_3$  nanopowders formation under glycine-nitrate combustion conditions. *Russ. J. Appl. Chem.*, 2014, **87**(2), P. 167–171.
- [67] State diagrams of silicate systems. Directory. Issue 2. Metal-oxygen compounds of silicate systems. Ed. N.A.Toropova. Science, Leningrad, 1969, P. 295–298, P. 359–363. (Total 372 p). In Russian.
- [68] Shannon R.D. Revised effective ionic radii and systematic studies of interatomic distances in halides and chalcogenides. *Acta Crystallographica Section A*, 1976, **A32**, P. 751–767.
- [69] Gusarov V.V., Semin E.G., Suvorov S.A. Thermodynamics of heterovalent isomorphous mixtures of  $\text{Be}_{1-1.5x}\text{Me}_x\text{O}$  (Me is a 3d element). *Russ. J. Appl. Chem.*, 1983, **56**(9), P. 1956–1958. In Russian
- [70] Gusarov V.V., Egorov F.K., Ekimov S.P., Suvorov S.A. Mossbauer study of kinetics of film state formation under the interaction of magnesium and iron-oxides. *Zh. Fiz. Khim.*, 1987, **61**(6), P. 1652–1654. In Russian
- [71] Gusarov V.V., Suvorov S.A. Thickness of 2-dimensional nonautonomous phases in local equilibrium polycrystalline systems based on a single bulk phase. *Russ. J. Appl. Chem.*, 1993, **66**(7), P. 1212–1216.
- [72] Gusarov V.V., Popov I.Yu. Flows in Two-dimensional nonautonomous phases in polycrystalline system. *Nuovo Cimento della Societa Italiana di Fisica D*, 1996, **18D**(7), P. 799–805.
- [73] Gusarov V.V., Almjasheva O.V. The role of non-autonomous state of matter in the formation of structure and properties of nanomaterials. Chapter 13 in the book *Nanomaterials: properties and promising applications*. Ed A.B. Yaroslavtsev. Scientific World Publishing House, Moscow, 2014, P. 378–403. in Russian
- [74] Kirillova S.A., Panchuk V.V., Semenov V.G., Almjasheva O.V. Solid-phase interaction in the  $\text{ZrO}_2\text{-Fe}_2\text{O}_3$  nanocrystalline system. *Nanosystems: Phys., Chem., Math.*, 2018, **9**(6), P. 763–769.

---

Submitted 28 October 2022; accepted 17 November 2022

#### Information about the authors:

Denis D. Averkiev – Ioffe Institute, St. Petersburg, 194021, Russia; St. Petersburg State Electrotechnical University “LETI”, St. Petersburg, 197376, Russia; swnesli2019@gmail.com

Lyudmila L. Larina – Solar Photovoltaic Laboratory, Emanuel Institute of Biochemical Physics, Moscow, Russia

Oleg I. Shevaleevskiy – Solar Photovoltaic Laboratory, Emanuel Institute of Biochemical Physics, Moscow, Russia; ORCID 0000-0002-8593-3023; shevale2006@yahoo.com

Oksana V. Almjasheva – Ioffe Institute, St. Petersburg, 194021, Russia; St. Petersburg State Electrotechnical University “LETI”, St. Petersburg, 197376, Russia; ORCID 0000-0002-6132-4178; almjasheva@mail.ru

Conflict of interest: the authors declare no conflict of interest.

## Thermal stability of the waylandite-structured nanocrystalline $\text{BiAl}_3(\text{PO}_4)_2(\text{OH})_6$

Dmitry P. Elovikov<sup>1,2,a</sup>, Olga V. Proskurina<sup>1,3,b</sup>, Maria V. Tomkovich<sup>1,c</sup>,  
Valery L. Ugolkov<sup>4,d</sup>, Victor V. Gusarov<sup>1,e</sup>

<sup>1</sup>Ioffe Institute, St. Petersburg, Russia

<sup>2</sup>St. Petersburg Electrotechnical University “LETI”, St. Petersburg, Russia

<sup>3</sup>St. Petersburg State Institute of Technology, St. Petersburg, Russia

<sup>4</sup>I. V. Grebenshchikov Institute of Silicate Chemistry of the Russian Academy of Sciences,  
St. Petersburg, Russia

<sup>a</sup>syncdima@mail.ru, <sup>b</sup>proskurinaov@mail.ru, <sup>c</sup>maria.tom83@gmail.com, <sup>d</sup>ugolkov.52@gmail.com,

<sup>e</sup>victor.v.gusarov@gmail.com

Corresponding author: Dmitry P. Elovikov, syncdima@mail.ru

**ABSTRACT** A nanocrystalline powder of the waylandite-structured bismuth hydroaluminophosphate was obtained under hydrothermal conditions at 200 °C, 7 MPa and pH 7, and characterized by X-ray diffractometry, scanning electron microscopy (SEM), and energy dispersive microanalysis (EDAX). The simultaneous thermal analysis and high-temperature X-ray diffractometry have shown that the crystal-chemical formula of this compound can be represented as  $\text{BiAl}_3(\text{PO}_4)_2\text{O}(\text{OH})_4 \cdot (\text{H}_2\text{O})$ . This compound retains its structure and crystallite size (~65 nm) up to about 500 °C. It has been determined that the decomposition of this compound in the 540–800 °C range results in the formation of  $\text{Bi}_2\text{O}_3$ ,  $\text{Bi}_2\text{Al}_4\text{O}_9$  and  $\text{AlPO}_4$  phases. At temperatures above 800 °C, a complete thermal decomposition of  $\text{Bi}_2\text{Al}_4\text{O}_9$  and the formation of crystalline  $\alpha\text{-Al}_2\text{O}_3$  occur in this system, while  $\text{Bi}_2\text{O}_3$  keeps evaporating during the isothermal exposure.

**KEYWORDS** nanocrystals, waylandite-structured,  $\text{BiAl}_3(\text{PO}_4)_2\text{O}(\text{OH})_4 \cdot (\text{H}_2\text{O})$ , thermal stability, hydrothermal synthesis, nature-like technologies.

**ACKNOWLEDGEMENTS** X-ray diffraction studies and elemental analyses of samples were performed employing the equipment of the Engineering Center of the St. Petersburg State Institute of Technology (Technical University). The research was supported by the Russian Science Foundation Grant 21-13-00260

**FOR CITATION** Elovikov D.P., Proskurina O.V., Tomkovich M.V., Ugolkov V.L., Gusarov V.V. Thermal stability of the waylandite-structured nanocrystalline  $\text{BiAl}_3(\text{PO}_4)_2(\text{OH})_6$ . *Nanosystems: Phys. Chem. Math.*, 2022, **13** (6), 662–667.

### 1. Introduction

In recent years, there has been an active interest in the development of new functional materials based on synthetic minerals and of their technologies (nature-like technologies). Such interest is primarily due to the possibility of obtaining new materials with unique properties [1–3].

Phosphates of the alunite supergroup are an extensive class of inorganic compounds with the  $AB_3(\text{PO}_4)_2(\text{OH})_6$  chemical formula, where *A* is Ce, La, Nb, Sm, Ca, Sr, Pb, Ba, Bi, and *B* is Al, Fe, V; they are similar in their structural parameters, syngony (trigonal/hexagonal), space group ( $R\bar{3}m$ ), and represent crystals with the hexagonal scalenohedron geometry [4–10].

The relevance of obtaining and studying such phosphates, in particular, lies in the prospects of using them as matrices for toxic and radioactive waste due to their structural features, thermal stability and high ability to ionic substitution of toxic Hg, As, Tl, Sb, Cr, Ni, Ca, radioactive K, Sr, Th, U, Ra, Pb and rare earths [10–14]. Data on the synthesis of these compounds are scanty and have a number of shortcomings. This is determined by the fact that the preparation of such compounds is complicated by the long duration of crystalline phases formation, from two weeks to six months [11, 12, 15, 16]. It should be noted that in some of the listed works the performed synthesis used natural minerals and yielded mixtures of phases rather than individual compounds. The mentioned works contain no data on the kinetics and mechanisms of compounds formation.

The study of the thermal behavior of phases is of fundamental scientific interest. An analysis of the literature on the thermal stability of phosphates of the alunite supergroup showed the paucity of the available data [12, 15, 17, 18]. In most scientific works, the objects of study are natural minerals which contain impurity components and are phases of variable composition. Phosphates of the alunite supergroup tend to include impurity cations and anions from the environment

into their structure, which affects the results of studying their properties. There are no data on the study of individual compounds.

To obtain hydroxide and oxide phases, methods of hydrothermal, hydrothermal-microwave and hydrothermal-ultrasonic treatment [19–24] are widely used. Hydrothermal synthesis has produced many artificial analogs of minerals [25–30] positively differing from natural ones by the strictly defined composition and morphology, and prescribed size distribution of particles. An analysis of the currently available scientific literature has shown that the waylandite-structured  $\text{BiAl}_3(\text{PO}_4)_2(\text{OH})_6$  crystalline phase was successfully obtained for the first time under hydrothermal conditions [31].

There is no information on the thermal stability and thermal behavior of the  $\text{BiAl}_3(\text{PO}_4)_2(\text{OH})_6$  compound. In this regard, the present work is aimed at studying the thermal stability of the waylandite-structured nanocrystalline  $\text{BiAl}_3(\text{PO}_4)_2(\text{OH})_6$ .

## 2. Experimental

To obtain waylandite-structured nanocrystalline  $\text{BiAl}_3(\text{PO}_4)_2(\text{OH})_6$  under hydrothermal conditions, the following reagents were used:  $\text{Bi}(\text{NO}_3)_3 \cdot 5\text{H}_2\text{O}$  (p.a.),  $\text{Al}(\text{NO}_3)_3 \cdot 9\text{H}_2\text{O}$  (puriss.),  $(\text{NH}_4)_2\text{HPO}_4$  (p.a.),  $\text{HNO}_3$  (puriss. spec.), and  $\text{NaOH}$  (puriss.). Bismuth and aluminum nitrate samples, calculated to obtain  $\text{BiAl}_3(\text{PO}_4)_2(\text{OH})_6$ , were dissolved in 6 M aqueous  $\text{HNO}_3$  solution with stirring until complete dissolution. An aqueous solution of  $(\text{NH}_4)_2\text{HPO}_4$  prepared by dissolving a sample calculated according to stoichiometry in distilled water, was added dropwise to the resulting solution. Next, a 4 M aqueous  $\text{NaOH}$  solution was added dropwise to the resulting suspension with stirring, until pH 7 was reached.

Hydrothermal treatment of suspensions was carried out in steel autoclaves with Teflon chambers at 200 °C and a pressure of 7 MPa for 12 days in a hydrothermal fluid at pH=7. The resulting precipitate was separated by centrifugation, rinsed with distilled water until neutral, and dried at 80 °C for 6 hours.

The determination of the morphology and particle size, and of elemental composition of the samples was carried out by scanning electron microscopy (SEM) and energy dispersive microanalysis (EDAX) using a Tescan Vega 3 SBH electron microscope (TESCAN Brno, Czech Republic) with an Inca X-Act elemental analysis attachment (Oxford Instruments plc, Great Britain).

X-ray diffraction measurements of the powder sample were carried out on a Rigaku SmartLab 3 diffractometer (Rigaku, Japan), equipped with an X-ray tube with a copper anode, in the Bragg-Brentano geometry.  $\text{CuK}\alpha$  doublet radiation was monochromatized using a nickel  $K\beta$  filter. The shooting was carried out in air at a constant temperature of 25 °C. The size of the crystallites was calculated by the Hall method for peaks  $10\bar{1}1$ ,  $11\bar{2}0$ ,  $11\bar{2}3$ ,  $02\bar{2}4$  and  $30\bar{3}3$ .

The high-temperature X-ray diffraction analysis of the powder sample was carried out on an XRD-7000 diffractometer (Shimadzu, Japan) with an HTK 1200 N high-temperature attachment (Anton Paar, Austria).

Possible crystalline phases were identified using PDF-2 (Powder Diffraction File-2) [32] and Crystallography Open Database [33] powder databases.

The simultaneous thermal analysis coupled with mass spectrometry for the analysis of evolved gases employed an STA 429 CD in combination with a QMS 403 C (NETZSCH, Germany) quadrupole mass spectrometer with a heating rate of 10 °C/min from 25 to 950 °C.

## 3. Results and discussion

Thermal studies were carried out on powdered nanocrystalline  $\text{BiAl}_3(\text{PO}_4)_2(\text{OH})_6$  obtained by hydrothermal synthesis at pH 7. The elemental analysis showed that the bismuth, aluminum and phosphorus ratio in the initial samples corresponds to the stoichiometry of the individual  $\text{BiAl}_3(\text{PO}_4)_2(\text{OH})_6$  compound with an error in determining the elemental composition up to 5 at. %. All peaks in the X-ray diffraction pattern (Fig. 1) correspond to the waylandite-structured  $\text{BiAl}_3(\text{PO}_4)_2(\text{OH})_6$  [31]. The crystallite size is ~65 nm.

According to the SEM data presented in Fig. 2, it can be seen that the compound particles after synthesis are represented by rod-like aggregates composed by smaller particles. At heating the sample up to 1000 °C, the particle morphology changes only slightly, while the heating to temperatures above 1000 °C leads to a sharp change in particle morphology (Fig. 2).

According to the simultaneous thermal analysis data using mass spectrometry, four areas of water release from the sample can be noted (Fig. 3).

The first region (80–318 °C), characterized by a loss of ~1 wt. %, is associated with the removal of the adsorbed water from the sample. The second region (318–498 °C), characterized by a loss of ~3.5 wt. % of water, is associated with an endothermic effect that is well pronounced in the thermogram and can be associated with the removal of a part of water from the  $\text{BiAl}_3(\text{PO}_4)_2(\text{OH})_6$  compound. At the same time, according to the X-ray diffraction data, the initial structure of waylandite does not undergo any changes (Fig. 4). Consequently, it would be apparently more correct to represent the crystal-chemical formula of this compound as  $\text{BiAl}_3(\text{PO}_4)_2(\text{OH})_4 \cdot (\text{H}_2\text{O})$ . In this regard, this formula is similar to that adopted for the  $\text{CaAl}_3(\text{PO}_4)_2(\text{OH})_5 \cdot (\text{H}_2\text{O})$  compound with a similar structure [17]. The third (498–597 °C) and fourth (597–600 °C) regions, which are difficult to separate from each other according to thermogravimetric data and the results of differential thermal analysis, and are characterized by a weight loss of ~3.2 and ~2.4 wt. %, respectively, are associated with the process of  $\text{BiAl}_3(\text{PO}_4)_2(\text{OH})_4 \cdot (\text{H}_2\text{O})$  dehydroxylation. In this case, sample amorphization occurs

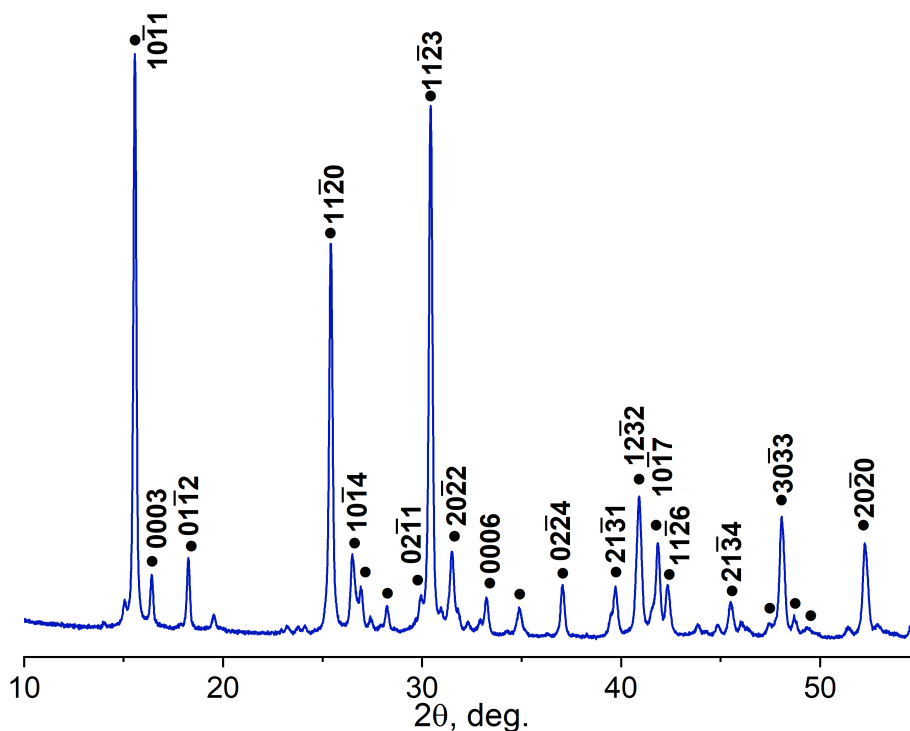


FIG. 1. X-ray diffraction pattern of  $\text{BiAl}_3(\text{PO}_4)_2(\text{OH})_6$  synthesized under hydrothermal conditions. The X-ray diffraction pattern shows the Miller-Brave ( $hkl$ ) indices of the most intense peaks of the waylandite-structured compound

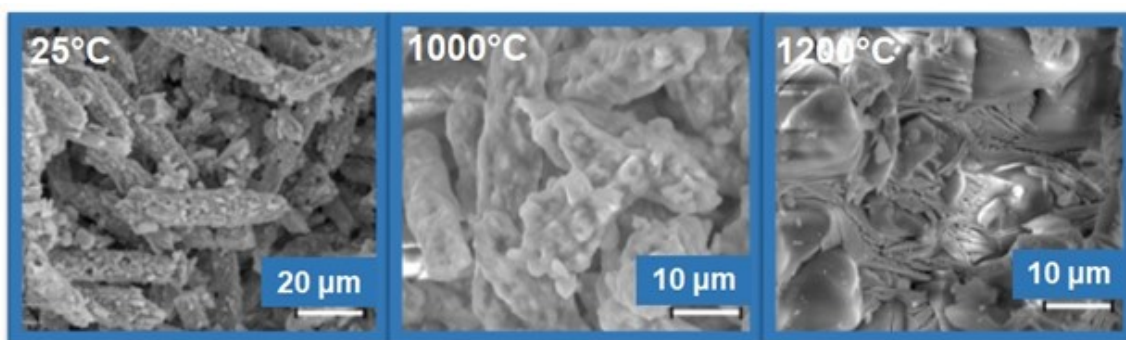
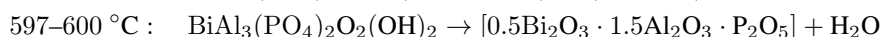
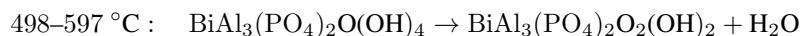
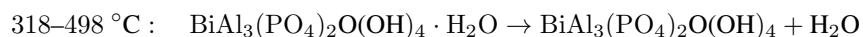


FIG. 2. SEM images of samples before and after heat treatment at 1000 and 1200°C

after the removal of all water from it. According to the calculation of the mass loss by the sample, each of the regions Nos. 2, 3, and 4 (Fig. 3) accounts for the removal of one  $\text{H}_2\text{O}$  molecule per  $\text{BiAl}_3(\text{PO}_4)_2(\text{OH})_4 \cdot (\text{H}_2\text{O})$  formula.

Thus, the above-described processes of stepwise separation of water from the compound can be represented as follows:



It should be noted that the presented scheme suggests that a possibly metastable  $\text{BiAl}_3(\text{PO}_4)_2\text{O}_2(\text{OH})_2$  phase exists in a very narrow temperature range (about 597 °C).

According to high-temperature X-ray diffraction data, the onset of decomposition of the waylandite-structured phase with the appearance of peaks of the  $\text{Bi}_2\text{Al}_4\text{O}_9$  phase, is observed at temperatures of about 500 °C (Fig. 4). During the isothermal exposure of the sample at 540 °C for about 30 min, peaks of the waylandite-structured phase are already weakly expressed in the diffraction pattern, and the appearance of trace amounts of crystalline  $\text{AlPO}_4$  can be noticed in addition to peaks of the  $\text{Bi}_2\text{Al}_4\text{O}_9$  phase (Fig. 4). Some temperature shift of phase transformation effects to lower temperatures according to high-temperature diffraction data compared to the data of simultaneous thermal analysis, is explained by the difference in sample heating conditions. The higher temperatures of the effects recorded by the simultaneous thermal

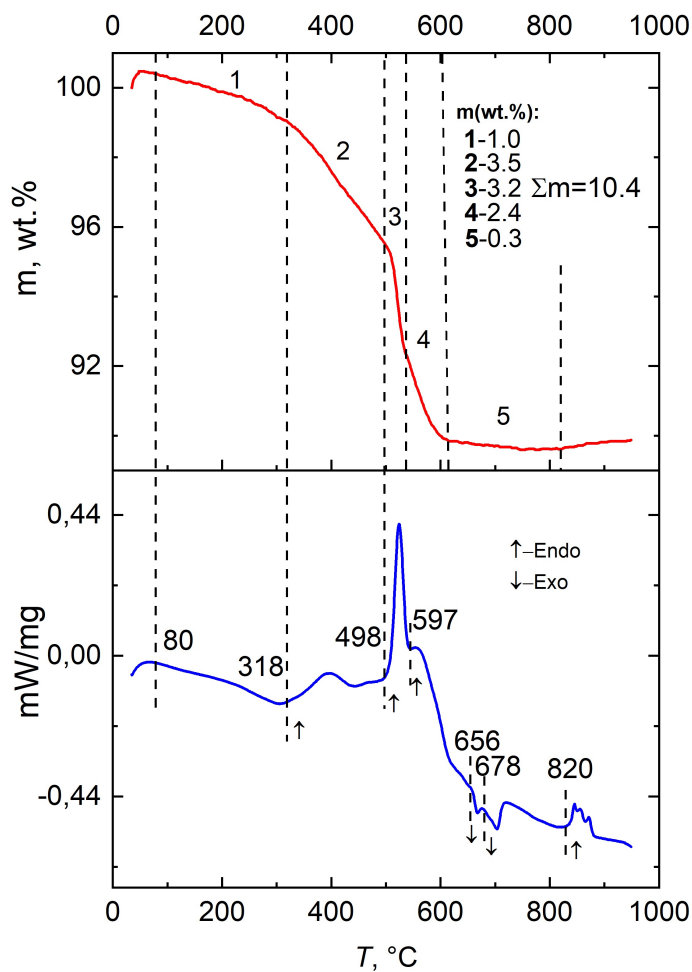


FIG. 3. Simultaneous thermal analysis data for the nanocrystalline  $\text{BiAl}_3(\text{PO}_4)_2(\text{OH})_6$  synthesized under hydrothermal conditions

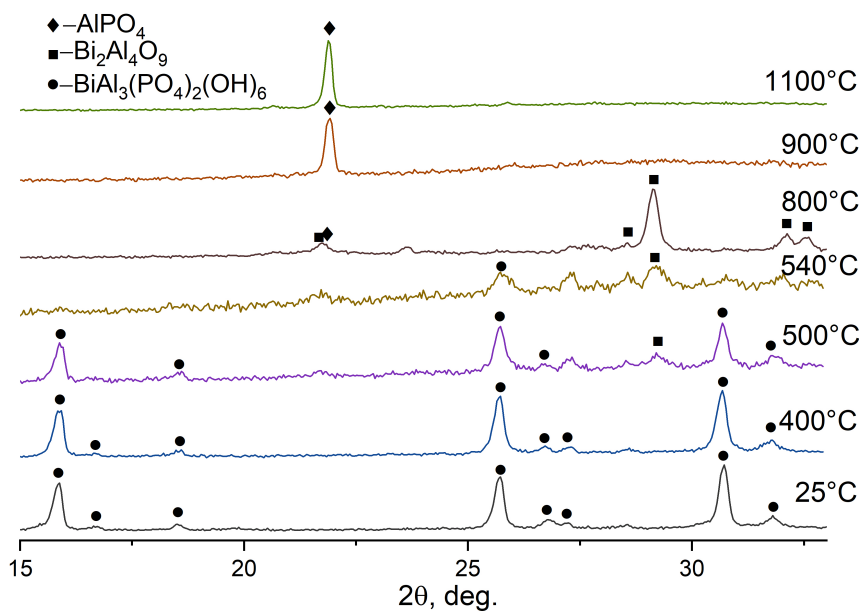


FIG. 4. High-temperature X-Ray diffraction data for the nanocrystalline  $\text{BiAl}_3(\text{PO}_4)_2\text{O}(\text{OH})_4 \cdot (\text{H}_2\text{O})$  obtained under hydrothermal conditions.

analysis, are explained by the thermal inertia of the system, which always manifests itself under conditions of a constant heating rate [34, 35] of the samples. The exothermic peaks in the 656–720 °C temperature range noticed in the DTA curve (Fig. 3) are apparently associated with crystallization of the  $\text{Bi}_2\text{Al}_4\text{O}_9$ -,  $\text{Bi}_2\text{O}_3$ - and  $\text{AlPO}_4$ -based phases from the amorphous phase that formed during  $\text{BiAl}_3(\text{PO}_4)_2(\text{OH})_4 \cdot (\text{H}_2\text{O})$  dehydration. According to high-temperature X-ray diffraction data, the process of crystallization of these phases can be considered almost complete at a temperature of about 800 °C (Fig. 4). Endothermic peaks in the 810–885 °C range in the DTA curve (Fig. 3) are associated, as can be concluded from the literature data [36–38], with the processes of eutectic phase melting and, possibly, phase transitions in the  $\text{Bi}_2\text{O}_3$ – $\text{Al}_2\text{O}_3$ – $\text{P}_2\text{O}_5$  system.

It should be noted that according to the data on the broadening of X-ray diffraction lines, the sizes of crystallites in the waylandite-structured phase remain at a level of ~65 nm within the entire temperature range of its existence (25–500 °C).

An analysis of high-temperature X-ray diffraction data (Fig. 3) and elemental analysis of the samples, which showed a sharp decrease in the bismuth content at processing temperatures above 900 °C, evidence that bismuth aluminate  $\text{Bi}_2\text{Al}_4\text{O}_9$  decomposition at these temperatures is accompanied by melting and evaporation of bismuth oxide  $\text{Bi}_2\text{O}_3$ , which is consistent with the data from phase diagrams [36–38].

#### 4. Conclusions

It has been shown that rod-like particles, which are aggregates of nanocrystals based on a waylandite-structured phase, form under hydrothermal conditions at pH 7. The crystal-chemical formula of the corresponding compounds can be represented as  $\text{BiAl}_3(\text{PO}_4)_2\text{O}(\text{OH})_4 \cdot (\text{H}_2\text{O})$ . It has been established that the structure of this compound is thermally stable up to about 500 °C, despite the fact that partial dehydration of the compound and formation of  $\text{BiAl}_3(\text{PO}_4)_2\text{O}(\text{OH})_4$  take place in the temperature range of about 300–500 °C. The size of phase crystallites remains at a level of about 65 nm in the temperature range up to 500 °C. The complete dehydration of the compound with the formation of an amorphous phase occurs in the range of 500–600 °C. The heating up to 800 °C leads to the formation of a mixture of  $\text{AlPO}_4$ ,  $\text{Bi}_2\text{O}_3$ , and  $\text{Bi}_2\text{Al}_4\text{O}_9$  crystalline phases. An increase of the temperature up to 900 °C and above leads to the decomposition of bismuth aluminate  $\text{Bi}_2\text{Al}_4\text{O}_9$  and the evaporation of bismuth oxide.

#### References

- [1] Kotova O. New adsorbent materials on the base of minerals and industrial waste. *Materials Science and Engineering*, 2019, **613**(1), P. 012001.
- [2] Wei L., Li Z., Ye G., Rietveld L.C., van Halem D. Comparative study of low-cost fluoride removal by layered double hydroxides, geopolymers, softening pellets and struvite. *Environmental Technology*, 2022, **43**(27), P. 4306–4314.
- [3] McMillen C.D., Kolis J.W. Hydrothermal synthesis as a route to mineralogically-inspired structures. *Dalton Transactions*, 2016, **45**(7), P. 2772–2784.
- [4] Mills S.J., Kampf A.R., Raudsepp M., Birch W.D. The crystal structure of waylandite from Wheal Remfry, Cornwall, United Kingdom. *Mineralogy and Petrology*, 2010, **100**(3), P. 249–253.
- [5] Repina S.A., Popova V.I., Churin E.I., Belogub E.V., Khiller V.V. Florencite-(Sm)-(Sm,Nd) $\text{Al}_3(\text{PO}_4)_2(\text{OH})_6$ : A new mineral species of the alunite-jarosite group from the Subpolar Urals. *Geology of Ore Deposits*, 2011, **53**(7), P. 564–574.
- [6] Mills S.J., Kampf A.R., Raudsepp M., Christy A.G. The crystal structure of Ga-rich plumbogummite from Tsumeb, Namibia. *Mineralogical Magazine*, 2009, **73**(5), P. 837–845.
- [7] Blount A.M. The crystal structure of crandallite. *American Mineralogist*, 1974, **59**, P. 41–47.
- [8] Bayliss P., Kolitsch U., Nickel E.H., Pring A. Alunite supergroup: recommended nomenclature. *Mineralogical Magazine*, 2010, **74**(5), P. 919–927.
- [9] Kolitsch U., Tiekink E., Slade P., Taylor M.R., Pring A. Hinsdalite and plumbogummite, their atomic arrangements and disordered lead sites. *European Journal of Mineralogy*, 1999, **11**, P. 513–520.
- [10] Kolitsch U., Pring A. Crystal chemistry of the crandallite, beudantite and alunite groups: a review and evaluation of the suitability as storage materials for toxic metals. *Journal of Mineralogical and Petrological Sciences*, 2001, **96**(2), P. 67–78.
- [11] Monteagudo J.M., Duran A., Carmona M.S., Schwab R.G., Higuera P. Elimination of inorganic mercury from waste waters using crandallite-type compounds. *Journal of Chemical Technology & Biotechnology*, 2003, **78**(4), P. 399–405.
- [12] Gilkes R.J. Synthesis, Properties, and Dehydroxylation of Members of the Crandallite-Goyazite Series. *Mineralogical Magazine*, 1983, **47**, P. 221–227.
- [13] Monteagudo J.M., Duran A., Martin I.S., Schwab R.G. Treatment of aqueous solutions containing nickel using crandallite-type compounds. *Journal of Chemical Technology & Biotechnology*, 2005, **81**(3), P. 262–267.
- [14] Owen D.N., Cook N.J., Rollog M., Ehrig K.J., Schmandt D.S., Ram R., Brugger J., Ciobanu C.L., Wade B., Guagliardo P. REE-, Sr-, Ca-aluminum-phosphate-sulfate minerals of the alunite supergroup and their role as hosts for radionuclides. *American Mineralogist*, 2019, **104**(12), P. 1806–1819.
- [15] Hikichi Y., Ohsato H., Miyamoto M. Syntheses and thermal changes of plumbogummite-group phosphate minerals. *Journal of the Mineralogical Society of Japan*, 1989, **19**(2), P. 67. (in Japanese).
- [16] Schwab R.G., Pimpl T., Schukow H., Stolle A., Breiting D.K. Compounds of the crandallite-type: Synthesis, properties and thermodynamic data of pure crandallite and woodhouseite. *Neues Jahrbuch für Mineralogie – Monatshefte*, 2004, **9**, P. 385–409.
- [17] Frost R.L., Palmer S.J., Pogson R.E. Thermal stability of crandallite  $\text{CaAl}_3(\text{PO}_4)_2(\text{OH})_5 \cdot (\text{H}_2\text{O})$  A 'Cave' mineral from the Jenolan Caves. *Journal of Thermal Analysis and Calorimetry*, 2012, **107**(3), P. 905–909.
- [18] Francisco E.A.B., Prochnow L.I., Motta de Toledo M.C., Ferrari V.C., de Jesus S.L. Thermal treatment of aluminous phosphates of the crandallite group and its effect on phosphorus solubility. *Sci. agric. (Piracicaba, Braz.)*, 2007, **64**(3), P. 269–274.
- [19] Pozhidaeva O.V., Korytkova E.N., Romanov D.P., Gusarov V.V. Formation of  $\text{ZrO}_2$  Nanocrystals in Hydrothermal Media of Various Chemical Compositions. *Russian Journal of General Chemistry*, 2002, **72**(6), P. 849–853.

- [20] Filippova A.D., Rumyantsev A.A., Baranchikov A.E., Kolesnik I.V., Ivanova O.S., Efimov N.N., Khoroshilov A.V., Ivanov V.K. Hydrothermal Synthesis of  $\gamma\text{-WO}_3$  and  $h\text{-WO}_3$  Powders in the Presence of Citric Acid and Their Photoprotective Properties. *Russian Journal of Inorganic Chemistry*, 2022, **67**(6), P. 780–789.
- [21] Meskin P.E., Gavrilov A.I., Maksimov V.D., Ivanov V.K., Churagulov B.P. Hydrothermal/microwave and hydrothermal/ultrasonic synthesis of nanocrystalline titania, zirconia, and hafnia. *Russian Journal of Inorganic Chemistry*, 2007, **52**(11), P. 1648–56.
- [22] Bachina A.K., Almjasheva O.V., Popkov V.I. Formation of  $\text{ZrTiO}_4$  under Hydrothermal Conditions. *Russian Journal of Inorganic Chemistry*, 2022, **67**(6), P. 830–838.
- [23] Enikeeva M.O., Proskurina O.V., Danilovich D.P., Gusarov V.V. Formation of nanocrystals based on equimolar mixture of lanthanum and yttrium orthophosphates under microwave-assisted hydrothermal synthesis. *Nanosyst.: Phys. Chem. Math.*, 2020, **11**(6), P. 705–715.
- [24] Lomakin M.S., Proskurina O.V., Levin A.A., Sergeev A.A., Leonov A.A., Nevedomsky V.N., Voznesenskiy S.S. Pyrochlore Phase in the  $\text{Bi}_2\text{O}_3\text{-Fe}_2\text{O}_3\text{-WO}_3\text{-(H}_2\text{O)}$  System: its Formation by Hydrothermal-Microwave Synthesis and Optical Properties. *Russian Journal of Inorganic Chemistry*, 2022, **67**(6), P. 820–829.
- [25] Nikolaev A.I., Gerasimova L.G., Maslova M.V., Shchukina E.S. Synthetic analogues of natural titanosilicate mesoporous minerals as potential functional materials. Synthesis and application. *IOP Conference Series: Materials Science and Engineering*, 2019, **704**(1), P. 012003.
- [26] Enikeeva M.O., Kenges K.M., Proskurina O.V., Danilovich D.P., Gusarov V.V. Influence of Hydrothermal Treatment Conditions on the Formation of Lanthanum Orthophosphate Nanoparticles of Monazite Structure. *Russian Journal of Applied Chemistry*, 2020, **93**(4), P. 540–548.
- [27] Khrapova E.K., Kozlov D.A., Krasilin A.A. Hydrothermal Synthesis of Hydrosilicate Nanoscrolls ( $\text{Mg}_{1-x}\text{Co}_x$ ) $_3\text{Si}_2\text{O}_5(\text{OH})_4$  in a  $\text{Na}_2\text{SO}_3$  Solution. *Russian Journal of Inorganic Chemistry*, 2022, **67**(6), P. 839–849.
- [28] Gavryushkin P.N., Thomas V.G., Bolotina N.B., Bakakin V.V., Golovin A.V., Seryotkon Y.V., Fursenko D.A., Litasov K.D. Hydrothermal Synthesis and Structure Solution of  $\text{Na}_2\text{Ca}(\text{CO}_3)_2$ : “Synthetic Analogue” of Mineral Nyerereite. *Crystal Growth & Design*, 2016, **16**(4), P. 1893–1902.
- [29] Thomas V.G., Demin S.P., Foursenko D.A., Bekker T.B. Pulsation processes at hydrothermal crystal growth (beryl as example). *Journal of Crystal Growth*, 1999, **206**(3), P. 203–214.
- [30] Korytkova E.N., Pivovarova, L.N., Drosdova I.A., Gusarov V.V. Hydrothermal synthesis of nanotubular Co-Mg hydrosilicates with the chrysotile structure. *Russian Journal of General Chemistry*, 2007, **77**(10), P. 1669–1676.
- [31] Elovikov D.P., Tomkovich M.V., Levin A.A., Proskurina O.V. Formation of the  $\text{BiAl}_3(\text{PO}_4)_2(\text{OH})_6$  Compound with a Waylandite Structure under Hydrothermal Conditions. *Russian Journal of Inorganic Chemistry*, 2022, **67**(6), P. 850–860.
- [32] Fawcett T.G., Kabekkodu S.N., Blanton J.R., Blanton, T.N. Chemical analysis by diffraction: the Powder Diffraction File. *Powder Diffraction*, 2017, **32**(2), P. 63–71.
- [33] Gražulis S., Merkys A., Vaitkus A. Crystallography Open Database (COD) W., Yip, S. (eds) Handbook of Materials Modeling. Springer, Cham. In: Andreoni, 2020, 1863 p.
- [34] Šesták J. Dynamic Character of Thermal Analysis Where Thermal Inertia Is a Real and Not Negligible Effect Influencing the Evaluation of Non-Isothermal Kinetics: A Review. *Thermo*, 2021, **1**(2), P. 220–231.
- [35] Holba P., Šesták J. Heat inertia and its role in thermal analysis. *Journal of Thermal Analysis and Calorimetry*, 2015, **121**(1), P. 303–307.
- [36] Speranskaya E.I., Skorikov V.M., Safronov G.M., Gaidukov E.N. System  $\text{Al}_2\text{O}_3\text{-Bi}_2\text{O}_3$ . *Inorganic Materials*, 1970, **6**(7), P. 1201–1202.
- [37] Oudich F., David N., Mathieu S., Vilasi M. Phase equilibria investigations and thermodynamic modeling of the system  $\text{Bi}_2\text{O}_3\text{-Al}_2\text{O}_3$ . *Journal of Nuclear Materials*, 2015, **457**, P. 72–79.
- [38] Levin E.M., Roth R.S. Polymorphism of Bismuth Sesquioxide. II. Effect of Oxide Additions on the Polymorphism of  $\text{Bi}_2\text{O}_3$ . *Journal of Research of the National Bureau of Standards. Section A*, 1964, **68**(2), P. 197–206.

---

Submitted 29 August 2022; accepted 17 October 2022

#### Information about the authors:

Dmitry P. Elovikov – Ioffe Institute, 194021 St. Petersburg, Russia; St. Petersburg Electrotechnical University “LETI”, 197022 St. Petersburg, Russia; ORCID 0000-0003-4345-6086; syncdima@mail.ru

Olga V. Proskurina – Ioffe Institute, 194021 St. Petersburg, Russia; St. Petersburg State Institute of Technology, 190013 St. Petersburg, Russia; ORCID 0000-0002-2807-375X; proskurinaov@mail.ru

Maria V. Tomkovich – Ioffe Institute, 194021 St. Petersburg, Russia; ORCID 0000-0002-1537-4107; maria.tom83@gmail.com

Valery L. Ugolkov – I. V. Grebenshchikov Institute of Silicate Chemistry of the Russian Academy of Sciences, 199034 St. Petersburg, Russia; ORCID 0000-0003-2895-0625; ugolkov.52@gmail.com

Victor V. Gusarov – Ioffe Institute, 194021 St. Petersburg, Russia; ORCID 0000-0003-4375-6388; victor.v.gusarov@gmail.com

*Conflict of interest:* the authors declare no conflict of interest.

## Multi-order and structural mechanism of atom nanocluster formation in rhombohedral Cu–Zr-thiospinels

Valeriy M. Talanov<sup>1,a</sup>, Mikhail V. Talanov<sup>2,b</sup><sup>1</sup>Platov South-Russian State Polytechnic University, Rostov region 346428, Russia<sup>2</sup>Southern Federal University, Rostov-on-Don, Russia<sup>a</sup>valtalanov@mail.ru, <sup>b</sup>mvtalanov@gmail.com

Corresponding author: Valeriy M. Talanov, valtalanov@mail.ru

PACS 61.50.Ks, 36.40.-c

**ABSTRACT** A structural mechanism for the formation of nanoclusters and the rhombohedral modification of  $\text{CuZr}_{1.86(1)}\text{S}_4$  has been proposed. Group-theoretical and crystal-chemical methods are used to study the features of the crystal structure and multi-order in Cu–Zr-thiospinel. A multi-order is a structural organization of a material, in the formation of which different degrees of freedom of a crystal participate. It has been proven that the rhombohedral structure of  $\text{CuZr}_{1.86(1)}\text{S}_4$  is formed as a result of displacements and orderings of all types of atoms. It is theoretically shown that the formation of a rhombohedral phase is associated not only with the lattice, but also with the charge and, possibly, orbital degrees of freedom of the crystal. Theory predicts that the rhombohedral phase must be an improper ferroelastic. An important feature of the rhombohedral structure is metal nanoclusters: “bunch” of dimers, trimers, and tetrahedra. Bunch of dimers are an unusual type of self-organization of atoms in rhombohedral spinel-like structures, formed by atoms of two (tetrahedral and octahedral) frustrated crystal sublattices.

**KEYWORDS** order parameter, multi-order, structural mechanism, rhombohedral modification, nanocluster

**ACKNOWLEDGEMENTS** The reported study was funded by Russian Science Foundation (RSF) – research projects No. 22-22-00183, <https://rscf.ru/project/22-22-00183/>

**FOR CITATION** Talanov V.M., Talanov M.V. Multi-order and structural mechanism of atom nanocluster formation in rhombohedral Cu–Zr-thiospinels. *Nanosystems: Phys. Chem. Math.*, 2022, **13** (6), 668–677.

### 1. Introduction

Copper thiospinels with a chemical formula  $\text{CuB}_2\text{S}_4$  (where B is a transition metal) attract much attention because of wide variety of the physical properties. These are superconductivity ( $\text{CuRh}_2\text{S}_4$  [1, 2],  $\text{Cu}_{1-x}\text{Zn}_x\text{Ir}_2\text{S}_4$ ,  $0.25 \leq x \leq 0.8$  [3–5]), pressure-induced superconductor-insulator transition in  $\text{CuRh}_2\text{S}_4$  [6], charge ordering and charge-density waves in  $\text{CuV}_2\text{S}_4$  [7,8], exotic types of orbital ordering (orbital octamers in  $\text{CuIr}_2\text{S}_4$  [9]), large negative magnetoresistance in  $\text{CuCrZrS}_4$  [10], unusual short-range magnetic ordering in  $\text{Cu}_{1/2}\text{In}_{1/2}\text{Cr}_2\text{S}_4$  [11], quantum spin liquid and/or heavy fermion-like states (as assumed in  $\text{CuTi}_2\text{S}_4$  [12]). In many cases, the unique properties are related to a specific structural feature of  $\text{AB}_2\text{X}_4$  spinels: the presence of a three-dimensional network of tetrahedra  $(\text{B}_4)_\infty$  (the so-called pyrochlore sublattice) formed by octahedral B cations (Fig. 1). Such a lattice is an integral part of many crystals belonging to various structural types (pyrochlores, spinels, Laves phases (C15), compounds of the  $\beta$ -alumina family and others). Anderson proved that the pyrochlore lattice causes strong geometrical frustration effects, which are responsible for the unusual physical properties of the crystals [13]. Geometric frustration causes the degeneracy of the ground state of the crystals, which leads to the fact that even a slight external perturbation can affect the properties of matter and, in particular, lead to the formation of exotic phases with unusual properties, nontrivial atomic, charge and orbital ordering. One of the degeneracy removal mechanisms is the formation of metal clusters, called “orbital molecules”, in the form trimers in  $\text{Fe}_3\text{O}_4$  [14], octamers in  $\text{CuIr}_2\text{S}_4$  [9, 15], dimers in  $\text{MgTi}_2\text{O}_4$  [16–18], and metal clusters in many other substances [19–22].

In our previous works [21,23,24], we studied the structural mechanisms of the formation of “orbital molecules” in the crystals using crystal chemical and group-theoretical approaches and showed the involvement of different degrees of freedom (lattice, spins, orbitals, and charges) in the formation of these “molecules”. The emergence of a complex multi-order state is expected in the rhombohedrally distorted spinels with the  $R\bar{3}m$  space group [25,26]. In addition, it is important to note that the  $\text{CuZr}_2\text{O}_4$  compound is a structural analogue of  $\text{CuTi}_2\text{S}_4$  and crystallizes in the spinel type of structure [27]. When  $\text{CuTi}_2\text{S}_4$  prepared in a flux at low temperatures, the rhombohedral form is obtained. In the cubic form the Cu–Ti distances are too large for a significant interaction, while in the rhombohedral form that distance is much shorter and perhaps this interaction plays a role in the stabilization of the rhombohedral phase [28]. The rhombohedral phase of  $\text{CuTi}_2\text{S}_4$

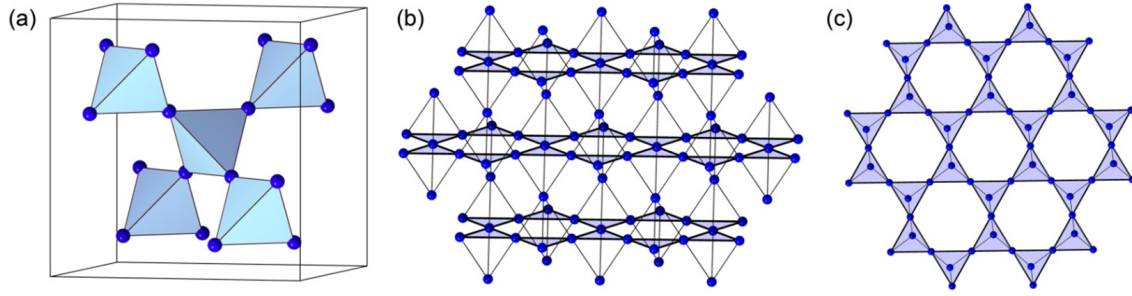


FIG. 1. The pyrochlore B-sublattice of spinels. A three dimensional network of tetrahedra (a), B-spinel sublattice as a stacking of kagome layers (b), view of a plane perpendicular to the [111]-type direction in the spinel (c).

contains various metal clusters [25]. Therefore, we can expect the existence of similar clusters in the rhombohedral phase of  $\text{CuZr}_2\text{O}_4$ . However, the rhombohedral phase in Cu–Zr-thiospinel is obtained only at a nonstoichiometric composition  $\text{CuZr}_{1.86(1)}\text{S}_4$ , in which, as can be assumed by analogy with  $\text{CuTi}_2\text{S}_4$ , Cu–Zr interactions stabilize the existence of a rhombohedral phase with a deficit of zirconium atoms and, consequently, the formation clusters.

In this work, we consider a multi-order and structural mechanism of the formation of metal nanoclusters in known rhombohedral nonstoichiometric thiospinel  $\text{CuZr}_{1.86(1)}\text{S}_4$ .

## 2. Critical and noncritical order parameters

Cubic spinel phase of  $\text{CuZr}_2\text{S}_4$  crystallizes in the  $Fd\bar{3}m$  space group with the unit cell dimension  $a_c = 10.378(3)$  Å (anions located in Wyckoff position  $32e$  with “adjusted” parameter  $x$  equal 0.375) [27]. The rhombohedral modification of the thiospinel with non-stoichiometric composition  $\text{CuZr}_{1.86(1)}\text{S}_4$ , has been synthesized by the reaction of the constituent elements in an alkali metal halide flux and structurally characterized by single crystal X-ray diffraction techniques [28]. The title compound crystallizes in the rhombohedral space group  $R\bar{3}m$  [28]. This compound is isostructural with the rhombohedral modification of  $\text{CuTi}_2\text{S}_4$  (only the Zr(2) site has partial occupancy [28]). By using the concept of the critical irreducible representation (irrep), we establish the structure mechanism of a rhombohedral phase formation from the high symmetry cubic phase (parent phase). The first Brillouin zone of a face-centred cubic lattice contains four points of high symmetry, namely:  $\mathbf{k}_{11}(\Gamma)$ ,  $\mathbf{k}_{10}(X)$ ,  $\mathbf{k}_9(L)$  and  $\mathbf{k}_8(W)$  [29]. For these points there are stars of the following wavevectors:

$$\mathbf{k}_{11} = 0; \quad \mathbf{k}_{10} = \frac{1}{2}(b_1 + b_2); \quad \mathbf{k}_9 = \frac{1}{2}(b_1 + b_2 + b_3); \quad \mathbf{k}_8 = \frac{b_1}{4} - \frac{b_2}{4} + \frac{b_3}{2}.$$

Using the results of a group-theoretical analysis, we find that the phases with a space group  $R\bar{3}m$  can be generated by three-dimensional irrep  $\mathbf{k}_{11}(\tau_7) (\Gamma_5^+)^1 (1)$ , as well as six-dimensional irreps  $\mathbf{k}_{10}(\tau_1)(X_3) (4)$  and  $\mathbf{k}_{10}(\tau_3) (X_1) (4)$ , four-dimensional irreps  $\mathbf{k}_9(\tau_1) (L_1^+) (8, 2)$  and  $\mathbf{k}_9(\tau_4) (L_2^-) (8, 2)$ . The expression  $\mathbf{k}_j(\tau_i)$  means the star of wave vectors  $\mathbf{k}_j$ ,  $i$  – number corresponding irrep  $\tau$  for given star  $\mathbf{j}$  (according to [29]). The multiplication in the primitive cell volumes as a result of the  $Fd\bar{3}m \rightarrow R\bar{3}m$  phase transitions is shown in parentheses.

The results of the group-theoretical analysis show that the calculated distribution of the atoms on Wyckoff positions of the  $R\bar{3}m$ -phase is consistent with the experimental data [28] only in the case of phase generated by irrep  $\mathbf{k}_9(\tau_4) (L_2^-)$ . In Table 1 space groups of all possible low-symmetry phases, induced by irrep  $\mathbf{k}_9(\tau_4) (L_2^-)$ , and corresponding components of four-dimensional order parameter are given. A similar table was given earlier in the [25], but in this paper we supplemented it with secondary order parameters, which allow us to discuss the concept of multi-order on the rhombohedrally distorted spinel structure. Besides the change of primitive cell volumes as a result of the structural phase transitions ( $V/V_0$ ), vectors of the primitive cell translations ( $\mathbf{a1}$ ,  $\mathbf{a2}$ ,  $\mathbf{a3}$ ), structure formulas of low-symmetry phases are presented. The superscript index in the structural formula means the type of Wyckoff position according to International Tables for Crystallography [30]. Superscript on the brackets means the number of repetition of Wyckoff position in the structural formula.

<sup>1</sup>In parentheses, the notations are given for irreducible representations in accordance with Miller–Love.

Table 1: Low-symmetry crystal phases induced by irrep  $\mathbf{k}_9(\tau_4)$  ( $L_2^-$ ) of space group  $Fd\bar{3}m$ 

No	Critical OP	Noncritical OPs	Space group	$\frac{V}{V_0}$	Translations of primitive cell of spinel structure	Structural formula
1	(00 $\eta\eta$ )	$\Gamma_3^+(a, \sqrt{3}a)$ , $\Gamma_5^+(0, a, 0)$ , $L_3^-(0, 0; 0, 0; a, \frac{\sqrt{3}}{3}a; a, \frac{\sqrt{3}}{3}a)$ , $X_1(0, 0; a, 0; 0, 0)$	$Cmcm$ (No 63)	4	$2a_2 + 2a_3 - 2a_1$ , $2a_3 + 2a_1 - 2a_2$ , $2a_1 + 2a_2 - 2a_3$	$(A^c)^2 A_2^g$ $(B_2^g)^2 B_2^f B_2^c$ $(X_2^g)^4 (X_2^f)^2 X^h$
2	( $\eta\eta\eta\eta$ )	$\Gamma_2^-(a)$ , $L_1^+(a; a; a; a)$ , $X_1(a, a; a, a; a, a)$	$F\bar{4}3m$ (No 216)	8	$2a_2 + 2a_3 - 2a_1$ , $2a_3 + 2a_1 - 2a_2$ , $2a_1 + 2a_2 - 2a_3$	$A^a (A_4^e)^2 A_6^g A^b$ $(B_4^e)^2 (B_{12}^h)^2$ $(X_4^e)^4 (X_{12}^h)^4$
3	(00 $\eta$ )	$\Gamma_5^+(a, a, a)$	$R\bar{3}m$ (No 166)	2	$a_2 - a_1$ , $a_1$ , $2a_1 + 2a_2 + 2a_3$	$(A_{1/2}^c)^2$ $B_{1/4}^a B_{1/4}^b B_{3/2}^h$ $(X_{1/2}^c)^2 (X_{3/2}^h)^2$
4	( $\eta\eta\eta$ )	$\Gamma_5^+(a, a, a)$ , $L_1^+(a; 0; 0; 0)$ , $L_3^-(0, 0; a, \frac{\sqrt{3}}{3}a; -a, \frac{\sqrt{3}}{3}a$ ; $0, -\frac{2\sqrt{3}}{3}a)$ , $X_1(a, 0; a, 0; a, 0)$ , $X_3(a, -a; a, -a; a, -a)$	$R\bar{3}m$ (No 166)	8	$2a_3$ , $-2a_2$ , $6a_2 - 2a_1 - 2a_3$	$(A_{1/8}^c)^2 (A_{3/8}^h)^2$ $(B_{3/8}^h)^3 B_{1/8}^c$ $B_{3/8}^g B_{3/8}^f$ $(X_{3/8}^h)^6 X_{1/8}^c$ $X_{3/8}^c (X_{6/8}^i)^2$
5	( $\eta_1\eta_1\eta_2$ )	$\Gamma_3^+(a, 0)$ , $\Gamma_4^+(a, -a, 0)$ , $\Gamma_5^+(a, b, b)$ , $L_1^+(a; 0; 0; 0)$ , $L_3^+(a, 0; 0, 0; 0, 0; 0, 0)$ , $L_1^-(0; a; -a; 0)$ , $L_3^-(0, 0; a, b; -a, b; 0, c)$ , $X_1(a, 0; a, 0; b, 0)$ , $X_2(a, 0; -a, 0; 0, 0)$ , $X_3(a, -a; a, -a; b, -b)$ , $X_4(a, -a; -a, a; 0, 0)$	$C2/m$ (No 12)	8	$4a_2 - 2a_3$ , $2a_3$ , $2a_1 - 2a_2$	$(A_{1/8}^i)^4 (A_{2/8}^j)^2$ $(B_{2/8}^j)^4 (B_{1/8}^i)^4$ $B_{1/8}^h B_{1/8}^g$ $(X_{2/8}^j)^{12} (X_{1/8}^i)^8$
6	( $\eta_1\eta_2\eta_2\eta_2$ )	$\Gamma_5^+(a, a, a)$ , $\Gamma_2^-(a)$ , $\Gamma_4^-(a, a, a)$ , $L_1^+(a; b; b; b)$ , $L_3^+(0, 0; a, -\sqrt{3}a; a, \sqrt{3}a; -2a, 0)$ , $L_3^-(0, 0; a, \frac{\sqrt{3}}{3}a; -a, \frac{\sqrt{3}}{3}a; 0$ ; $-\frac{2\sqrt{3}}{3}a)$ , $X_1(a, b; a, b; a, b)$ , $X_4(a, a; a, a; a, a)$ , $X_3(a, -a; a, -a; a, -a)$	$R\bar{3}m$ (No 160)	8	$2a_1$ , $2a_1 - 2a_3$ , $6a_2 - 2a_1 - 2a_3$	$(A_{1/16}^a)^4 (A_{3/16}^b)^4$ $(B_{3/16}^b)^6 (B_{1/16}^a)^2$ $(B_{6/16}^c)^2$ $(X_{3/16}^b)^{12} (X_{1/16}^a)^4$ $(X_{6/16}^c)^4$

7	$(\eta_1\eta_1\eta_2\eta_2)$	$\Gamma_3^+(a, \sqrt{3}a),$ $\Gamma_5^+(0, a, 0),$ $\Gamma_2^-(a),$ $\Gamma_3^-(a, \sqrt{3}a),$ $\Gamma_4^-(a, 0, 0),$ $L_1^+(a; a; b; b),$ $L_3^+(a, -\sqrt{3}a; a, -\sqrt{3}a; b, -\sqrt{3}b;$ $b, -\sqrt{3}b),$ $L_3^-(a, \frac{\sqrt{3}}{3}a; a, \frac{\sqrt{3}}{3}a; b, \frac{\sqrt{3}}{3}b;$ $b, \frac{\sqrt{3}}{3}b),$ $X_1(a, a; b, c; a, a),$ $X_2(a, a; 0, 0; -a, -a),$ $X_3(a, 0; 0, 0; 0, -a),$ $X_4(0, a; 0, 0; a, 0)$	<i>Imm2</i> (No 44)	8	$2a_3,$ $2a_1 - 2a_2,$ $2a_1 + 2a_2 - 2a_3$	$(A_{1/16}^a)^2(A_{2/16}^c)^2A_{4/16}^e$ $(A_{2/16}^d)^2(A_{1/16}^b)^2$ $(B_{2/16}^c)^4(B_{2/16}^d)^4$ $(B_{4/16}^e)^4$ $(X_{2/16}^c)^8(X_{2/16}^d)^8$ $(X_{4/16}^e)^8$
8	$(0\eta_1\eta_2)$	$\Gamma_3^+(a, \sqrt{3}a),$ $\Gamma_4^+(0, a, a),$ $\Gamma_5^+(a, b, -a),$ $L_3^-(0, 0; 0, 0; a, \frac{\sqrt{3}}{3}a; b, \frac{\sqrt{3}}{3}b),$ $X_1(0, 0; a, 0; 0, 0),$ $X_4(0, 0; a, -a; 0, 0)$	<i>C2<sub>1/m</sub></i> (No 11)	4	$a_1 + a_2,$ $a_2 - a_1,$ $2a_3 - a_1 - a_2$	$(A_{1/4}^e)^4(B_{1/4}^e)^4$ $(B_{2/4}^f)^2$ $(X_{1/4}^e)^8(X_{2/4}^f)^4$
9	$(\eta_1\eta_2\eta_2\eta_3)$	$\Gamma_3^+(a, 0),$ $\Gamma_4^+(a, -a, 0),$ $\Gamma_5^+(a, b, b),$ $\Gamma_2^-(a),$ $\Gamma_3^-(a, 0),$ $\Gamma_4^-(a, a, b),$ $\Gamma_5^-(0, a, -a),$ $L_1^+(a; b; b; c),$ $L_2^+(0; a; -a; 0),$ $L_3^+(a, 0; b, c; b, -c; d, 0),$ $L_1^-(0; a; -a; 0),$ $L_3^-(0, a; b, c; -b, c; 0, d),$ $X_1(a, b; a, b; c, d),$ $X_2(a, b; -a, -b; 0, 0),$ $X_3(a, b; -b, -a; c, -c),$ $X_4(a, b; b, a; c, c)$	<i>Cm</i> (No 8)	8	$4a_2 - 2a_3,$ $2a_3,$ $2a_1 - 2a_2$	$(A_{1/16}^a)^8(A_{2/16}^b)^4$ $(B_{2/16}^b)^{12}(B_{1/16}^a)^8$ $(X_{2/16}^b)^{24}(X_{1/16}^a)^{16}$
10	$(\eta_1\eta_2\eta_3)$	$\Gamma_2^+(a),$ $\Gamma_3^+(a, b),$ $\Gamma_4^+(a, b, c),$ $\Gamma_5^+(a, b, c),$ $L_1^+(a; 0; 0; 0),$ $L_2^+(a; 0; 0; 0),$ $L_3^+(a, b; 0, 0; 0, 0; 0, 0),$ $L_1^-(0; a; b; c),$ $L_3^-(0, 0; a, b; c, d; e, f),$ $X_1(a, 0; b, 0; c, 0),$ $X_2(a, 0; b, 0; c, 0),$ $X_3(a, -a; b, -b; c, -c),$ $X_4(a, -a; b, -b; c, -c)$	<i>Pi</i> (No 2)	8	$2a_1,$ $2a_2,$ $2a_3$	$(A_{1/8}^i)^8$ $(B_{1/8}^i)^{16}$ $(X_{1/8}^i)^{32}$

11	$(\eta_1\eta_2\eta_3\eta_4)$	$\Gamma_2^+(a),$ $\Gamma_3^+(a, b),$ $\Gamma_4^+(a, b, c),$ $\Gamma_5^+(a, b, c),$ $\Gamma_1^-(a),$ $\Gamma_2^-(a),$ $\Gamma_3^-(a, b),$ $\Gamma_4^-(a, b, c),$ $\Gamma_5^-(a, b, c),$ $L_1^+(a; b; c; d),$ $L_2^+(a; b; c; d),$ $L_3^+(a, b; c, d; e, f; g, h),$ $L_1^-(a; b; c; d),$ $L_3^-(a, b; c, d; e, f; g, h),$ $X_1(a, b; c, d; e, f),$ $X_2(a, b; c, d; e, f),$ $X_3(a, b; c, d; e, f),$ $X_4(a, b; c, d; e, f)$	$P1$ (No 1)	8	$2a_1,$ $2a_2,$ $2a_3$	$(A_{1/16}^a)^{16}$ $(B_{1/16}^a)^{32}$ $(X_{1/16}^a)^{64}$
----	------------------------------	---	----------------	---	------------------------------	---

Note.  $V/V_0$  is the change in the primitive cell volume as a result of the structural phase transition. The superscript index in the structural formula means the type of Wyckoff position according to International Tables for Crystallography. The superscript on the brackets is the repetition number of the position.

### 3. Multi-order and structural mechanism formation of the rhombohedral modification

The structural mechanism for the formation of low-symmetry modifications of crystals is determined by interaction of all freedom degrees of a crystal, including lattice, charge, orbital and spin. The A-atoms occupy Wyckoff position  $8a$  (site symmetry  $\bar{3}m$ ), B-Wyckoff position  $16d$  (site symmetry  $\bar{4}3m$ ), X-Wyckoff position  $32e$  (site symmetry  $3m$ ) in the cubic  $Fd\bar{3}m$ -phase of normal spinel. Therefore structural formula of cubic spinel  $AB_2X_4$  is  $(A)^{8a}[B_2]^{16d}X_4^{32e}$  or applied to  $CuZr_{1.86(1)}S_4$  it is  $(Cu)^{8a}[Zr_{1.86(1)}]^{16d}S_4^{32e}$ . As a result of a hypothetical structural phase transition, the Wyckoff positions split. To find the splitting of the Wyckoff positions and calculate the structure of the rhombohedral phase, it is necessary to establish whether the critical irrep is included in the permutation, mechanical, magnetic and orbital representations of the spinel structure, as well as to elucidate the role of noncritical order parameters in the formation of a low-symmetry structure [24, 31–33].

The critical four dimensional irrep  $\mathbf{k}_9(\tau_4)$  ( $L_2^-$ ) enters into the mechanical representation and permutation representation of the spinel structure on Wyckoff positions  $8a$ ,  $16d$  and  $32e$  [24, 31–33], as well as in the  $e_g$ - and  $t_{2g}$ -orbital representations on Wyckoff position  $8a$  and  $16d$ . This means that the formation of a low-symmetry phase occurs according to a complex mechanism, including displacements of tetrahedral and octahedral cations, anions and as well as also ordering of all atom types. In addition, the formation of a rhombohedral phase can be accompanied by a charge and orbital ordering of tetrahedral and octahedral cations.

Group-theoretical analysis showed that the formation of the rhombohedral phase is accompanied by the following types of atom ordering:

- binary tetrahedral cation ordering (order type 1:1);
- ternary octahedral cation ordering (order type 1:1:6);
- quarternary anion ordering (order type 1:1:3:3).

As a result, the theoretical structural formula of a low-symmetry rhombohedral  $R\bar{3}m$ -spinel modification should be  $A_{1/2}^{2c}A_{1/2}^{2c}B_{1/4}^{1a}B_{1/4}^{1b}B_{3/2}^{6h}X_{1/2}^{2c}X_{1/2}^{2c}X_{3/2}^{6h}X_{3/2}^{6h}$  (the rhombohedral presentation) or  $A_{1/2}^{6c}A_{1/2}^{6c}B_{1/4}^{3a}B_{1/4}^{3b}B_{3/2}^{18h}X_{1/2}^{6c}X_{1/2}^{6c}X_{3/2}^{18h}X_{3/2}^{18h}$  (the hexahedral presentation). Attached to  $CuZr_{1.86(1)}S_4$  the latest structural formula is  $Cu(1)_{1/2}^{6c}Cu(2)_{1/2}^{6c}Zr(1)_{1/4}^{3a}Zr(2)_{1/4}^{3b}Zr(3)_{3/2}^{18h}S(1)_{1/2}^{6c}S(2)_{1/2}^{6c}S(3)_{3/2}^{18h}S(4)_{3/2}^{18h}$ . The derived theoretical structural formula exactly agrees with the experimental data [28]. It follows from the structural formula that in the structure of  $CuZr_{1.86(1)}S_4$  there are two structurally different copper atoms, three zirconium atoms, and four sulfur atoms. The structural difference between atoms of the same element can be associated with differences in charges, orientation and filling of orbitals with electrons, as well as other electronic characteristics of atoms. In particular, in  $CuZr_{1.86(1)}S_4$ , ordering of charges is possible, because copper, zirconium, sulfur atoms occupy some different Wyckoff positions in the rhombohedral spinel modification.

This theoretical result in principle agrees with the calculations [28]. The oxidation state of Cu atoms in the title compound is assigned +1, consistent with the Cu–S bond distances and the density of states. The calculated Madelung potentials and sums of bond valences show some difference for the three Zr positions, but this difference is not large, as

might be expected for the oxidation states of zirconium atoms with formal charges of 4+ and 3+ [27]. Charge distribution should be  $(\text{Cu}^+)_4\text{Zr}(1)^{4+}\text{Zr}(2)^{3+}\text{Zr}(3)_6^{3.5+}(\text{S}^{2-})_{16}$  according to the crystal bond lengths analysis and electronic structure calculations [28]. Our calculation predicts that copper atoms should differ from each other in physical characteristics, and possibly also in charges. Since the exact charges of metallic atoms are not known, we note that our calculations point to the fundamental possibility of orbital ordering in the formation of Zr(3)–Zr(3) bonds. The group-theoretical analysis predicted that at the formation of low-symmetric ordered  $R\bar{3}m$ -phase does not involve the rotations and tilts of tetrahedra and octahedra [31]. An important result of theoretical calculations is the prediction of the improper ferroelasticity of the rhombohedral phase, since the components of the secondary order parameter  $(\xi, \xi, \xi)$  induced by  $\mathbf{k}_{11}(\tau_7)$  ( $\Gamma_5^+$ ) (Table 1) are proportional to the shear components  $u_{xy}, u_{xz}, u_{yz}$  of the strain tensor  $u_{ij}$  [34]. Thus, the multi-order in the rhombohedral phase of  $\text{CuZr}_{1.86(1)}\text{S}_4$  is related to the lattice, charge, and possibly orbital degrees of freedom of the crystal. This multi-order causes the possibility of an improper ferroelasticity in the title compound.

Group-theoretical methods allow us to make an approximate estimate of free atomic parameters and atomic coordinates in the rhombohedral spinel modification [35, 36]. We emphasize that it is impossible to find the exact values of free atom parameters (“gliding” parameters) within the framework of the group-theoretical methods. For  $\text{CuZr}_{1.86(1)}\text{S}_4$  using the ISOTROPY program we get the formula for approximate estimate of the coordinates of atoms:  $\text{Cu}(1)^{6c}$  ( $z' = 5/16$ ),  $\text{Cu}(2)^{6c}$  ( $z' = 3/16$ ),  $\text{Zr}(1)^{3a}$ ,  $\text{Zr}(2)^{3b}$ ,  $\text{Zr}(3)^{18h}$  ( $x' = 1/6, z' = 7/12$ ),  $\text{S}^{18h}$  ( $x' = -1/6 - 4/3x, z' = 1/6 - 1/6x$ ),  $\text{S}^{18h}$  ( $x' = 1/6 - 4/3x, z' = 1/3 - 1/6x$ ),  $\text{S}^{6c}$  ( $z' = 1/4 - 1/2x$ ),  $\text{S}^{6c}$  ( $z' = 1/4 + 1/2x$ ). The superscript index in this formula are the atom coordinates in agreement with International Tables for Crystallography; the values of  $x'$  and  $z'$  are the values of the adjusted parameters of the corresponding Wyckoff positions,  $x$  – theory parameter for the given Wyckoff position. Note that for some positions of atoms, good agreement is obtained between the theoretical and experimental coordinates of atoms (Cu(1), Cu(2), Zr(1), Zr(2)), and for some atoms (for example, Zr(3)) the resulted theoretical and experimental data do not agree. The quantitative discrepancy between the theoretical and experimental coordinates of some atoms can appear due to several reasons. We note only three of them related to the title compounds.

- (1) *Sample metastability.* In metastable structures, atoms (all atoms or only a part of them) have coordinates that differ from the coordinates of atoms in thermodynamically stable structures. The possible metastability of  $\text{CuZr}_{1.86(1)}\text{S}_4$  is indicated by the fact that the crystal structure of the title compound critically depends on the technology of its manufacturing.
- (2) *Partial atomic occupancy of Wyckoff positions.* The group-theoretical calculations do not take into account the partial occupation of the corresponding Wyckoff positions by some atoms (in the case of  $\text{CuZr}_{1.86(1)}\text{S}_4$ , Zr(2) atoms partially occupy the 3b Wyckoff position [28]).
- (3) *The role of noncritical representations in low-symmetry structure formation.* A critical irrep completely defines the symmetry of the low-symmetry phase in vicinity transition point  $T_c$ . The role of noncritical degrees of freedom near the phase transition temperature is insignificant. Far from the  $T_c$ , the contribution of noncritical degrees of freedom to the formation of a low-symmetry structure can become significant [35]. And therefore, taking into account these degrees of freedom is necessary for an adequate representation of the calculated structure. A method for finding noncritical atomic displacements and noncritical orderings was proposed in [33]. According to Landau theory of phase transition the components of the critical and noncritical (secondary) order parameters are proportional to  $|T - T_c|^{1/2}$  and  $|T - T_c|^{n/2}$  respectively. Here  $n$  is the least direct symmetrized power of the critical irrep, which contains the noncritical irrep. The second direct symmetrized power of the critical irrep  $\mathbf{k}_9(\tau_4)$  ( $L_2^-$ ) ( $n = 2$ ) contains the noncritical irrep  $\mathbf{k}_{11}(\tau_7)$  ( $\Gamma_5^+$ ). Our group-theoretical calculation shows that in case of the  $\text{CuZr}_{1.86(1)}\text{S}_4$ , noncritical (secondary) order parameter  $(\xi, \xi, \xi)$  generated by  $\mathbf{k}_{11}(\tau_7)$  ( $\Gamma_5^+$ ) must play an important role in the structure formation. The critical irrep  $\mathbf{k}_{11}(\tau_7)$  ( $\Gamma_5^+$ ) is included in the mechanical representation constructed for the 8a and 32e sites of the parent spinel structure and the permutation representation constructed for the 16d and 32e sites. This means that the structure of the low-symmetry ordered  $R\bar{3}m$ -phase is formed as a result of the additional displacements of Cu and S atoms and additional ordering of Zr cations and S anions (in both cases the type of order is 1:3). Our theory predicts a linear dependence of  $|T - T_c|$  on the Cu and S atoms displacements and weak superstructure reflexes, corresponding to 1:3 ordering of the Zr cations and 1:3 ordering of the S anions. All three of the above factors have a significant impact on the formation of the  $\text{CuZr}_{1.86(1)}\text{S}_4$  rhombohedral structure.

#### 4. Results of crystal-chemical design and general discussion

One peculiar feature of the  $\text{CuZr}_{1.86(1)}\text{S}_4$  rhombohedral structure is metal clustering. In contrast to the  $\text{AlV}_2\text{O}_4$  rhombohedral structure, in which the formation of heptamers [20] (or trimers [21]) occurs by vanadium atoms ordering, located in octahedral sites of the initial cubic spinel, in the formation of metal clusters in  $\text{CuZr}_{1.86(1)}\text{S}_4$  rhombohedral structure not only the octahedral zirconium atoms but also tetrahedral atoms of copper takes part (Figs. 2, 3).

Atoms of Cu(2) and Zr(3) form “bunch” of dimers (Fig. 3). Each “bunch” consists of three [Cu(2)–Zr(3)]-dimers which are joined by common Cu(2)-atom. Each Cu(2) atom is surrounded by three Zr(3) atoms, resulting in three Cu(2)–Zr(3) interatomic distances of 2.937 Å. The shortest Cu–Zr distance in cubic spinel is much longer and equals 4.304 Å.

This distance is too large for a significant interaction, while Cu(2)–Zr(3) interatomic distance in the rhombohedral form of  $\text{CuZr}_{1.86(1)}\text{S}_4$  is the shortest among all the bond lengths of the metal-metal. Note that Zr(1)- and Zr(3)-atoms also form [Zr(1)–Zr(3)]-dimers, but with a much larger interatomic distance 3.787 Å (on Fig. 4 they are shown blue). Thus, the “bunches” of [Cu(2)–Zr(3)]-dimers are the smallest size metal clusters.

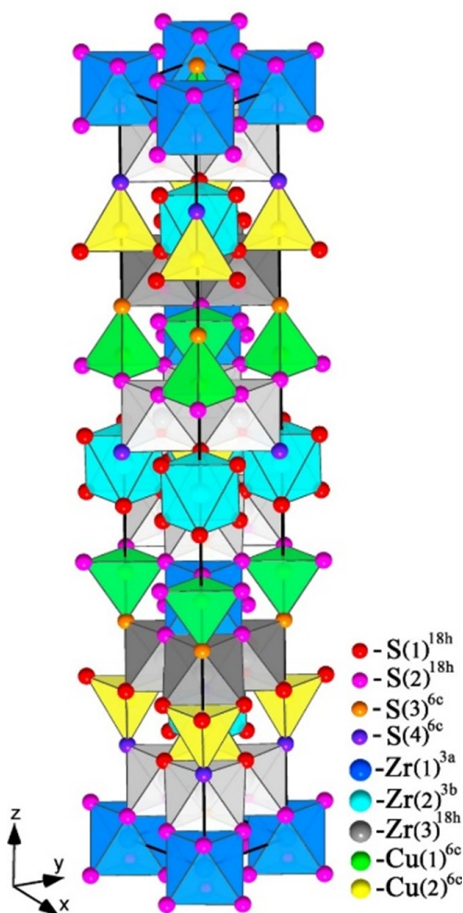


FIG. 2. Low-symmetry ordered  $R\bar{3}m$ -structure of  $\text{CuZr}_{1.86(1)}\text{S}_4$ . Polyhedral presentation in the form of  $\text{Cu}(2)[\text{S}(3)_3\text{S}(2)]$  (yellow) and  $\text{Cu}(1)[\text{S}(4)_3\text{S}(1)]$  (green) tetrahedra and  $\text{Zr}(1)[\text{S}(3)_6]$  (dark blue),  $\text{Zr}(2)[\text{S}(4)_6]$  (blue),  $\text{Zr}(3)[\text{S}(1)\text{S}(2)\text{S}(3)_2\text{S}(4)_2]$  (gray) octahedral is presented.

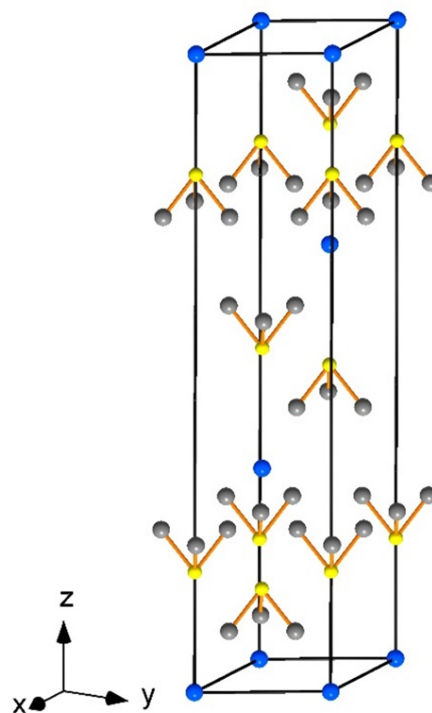


FIG. 3. “Bunch” of [Cu(2)–Zr(3)]-dimers

On the kagome lattice, there are two kinds of Zr(3)–Zr(3) bonds (zirconium dimers  $[\text{Zr}(3)_2]$ ) with different bond lengths: the shorter (black) is 3.579 Å and the longer (dark blue) is 3.773 Å (Fig. 4). These dimers alternate in the kagome lattice (Fig. 4). It is interesting to note, that distance Zr–Zr in the cubic form of  $\text{CuZr}_{1.86(1)}\text{S}_4$  is equal to 3.670 Å. Zr(3)-atoms, belonging to the “bunch”, form two types of  $[\text{Zr}(3)_3]$ -trimers with interatomic distances  $\text{Zr}(3)\text{–Zr}(3) = 3.579$  Å and  $\text{Zr}(3)\text{–Zr}(3) = 3.773$  Å (Fig. 4). Alternating  $[\text{Zr}(3)_3]$ -trimers, having short and long interatomic distances  $\text{Zr}(3)\text{–Zr}(3)$ , form a kagome layer (Fig. 4). These trimers are at the basis of four types of tetrahedra. Each trimer, formed by bonds  $\text{Zr}(3)\text{–Zr}(3)$ , is the basis for the metal  $[\text{Cu}(2)\text{Zr}(3)_3]$ -tetrahedra and  $[\text{Cu}(1)\text{Zr}(3)_3]$ -tetrahedra with S(3)-atoms in the centre (Fig. 4). Each trimer, formed by more longer bonds  $\text{Zr}(3)\text{–Zr}(3)$ , is the basis for the metal  $[\text{Zr}(1)\text{Zr}(3)_3]$ -tetrahedra and  $[\text{Cu}(2)\text{Zr}(3)_3]$ -tetrahedra with S(4)-atoms in the centre (Fig. 4).

There are two different types of kagome-layers binding in the structure of title compound  $\text{CuZr}_{1.86(1)}\text{S}_4$ . The first type of binding between the displaced kagome-layers relative to each other is realized by means of metal clusters – heptamers  $[\text{Zr}(1)\text{Zr}(3)_6]$  (Fig. 4). The second type of binding kagome-layers is realized between the undisplaced kagome-layers relative to each other by means of  $[\text{Cu}(2)\text{Zr}(3)_3]$ -tetrahedra and S(4) $[\text{Cu}(2)\text{Zr}(3)_3]$ -tetrahedra with S(4)-atoms in the centre (Fig. 5).

Displaced and undisplaced kagome layers alternate with each other in the structure of  $\text{CuZr}_{1.86(1)}\text{S}_4$  rhombohedral spinel modification. Note that there is only one type of kagome-layers binding in the structure of the parent (cubic spinel) phase (Fig. 1). In the rhombohedral structure of  $\text{CuZr}_{1.86(1)}\text{S}_4$ , it is possible to distinguish Zr(1)-heptamers, which are

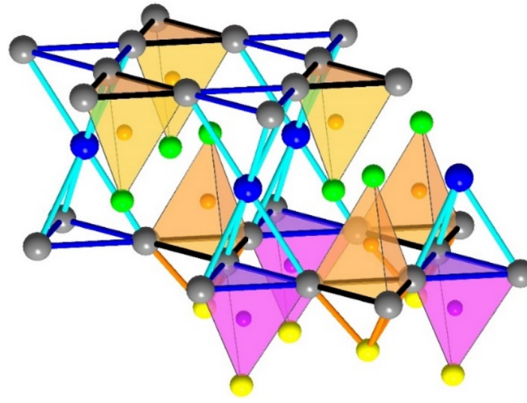


FIG. 4. Two types of  $[\text{Zr}(3)_2]$ -dimers (dark blue and black) and  $[\text{Zr}(3)_3]$ -trimers,  $[\text{Cu}(2)\text{Zr}(3)_3]$ - and  $[\text{Zr}(1)\text{Zr}(3)_3]$ -tetrahedral metal clusters,  $\text{S}(3)[\text{Cu}(1)\text{Zr}(3)_3]$ - (light brown) and  $\text{S}(4)[\text{Cu}(2)\text{Zr}(3)_3]$ - (pink) tetrahedral clusters are shown

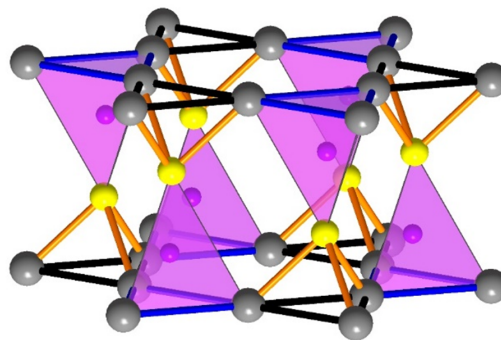


FIG. 5. Binding between kagome-layers with the help  $\text{S}(4)[\text{Cu}(2)\text{Zr}(3)_3]$ -tetrahedra

analogs of V-heptamers in the structure of  $\text{AlV}_2\text{O}_4$  [20]. Here, all the  $\text{Zr}(1)$  atoms are sandwiched by two  $[\text{Zr}(3)_3]$ -trimers (Fig. 4), but none of the  $\text{Zr}(2)$  atoms are sandwiched by two  $[\text{Zr}(1)_3]$ -trimers.  $\text{Zr}(2)$  atoms are sandwiched by two  $[\text{S}(1)_3]$ -trimers, forming heptamer  $[\text{Zr}(2)\text{S}(1)_6]$  (Fig. 6).

In this heptamer, the interatomic distances  $\text{S}(1)\text{--}\text{S}(1)$  and  $\text{Zr}(2)\text{--}\text{S}(1)$  are 3.570 and 2.583 Å, respectively. This formula means that the  $\text{Zr}(1)^{4+}$  ion has no  $t_{2g}$  orbitals, i.e. there are no chemical bonding between  $\text{Zr}(1)$ - and  $\text{Zr}(3)$ -atoms. Therefore, the formation of Zr-heptamers is improbable. Besides the calculated densities of states of rhombohedral modification show that  $\text{Cu}(1)\text{--}\text{Zr}(3)$  and  $\text{Zr}(3)\text{--}\text{Zr}(3)$  interactions in “bunch” of dimers and  $[\text{Zr}(3)_3]$ -trimers (with interatomic distances  $\text{Zr}(3)\text{--}\text{Zr}(3)$  3.579 Å) have bonding character [28].

The nonstoichiometry of Zr deficient rhombohedrally distorted spinel related compound,  $\text{CuZr}_{1.86(1)}\text{S}_4$ , has no effect on the calculated structural formula and, consequently, on the structural motif of the rhombohedral phase (Figs. 2, 3). Nonstoichiometry leads to the fact that a part of the Wyckoff positions occupied by zirconium atoms in the rhombohedral

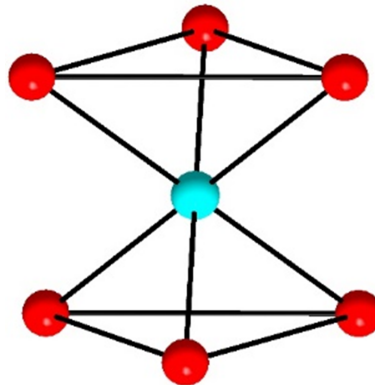


FIG. 6. The  $[\text{Zr}(2)\text{S}(1)_6]$ -heptamer

phase are vacant. This means that in a nonstoichiometric compound, the number of Zr-containing nanoclusters will decrease compared to the idealized stoichiometric structure, but their types will remain unchanged.

## 5. Conclusions

The main result of the study is the establishing of multi-order in the  $\text{CuZr}_{1.86(1)}\text{S}_4$  rhombohedral structure which associate with the nanocluster formation (dimers, trimers, and a unique type of clusters – “bunch” of dimers) according to a complex mechanism, including ordering and displacement of all atoms, charge ordering, and, possibly, orbital ordering in the  $[\text{Zr}(3)]_3$ -trimers. The group-theoretical analysis made it possible to predict the possible improper ferroelasticity of  $\text{CuZr}_{1.86(1)}\text{S}_4$  rhombohedral phase. It is also important to note that only two substances are known among all spinels, namely,  $\text{CuTi}_2\text{S}_4$  [25] and  $\text{CuZr}_{1.86(1)}\text{S}_4$ , which form metal cluster “bunch” of dimers whose atoms are simultaneously part of two frustrating sublattices<sup>2</sup> of the crystal structure (metal clusters in all known materials with a pyrochlore sublattice formed by atoms of only one geometrically frustrating sublattice). Therefore, “bunch” of  $[\text{Cu}(1)\text{--Zr}(3)]$ -dimers, which are metallic “molecules”, represent a new type of self-organization of atoms in crystals. This means that it is possible to rationally design new materials with unusual physical properties based on  $R\bar{3}m$  ordered spinels. Further studies of the physical properties of solid solutions based on  $R\bar{3}m$  ordered spinels, as well as their study under pressure, may lead to the discovery of their unusual physical properties.

## References

- [1] Bitoh T., Hagino T., et al. Superconductivity in Thiospinel  $\text{CuRh}_2\text{S}_4$ . *J. Phys. Soc. Jpn.*, 1992, **61** (8), P. 3011–3012.
- [2] Hagino T., Seki Y., et al. Superconductivity in spinel-type compounds  $\text{CuRh}_2\text{S}_4$  and  $\text{CuRh}_2\text{Se}_4$ . *Phys. Rev. B*, 1995, **51** (18), P. 12673–12684.
- [3] Suzuki H., Furubayashi T., et al. Metal-Insulator Transition and Superconductivity in Spinel-Type System  $\text{Cu}_{1-x}\text{Zn}_x\text{Ir}_2\text{S}_4$ . *J. Phys. Soc. Jpn.*, 1999, **68**, P. 2495–2497.
- [4] Cao G., Kitazawa H., et al. Superconductivity in Zn-doped  $\text{CuIr}_2\text{S}_4$ . *Physica C: Superconductivity*, 2000, **341–348**, P. 735–736.
- [5] Cao G., Furubayashi T., et al. Suppression of metal-to-insulator transition and appearance of superconductivity in  $\text{Cu}_{1-x}\text{Zn}_x\text{Ir}_2\text{S}_4$ . *Phys. Rev. B*, 2001, **64**, 214514.
- [6] Ito M., Hori J., et al. Pressure-Induced Superconductor-Insulator Transition in the Spinel Compound  $\text{CuRh}_2\text{S}_4$ . *Phys. Rev. Lett.*, 2003, **91**, 077001.
- [7] Sekine T., Uchinokura K., et al. Electrical and thermal properties in  $\text{CuV}_2\text{S}_4$ . *Solid State Commun.*, 1984, **51**, P. 187–189.
- [8] Mahy J., Colatis D., Van Dyck D., Amelinck S. Electron diffraction evidence for domain structures in the low-temperature incommensurate phase in  $\text{CuV}_2\text{S}_4$ . *J. Solid State Chem.*, 1987, **68**, P. 320–329.
- [9] Radaelli P.G., Horibe Y., et al. Formation of isomorphous  $\text{Ir}^{3+}$  and  $\text{Ir}^{4+}$  octamers and spin dimerization in the spinel  $\text{CuIr}_2\text{S}_4$ . *Nature*, 2002, **416**, P. 155–158.
- [10] Furubayashi T., Suzuki H., Kobayashi N., Nagata S. Large negative magnetoresistance in thiospinel  $\text{CuCrZrS}_4$ . *Solid State Commun.*, 2004, **131**, P. 505–508.
- [11] Plumier R., Sougi M., Lecomte M. Observation of an unusual short range magnetic ordering in spinel  $\text{Cu}_{1/2}\text{In}_{1/2}\text{Cr}_2\text{S}_4$ . *Phys. Lett. A*, 1977, **60**, P. 341–344.
- [12] Isoda M., Mori S. Magnetic Correlation and Breakdown of Fermi Liquid Picture in Frustrated Itinerant Electron Magnet. *J. Phys. Soc. Jpn.*, 2000, **69**, P. 1509–1516.
- [13] Anderson P.W. Ordering and Antiferromagnetism in Ferrites. *Phys. Rev.*, 1956, **102**, P. 1008–1013.
- [14] Attfield J.P. Magnetism and the Trimeron Bond. *Chem Mater.*, 2022, **34** (7), P. 2877–2885.
- [15] Furubayashi T., Matsumoto T., Hagino T., Nagata S. Structural and Magnetic Studies of Metal-Insulator Transition in Thiospinel  $\text{CuIr}_2\text{S}_4$ . *Phys. Soc. Jpn.*, 1994, **63**, P. 3333–3339.
- [16] Isobe M., Ueda Y.Y. Observation of Phase Transition from Metal to Spin-Singlet Insulator in  $\text{MgTi}_2\text{O}_4$  with  $S = 1/2$  Pyrochlore Lattice. *Phys. Soc. Jpn.*, 2002, **71**, P. 1848–1851.
- [17] Schmidt M., Ratcliff W., et al. Spin Singlet Formation in  $\text{MgTi}_2\text{O}_4$ : Evidence of a Helical Dimerization Pattern. *Phys. Rev. Lett.*, 2004, **92**, 056402.
- [18] Talanov V.M., Shirokov V.B., Ivanov V.V., Talanov M.V. Theory of Structural Phase Transition in  $\text{MgTi}_2\text{O}_4$ . *Crystallogr. Reports*, 2015, **60** (1), P. 101–110.
- [19] Matsuno K.I., Katsufuji T., et al. Charge Ordering in the Geometrically Frustrated Spinel  $\text{AlV}_2\text{O}_4$ . *J. Phys. Soc. Jpn.*, 2001, **70**, P. 1456–1459.
- [20] Horibe Y., Shingu M., et al. Spontaneous Formation of Vanadium Molecules in a Geometrically Frustrated Crystal:  $\text{AlV}_2\text{O}_4$ . *Phys. Rev. Lett.*, 2006, **96**, 086406.
- [21] Talanov M.V., Shirokov V.B., et al. Vanadium clusters formation in geometrically frustrated spinel oxide  $\text{AlV}_2\text{O}_4$ . *Acta Crystallogr. B*, 2018, **74**, P. 337–353.
- [22] Khomskii D.I., Streltsov S.V. Orbital Effects in Solids: Basics, Recent Progress, and Opportunities. *Chem. Rev.*, 2021, **121** (5), P. 2992–3030.
- [23] Talanov M.V., Talanov V.M. Structural Diversity of Ordered Pyrochlores. *Chem. Mater.*, 2021, **33**, P. 2706–2725.
- [24] Talanov V.M., Shirokov V.B., Talanov M.V. Unique atom hyper-kagome order in  $\text{Na}_4\text{Ir}_3\text{O}_8$  and in low-symmetry spinel modifications. *Acta Crystallogr. A*, 2015, **71**, P. 301–318.
- [25] Talanov M.V., Shirokov V.B., Talanov V.M. Phenomenological thermodynamics and the structure formation mechanism of the  $\text{CuTi}_2\text{S}_4$  rhombohedral phase. *Phys. Chem. Chem. Phys.*, 2016, **18**, P. 10600–10606.
- [26] Talanov M.V. Two different mechanisms of metal cluster formation in the rhombohedral spinel structures:  $\text{AlV}_2\text{O}_4$  and  $\text{CuZr}_{1.86(1)}\text{S}_4$ . *Crystal Growth & Design*, 2018, **18**, P. 3433–3440.
- [27] Trighet L., Rouxel J. Le spinelle direct  $\text{CuZr}_2\text{S}_4$ . *C.R. Acad. Sc. Ser. C, Sci. Chim.*, 1968, **267** (18), P. 1322–1324.
- [28] Dong Y., McQuir M.A., Yun H., DiSalvo F.J. Synthesis, crystal structure, and properties of the rhombohedral modification of the thiospinel  $\text{CuZr}_{1.86(1)}\text{S}_4$ . *J. Solid State Chem.*, 2010, **183**, P. 606–612.

<sup>2</sup>The A-site ions ( $\text{Cu}^+$ ) are arranged in a diamond lattice. The A-site as well as the B-site cations in the spinel structure form lattices prone to strong frustration effects. The spinel structure exhibits very unusual ground states due to geometric frustration, the strength of which depends on the ratio of exchange interactions between and within the sublattices of two interpenetrating face-centered cubic lattices.

- [29] Kovalev O.V. *Representations of Crystallographic Space Groups. Irreducible Representations, Induced Representations and Co-representations.* Ed. by H.T. Stokes and D.M. Hatch, Taylor and Francis Ltd., London, 1993, 349 p.
- [30] *International tables for crystallography, volume A, Space-group symmetry.* Ed. by T. Hahn, Fifth edition, Springer, 2005, 911 p.
- [31] Talanov V.M., Shirokov V.B. Tilting structures in spinels. *Acta Crystallogr. A*, 2012, **68**, P. 595–606.
- [32] Talanov V.M., Shirokov V.B. Atomic order in spinel structure – a group-theoretical analysis. *Acta Crystallogr. A*, 2014, **70**, P. 49–63.
- [33] Sakhnenko V.P., Talanov V.M., Chechin G.M. Group-Theoretic Analysis of the Full Condensed Complex Arising upon Structural Phase Transformations. *Fiz. Met. Metalloved.*, 1986, **62**, P. 847–856.
- [34] Sakhnenko V.P., Talanov V.M. Deformational phase transitions in crystals of cubic classes. Deformations of Stretching. *Phys. Solid State*, 1980, **22**, P. 785–792.
- [35] Stokes H.T., Hatch D.M., 2007, ISOTROPY, URL: <http://stokes.byu.edu/iso/isotropy.html>.
- [36] Stokes H.T., Kisi E.H., Hatch D.M., Howard C.J. Group-theoretical analysis of octahedral tilting in ferroelectric perovskites. *Acta Crystallogr. B*, 2002, **58**, P. 934–938.

---

Submitted 4 April 2022; revised 27 October 2022; accepted 8 November 2022

*Information about the authors:*

Valeriy M. Talanov – Platov South-Russian State Polytechnic University, Rostov region 346428, Russia;  
ORCID 0000-0002-1269-2521; [valtalanov@mail.ru](mailto:valtalanov@mail.ru)

Mikhail V. Talanov – Southern Federal University, Rostov-on-Don, Russia; ORCID 0000-0002-5416-9579;  
[mvtalanov@gmail.com](mailto:mvtalanov@gmail.com)

*Conflict of interest:* the authors declare no conflict of interest.

## Studies on Sn doped cadmium sulfide thin films as highly selective green light photosensors

Yogesh C. Sharma<sup>1</sup>, Snehal D. Patil<sup>2,3</sup>, Harshal A. Nikam<sup>2,3</sup>, Padmaja Sharma<sup>4</sup>, Dinesh B. Borse<sup>3</sup>, Devidas R. Patil<sup>3</sup>

<sup>1</sup>Department of Physics, Jaipur National University, Jagatpura, Jaipur-302017, Rajasthan, India

<sup>2</sup>Department of Physics, Vivekananda Global University, Jagatpura, Jaipur-303012, Rajasthan, India

<sup>3</sup>Bulk and Nanomaterials Research Lab, Department of Physics, R. L. College, Parola, Jalgaon-425111, Maharashtra, India

<sup>4</sup>Department of Electronics and Communication Engineering, BIT Mesra, Jaipur Centre, Malviya Industrial Area, Jaipur 302017, Rajasthan, India

Corresponding author: Yogesh C. Sharma, [yc.sharma.vit@gmail.com](mailto:yc.sharma.vit@gmail.com)

PACS 07.07.Df, 73.50.Lw, 61.10.Nz, 85.60.Gz

**ABSTRACT** Thin films of Tin (Sn) doped Cadmium Sulfide (CdS) have been grown by chemical bath deposition technique. It was observed that all fabricated thin films (doped & undoped) were polycrystalline with nanoscaled crystallites and cubic crystal structure of CdS. SEM micrographs show nanorod structure of CdS and Sn doped CdS. EDS analysis shows the deficiency of sulfur and excess of cadmium in the films. UV-VIS spectroscopy confirms increase in band gap with doping of the films. Microstructural analysis shows that the particle size increases with increasing concentration of the Sn on excitation with 483 nm. The gravimetric analysis shows that the thickness of the pure CdS thin film measured is 134.41 nm, which increases with doping concentrations of tin. Electrical conductivity measurements show that the material switches its Negative Temperature Coefficient (NTC) to Positive Temperature Coefficient (PTC) nature with increase in temperature. TEP measurements show n type semiconducting nature of the films which is highly photo sensitive. The pure CdS thin film was observed to be less sensitive to the green light, however, the Sn (3 wt%) doped CdS thin films exhibit enhanced photo response particularly to green light.

**KEYWORDS** photosensors, thermoelectric, X-ray diffraction, photodetectors

**ACKNOWLEDGEMENTS** Authors thank JNU, Jaipur for generous financial help to complete this research works.

**FOR CITATION** Sharma Y.C., Patil S.D., Nikam H.A., Sharma P., Borse D.B., Patil D.R. Studies on Sn doped cadmium sulfide thin films as highly selective green light photosensors. *Nanosystems: Phys. Chem. Math.*, 2022, **13** (6), 678–687.

### 1. Introduction

Today's world is facing many problems about the availability of energy in sufficient amount. So, the researchers are focusing their attention towards the generation of green and clean energy, particularly the solar energy. Many solar cells are already available in the market, but their cost is very high, so everyone can not afford them. Intensive work on the solar cell fabrication with low cost materials is needed for increasing of the installations availability. Efforts have been made with earth abundant elements like  $\text{Cu}_2\text{ZnSnS}_4$  (CZTS) which have direct band gap ( $E_g \sim 1.5$  eV) and high absorption coefficient [1–3]. The  $\text{Cd}_x\text{Sn}_{1-x}\text{S}_3$  films are used in solar cell as they have a relatively wide band gap as compared to the CdS thin films. The high band gap of ternary Sn doped CdS thin film has less window absorption loss, which can be replaced with CdS thin film in the solar cell systems [4, 5].

Meshram et al. have fabricated the CdS thin film using spray pyrolysis method and studied its structural and optical properties [6]. Furthermore, the Sn doped CdS thin films were fabricated by using chemical bath deposition technique by Roy et al. who have studied their optical and electrical properties [7]. It was reported that the effect of Sn doping on the photoluminescence and electrical properties of the CdS thin film changes the properties significantly. The influence of Sn doping on the CdS thin film prepared by ultrasonic spray pyrolysis had been reported by Eygi et al. and their photoluminescence and electrical properties have been reported [8]. But the studies on synthesis of Sn doped CdS thin films and their photo-sensing performance and needs a further attention. For thin film fabrication, various deposition techniques have been used by various resources viz. spray pyrolysis [9], chemical vapor deposition [10], thermal evaporation [11], molecular beam epitaxy [12], RF sputtering [13], chemical bath deposition [14], etc. Out of these techniques, the chemical bath deposition (CBD) technique has been used extensively to fabricate the thin films because it is a low cost simple technique, which does not require high quality substrates, vacuum system, huge instrumentation, large power handling

and consumption, large area coatings, etc. Therefore, an attempt has been made to deposit the Sn doped CdS thin films by this technique and optimize their properties.

In this study, the Sn doped CdS thin films have been fabricated on the glass substrates using chemical bath deposition (CBD) technique. The thin films were characterized by X-ray diffraction (XRD), scanning electron microscopy (SEM), energy dispersive spectroscopy (EDS), UV-VIS absorption, photoluminescence (PL), gravimetric analysis for film thickness measurement and electrical measurement techniques to study their structural, morphological, optical, physical and electrical properties. The EDS measurements have been carried out to find the presence of different elements in the materials of thin films. The photoluminescence measurement of the Sn doped CdS thin films have been monitored on excitation with 483 nm. The thermo-electrical measurements have been carried out to confirm the semiconducting nature of thin films. The photo response of the thin films has been monitored to see the effect of Sn dopant.

## 2. Experimental details

### 2.1. Preparation of Sn doped CdS thin films

The substrates used in this study for fabrication of thin films are borosilicate glass, which were cleaned following the standard procedure. The glass plates were cleaned using double distilled water at temperature 80 °C. For further cleaning, the substrates were kept in chromic acid for 15 min and were washed thoroughly in distilled water to remove the acid. Then the washed substrates were immersed in a soap solution for 5 min and washed thoroughly again in distilled water. The substrates were finally cleaned in ultrasonic cleaner and dried under IR lamp.

In order to fabricate the pure and the Sn doped CdS thin films with different concentrations of Sn, viz. 1, 3, 5 and 7 wt% by chemical bath deposition technique, the 0.1 M aqueous solution of Cadmium Nitrate was prepared and Ammonium Hydroxide was added to this solution slowly drop wise (0.1 ml/min) with a constant stirring on the hotplate stirrer, till the ppt forms at pH equals to 8.9. The ppt vanishes with further progress in reaction and the solution becomes transparent. An aqueous solution of 0.1 M thiourea was added to this transparent solution and thereafter 0.1 M aqueous solution of Tin Chloride was added as dopant in different proportions viz. 0, 1, 3, 5 and 7 wt%. Finally, the ultrasonicated, cleaned and dried substrates were dipped in the beakers at constant temperature of 41 °C for 1.5 hr. The substrates were taken out from solution and washed with double distilled water. These substrates were annealed at 150 °C for 30 min. Thin films thus obtained were used for further investigations.

### 2.2. Characterization of films

The XRD patterns of the thin films have been monitored using X-ray diffractometer D8 Advance (Model no. Bruker AXS GmbH, Germany) to confirm the crystalline nature, phase and to calculate the crystallite size. The morphology of the thin films was recorded using Hitachi field emission scanning electron microscope (FE-SEM Model no. S 4800 Type II). The EDS measurements were carried out using X-Flash 5030 detector (Model no. Bruker AXS GmbH, Germany). The UV-visible absorption measurements were carried out using UV-Hitachi 2900). The PL spectroscopic measurements were carried out on excitation with 483 nm wavelength from a Xenon lamp using Fluoromax-4 spectrofluorometer. Gravimetric analysis was done to measure the film thickness. Thermo-emf measurements were made by TEP setup. Electrical properties of thin films were measured with the help of static gas sensing setup.

## 3. Material characterizations

### 3.1. Structural properties (XRD)

The X-ray diffraction (XRD) patterns of the pure and Sn doped CdS thin films with different concentrations of Sn (viz. 0, 1, 3 and 5 wt%) are shown in Fig. 1. The XRD pattern reveals that the thin films are polycrystalline in nature. The XRD patterns match well with JCPDS File no. 80-0019 and the phases are found to be cubic for the pure and Sn doped thin films. It is evident from XRD analysis that tin doping has not changed the cubic structure of pure CdS even after doping. The lattice parameters of CdS thin films are found to be  $a = 5.811$  and  $\alpha = \beta = \gamma = 90^\circ$  with space group  $F4\bar{3}m$  (206). The indexing of the XRD peaks has been done using the JCPDS File. The average crystallite size ( $d$ ) for each sample has been calculated by Scherer's formula:  $d = 0.9\lambda/\beta \cos \theta$  for the pure and (1, 3 and 5 wt%) Sn doped CdS thin films and their values are found to be as 6.067, 6.589, 8.943 and 21.487 nm, respectively. Thus, the crystallite size of the thin film increases with the increase in the concentrations of Sn.

### 3.2. Microstructural analysis (SEM)

Figure 2 shows the scanning electron micrographs of the pure CdS and (1, 3 and 5 wt%) Sn doped CdS thin films annealed at 150 °C for 30 min. The pure CdS thin film consists of thin nanorods overlying to each other and their size is found to lie in the range of 14.9 – 29.8 nm (Fig. 2a). Fig. 2(b) depicts the micrograph of (1 wt%) Sn doped CdS thin film, which consists large number of nanorods bound with each other associated with the nanosheets and are agglomerated. The film also shows a bulk like structure with porosity in the range of 67.1 – 2.0 nm. Whereas, in 3 wt% Sn doped sample, the particle size is found to be in the range of 22.1 – 40.8 nm with nanosheets (Fig. 2c). Fig. 2(d) depicts the micrograph

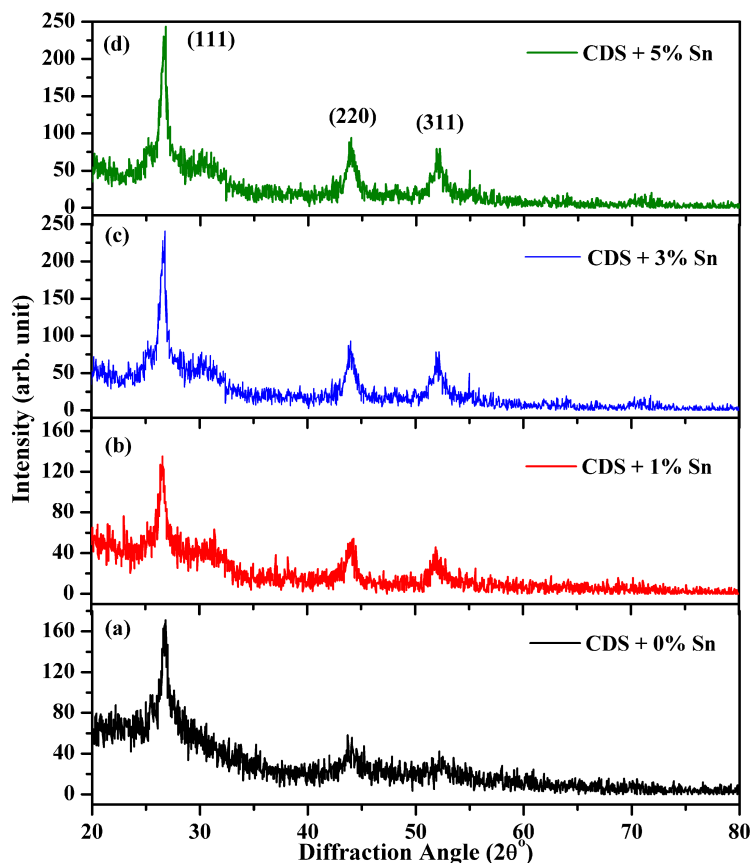


FIG. 1. The XRD patterns of the (a) 0 wt%, (b) 1 wt%, (c) 3 wt% and (d) 5 wt% Sn doped CdS thin films

of 5 wt% Sn doped CdS thin film, which consists of large number of nanosheets bound with each other associated with the crystallite size in the range of 20 – 48.2 nm.

### 3.3. Energy dispersive analysis by X-rays (E-DAX)

The quantitative elemental compositions of the pure CdS and Sn doped CdS thin films with different concentrations of Sn (viz. 1, 3 and 5 wt%) have been analyzed using an energy dispersive spectrometer and the atom % of the Cd, S and Sn elements are summarized in Table 1.

TABLE 1. Elemental compositions in the pure CdS and Sn doped CdS thin films

Elements	Doping Concentrations (wt %)				
	0 (Pure) (Expected)	0 (Pure) (Observed)	1	3	5
Cd	77.80	97.62	87.87	85.06	76.18
S	22.20	02.38	10.69	10.09	17.57
Sn	00.00	00.00	01.44	04.85	06.25
Sn doped CdS	100	100	100	100	100

Stoichiometrically expected mass % of Cd and S in CdS is 77.80 and 22.20, respectively. However, experimentally observed mass % of Cd and S in CdS is 97.62 and 2.38, respectively. Thus, the pure CdS is sulfur deficient thin film, which increases the semiconducting nature of the material. The masses % of Cd and S in the samples (Table 1) are not as per the stoichiometric proportion and all the Sn doped samples are observed to be sulfur deficient CdS, which favors the semiconducting nature. It has been reported by Husham et al. that the sulfur deficient Sn doped CdS thin film shows high photosensing performance of the films [15]. If the film is very thin it contains less sulfur contents [16]. We have also

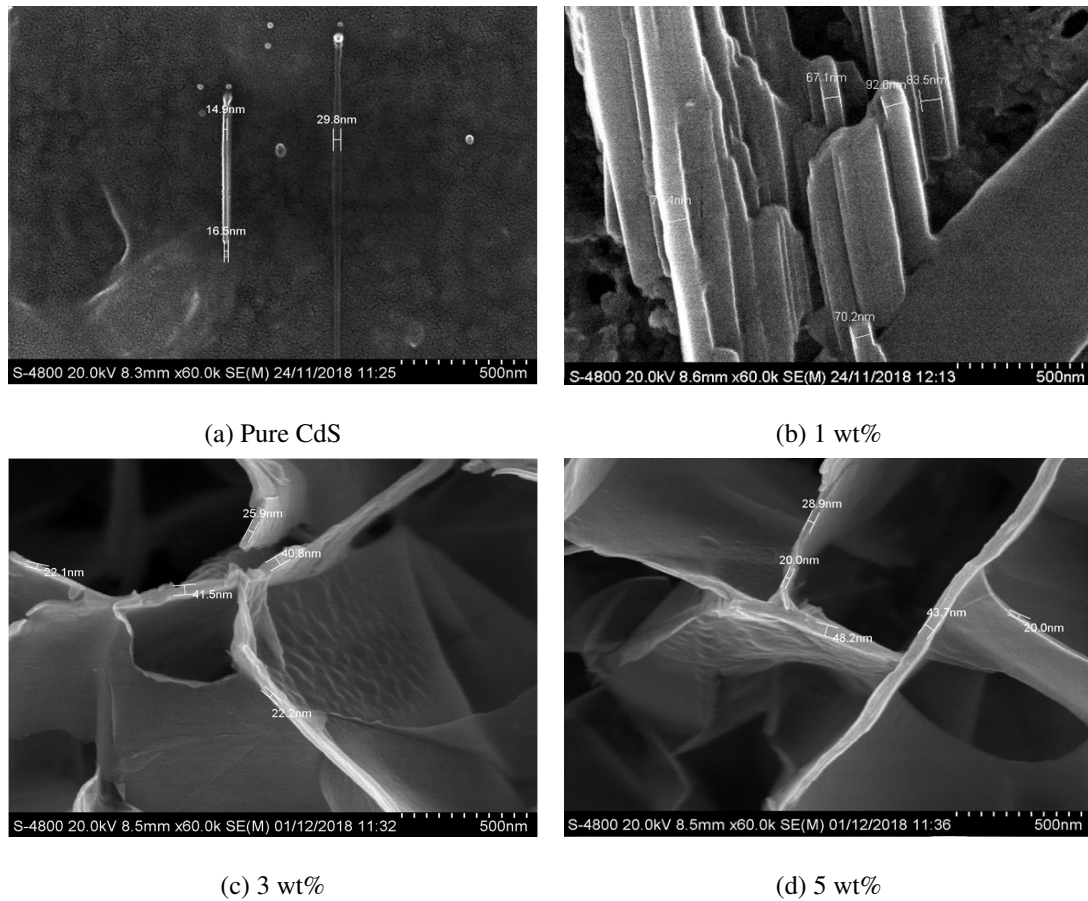


FIG. 2. SEM Micrographs of (a) Pure CdS, (b) 1 wt%, (c) 3 wt % and (d) 5 wt % of Sn in CdS thin film

observed that the sulfur deficient Sn doped CdS thin film (3 wt%) exhibits the crucial photosensing performance. The E-DAX analysis shows the presence of Sn, Cd and S elements in the thin film.

### 3.4. Gravimetric analysis

Thin film is a 2D solid film whose third dimension is restricted to nanoscale and whose properties could be changed in accordance with the change in the third dimension, irrespective of the size of the remaining two dimensions. Thus, electric, electronic and optical properties of the materials of the film can be tailored by varying the film thickness, which can be measured by gravimetric analysis as per the eq. (1) [17, 18]:

$$t = \frac{M}{A \cdot \rho}, \quad (1)$$

where  $t$  is the thickness of the thin film,  $M$  is the mass of the deposited material (film) on the substrate ( $M$  is the mass of the substrate with deposited film minus the mass of the substrate without deposition),  $A$  is the area of the film,  $\rho$  is the density of the material.

Film thicknesses of pure CdS and Sn doped CdS thin films with different concentrations of Sn (viz. 1, 3 and 5 wt%) were analyzed using gravimetric analysis in the laboratory which leads to conclusion that the film thickness increases with doping concentrations of Sn. The results are summarized in Table 2.

### 3.5. Optical properties

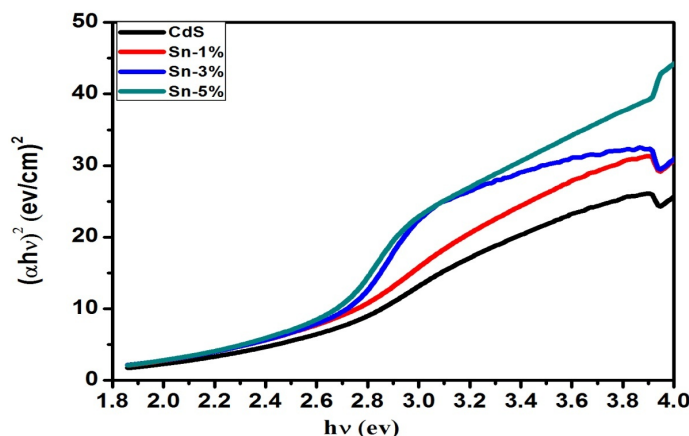
3.5.1. *UV-visible measurements.* The optical band gap of the pure CdS and Sn doped CdS thin films with different concentrations of Sn (viz. 1, 3 and 5 wt%) has been calculated by using the Wood and Tauc formula [19]:

$$\alpha = \frac{B(h\nu - E_g)^m}{h\nu},$$

where,  $E_g$  is the optical band gap energy,  $h\nu$  and  $B$  are an energy of the incident photon and the band tailoring constant, respectively. The value of  $m$  was chosen as 1/2 for direct band gap allowed transitions [20]. Fig. 3 depicts the variation of  $(\alpha h\nu)^2$  versus  $h\nu$  for the pure CdS and the Sn doped CdS thin films with different concentrations of Sn (viz. 1, 3 and 5 wt%). The optical band gap of the pure CdS thin film was found to be 2.32 eV, which matches to the earlier reported value [21–24]. The optical band gaps of Sn doped CdS thin films are found to be 2.35, 2.41 and 2.43 eV for the 1, 3 and

TABLE 2. Film thickness of pure CdS and Sn doped CdS thin films

S. No.	Material Composition of Thin Film	Film Thickness (in nm)	Average Crystallite Size (in nm)
1	Pure CdS	134.41	6.067
2	Sn (1 wt%) CdS	158.07	6.589
3	Sn (3 wt%) CdS	162.34	8.943
4	Sn (5 wt%) CdS	193.22	21.487

FIG. 3. Variation of  $(\alpha h\nu)^2$  versus  $h\nu$  of pure CdS and the Sn doped CdS thin films

5 wt% concentrations, respectively. Thus, the optical band gaps of the thin films are found to increase with increase in the concentrations of Sn.

**3.5.2. Photoluminescence measurements.** The photoluminescence spectra of the pure CdS and the Sn doped CdS thin films with different concentrations of Sn (viz. 1, 3 and 5 wt%) recorded in the range of 500 – 550 nm on excitation with 483 nm are shown in Fig. 4. The pure CdS thin film does not show any photoluminescence. However, the Sn doped CdS thin films exhibits weak emission in the green region centered at 520 nm. The intensity of the green emission increases on increasing the concentrations of Sn contents. The 1 wt% Sn doped CdS thin film emits the green color and enhances up to 3 wt% doped thin film. Above 3 wt%, the emission intensity is found to decrease due to concentration quenching as the concentration was increased to 5 wt%. This is due to the fact that at higher concentrations, the inter-nuclear separation between the atoms becomes smaller than the critical distance and the excitation energy migrates to the energy killing centers [25]. Thus, the emission intensity is maximum for the 3 wt% concentration of Sn.

There are several factors responsible for an increase in the emission intensity. When the thin film is annealed, the surface defects are reduced significantly. This also reduces the impurity elements present in the thin film [26]. As discussed earlier, when the Sn is doped in the CdS thin film the crystallinity of the film is improved and the crystallite size was increased slightly from 74 to 108 nm. It is also clear from SEM analysis that the particle size of the thin film was increased from 20 to 52 nm after doping the Sn element. This can enhance the photoluminescence intensity. Wang et al. have observed an intense photoluminescence for larger particle size due to high volume to surface area ratio [27]. Recently, Yadav et al. have also reported that the larger particles can easily absorb more incident photons and give an intense photoluminescence [28]. They have also annealed the samples and found significant enhancement in the emission intensity due to an increase in crystallinity and particles size. They observed a reduction in the impurity ions on annealing the samples. In the present case, the increase in the emission intensity has been observed due to the improvement in the particle size of the thin film after Sn doping. As a result, the Sn doped CdS thin film may be used in the optoelectronic devices.

## 4. Electrical properties

### 4.1. I–V characteristics

The photocurrent ( $I$ ) of the pure CdS and Sn doped CdS thin films with different concentrations of Sn (viz. 1, 3 and 5 wt%) has been measured at different input voltages ( $V$ ) and the plots thus obtained are shown in Fig. 5. It has been

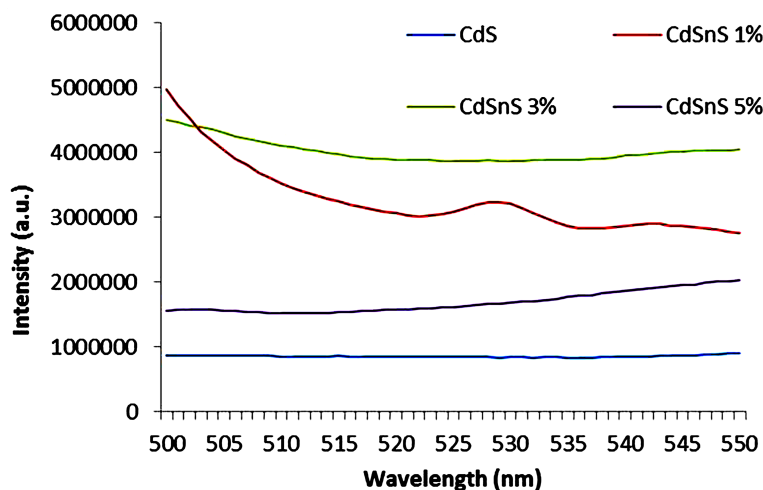


FIG. 4. Photoluminescence spectra of the as-deposited pure CdS and the Sn doped CdS thin films with different concentrations of Sn (viz. 1, 3 and 5 wt%)

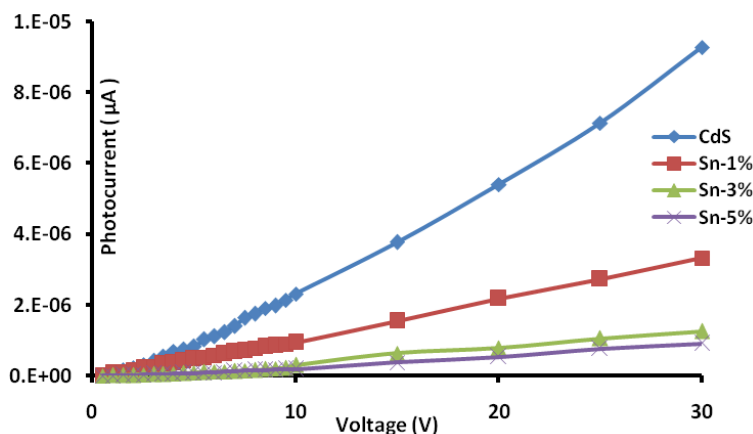


FIG. 5. I–V characteristics of the pure CdS and Sn doped CdS thin films

observed that the photocurrent generated in the pure CdS thin films is maximum as compared with the Sn doped CdS thin films, which may be attributed to the fact that as the doping concentration increases the energy band gap also increases. The nature of the I–V plot is found nearly linear for the pure and Sn doped CdS thin films.

**4.2. Electrical conductivity**

Figure 6 shows a variation of logarithm of the electrical conductivity with reciprocal of operating temperature of the pure CdS and the Sn doped CdS thin films with different concentrations of Sn (viz. 1, 3 and 5 wt%). At higher temperature, i.e. at 150 °C, the conductivity was high, which decreases with the decrease in the operating temperature, i.e. up to 130 °C. Thus, the film exhibits the negative temperature coefficient of resistance up to 130 °C. The conductivity of the film increases further with the decrease in operating temperature, exhibiting the positive temperature coefficient of resistance. This proves the semiconducting nature of the Sn doped CdS thin films. The electrical conductivity is found to be maximal for the 3 wt% Sn doped CdS thin film.

**5. Photo response of the thin films**

**5.1. Time based performance**

Photo response (*S*) of the photo sensor is defined as the ratio of the change in photo currents generated upon exposure of the light rays and in dark to the photocurrent in light rays. Fig. 7 depicts the variation of photo response of the pure CdS and the Sn doped CdS thin films with different concentrations of Sn (viz. 1, 3, 5, and 7 wt%) with respect to exposure time for different colors (wavelengths) of light. It is observed from the Fig. 7(a) that the photo response of pure CdS thin film increases with the increase in time of exposure of green, blue and yellow colors of light. However, the negligible photo response was observed for the red and ordinary light. These films are relatively less sensitive for the blue and yellow light.

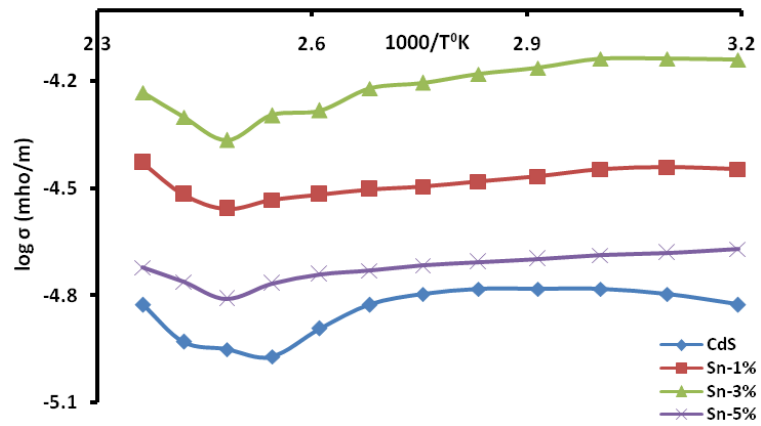


FIG. 6. Conductivity-temperature profile of pure CdS and the Sn doped CdS thin films with different concentrations of Sn (i.e. 1, 3 and 5 wt%)

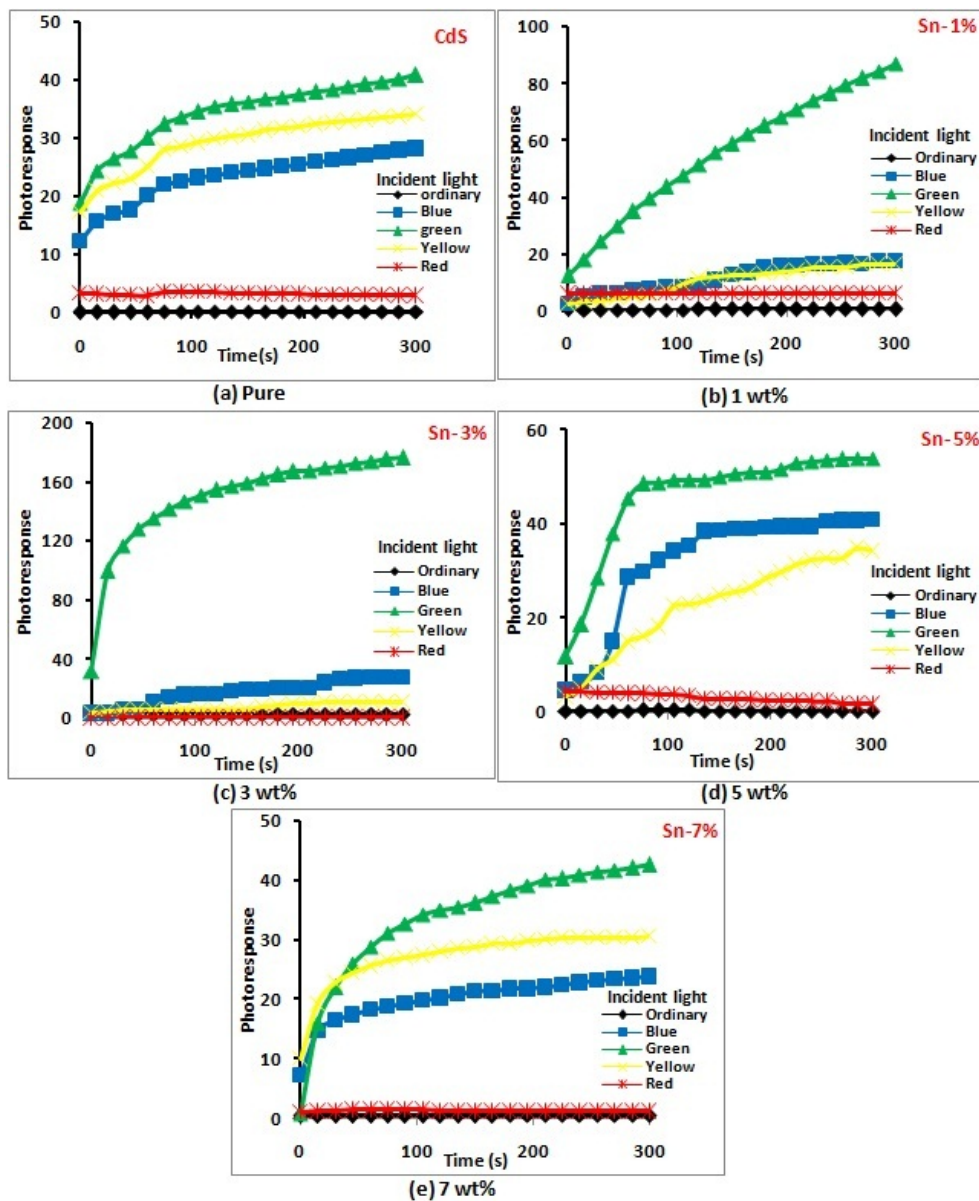


FIG. 7. Variation of photo response of the pure CdS and Sn doped CdS thin films with different concentrations of Sn (i.e. 1, 3, 5, and 7 wt%) with time

From Figs. 7(b–e) it is clear that the Sn doped CdS thin films are highly sensitive and selective to the green light while less responsive to the other wavelengths, viz. blue, red, yellow, etc. Further, this is found to increase with the increase in the Sn doping concentration up to 3 wt% and it is decreased considerably for 5 and 7 wt% of Sn concentrations. This may be attributed to the excitation of the material by photon of the wavelength in between 520 to 560 nm. Upon exposure of the photon of wavelength in this region, the free electrons move to the conduction band and constitute to enhance the photo current. The Sn doped CdS thin films exhibit crucial response to only green light among all, which may be attributed to the fact that, due to doping of Sn atoms, some periodic arrangements of the crystals disturbs, though in smaller extent and crystal structure does not gets changed even after doping by Sn. This arrangement modifies the energy levels of the crystals, results in shifting of absorbance towards green wavelength.

**5.2. Doping concentration based performance**

Figure 8 shows the green light photo response as a function of doping concentrations of Sn in the CdS thin films. It has been observed that, the pure CdS thin film was less sensitive to green light and the photo response of the Sn doped thin film increases up to 3 % Sn doping concentration and then decreases further for 5 and 7 wt% concentration.

**6. Thermo electric power (TEP)**

Figure 9 depicts the variation of thermo emf as a function of temperature difference of the pure and modified samples of CdS thin films. It is observed from Fig. 9 that the thermo emf decreases with increase in the temperature of hot end keeping the temperature of cold end constant at 32 °C, i.e. at room temperature.

In semiconductor, temperature gradient yield thermoelectric effect in which phonons travels preferentially from the hot end to the cold end due to phonon-electron interaction. It is seen that TEP measurements, thermal gradient establish change of density of charge defect states by capturing electrons and holes which can take place due to the process of diffusion.

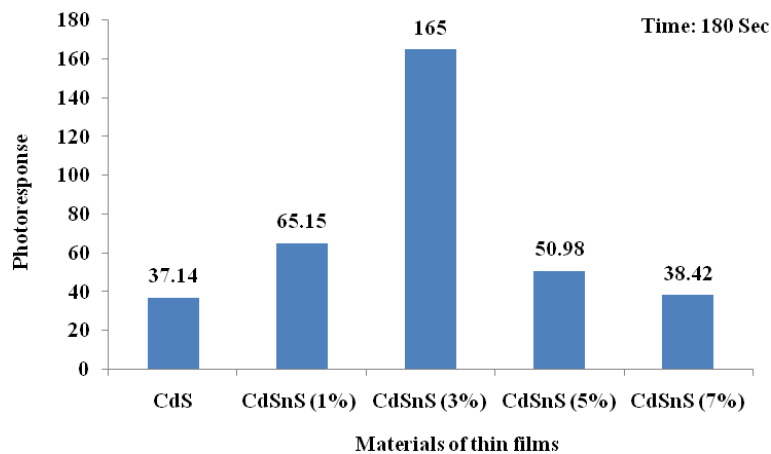


FIG. 8. Variation of the photo response of green light with Sn doping concentrations in the CdS films

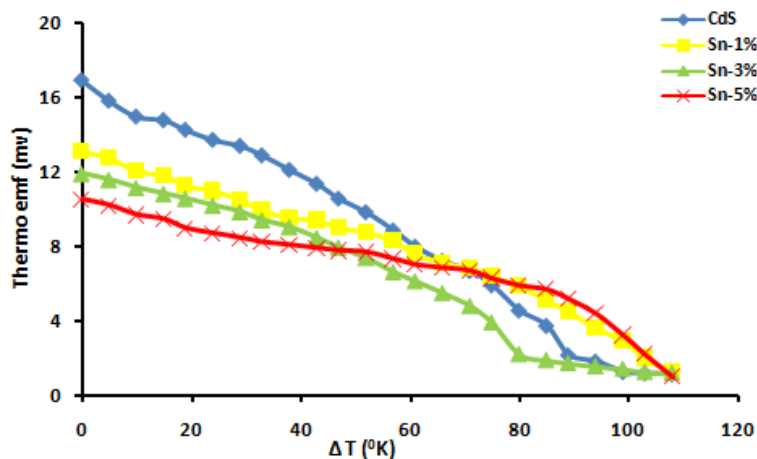


FIG. 9. Variation of thermo emf with temperature difference for Sn doped CdS thin films with different concentrations (0, 1, 3 and 5 wt%)

Thermoelectric power measurement is useful tool for measurement of carrier type. The developed thermoelectric voltage due to temperature difference across ends of material is directly depending on carrier concentrations. It is called as Seebeck effect. Fig. 9 shows the increase in the conductivity of material attributes to the decrease in mobility of charge carrier and carrier concentrations. From the above discussion, it is clear that as the polarity of thermally generated voltage at the hot end is positive one conclude that the material has the n-type nature.

## 7. Conclusions

The Sn doped CdS thin films have been grown successfully using chemical bath deposition technique. Gravimetric analysis was used to measure the film thickness. It was confirmed from XRD analysis that the cubic structure of pure CdS has not been changed even after doping CdS with Sn, as sulfur atoms in the crystal replaces Sn. The microstructural analysis shows the increase in the particle size and the film thicknesses with increasing concentration of the Sn on excitation with 483 nm. It was observed from the UV spectroscopy that the band gap increases with dopant concentration, particularly Sn, increase. The Sn doped CdS thin films show the n-type semiconducting nature. The pure CdS thin film was observed to be less sensitive even to the green light; however, the Sn doped CdS thin films exhibit crucial photo response to the green light. Thus, the Sn doped CdS thin films may be useful in the fabrication of optoelectronic devices and solar cells.

## References

- [1] Gilic M., Trajic J., Romcevic N., Romcevic M. Optical properties of CdS thin films. *Optical Materials*, 2013, **35**, P. 1112–1117.
- [2] Xiao Z., Feng Li Y., Yao B. Band gap engineering of  $\text{Cu}_2\text{Cd}_x\text{Zn}_{1-x}\text{SnS}_4$  alloy for photovoltaic applications: A complimentary experimental and first principal study. *J. of Applied Phys.*, 2013, **114**, 183506.
- [3] Kim J.H., Shin D.H. Growth of Sn (O,S)<sub>2</sub> buffer layers and its application to Cu (In, Ga) Se<sub>2</sub> solar cells. *Current Applied Physics*, 2014, **14**, P. 1803–1808.
- [4] Ferekides C.S., Marinsky D., et al. High efficiency CSS CdTe solar cells. *Thin Solid Films*, 2000, **361–362**, P. 520–526.
- [5] Dimroth F. High efficiency solar cells from III–V compound semiconductors. *Phys. Stat. Sol.*, 2006, **3**, P. 373–379.
- [6] Meshram R.S., Suryavanshi B.M., Thombre R.M. Structural and optical properties of CdS thin films obtained by spray pyrolysis. *Adv. Appl. Sci. Res.*, 2012, **3** (3), P. 1563–1571.
- [7] Roy P., Srivastava S.K. In situ deposition of Sn-doped CdS thin films by chemical bath deposition and their characterizations. *J. Phys. D: Appl. Phys.*, 2006, **39**, P. 4771–4776.
- [8] Eygi Z.D., Demirsencuk B., Bilgin V. Influence of Sn doping on CdS thin film grown by ultrasonic spray pyrolysis. *Int. J. Thin Film. Sci. Tec.*, 2016, **5** (2), P. 103–106.
- [9] Ravangave L.S., Biradar U.V., Misal S.D. The effect of ionic composition on structural and optical properties of  $\text{Cd}_x\text{Zn}_{1-x}\text{S}$  thin films growth by spray pyrolysis. *Int. J. of Sci. Res. Publications*, 2012, **2** (6).
- [10] Karn A., Kumar N., Aravindan S. Chemical Vapour Deposition synthesis of novel indium oxide nanostructures in strongly reducing growth ambient. *J. Nanostruct.*, 2017, **7** (1), P. 64–76.
- [11] Rahman K.S., Haque F., Khan N.A., Islam M.A. Effect of  $\text{CdCl}_2$  Treatment on Thermally Evaporated CdTe Thin Films. *Chalcogenide Letters*, 2014, **11** (3), P. 129–139.
- [12] Camacho R.E., Morgan A.R., Flores M.C., McLeod T.A. Carbon Nanotube Arrays for Photovoltaic Applications. *Nano. Ele. Applications*, 2007, **59**, P. 39–42.
- [13] Xu N., Li P., Hao Y., Wang X. Effect of sputtering power on Cd/Zn atomic ratio and optical properties of  $\text{Cu}_2\text{Zn}_x\text{Cd}_{1-x}\text{SnS}_4$  thin films deposited by magnetron sputtering: An experimental and first-principle study. *Chem. Phys. Lett.*, 2016, **660**, P. 132–135.
- [14] Kamal T., Parvez S., et al. Chemical bath deposition of CdS layer for thin film solar cell. *SAJREST*, 2017, **2** (3), P. 610–617.
- [15] Husham M., Hassan Z., Selman A.M., Allam N.K. Microwave assisted chemical bath deposition of nanocrystalline CdS thin films with superior photodetection characteristics. *Sens. Actuators A*, 2015, **230**, P. 9–16.
- [16] Ikhmayies S.J., Juwhari H.K., Ahmad-Bitar R.N. Nanocrystalline CdS: in thin films prepared by the spray-pyrolysis technique. *J. Lumin.*, 2013, **141**, P. 27–32.
- [17] Ohring M. *Materials science of thin films: Deposition and structure*. Academic press, 2002.
- [18] Khairnar V.S., Ph. D. Thesis, Sant Gadgebaba Amravati University, Amravati, 2019, Chapter 2, P. 56–86.
- [19] Wood D.L., Tauc J. Weak absorption tails in amorphous semiconductors. *Phys. Rev. B*, 1972, **5**, P. 3144–3151.
- [20] Yadav R.S., Rai S.B. Surface analysis and enhanced photo-luminescence via  $\text{Bi}^{3+}$  doping in a  $\text{Tb}^{3+}$  doped  $\text{Y}_2\text{O}_3$  nano-phosphor under UV excitation. *J. Alloys Compds.*, 2017, **700**, P. 228–237.
- [21] Oladeji I.O., Chow L., et al. Comparative study of CdS thin films deposited by single, continuous, and multiple dip chemical processes. *Thin solid films*, 2000, **359**, P. 154–159.
- [22] Tec-Yam S., Patino R., Oliva A.I. Chemical bath deposition of CdS films on different substrate orientations. *Cur. Appl. Phys.*, 2000, **11**, P. 914–920.
- [23] Phuruangrat A., Thongtem T., Thongtem S. Effect of Cd and S sources on the morphologies of CdS synthesized by solvothermal in the mixed solvents. *Current applied physics*, 2009, **9** (3), P. S201–S204.
- [24] Muthukumarasamy N., Jayakumar S., Kannan M.D., Balasundarapraphu R. Structural phase change and optical band gap bowing in hot wall deposited  $\text{CdSe}_x\text{Te}_{1-x}$  thin films. *Solar Energy*, 2009, **83**, P. 522–526.
- [25] Afzaal M., Brien P.O. Recent developments in II–VI and III–VI semiconductors and their applications in solar cells. *J. Mater. Chem.*, 2006, **16**, P. 1597–1602.
- [26] Yadav R.S., Dhoble S.J., Rai S.B. Improved photon upconversion photoluminescence and intrinsic optical bistability from a rare earth co-doped lanthanum oxide phosphor via  $\text{Bi}^{3+}$  doping. *New J. Chem.*, 2018, **42**, P. 7272–7282.
- [27] Wang F., Deng R., et al. Tuning upconversion through energy migration in core–shell nanoparticles. *Nat. Mater.*, 2011, **10**, P. 968–973.
- [28] Yadav R.S., Verma R.K., Rai S.B. Intense white light emission in  $\text{Tm}^{3+}/\text{Er}^{3+}/\text{Yb}^{3+}$  co-doped  $\text{Y}_2\text{O}_3$ -ZnO nano-composite. *J. of Phys. D: Appl. Phys.*, 2013, **46**, 275101.

---

*Submitted 13 June 2021; revised 10 October 2022; accepted 12 October 2022*

*Information about the authors:*

*Yogesh C. Sharma* – Department of Physics, Jaipur National University, Jagatpura, Jaipur-302017, Rajasthan, India; ORCID 0000-0003-3532-6097; Mobile: +919664075093, +917597776818; yc.sharma.vit@gmail.com

*Snehal D. Patil* – Department of Physics, Vivekananda Global University, Jagatpura, Jaipur-303012, Rajasthan, India and Bulk and Nanomaterials Research Lab, Department of Physics, R. L. College, Parola, Jalgaon-425111, Maharashtra, India; ORCID 0000-0002-4374-8663; snehal.23993@gmail.com

*Harshal A. Nikam* – Department of Physics, Vivekananda Global University, Jagatpura, Jaipur-303012, Rajasthan, India and Bulk and Nanomaterials Research Lab, Department of Physics, R. L. College, Parola, Jalgaon-425111, Maharashtra, India; ORCID 0000-0002-6806-3919; nikamharshal19@gmail.com

*Padmaja Sharma* – Department of Electronics and Communication Engineering, BIT Mesra, Jaipur Centre, Malviya Industrial Area, Jaipur 302017, Rajasthan, India; ORCID 0000-0002-5999-3559; padmaja121003@gmail.com

*Dinesh B. Borse* – Bulk and Nanomaterials Research Lab, Department of Physics, R. L. College, Parola, Jalgaon-425111, Maharashtra, India; ORCID 0000-0002-8356-0139; tdborse@gmail.com

*Devidas R. Patil* – Bulk and Nanomaterials Research Lab, Department of Physics, R. L. College, Parola, Jalgaon-425111, Maharashtra, India; ORCID 0000-0003-2982-3636; prof\_drpatil@yahoo.in

*Conflict of interest:* the authors declare no conflict of interest.

## Polymer nanocarbon materials as ion-to-electron transducers in solid-contact ion-selective electrodes

Konstantin Yu. Zhizhin<sup>a</sup>, Evgeniy S. Turyshev<sup>b</sup>, Aleksander V. Kopytin<sup>c</sup>, Liliya K. Shpigun<sup>d</sup>, Nikolay T. Kuznetsov, Nikolay P. Simonenko, Natalya N. Zamyatina<sup>e</sup>, Mukhammadislom S. Madraimov, Gleb I. Betenev

N. S. Kurnakov Institute of General and Inorganic Chemistry of Russian Academy of Sciences, Moscow, Russia

<sup>a</sup>kyuzhizhin@igic.ras.ru, <sup>b</sup>tyrishev@gmail.com, <sup>c</sup>ionix@igic.ras.ru,

<sup>d</sup>liliaspigun@gmail.com, <sup>d</sup>shpigun@igic.ras.ru, <sup>e</sup>yatina\_76@bk.ru

Corresponding author: Liliya K. Shpigun, liliaspigun@gmail.com, shpigun@igic.ras.ru

PACS 07.07.Df, 82.39.wj, 82.80-d

**ABSTRACT** Carbon nanoparticles materials in polymer modification have gained particular importance in modern potentiometric studies after they were discovered to be ion-to-electron transducers in solid-contact ion-selective electrodes (SC-ISEs). This paper describes the preparation and comparative evaluation of poly(vinyl chloride) (PVC) and Nafion membranes incorporated with light fullerene C60, single carbon nanotubes (SWCNTs) and their mixture as transducer interlayers in the SC-ISE based on the ion-sensing PVC-membrane containing a high lipophilic 2-[bis-octadecyl sulfonic)-*c/oso*-decaborate anion. The best electroanalytical performance was achieved for the sensor fabricated with the transducer made by combining two transducing layers, a Nafion film modified with fullerene C60 and a plasticized PVC film modified with SWCNTs-C60 hybrid filler, which were sequentially applied onto the substrate carbosital electrode surface. The test results showed that the newly prepared a layer-by-layer SC-ISE is suitable for the sensitive determination of local anesthetics and some other protonable nitrogen-containing drugs.

**KEYWORDS** nanocarbon-doped polymers, fullerene C60/SWCNTs, solid-contact ion-selective electrode, ion-to-electron transducing materials, local anesthetics.

**ACKNOWLEDGEMENTS** The authors acknowledge the support of the Ministry of Science and Higher Education of Russia (Grant Agreement No 075-15-2020-782).

**FOR CITATION** Zhizhin K.Yu., Turyshev E.S., Kopytin A.V., Shpigun L.K., Kuznetsov N.T., Simonenko N.P., Zamyatina N.N., Madraimov M.S., Betenev G.I. Polymer nanocarbon materials as ion-to-electron transducers in solid-contact ion-selective electrodes. *Nanosystems: Phys. Chem. Math.*, 2022, **13** (6), 688–697.

### 1. Introduction

Over the last few years, the development of nanostructured materials as ion-to-electron transducers in solid-contact ion-selective electrodes (SC-ISEs) is of a great interest in the electroanalytical chemistry [1]. SC-ISEs are asymmetric devices, in which an ion-sensing membrane (ISM) contacts with a solid-contact layer (ion-to-electron transducer) on one side, and with the sample solution to be analyzed on the other side (Fig. 1).

Nikolsky and Materova were the first to propose some basic criteria for manufacturing SC-ISEs with stable and reproducible potentials measured under open circuit conditions [2]. Currently, it is a reversible mechanism of transition from ion current to electron current, high bulk capacity to produce a stable potential, high degree of hydrophobicity to eliminate the undesirable water layer between the electron conductor and the ISM, and the absence of side reactions in the ion-to-electron transduction process. Although the range of available materials with ionic-electronic hybrid conductivity is extensive, carbon nanoparticles (CNPs) are particularly favored. The high hydrophobicity, chemical stability, large electric double-layer (EDL) and remarkable charge-transfer capability provide CNPs some advantages over other ion-to-electron transducers [3]. However, self-aggregation or rearrangement due to strong van der Waals interactions between neighboring sheets can lead to loss of their active surface area and electrical conductivity. The incorporation of CNPs in polymer matrices assists in overcoming these difficulties [4–7].

It should be noted that traditional carbon-based electrodes like graphite, glassy carbon or carbosital directly coated with an ISM can also be considered as solid-contact potentiometric sensors. The electrochemical process can occur by a purely electronic mechanism due to the transfer of free electrons from the polyconjugate system of graphite-like carbon crystallites to the adsorbed or dissolved potential-determining ions. Unfortunately, in this case, the resulting EDL has a very small capacitance, which leads to a poor reproducibility and a significant drift of the standard electrode potential ( $E'_o$ ) during the time [8]. To solve the historical problem of poor potential stability, it has been proposed to disperse carbon

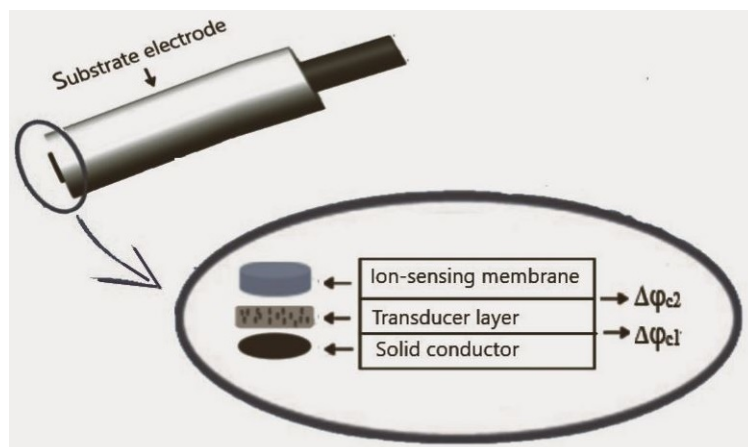


FIG. 1. Schematic representation of SC-ISEs based on the solid contact with CNPs

nanoparticles (CNPs) directly into the polymer membrane composition [9–11] or to include an ion-to-electron transducer layer (SC-layer) as an intermediate support between the polymer ISM and the solid conductor [12–15].

Different types of polymers and nanofillers have been proposed so far to prepare SC-transducers. Remarkable examples of using nanocomposites of conducting polymers (CPs) with CNPs have been reported [16–24]. However, most of CPs can have drawbacks such as high electroactivity that promotes non-specific chemical reactions, sensitivity to  $\text{CO}_2$ , pH or light. In addition, the formation of an undesirable aqueous film between the ISM and the inner SC is often observed [25, 26]. From our point of view, it is of interest to prepare solid-contacts by using CNPs-doped non-conductive polymer matrices, as they seem to form three-dimensional nanostructures that can provide a significant improvement in the performance characteristics of SC-ISEs. The incorporation of CNPs into polymer matrices is explored as a strategy to obtain composite materials with electrical properties. In particular, the creation of conductive nanocomposites of PVC with CNPs (graphene, fullerenes, carbon nanotubes, etc.) and characterization of their specific properties are described in several publications [27–34]. According to the literature, the introduction of CNPs can lower the resistivity of PVC-matrix by several orders of magnitude [28]. For Nafion-CNPs composites, this is mainly achieved through either ionic movement or electron self-exchange between dopant species [35–40]. Recently, the synthesized PVC/mixed graphene-carbon nanotube nanocomposite was proposed for the development of an amperometric  $\text{Ag}^+$ -sensor [41]. The development of SC-ISE with two PVC-based sandwiched membranes was described [42]. The first membrane contains suspension of halogen salts of silver and alkaline metals as well as silver nanoparticles and is placed on Ag substrate or conducting substrate covered with silver. It acts as a solid contact of an ion-selective electrode when covered with the second PVC membrane sensitive to potassium, sodium or chloride ions. However, as far as we know, there is still no information on using CNPs-PVC composite materials as SC-layers in ISEs.

In this paper, we investigated the possibility to fabricate SC-ISEs, in which the SC-layer was prepared by incorporating single-walled nanotubes (SWCNTs), light fullerene C60 or their hybrid mixture into plasticized PVC- and Nafion-membranes. The primary goal of the study was to evaluate the prepared nanostructured materials as intermediate ion-to-electron transducing layers in the potentiometric membrane sensor based on ion-pair complexes of cesium cation with 2-[bis-octadecyl-sulfonic]-*closo*-decaborate anion ( $\text{Cs}[\text{B}_{10}\text{H}_9\text{S}(\text{n}-\text{C}_{18}\text{H}_{37})_2]$ ). Recently, we have shown that the indicated lipophilic anion demonstrated high sensitivity to cationic protonated forms of local anesthetic drugs [43]. For this reasons, an amino-ester anesthetic procaine (2-diethyl-aminoethyl-4-aminobenzoate) was chosen as a model determinant.

## 2. Materials and methods

### 2.1. Reagents and solutions

The commercial carbon nanomaterials, such as fullerene C60 (99.5 %, Bucky USA) and SWCNTs (> 90 %, 0.7–0.9 nm diameter, Aldrich) were used. High molecular weight poly(vinyl chloride) (PVC), Nafion solution (5 % w/w in EtOH), bis(1-butylpentyl)adipate (BBPA) and tetrahydrofuran (THF), procaine hydrochloride (Pro-HCl, 99 %, p/p purity), lidocaine hydrochloride monohydrate (Lid-HCl, 99.9 % p/p purity), articaine hydrochloride (Art-HCl,  $\geq 98$  % p/p purity), adenine (6-aminopurine,  $\geq 99$  % p/p purity), adrenaline (( $\pm$ )-epinephrine hydrochloride, 95 % p/p purity) were purchased from Merck KGaA and used without prior purification. The stock standard solutions of these analytes (0.01 M) were prepared by dissolving precise amounts of each compound in water or 0.001 M HCl. The working standard solutions were prepared daily from the stock solutions by serial dilution. All other chemicals were of analytical or pharmaceutical grade and their solutions were prepared with redistilled water.

## 2.2. Processing of polymer nanocomposite suspensions

As polymer matrixes for C60 and SWCNTs, we chose PVC and Nafion, which are known to allow a relative uniform distribution of CNPs in the composite volume with their minimal aggregation. Initial suspensions of polymer composites were achieved by dispersing fullerene C60, SWCNTs or their mixture into a plasticized PVC solution, and fullerene C60 into a Nafion alcohol solution under ultrasonic irradiation conditions. In order to reach the better homogeneous distribution of CNPs (SWCNTs and C60) in a plasticized PVC-matrix, a multi-step procedure was used. In the first step, a PVC solution in dry freshly distilled THF (25 w/v %) was prepared by stirring for 3 h at 30 °C. Then, a plasticizer (BBPA) was added to the PVC solution under effective stirring and at room temperature. Finally, an appropriate amount of CNPs was incorporated into the plasticized polymer solution with the aid of irradiation in an ultrasonic water bath during 30 min. The stable C60-Nafion dispersion (0.5 wt. %) was prepared by dissolving the fullerene powder in 2.3 mL of Nafion (2.5 w/v %) followed by ultrasonic treatment of the resulting mixture for about 60 min.

## 2.3. Preparation of an ion-sensitive membrane precursor solution

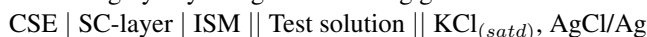
Precursor solution of ISM of the following composition (wt. %) was prepared: membrane-active compound – 1.2; plasticizer (BBPA) – 69.8; PVC – 29.0. The components were dissolved in 2.0 mL of dry freshly distilled THF. After the membrane cocktail was homogeneously mixed, it was stored at 4 °C. The electroactive compound (Cs[B<sub>10</sub>H<sub>9</sub>S(n-C<sub>18</sub>H<sub>37</sub>)<sub>2</sub>]) was synthesized and identified in the laboratory of chemistry of light elements and clusters of the N. S. Kurnakov Institute of General and Inorganic Chemistry of RAS [44].

## 2.4. Potentiometric sensor fabrication

All testing SC-ISEs were fabricated using a carbosital (CS) electrode (Wolta, Russia). Before modification, the CS surface was mechanically polished with 0.3 and 0.05 μm alumina powders. Then, it was thoroughly cleaned by ultrasonication with ethanol and deionized water, in order to remove residual alumina particles. After that, 20 μL of the corresponding PVC-based nanocomposite suspension (in 10 μL aliquots) was applied to the freshly cleaned CS surface and left to dry at 34 °C in a pressure chamber. In case of preparing the bilayer transducer, 10 μL of the C60-Nafion suspension (in aliquots of 5 μL) was firstly deposited onto the CS surface and left to dry for at least 1 h by rotor evaporating at 36 °C under vacuum, forming a thin film with a thickness of approximately 100 μm. Further, the modified electrode was coated with a precursor solution of ISM (in two portions of 25 μL) to form a potentiometric sensor. The ISM thickness was about 400 μm. Before using, each sensor was soaked in 1.0 × 10<sup>-3</sup> M Pro-HCl solution for 24 h, in order to establish the membrane – solution equilibrium. The uptake of water was necessary for reaching stable electrode potentials. The sensors were kept dry in an opaque closed vessel while not in use.

## 2.5. Measurements

To characterize the prepared SC-ISEs, morphological observation and potentiometric investigation at the room temperature (25 ± 2 °C) were performed. All potentiometric measurements were made with a pH/ion analyzer Radelkis OP-300 “Hungary” by using the following galvanic circuit:



The ultrasonic bath (Elmasonic One, Germany, 35-kHz ultrasound) was used in all experiments. The surface morphology of carbon nanomaterials was examined with a scanning electron microscope (SEM, Carl Zeiss NVision 40, Germany).

## 3. Results and discussion

### 3.1. Morphological characterization of the polymeric nanocomposite materials

Polymeric matrices filled with CNPs are nanosystems with very strong mechanical and electrical properties, which are mainly due to the interaction between the matrix and the nanofiller. It should be noted, however, that many aspects of nanoparticle diffusion in a polymer are still far from being solved [45]. This is especially related to their possible aggregation both while preparing polymer nanocomposite suspensions and during the formation of the polymer film on the surface of the substrate electrode. Self-aggregation or rearrangement of carbon nanofillers due to strong van der Waals interactions can lead to changes of the effective surface area and the electrical conductivity of composites. Obviously, the homogeneous dispersion of CNPs in the polymer matrix plays a key role in preserving their functionality as ion-electronic transducers. The literature review in this field showed that one of the ways to achieve a high degree of homogeneity of the polymeric nanocomposite material is the use of ultrasonic processing [46].

Since the potentiometric response of SC-ISEs is related to the physical properties of SC-layers, the morphology of the surface of CNPs-PVC composites was investigated before and after ultrasonication. Observation of the prepared composite materials showed that the dopant distribution in the plasticized PVC-matrix was heterogeneous (Fig. 2).

The aggregated CNPs may be visible, especially in the areas of interstructural defect zones in PVC. The distributed nanofillers are supposed to be aggregated and tend to re-stack to each other, while PVC macromolecules surround them to core shell structure. The ultrasonic treatment led to splitting of the bundles and forming micelles, which can be

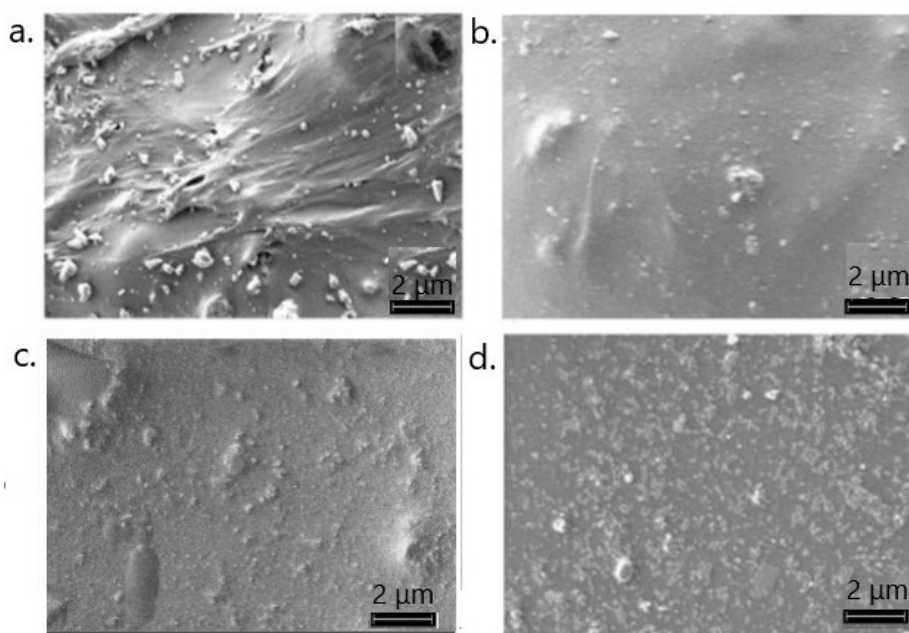


FIG. 2. SEM images of the surface fragments of the plasticized PVC membrane with SWCNT (a, b) and fullerene C60 (c,d) before (a,c) and after (b,d) ultrasonication. The content of nanofillers – 5.0 wt. %

single nanostructures or small-diameter bundles surrounded by plasticizer molecules. The plasticizer probably serves as a carrier of nanoparticles for their distribution in the PVC-matrix [27–30]. It can be assumed the formation of an electrically conductive structure with a segregated scheme of the CNPs arrangement occurs at the polymeric “cores”, completely or partially covered by conducting nanofillers. SEM observations demonstrated that the addition of the C60 to SWCNTs improved their dispersibility in the polymeric matrix (Fig. 3).

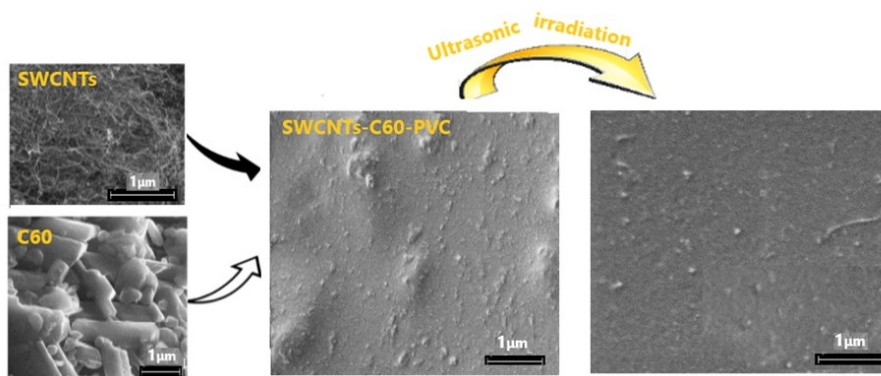


FIG. 3. SEM images demonstrating the formation of the SWCNT-C60-PVC hybrid membrane

Fig. 4 demonstrates the photos of the preparation of C60-Nafion composite membrane. As it can be seen, ultrasonic irradiated C60-Nafion solution has a brown color.

Evidently, the microstructure of Nafion, including the side-pendant ( $-\text{CF}_2-\text{CF}_2-$ ) chains and the highly polar sulfonic terminals as well as the crystalline of PTFE, was changed by the dispersion of C60. As indicated earlier, the fullerene can form both non-covalent binding and donor-acceptor complexes with polymers [47]. Being highly hydrophobic and electronically neutral with zero charge on each atom, C60 can be surrounded by the Nafion chain (oligomer). Probably, the fullerene molecules and their agglomerates are mainly located in the hydrophobic phase of the Nafion matrix creating structure defects or additional paths of proton conduction [48, 49].

### 3.2. Potentiometric performance of the prepared SC-ISEs. Electrode response evaluation

The exact mechanism of functioning of carbon nanomaterials in SC-ISEs has yet to be studied in detail, their behavior as ion-to-electron transducers may be due to electrostatic coupling: the presence of charged ions in an ion-sensitive membrane in close contact with a SC-layer may provide electronic capacitive coupling [50]. The potentiometric response

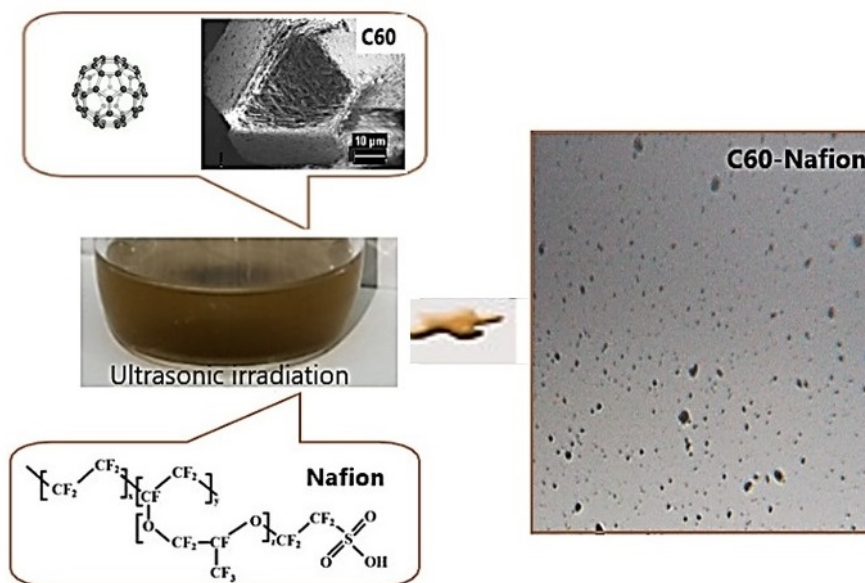


FIG. 4. Schematic illustration of fabrication and photographs of the C60-Nafion composite membrane

of a SC-ISE ( $E$ ) can be determined by the sum of the interphase potentials, as follows:

$$E = \Delta\varphi_{c1} + \Delta\varphi_{c2} + \Delta\varphi_{c3} \quad (1)$$

The potential jump  $\Delta\varphi_{c1}$  at the solid conductor/SC-layer interface is usually very small ( $\approx 0$ ) since most of the nanomaterials used have a high electronic conductivity. The potential jump  $\Delta\varphi_{c2}$  at the SC-layer/ISM interface depends on the amount of charge and the EDL capacitance. If the EDL capacitance is high, the potential change would be small or even near zero. The interfacial potential  $\Delta\varphi_{c3}$  at the ISM/solution sample interface can be described by the well-known Nernst equation or by the semi-empirical Nikolsky-Eisenman equation, according to the phase-boundary potential model, which is based on the assumptions of full thermodynamic equilibrium [51, 52]. As a rule, the e.m.f. for the electrochemical cell ( $E_{cell}$ ) is the sum of all phase boundary potentials and it can be described by the following equation of electrode potential dependence on the logarithm of the ionic activity ( $a_i$ ):

$$E_{cell} = E'_o + s \log a_i, \quad (2)$$

where  $s$  is the slope of a linear electrode response curve;  $E'_o$  is a constant for a given galvanic cell, which depends on the reference electrode potential and all interphase potentials, including  $\Delta\varphi_{c1}$  and  $\Delta\varphi_{c2}$ , except of the interphase potential  $\Delta\varphi_{c3}$  at the ISM/sample solution interface.

Key parameters for evaluating the potentiometric response of SC-ISEs include its sensitivity to a potential-determining ion, signal stability, and reproducibility of the apparent standard potential ( $E'_o$ ). These parameters are largely determined by the nature and concentration of nanofillers in the SC-layer. We performed a series of experiments to compare the potentiometric behavior of the sensors fabricated using different CNPs-filled PVC-matrices as SC-layers (Sensors no. 1–6). The corresponding potentiometric response characteristics for the sensors no. 1–3 towards protonated procaine cations are summarized in Table 1. The mean values of standard potentials and slopes were determined on the basis of calibration plots in the concentration range  $1 \times 10^{-6} - 0.01$  M. As it can be concluded from the obtained results, all prepared sensors provided similar linear calibration graph slopes close to Nernstian response for single-charged ions (slope =  $59.2 \text{ mV} \cdot \text{dec}^{-1}$ ,  $25^\circ \text{C}$ ) within the wide range of the  $\text{ProH}^+$  activity (concentration). It is obvious that their response towards  $\text{ProH}^+$  is determined by the potential-signal appeared mainly by the ISM/sample solution surface reactions [53]. In contrast, the  $E'_o$  value was found to be dependent on the SC-layer composition. This effect is caused primarily by a change in the interphase potential jump  $\Delta\varphi_{c2}$  at the SC-layer/ISM interface. In other words,  $E'_o$  is largely determined by the nature of CNPs in the SC-layer, their interactions with the polymer matrix and with each other. It is noteworthy that the  $E'_o$  obtained for the sensor containing the SC-layer with fullerene nanomolecules is significantly lower than in the case of SWCNTs. This may be due to the special properties of this transducer, in particular to the ability of magical fullerene nanoclusters to non-covalently binding with the plasticized polymer [54].

Remarkably that the  $E'_o$  value highly decreased for sensor no. 3 containing the mixture of SWCNTs and C60 (5.0 wt.%, 1:1). More importantly, this effect was accompanied with the reducing the lower limit of detection (LOD) of  $\text{ProH}^+$  cations. Perhaps, the physicochemical characteristics of this material are not simply a sum of fullerenes and nanotubes. The combination of two nanofillers in a polymer matrix can cause a synergistic effect attributed to their

TABLE 1. Comparative data of potentiometric response characteristics of the fabricated SC-ISEs in Pro-HCl solutions (n=5)

Sensor no.	CNPs (5 wt. %)	Slope, mV·dec. <sup>-1</sup>	Linear range, M	LOD, M	Response time, $\tau_{95}$ ( $\geq 1 \times 10^{-6}$ M)	$E'_o$ , mB
Sensor 1	SWCNTs	$59.2 \pm 0.3$	$9 \times 10^{-7} - 1 \times 10^{-2}$	$10^{-6.52}$	10	421.7
Sensor 2	C60	$59.0 \pm 0.3$	$1 \times 10^{-6} - 1 \times 10^{-2}$	$10^{-6.40}$	12	124.8
Sensor 3	SWCNTs-C60	$58.9 \pm 0.2$	$5 \times 10^{-7} - 1 \times 10^{-2}$	$10^{-7.05}$	7	40.8

large specific surface area and increased electrical properties. This hypothesis can be confirmed by previously published studies [41,55].

Notably, the potentiometric characteristics of such a sensor depend on the content of SWCNTs and C60 in the SC-layer (Fig. 5). It was found that the increasing the nanofiller concentrations  $> 5.0$  wt.% caused the worsening the electrode response characteristics. Perhaps, the heterogeneity of the polymeric film structure increases in the area of high nanofiller concentrations. It can be associated with the formation of inhomogeneities (fullerene clusters, etc.), which reduce the conductivity of the SC-layer by strengthening the physical network of intermolecular contacts and reducing the free path of charge carriers.

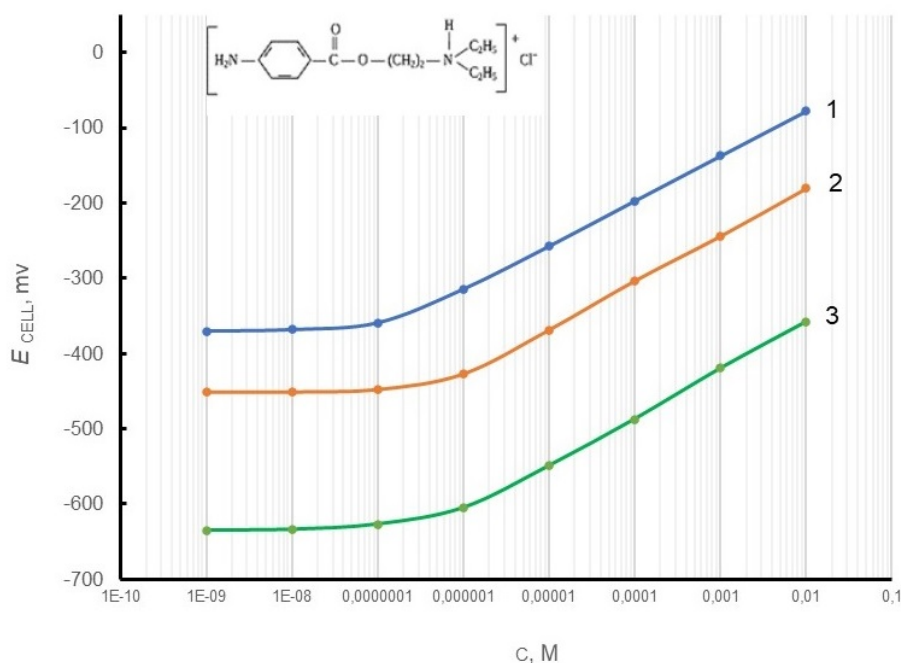


FIG. 5. Electrode functions characterizing the potentiometric response of CS/SWCNT-C60-PVC-ISEs (Sensors no. 3 – 5) towards a protonated procaine cation. The content of the hybrid mixture in SC-layer (wt. %): 1 – SWCNTs/C60 = 2.5/2.5 (Sensor no. 3); 2 – SWCNTs/C60 = 15:5 (Sensor no. 4); 3 – SWCNTs/C60 = 10:10 (Sensor no. 5)

According to the literature, the solid-contact configuration of ISEs appears to be the only approach for wearable potentiometric ion sensing [56, 57]. In view of this goal, the stability of the SC-ISE signal is of crucial importance. A PVC-matrix may exhibit poor mechanical adhesion on electrode substrates. Compared to PVC, Nafion has good adhesion to most electrode surfaces and can protect the surfaces from fouling and deterioration. Therefore, in order to improved potential stability and extend the lifetime of the CS/SWCNT-C60-PVC transducer-based ISE (Sensor no. 3), we have incorporated an additional intermediate layer of C60-Nafion into its construction. Namely, the C60-doped Nafion-matrix was deposited onto the CSE surface followed by its modification with the SWCNTs- C60-PVC film.

To compare the stability and the reversibility of the potentiometric response of SC-ISEs based on the SWCNT-C60-PVC transducer (Sensor no. 3) and the C60-Nafion/SWCNT-C60-PVC transducer (Sensor no. 6), the both electrodes were inserted one-by-one in  $1 \times 10^{-5}$  M Pro-HCl,  $1 \times 10^{-4}$  M Pro-HCl and finally in  $1 \times 10^{-3}$  M Pro-HCl solution for 30 min, and then changed back to  $1 \times 10^{-5}$  M Pro-HCl solution. The potential was monitored over all these intervals.

It was found that CS/C60-Nafion/SWCNT-C60-PVC-based ISE revealed higher potential stability and reversibility than CS/SWCNT-C60-PVC-based ISE, especially when going back to the more dilute solutions (Fig. 6).

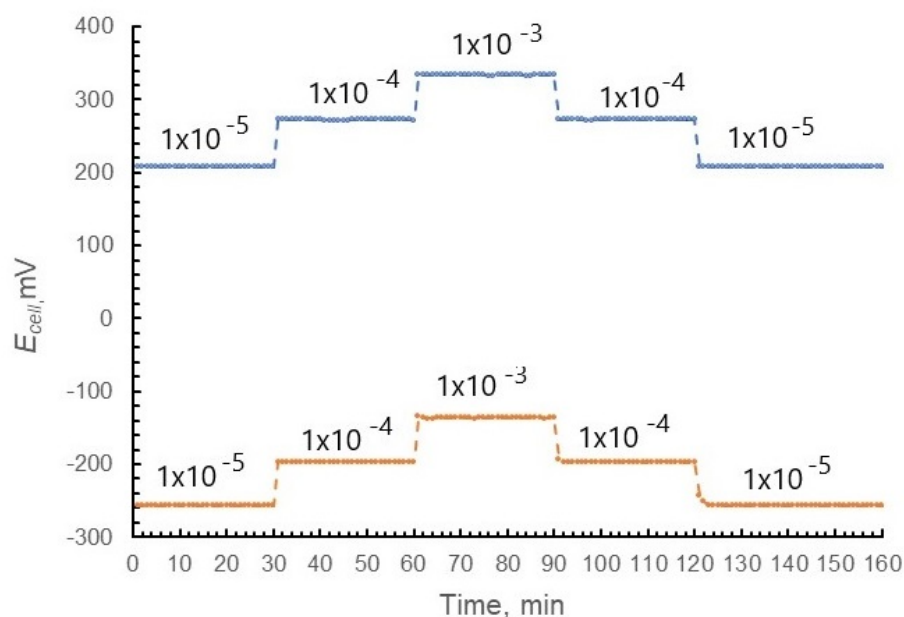


FIG. 6. Reversibility and stability test for (a) CS/SWCNT-C60-PVC-ISE (Sensor no. 3) and (b) CS/C60-Nafion/SWCNT-C60-PVC-ISE (Sensor no. 6) in Pro-HCl solutions (M)

TABLE 2. The analytical performance characteristics of CS/C60-Nafion/SWCNT-C60-PVC/ISM-ISE (Sensor 6) in the solutions of selected protonable nitrogen containing drugs

Sample	$E'_o$ , mB	Slope, $\text{mV} \cdot \text{decade}^{-1}$	Linear range, M	LOD, M
Procaine hydrochloride	506.0	$58.0 \pm 0.1$	$1 \times 10^{-7} - 1 \times 10^{-2}$	$10^{-7.15}$
Lidocaine hydrochloride	506.7	$57.9 \pm 0.2$	$1 \times 10^{-7} - 1 \times 10^{-2}$	$10^{-7.15}$
Articaine hydrochloride	511.9	$58.3 \pm 0.1$	$1 \times 10^{-7} - 1 \times 10^{-2}$	$10^{-7.26}$
Adenine (pH 3)	382.1	$40.5 \pm 0.2$	$1 \times 10^{-7} - 1 \times 10^{-3}$	$10^{-6.30}$
Adrenaline (pH 3)	295.7	$44.9 \pm 0.2$	$1 \times 10^{-4} - 1 \times 10^{-2}$	$10^{-4.40}$

The stability of the potentiometric response was characterized by the level of potential drift that is unrelated to changes in the ionic composition of the sample. It was found that the potential drifts of such electrodes during conditioning in  $1 \times 10^{-5}$  M Pro-HCl were  $\pm 0.14 \text{ mV h}^{-1}$  and  $\pm 0.33 \text{ mV h}^{-1}$  for sensor no. 6 and sensor no. 3, respectively. In addition, in case of the sensor no. 6, lower LOD ( $10^{-7.15}$ ) and shorter response time ( $\leq 5$  s) were achieved, and the standard derivation of a slope of the potentiometric response curve (s) was only  $0.12 \text{ mV} \cdot \text{decade}^{-1}$  (over 7 days). All of these results showed that the addition of the C60-Nafion layer improved the properties of the fabricated SC-ISE and reflected the high efficiency of the layer-by-layer ion-to-electron transducer. In this case, the plasticized SWCNTs-C60-PVC membrane plays the role of a binder (a kind of a porous solid contact) between the ion-sensitive membrane and the C60-Nafion layer.

### 3.3. Electroanalytical capability

Ion-selective electrodes are selective but not specific. They can respond to a variety of ions in solutions. In case of ion-pair complexes based ISMs, the selectivity is usually controlled by the free hydration energies of the ions and the specificity of their interaction with the binding center. For comparison, we have investigated response characteristics of the newly prepared CS/C60-Nafion/SWCNT-C60-PVC/ISM-ISE towards several important protonable nitrogen containing drugs like procaine. Of course, the ISM pretreatment required the formation of ion-pair complexes of analyte ions with the recognizing compound at the interface between the membrane and solution. Therefore, prior to measurements, the sensor was conditioned in a 1.0 mM solution of each determinant for 1–3 h. When measuring, we took into account that the membrane-active species are the protonated cationic forms of an analyte. As shown in Table 2, the fabricated sensor no. 6

showed a linear response for all analytes tested over a concentration range of almost 4 decades with considerable stability. The sub-Nernstian slopes obtained for adenine and adrenaline is likely due to the partial existence of biprotonated or non-protonated analyte forms in the solutions under study. Overall, the developed sensor can be recommended to the simple and fast control of the protonable nitrogen containing active ingredients in drugs.

#### 4. Conclusion

According to the latest trends, such as the concept of “green chemistry” and “wearable sensors”, solid-contact ion-selective electrodes should become excellent inexpensive, low energy and portable devices for the chemical analysis. This work demonstrated that nanocarbon-modified PVC composite materials show high efficiency as ion-to-electron transducers in SC-ISEs with operationally stable and reproducible potentials. The integration of the superior properties of nanocomposite PVC and Nafion membranes made it possible to create a layer-by-layer potentiometric membrane sensor for the highly sensitive determination of procaine and other protonable nitrogen-containing drugs in a wide range of concentrations.

#### References

- [1] Shao Y., Ying Y., Ping J. Recent advances in solid-contact ion-selective electrodes: functional materials, transduction mechanisms, and development trends. *Chem. Soc. Rev.*, 2020, **49**(13), P. 4405–4465.
- [2] Nikolskii B.P., Materova E.A. *Solid contact in membrane ion-selective electrodes*. Leningrad, 1985, 39 pp.
- [3] Zhang Y., Tang Y., Liang R., Zhong L., Xu J., Lu H., Xu X., Han T., Bao Y., Ma Y., et al. Carbon-based transducers for solid-contact calcium ion-selective electrodes: mesopore and nitrogen-doping effects. *Membranes*, 2022, **12**(9), P. 12090903.
- [4] Düzgün A., Zelada-Guillén G.A., Crespo G.A., Macho S., Riu J., Rius F.X. Nanostructured materials in potentiometry. *Anal. Bioanal. Chem.*, 2011, **399**(1), P. 171–181.
- [5] Yin T., Qin W. Applications of nanomaterials in potentiometric sensors. *Trends Anal. Chem.*, 2013, **51**, P. 79–86.
- [6] Bieg C., Fuchsberger K., Stelzle M. Introduction to polymer-based solid-contact ion-selective electrodes—basic concepts, practical considerations, and current research topics. *Anal. Bioanal. Chem.*, 2017, **409**(1), P. 45–61.
- [7] Huang M.-R., Li X.-G. Highly sensing and transducing materials for potentiometric ion sensors with versatile applicability. *Prog. Mater. Sci.*, 2022, **125**, P. 100885.
- [8] Fibbioli M., Morf W.E., Badertscher M., Rooij N.F. de, Pretsch E. Potential drifts of solid-contacted ion-selective electrodes due to zero-current ion fluxes through the sensor membrane. *Electroanalysis*, 2000, **12**(16), P. 1286–1292.
- [9] Birinci A., Eren H., Coldur F., Coskun E., Andac M. Rapid determination of trace level copper in tea infusion samples by solid contact ion-selective electrode. *J. Food Drug. Anal.*, 2016, **24**(3), P. 485–492.
- [10] Liu Y., Liu Y., Gao Y., Wang P. A general approach to one-step fabrication of single-piece nanocomposite membrane based  $Pb^{2+}$ -selective electrodes. *Sens. Actuator B Chem.*, 2019, **281**, P. 705–712.
- [11] Papp S., Kozma J., Lindfors T., Gyurcsányi R.E. Lipophilic multi-walled carbon nanotube-based solid contact potassium ion-selective electrodes with reproducible standard potentials. A comparative study. *Electroanalysis*, 2020, **32**(4), P. 867–873.
- [12] Crespo G.A., Macho S., Bobacka J., Rius F.X. Transduction mechanism of carbon nanotubes in solid-contact ion-selective electrodes. *Anal. Chem.*, 2009, **81**, P. 676–681.
- [13] Cuartero M., Bishop J., Walker R., Acres R.G., Bakker E., Marco R.De, et al. Evidence of double layer/capacitive charging in carbon nanomaterial-based solid contact polymeric ion-selective electrodes. *Chem. Commun.*, 2016, **52**(62), P. 9703–9706.
- [14] Cheong Y.H., Ge L., Lisak G. Highly reproducible solid contact ion selective electrodes: Emerging opportunities for potentiometry – A review. *Anal. Chim. Acta*, 2021, **1162**, P. 338304.
- [15] Gadhari N.S., Gholave J.V., Patil S.S., Patil V.R., Upadhyay S.S. Enantioselective high performance new solid contact ion-selective electrode potentiometric sensor based on sulphated  $\gamma$ -cyclodextrin-carbon nanofiber composite for determination of multichiral drug moxifloxacin. *J. Electroanal. Chem.*, 2021, **882**, P. 114981.
- [16] Bobacka J., Ivaska A., Lewenstam A. Potentiometric ion sensors. *Chem. Rev.*, 2008, **108**(2), P. 329–351.
- [17] Paczosa-Bator B. Ion-selective electrodes with superhydrophobic polymer/carbon nanocomposites as solid contact. *Carbon N Y*, 2015, **95**, P. 879–887.
- [18] Piek M., Piech R., Paczosa-Bator B. All-solid-state nitrate selective electrode with graphene/tetrathiafulvalene nanocomposite as high redox and double layer capacitance solid contact. *Electrochim. Acta*, 2016, **210**, P. 407–414.
- [19] Kałuza D., Jaworska E., Mazur M., Maksymiuk K., Michalska A. Multiwalled carbon nanotubes–poly (3-octylthiophene-2, 5-diyl) nanocomposite transducer for ion-selective electrodes: Raman spectroscopy insight into the transducer membrane interface. *Anal. Chem.*, 2019, **91**(14), P. 9010–9017.
- [20] Mousavi Z., Bobacka J., Lewenstam A., Ivaska A. Poly(3,4-ethylenedioxythiophene) (PEDOT) doped with carbon nanotubes as ion-to-electron transducer in polymer membrane-based potassium ion-selective electrodes. *J. Electroanal. Chem.*, 2009, **633**(1), P. 246–252.
- [21] Szűcs J., Lindfors T., Bobacka J., Gyurcsányi R.E. Ion-selective electrodes with 3D nanostructured conducting polymer solid contact. *Electroanalysis*, 2016, **28**(4), P. 778–786.
- [22] Boeva Z.A., Lindfors T. Few-layer graphene and polyaniline composite as ion-to-electron transducer in silicone rubber solid-contact ion-selective electrodes. *Sens. Actuators B Chem.*, 2016, **224**, P. 624–631.
- [23] Ardalani M., Shamsipur M., Besharati-Seidani A. A new generation of highly sensitive potentiometric sensors based on ion imprinted polymeric nanoparticles/multiwall carbon nanotubes/polyaniline/graphite electrode for sub-nanomolar detection of lead(II) ions. *J. Electroanal. Chem.*, 2020, **879**, P. 114788.
- [24] Abd-Rabboh H.S.M., H. Kamel A., Amr A.E.-G.E.. All-solid-state calcium sensors modified with polypyrrol (PPY) and graphene oxide (GO) as solid-contact ion-to-electron transducers. *Chemosensors*, 2020, **8**(4), P. 93.
- [25] Marco R. De, Veder J.-P., Clarke G., Nelson A., Prince K., Pretsch E. et al. Evidence of a water layer in solid-contact polymeric ion sensors. *Phys. Chem. Chem. Phys.*, 2008, **10**(1), P. 73–76.
- [26] Veder J.-P., Marco R. De, Clarke G., Chester R., Nelson A., Prince K. et al. Elimination of Undesirable Water Layers in Solid-Contact Polymeric Ion-Selective Electrodes. *Anal. Chem.*, 2008, **80**(17), P. 6731–6740.

- [27] Broza G., Piszczek K., Schulte K., Sterzynski T. Nanocomposites of poly(vinyl chloride) with carbon nanotubes (CNT). *Compos. Sci. Technol.*, 2007, **67**(5), P. 890–894.
- [28] Ashrapov A.K., Abdrakhmanova L.A., Nizarov R.K., Khosin V.G. *Development of effective ways of introducing nanofillers to PVC composites*. Kazan, Materials of RAACS XV workshop, 2010, V.1, P. 272–278.
- [29] Trommer K., Petzold C., Morgenstern B. Processing and properties of carbon nanotube PVC composites. *J. Appl. Chem.*, 2014, P. 1–10.
- [30] Seeponkai N., Wootthikanokkhan J., Thanachayanont C. Synthesis and characterization of fullerene functionalized poly(vinyl chloride) (PVC) and dehydrochlorinated PVC using atom transfer radical addition and AIBN based fullerenation. *J. Appl. Polym. Sci.*, 2013, **130**(4), P. 2410–2421.
- [31] Wilczewski S., Skórczewska K., Tomaszewska J., Lewandowski K. Structure and properties of poly(vinyl chloride)/graphene nanocomposites. *Polym. Test.*, 2020, **81**, P. 106282.
- [32] Francis E., Tippabattini J., Choi E.-S., Thomas S., Kim J. Morphology and dielectric properties of poly(vinyl chloride)-[multiwalled carbon nanotube-barium titanate] hybrid composite. *Nanosensors, Biosensors, Info-Tech Sensors and 3D Systems*, 2017, Portland, Oregon, April, 2017, P. 101671V.
- [33] Arunachalam P. Polymer-based nanocomposites for energy and environmental applications. In book: *Polymer-based nanocomposites for energy and environmental applications*. Elsevier, 2018, P. 185–203.
- [34] Skyrzewska K., Lewandowski K., Wilczewski S. Novel composites of poly(vinyl chloride) with carbon fibre/carbon nanotube hybrid filler. *Materials* (Basel), 2022, **15**(16), P. 5625.
- [35] Hu C., Yuan S., Hu S. Studies on electrochemical properties of MWNTs-Nafion composite films based on the redox behavior of incorporated  $\text{Eu}^{3+}$  by voltammetry and electrochemical impedance spectroscopy. *Electrochim. Acta*, 2006, **51**(15), P. 3013–3021.
- [36] Jung J.-H., Vadahanambi S., Oh I.-K. Electro-active nanocomposite actuator based on fullerene-reinforced Nafion. *Comp. Sci. Tech.*, 2010, **70**(4), P. 584–592.
- [37] Lee K., Lee J.-W., Kim S.-I., Ju B. Single-walled carbon nanotube/Nafion composites as methanol sensors. *Carbon*, 2011, **49**(3), P. 787–792.
- [38] Jeon J.-Y., Kang B.-C., Ha T.-J. Flexible pH sensors based on printed nanocomposites of single-wall carbon nanotubes and Nafion. *Appl. Surf. Sci.*, 2020, **514**, P. 145956.
- [39] Tajeu K.Y., Dongmo L., Tonle I.K. Fullerene/MWCNT/Nafion modified glassy carbon electrode for the electrochemical determination of caffeine. *Am. J. Analyt. Chem.*, 2020, **11**, P. 114–127.
- [40] Titova T.S., Yurova P.A., Kolganova I.S., Stenina L.A., Parshina A.V., Bobreshova O.V., Yaroslavtsev A.V. Potentiometric sensors based on nafion membranes modified by PEDOT for determining procaine, lidocaine and bupivacaine in aqueous solutions and pharmaceuticals. *J. Analyt. Chem.*, 2020, **75**, P. 1072–1079.
- [41] Hussein M.A., Alam M.M., Asiri Ab.M., Al-amshany Z.M., Hajeassa Kh.S., Rahman M.M., Ultrasonic-assisted fabrication of poly(vinyl chloride)/mixed graphene-carbon nanotube nanocomposites as a selective  $\text{Ag}^+$  ionic sensor. *J. Comp. Mat.*, 2019, 002199831882529.
- [42] Bartoszewicz B., Dabrowska S., Lewenstam A., Migdalski J., Calibration free solid contact electrodes with two PVC based membranes. *Sens. Actuators: B. Chem.*, 2018, **274**, P. 268–273.
- [43] Turyshev E.S., Kopytin A.V., Zhizhin K.Y., Kubasov A.S., Shpigun L.K., Kuznetsov N.T. Potentiometric quantitation of general local anesthetics with a new highly sensitive membrane sensor. *Talanta*, 2022, **241**, P. 123239.
- [44] Kubasov A.S., Turishev E.S., Kopytin A.V., Shpigun L.K., Zhizhin K.Y., Kuznetsov N.T. Sulfonium closo-hydridodecaborate anions as active components of a potentiometric membrane sensor for lidocaine hydrochloride. *Inorg. Chim. Acta*, 2021, **514**, P. 119992.
- [45] Perelmuter M.N. Mechanical modelling of nanotube-polymer adhesion. *Nanosystems: Physics, Chemistry, Mathematics*, 2011, **2**(2), P. 119–125.
- [46] Zhang D., Sun J., Lee L.J., Castro J.M. Overview of ultrasonic assisted manufacturing multifunctional carbon nanotube nanopaper based polymer nanocomposites. *Eng. Sci.*, 2020, **10**, P. 35–50.
- [47] Tasaki K., Gasa J., Wang H., DeSousa R. Fabrication and characterization of fullerene–Nafion composite membranes. *Polymer* (Guildf), 2007, **48**(15), P. 4438–4448.
- [48] Postnov D.V., Menshikov I.A., Postnov V.N., Melnikova N.A., Glumov O.V., Murin I.V. Nafion-based nanocomposites containing fulleroid materials. *Vestnik of St. Petersburg State University. Ser. 4*, 2012, P. 84–88.
- [49] Postnov D.V., Melnikova N.A., Postnov V.N., Semenov K.N., Murin I.V. Nafion-based nanocomposites with light fullerenes and their functionalized derivatives. *Rev. Adv. Mater. Sci.*, 2014, **39**(1), P. 20–24.
- [50] Lyu Y., Gan S., Bao Y., Zhong L., Xu J., Wang W. et al. Solid-contact ion-selective electrodes: response mechanisms, transducer materials and wearable sensors. *Membranes* (Basel), 2020, **10**(6), P. 128.
- [51] Bakker E. The phase-boundary potential model. *Talanta*, 2004, **63**(1), P. 3–20.
- [52] Bakker E., Pretsch E. Modern Potentiometry. *Angew. Chem. Int. Ed.*, 2007, **46**(30), P. 5660–5668.
- [53] Pungor E. The new theory of ion selective electrodes. *Sensors*, 2001, **1**, P. 1–12.
- [54] Badamshina E.R., Gafurova M.P. Characteristics of fullerene C60-doped polymers. *Polymer Sci. B*, 2008, **50**(7-8), P. 215–225.
- [55] Guldi D.M., Menna E., Maggini M., Marcaccio M., Paolucci D., Paolucci F., et al. Supramolecular hybrids of [60]fullerene and single-wall carbon nanotubes. *Chem - A. Eur. J.*, 2006, **12**(15), P. 3975–3983.
- [56] Cuartero M., Parrilla M., Crespo G.A. Wearable potentiometric sensors for medical applications. *Sensors*, 2019, **19**, P. 363–387.
- [57] Yeung K.K., Li J., Huang T., Hosseini I.I., Al Mahdi R., Alam M.M., Sun H., Mahshid S., Yang J., Ye T.T., et al. Utilizing gradient porous graphene substrate as the solid-contact layer to enhance wearable electrochemical sweat sensor sensitivity. *Nano Lett.*, 2022, **22**, P. 6647–6654.

---

Submitted 10 October 2022; revised 21 November 2022; accepted 23 November 2022

#### Information about the authors:

*Konstantin Yu. Zhizhin* – N. S. Kurnakov Institute of General and Inorganic Chemistry of Russian Academy of Sciences, Leninskii pr.31, Moscow 119991, Russia; ORCID 0000-0002-4475-124X; kyuzhizhin@igic.ras.ru

*Evgeniy S. Turyshev* – N. S. Kurnakov Institute of General and Inorganic Chemistry of Russian Academy of Sciences, Leninskii pr.31, Moscow 119991, Russia; ORCID 0000-0002-0594-5500; tyrishev@gmail.com

*Aleksander V. Kopytin* – N. S. Kurnakov Institute of General and Inorganic Chemistry of Russian Academy of Sciences, Leninskii pr.31, Moscow 119991, Russia; ORCID 0000-0003-3366-5167; ionix@igic.ras.ru

*Liliya K. Shpigun* – N. S. Kurnakov Institute of General and Inorganic Chemistry of Russian Academy of Sciences, Leninskii pr.31, Moscow 119991, Russia; ORCID 0000-0001-9749-2942; liliaspigun@gmail.com; shpigun@igic.ras.ru

*Nikolay T. Kuznetsov* – N. S. Kurnakov Institute of General and Inorganic Chemistry of Russian Academy of Sciences, Leninskii pr.31, Moscow 119991, Russia; ORCID 0000-0002-2562-6427

*Nikolay P. Simonenko* – N. S. Kurnakov Institute of General and Inorganic Chemistry of Russian Academy of Sciences, Leninskii pr.31, Moscow 119991, Russia; ORCID 0000-0002-4209-6034

*Natalya N. Zamyatina* – N. S. Kurnakov Institute of General and Inorganic Chemistry of Russian Academy of Sciences, Leninskii pr.31, Moscow 119991, Russia; yatina.76@bk.ru

*Mukhammadislom S. Madraimov* – N. S. Kurnakov Institute of General and Inorganic Chemistry of Russian Academy of Sciences, Leninskii pr.31, Moscow 119991, Russia

*Gleb I. Betenev* – N. S. Kurnakov Institute of General and Inorganic Chemistry of Russian Academy of Sciences, Leninskii pr.31, Moscow 119991, Russia

*Conflict of interest:* the authors declare no conflict of interest.

## High lignin content cellulose nanofibrils obtained from thermomechanical pulp

Anna A. Luginina<sup>1,a</sup>, Sergey V. Kuznetsov<sup>1,b</sup>, Alexander A. Alexandrov<sup>1,c</sup>, Radmir V. Gainutdinov<sup>2,d</sup>, Dmitrii I. Petukhov<sup>3,e</sup>, Valery V. Voronov<sup>1,f</sup>, Elena V. Chernova<sup>1,g</sup>, Pavel P. Fedorov<sup>1,h</sup>

<sup>1</sup>Prokhorov General Physics Institute of the Russian Academy of Sciences, Moscow, Russia

<sup>2</sup>Shubnikov Institute of Crystallography of Federal Scientific Research Centre Crystallography and Photonics of Russian Academy of Sciences, Moscow, Russia

<sup>3</sup>Lomonosov Moscow State University, Chemical department, Moscow, Russia

<sup>a</sup>ana@lst.gpi.ru, <sup>b</sup>kouznetzovsv@gmail.com, <sup>c</sup>alexandrov1996@yandex.ru, <sup>d</sup>rgaynutdinov@gmail.com, <sup>e</sup>di.petukhov@gmail.com, <sup>f</sup>voronov@lst.gpi.ru, <sup>g</sup>e-chernova@yandex.ru, <sup>h</sup>ppfedorov@yandex.ru

Corresponding author: P. P. Fedorov, ppfedorov@yandex.ru

**ABSTRACT** High-lignin content cellulose nanofibrils (LCNF) were successfully prepared from thermomechanical pulp through TEMPO-catalyzed oxidation, followed by ultrasonic treatment. Preparation protocols of the LCNFs included use of the mild pre-hydrolysis of the thermomechanical pulp and adjustment of sodium hypochlorite loading for the samples with the 23.8 and 14.1 wt.% lignin content, resulting in the increase of the carboxyl group content from 0.70 to 1.24 mmol/g. LCNFs had a diameter of  $14 \pm 5$  nm (AFM evaluation); and the LCNF morphology was affected by contents of both lignin and carboxyl groups. The translucent LCNF films were prepared by solution casting technique. They exhibited the heightened water contact angle of 75–82°, an increased thermal stability up to 275°C compared to lignin-free cellulose nanofibril films (39° and 203°C, respectively), and excellent UV-blocking ability in a wide spectrum range from 200 to 375 nm. The said LCNFs can be successfully used for manufacturing the packaging materials and/or making the biopolymer composites.

**KEYWORDS** cellulose, lignin, nanofibrils, nanocomposites, UV-blocking ability.

**ACKNOWLEDGEMENTS** This work was supported by the Ministry of Science and Higher Education within the State assignment to Prokhorov General Physics Institute of the Russian Academy of Sciences. The TG measurements were supported by the equipment of the Collective Use Center of the Prokhorov General Physics Institute of the Russian Academy of Sciences. We thank Volga Corporation for providing thermomechanical pulp sample. Authors express their sincere gratitude to Dr. Arthur I. Popov for his most kind assistance in the preparation of the present manuscript and Mr. Ilya Tronev for conductometric titration measurements.

**FOR CITATION** Luginina A.A., Kuznetsov S.V., Alexandrov A.A., Gainutdinov R.V., Petukhov D.I., Voronov V.V., Chernova E.V., Fedorov P.P. High lignin content cellulose nanofibrils obtained from thermomechanical pulp. *Nanosystems: Phys. Chem. Math.*, 2022, **13** (6), 698–708.

### 1. Introduction

Cellulose nanofibrils (CNF), obtained from various cellulose sources, attracted attention of modern researchers as “green alternative” for plastics used in polymer composites, packaging materials, optoelectronic and electronic materials, detectors, medicine and healthcare, etc. [1–10]. For the first time, CNFs were obtained by mechanical fibrillation of cellulose fibers in high-pressure homogenizer in 1983 [11, 12]. In subsequent years, researchers focused their attention at manufacturing completely bleached lignin-free CNFs by various cellulose fibrillation techniques such as microfluidization, grinding/refining, milling, cryo-crushing, steam explosion, and ultrasonication [13, 14]. Recently, a new strategy of direct conversion of lignocellulose into nanofibrils was suggested; and it resulted in the preparation of so-called lignin-containing nanofibrils (LCNF) [15–20]. Also, the said recent publications [16–18] disclose preparation of LCNF from various lignocellulose sources including wood species, plant-based biomass, unbleached kraft pulp, etc. Making LCNF is more efficient and ecologically friendly compared to CNF manufacturing because of the use of non-delignified raw material, requires less energy and smaller amounts of chemical reagents; it also allows more rational and complete use of renewable resources.

Lignin is an amorphous aromatic copolymer; it is a major incrusting ingredient of the plant cell walls: the latter are made up of durable cellulose nanofibrils that are built in the lignin-hemicellulose matrices [21]. Lignin is more hydrophobic than cellulose; it possesses UV-protecting, antibacterial and antioxidant properties [22, 23]. As a result, lignin is used as green reinforcing component of CNF UV-protecting films [24–26].

Composite nano-lignin CNF films have exhibited antibacterial activity against *Escherichia coli* and hemolytic streptococci [26]. Authors [27–29] emphasized that lignin improved hydrophobicity of LCNFs compared to the one of CNFs. As a result, enhanced LCNF hydrophobicity allowed use of the said materials as ingredients of hydrophobic matrix composites [30–33].

Thus, the thermomechanical pulp (TMP) with high content of lignin can become an important starting material for making LCNF in order to provide the manufactured materials with the hydrophobic, UV-protecting and/or antibacterial properties. However, the presence of lignin lowers efficiency of cellulose fibrillation under mechanical treatment [20]. The said fibrillation efficiency can be improved by preliminary enzymatic or chemical treatment like 2,2,6,6-tetramethylpiperidine-1-oxyl radical (TEMPO) mediated oxidation, which is used quite frequently because of the high homogeneity of obtained CNFs. Such TEMPO-catalyzed oxidation of cellulose was originally implemented by Isogai and Kato in 1998 [34], and it was optimized later by Isogai and Saito [35,36] for making CNFs from cotton and bleached pulp.

In view of the above said, the goals of our present study were preparation of lignin containing cellulose nanofibrils from thermomechanical pulp of spruce and making hydrophobic films with UV blocking effect based on the said nanofibrils.

## 2. Experimental methods

### 2.1. Materials

As the starting materials, we used 15 wt.% spruce thermomechanical pulp (TMP) (Volga company, Balakhna, Nizhny Novgorod region, Russia), powdered bleached woodkraft cellulose (PCC-0.25) (Polycell, Vladimir, Russia), 99% pure TEMPO (NIOCH SB RAS, Russia) 19 wt.% sodium hypochlorite solution; sodium bromide; sodium hydroxide; and hydrochloric acid (analytical grade) (all four reagents were supplied by Chimmed, Russia).

### 2.2. TMP pre-treatments

The TMP samples were squeezed out on a nylon mesh and dried under air for the further storage and use. Before their use, TMP specimens were ground in the laboratory mill LZM-1M with the rotary knife. Shredded TMP fibers (2.0 wt.%) were swollen in double distilled water at room temperature for 12 h, then refrigerated below 5°C for 30 days. The resulting samples were labeled as TMP<sub>pr</sub>.

### 2.3. Control samples

Lignin-free TEMPO-oxidized cellulose nanofibrils (TOCNF) samples were prepared from PCC-0.25 powdered wood bleached kraft cellulose according to the previously published technique [37] and served as control specimens.

### 2.4. TEMPO-mediated oxidation of TMP

TEMPO-mediated oxidation of TMP was carried out by modified [8,37] techniques (see protocols 1 and 2 below).

**2.4.1. Protocol 1.** 100 ml of 11.5 M HCl was slowly added under stirring to prepared as described above 500 g of lignocellulose fiber TMP<sub>pr</sub> (2.0 wt.%). Obtained ~2 M HCl solution was placed in the 80°C water bath and hydrolyzed under vigorous stirring for 30 min. The reaction was quenched by 10-fold dilution with cold double distilled water. Then, the obtained suspension was washed with double distilled water, using repeated centrifugation cycles, until pH 5.0 was reached. The content of hydrolyzed lignocellulose fiber was determined gravimetrically. 400 ml of aqueous solution of 0.1600 g TEMPO and 1.0000 g NaBr was added to the resulting suspension of 10 g of hydrolyzed lignocellulosic fiber in 600 ml of water, and the formed mixture was stirred for 10 minutes. Oxidation was initiated by slow dropwise addition of 11.9 wt.% NaClO solution (5 mmol/g TMP) with constant stirring at room temperature. The pH of the suspension was maintained at 10.2–10.5 and, if necessary, adjusted by adding 0.3 M NaOH. The oxidation reaction was completed and the suspension pH levelled off in about 50 min. Then, pH was further adjusted to about 7.0 by adding 0.5 M HCl. The supernatant was separated from the precipitate, the latter was suspended in H<sub>2</sub>O and centrifuged at 8000 rpm for 10 minutes. The centrifuged precipitate was redispersed in double distilled water, ultrasonicated in the ice bath at 35 kHz frequency for 30 minutes, and subjected to dialysis against water for 7 days. After dialysis, the suspension was once again ultrasonicated in an ice bath for 30 minutes. The resulting lignin-containing cellulose nanofibrils samples were labeled as LCNF<sub>1</sub> and stored at 4°C. The LCNF content in the LCNF<sub>1</sub> dispersion was determined gravimetrically.

**2.4.2. Protocol 2.** 500 g of lignocellulosic fiber TMP<sub>pr</sub> sample (2.0 wt.%), prepared as described above, was treated with 500 ml aqueous solution containing 0.1600 g TEMPO and 1.0000 g NaBr under stirring for 10 minutes. The oxidation was initiated by the slow addition of 11.9 wt.% aqueous NaClO to 10 mmol/g TMP under constant stirring at room temperature. The pH of the suspension was maintained at 10.2–10.5 and, if necessary, adjusted by adding 0.3 M NaOH. After 65 min, the oxidation reaction was completed, pH of the suspension stopped changing, and the reaction mixture pH was adjusted to about 7.0 by adding 0.5 M HCl. The further work-up procedure was similar to the one described above in the protocol 1. The resulting lignin-containing cellulose nanofibrils samples were labeled as LCNF<sub>2</sub> and stored at 4°C. The LCNF content in the LCNF<sub>2</sub> dispersion was determined gravimetrically.

## 2.5. Fabrication of lignin containing cellulose nanofibrils films

Suspensions of LCNF<sub>1</sub> or LCNF<sub>2</sub> were diluted with double distilled water to the 1.0–2.2 wt.% solids content. 10 ml specimens of the obtained suspensions were ultrasonicated in an ice bath for 5 minutes (UZG13-01/22 sonicator, 110 W, VNIITVCH), poured into polystyrene Petri dishes (35 mm diameter), and dried under ambient conditions for 3–4 days. After evaporation of the solvent, the formed LCNF<sub>1</sub> and LCNF<sub>2</sub> films were carefully separated from the plastic substrates as a self-standing structure. Subsequent drying of the films was carried out at 70 °C for 40 min.

## 2.6. Characterization

X-ray diffraction analysis of the samples was carried out on a Bruker D8 Advance diffractometer (Bruker AXS GmbH, Karlsruhe, Germany) on CuK $\alpha$ -radiation in the angular range 8–60 °2 $\theta$ , in steps of 0.02 °2 $\theta$ . The diffraction peak about 22.7 2 $\theta$  was used for TOCNF crystallinity index (IC, %) calculation by Segal's method [4].

Conductometric titration was used to determine carboxyl groups content in mmol/g of LCNF according to the protocol described elsewhere [38]. The conductivity values were recorded using conductometer Expert-002 at room temperature as the mean value of three measurements.

The surface morphology and roughness were investigated using a NTEGRA Prima atomic force microscope (NTMDT Spectrum Instruments, Russia) in tapping mode. All experiments were carried out under controlled conditions maintained by a TRACKPORE ROOM-05 measuring complex (purity class 5 ISO (100), the accuracy of maintaining air temperature in the range 23 ± 5 K is ±0.05 K, the relative air humidity is 55 ± 1 %). The average roughness (Ra) was measured from the AFM image for 10  $\mu\text{m}$  × 10  $\mu\text{m}$  scanning area.

Thermogravimetric analysis (TG) was performed in 23–650 °C range with 5 °C/min heating rate in a synthetic air flow (50 ml/min) and an argon flow (20 ml/min) using a STA 449F3 Jupiter calorimeter with a TG sensor (Netzsch, Germany). The weight part was preliminarily calibrated by the decomposition of a standard reagent, calcium oxalate hydrate CaC<sub>2</sub>O<sub>4</sub> · xH<sub>2</sub>O.

Fourier transform infrared spectroscopy (FTIR) was performed on an INFRALUM FT-08 spectrometer with ATR unit (Pike) from 400 to 4000 cm<sup>-1</sup>.

The transmission spectra were recorded using a Cary 5000 spectrophotometer in the 200–800 nm range.

The contact angle was measured on a FTA1000 Drop Shape Instrument B Frame System. The test sample was placed on a horizontal holder. The water was applied onto the surface of the test sample by a special microdosing syringe. The droplet volume was 100  $\mu\text{l}$ . The images were recorded using a CCD detector of 640·480 pixels. Images were obtained after 1 s application of the droplets. The measurements were performed at room temperature (24 ± 2 °C) and repeated 5 times on various fresh surfaces.

The chemical composition of dried up at 105 °C samples TMP and LCNF was determined in accordance with the standards of the Technical Association of the Pulp and Paper Industry (TAPPI). The holocellulose (alfa-cellulose + hemicelluloses) content was determined according to the method described in TAPPI 249-75. The alpha-cellulose content was then determined by T203-99. The difference between the values of holocellulose and alfa-cellulose content gives the hemicellulose content [39]. The lignin in lignocellulosic fiber (TMP, LCNF<sub>1</sub> and LCNF<sub>2</sub>) includes acid-insoluble lignin and acid-soluble lignin. Acid-insoluble lignin content was analyzed by reaction with 72% H<sub>2</sub>SO<sub>4</sub>, using a standard method recommended in TAPPI T222 om-88. The acid-soluble lignin content was determined in the filtrate after the separation of acid-insoluble lignin by the spectrophotometric method at a wavelength of 240 nm [40]. Each sample was tested three times, and the averaged values were obtained.

## 3. Results and discussion

### 3.1. Preparation of LCNF with different lignin contents

The chemical composition of the original lignocellulosic raw material was compared with the composition of obtained LCNF. Thermomechanical pulping is the process of producing wood pulp at elevated temperature and pressure in refiners from pre-steamed wood chips at a temperature of about 125 °C. With such thermo-hydrolytic treatment, some of the organic substances contained in wood can dissolve in water [41]. The chemical composition of samples on dry weight and yields of LCNF from each protocol are shown in Table 1. It can be seen from the data that the cellulose content and the total content of the main components in TMP<sub>pr</sub> slightly increased compared to wood chips, by 2.8% and 2.0%, respectively, which indicates the removal of extractives, including terpenes, resin and fatty acids.

The results showed that the LCNF<sub>1</sub> yield was slightly (1%) higher than the LCNF<sub>2</sub> yield. LCNF yield from native wood was about 2 times higher than TOCNF, Table 1. During TEMPO oxidation, the content of  $\alpha$ -cellulose in TOCNF increased, the content of hemicelluloses decreased, and lignin was absent. Previously, it was shown that selective oxidation of the primary hydroxyl groups of cellulose occurs, as well as the decomposition of hemicelluloses and the oxidation of lignin during TEMPO oxidation [35, 36]. The content of lignin decreased in both protocols when using TMP<sub>pr</sub>, much decreased by twice in protocol 2 when using higher doses of NaClO. The increase in oxidation in the case of LCNF<sub>2</sub> is confirmed by a higher carboxyl group content of 1.24 mmol/g compared to 0.70 mmol/g in LCNF<sub>1</sub>, Table 1. The amount of lignin decreased by Protocol 1 compared to TMP<sub>pr</sub> by 4.7%, however, the amount of lignin in LCNF<sub>1</sub> (23.8%)

TABLE 1. Chemical composition of samples on dry weight and yields of LCNF from each protocol

Sample	$\alpha$ -cellulose, wt. %	Hemicelluloses, wt. %	Lignin, wt. %			Yield, (%)		Carboxyl group content ( $C_{cg}$ ), mmol/g
			total	acid-insoluble	acid-soluble	process output	from native wood	
spruce wood <sup>[42]</sup>	42	25	29			–		–
TMP <sub>pr</sub>	44.8 ± 0.5	24.7 ± 0.2	28.5 ± 0.3	27.7	0.8	–	94 <sup>[41]</sup>	–
LCNF <sub>1</sub>	68.4 ± 0.5	5.7 ± 0.2	23.8 ± 0.3	23.1 ± 0.3	0.7 ± 0.2	65	61	0.70 ± 0.05
LCNF <sub>2</sub>	69.5 ± 0.5	14.3 ± 0.2	14.1 ± 0.3	11.3 ± 0.3	2.8 ± 0.2	64	60	1.24 ± 0.05
TOCNF <sup>[8]</sup>	96.0 ± 0.5	3.4 ± 0.2	0	0	–	70	30	1.12 ± 0.05
PCC-0.25 <sup>[8]</sup>	92.9 ± 0.4	5.2 ± 0.2	1.2 ± 0.3	1.2 ± 0.3	–	–	43 <sup>[43]</sup>	–

is much higher than in other studies [16, 17, 42]. With a decrease of acid-insoluble lignin content in LCNF<sub>2</sub>, increased of acid-soluble lignin content 2.1% compared to LCNF<sub>1</sub>. During TEMPO oxidation of TMP<sub>pr</sub> using higher doses of NaClO (10 mmol/g), part of the lignin decomposed, part of the lignin was oxidized to form fragments with a lower molecular weight of acid-soluble lignin. A similar effect was observed during TEMPO oxidation of poplar alkaline peroxide mechanical pulp [44]. According to protocol 1, a preliminary mild hydrolysis of TMP<sub>pr</sub> with dilute HCl was performed, followed by TEMPO oxidation. During mild hydrolysis of TMP<sub>pr</sub> with dilute acid, first of all, amorphous hemicelluloses are hydrolyzed, then partially amorphous regions of cellulose, lignin is not dissolved, but some structural changes of lignin can occur during this treatment [22, 41]. The significantly lower hemicellulose content in LCNF<sub>1</sub> compared to LCNF<sub>2</sub> is due to the mild hydrolysis step of Protocol 1 (Table 1). The appearance of the TMP<sub>pr</sub> suspension changed during the oxidation of TEMPO (Fig. 1). The original yellow-light brown TMP<sub>pr</sub> pulp was a suspension of swollen lignocellulose fibers in water with phase separation, Fig. 1a. The gel-like suspension on protocol 1 turned brown while the LCNF<sub>2</sub> gel-like suspension remained yellow, Figs. 1b and c. The change in the color of the LCNF<sub>1</sub> pulp to dark brown may be associated with an increase in chromophore groups in the lignin structure after treatment with dilute HCl.

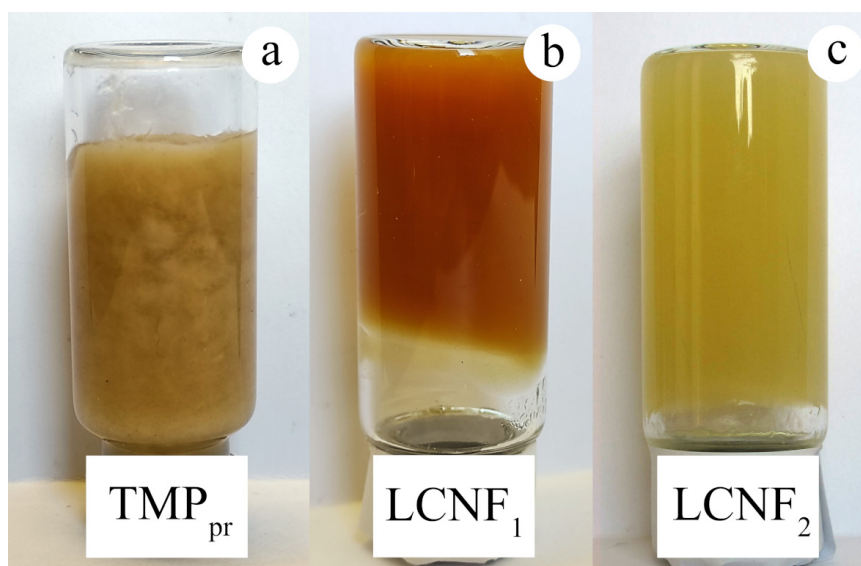


FIG. 1. Appearance of aqueous suspensions: (a) TMP<sub>pr</sub> (2.5 wt.%); (b) LCNF<sub>1</sub> (2.5 wt.%), (c) LCNF<sub>2</sub> (2.5 wt.%)

X-ray diffraction patterns of all samples contained diffraction peaks at  $2\theta = 22.3^\circ$  and  $2\theta = 14.8 - 16.8^\circ$  (double peak) that corresponded to the (200), ( $\bar{1}10$ ) and (110) crystallographic planes of monoclinic I $\beta$  cellulose [38] (Fig. 2). Obviously, the crystal structure of the samples treated according to Protocol 1 and 2 did not change and remained cellulose I. However, the crystallinity index (IC) varied significantly under different processing conditions. The high IC = 78.2% for the TOCNF sample was due to its high content of  $\alpha$ -cellulose, low content of amorphous hemicelluloses, and the absence of lignin. The IC value for LCNF<sub>1</sub> and LCNF<sub>2</sub> was 62.5% and 64.7%, respectively. This was consistent with the

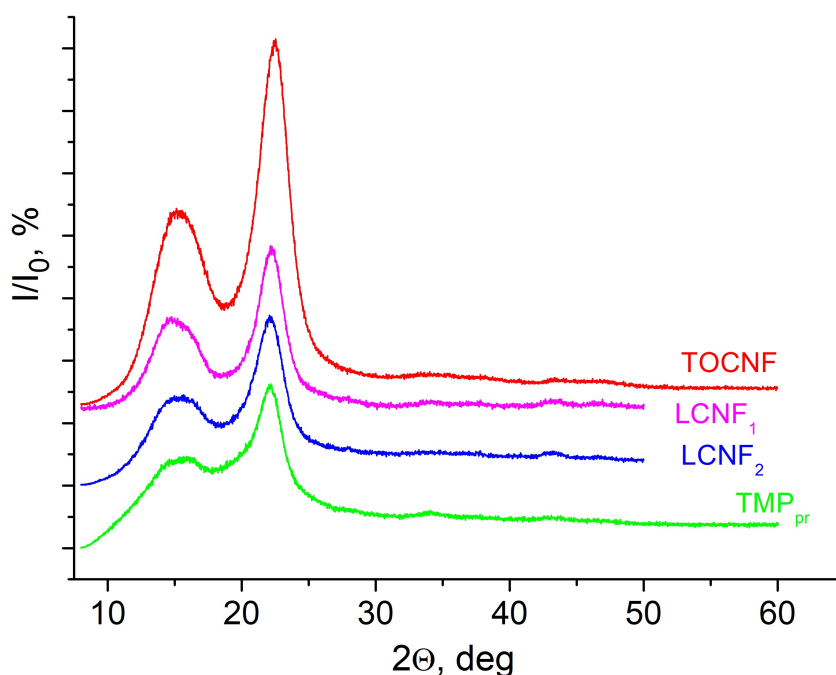


FIG. 2. XRD patterns of the  $\text{TMP}_{pr}$  and films:  $\text{LCNF}_1$ ,  $\text{LCNF}_2$ , TOCNF

TABLE 2. Physical properties of TOCNF,  $\text{LCNF}_1$ ,  $\text{LCNF}_2$  films

Sample	Particle size, nm		Crystallinity index (IC), %	Average roughness (Ra), nm	WCA, deg. (°)
	fibril diameter	sphere diameter			
$\text{LCNF}_1$	$14 \pm 5$	$14 \pm 8$	62.5	61	$75 \pm 2$
$\text{LCNF}_2$	$14 \pm 5$	$10 \pm 3$	64.7	37	$82 \pm 2$
TOCNF <sup>[8]</sup>	$19 \pm 5$	–	78.2	3	$39 \pm 3$

results of the content of  $\alpha$ -cellulose in them (Table 1). An increase in the intensity of the amorphous halo and lower value IC (53.3%) for  $\text{TMP}_{pr}$  was associated with a high content of hemicelluloses and lignin.

### 3.2. Characterization of chemical structures and morphology of $\text{LCNF}_1$ , $\text{LCNF}_2$ films

FTIR was carried out to characterize the chemical structure of LCNF with different lignin content (Fig. 3). FTIR spectra of all samples comprise absorption bands typical for cellulose:  $3284\text{--}3344\text{ cm}^{-1}$ ,  $2899$  and  $1644\text{ cm}^{-1}$  have been assigned to the stretching vibration of O–H hydrogen bond, C–H stretching, respectively. The  $1644\text{ cm}^{-1}$  band is associated with OH bending of the absorbed water vibrations. Three bands at  $1422\text{ cm}^{-1}$ ,  $1367\text{ cm}^{-1}$  and  $1315\text{ cm}^{-1}$  are associated with cellulose parent chain.  $1158\text{ cm}^{-1}$  band corresponds to the asymmetric bridge C–O–C stretching.  $1104\text{ cm}^{-1}$  and  $1026\text{ cm}^{-1}$  bands are associated with C–O–C pyranose ring skeletal vibrations. A small sharp band at  $898\text{ cm}^{-1}$  is attributed to the  $\beta$ -glycosidic linkages between the anhydroglucose rings in the cellulose [39].

For all samples at  $1607\text{ cm}^{-1}$  the absorption band associated with the C=O stretching vibration of the carboxylate groups the formed as a result of the TEMPO-mediated oxidation reaction can be observed [38]. The intensity of the band at  $1607\text{ cm}^{-1}$  is maximum for  $\text{LCNF}_2$  ( $C_{cg} = 1.24$ ), decreases with a decrease carboxyl group content for TOCNF ( $C_{cg} = 1.12$ ) is minimal for  $\text{LCNF}_1$  ( $C_{cg} = 0.70$ ).

Bands at  $1509\text{ cm}^{-1}$  and  $1262\text{ cm}^{-1}$  are attributed to C = C stretching vibration in the aromatic ring and the C–O stretching from lignin, respectively [45–47], are visible for  $\text{LCNF}_1$  and  $\text{LCNF}_2$  samples as shown in Fig. 5. With the decrease of lignin content (Table 1), the characteristic bands of lignin in  $\text{LCNF}_2$  samples weakened and disappear in lignin-free TOCNF. Additional absorption band in FTIR spectrum for  $\text{LCNF}_1$  at  $1705\text{--}1740\text{ cm}^{-1}$  is attributed to carbonyls group and the ester linkage of carboxylic group of the ferulic and p-coumaric acids of lignin [22, 48], which is due to the preliminary hydrolysis of dilute HCl according to protocol 1. The absence of this band in the  $\text{LCNF}_2$  spectrum confirms the assumption made.

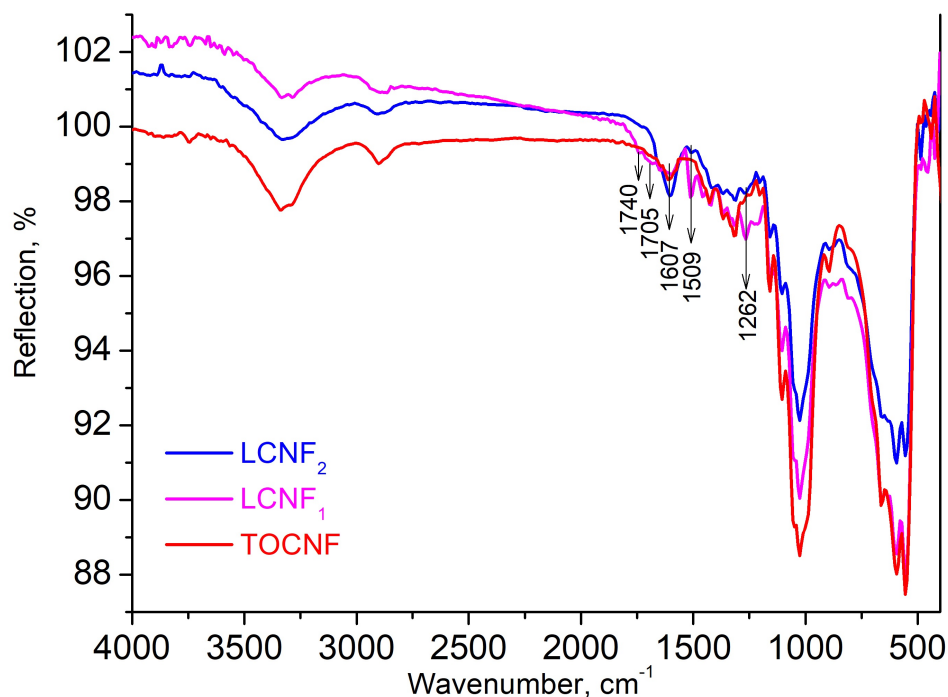


FIG. 3. FTIR spectra of: TOCNF, LCNF<sub>1</sub>, LCNF<sub>2</sub>

The morphology of LCNF and TOCNF films studied using AFM is shown in Fig. 3. The microstructure of TMP<sub>pr</sub> fibers is shown in Fig. 1S. The diameter and length of the TMP<sub>pr</sub> fiber were  $30 \pm 10 \mu\text{m}$  and  $750 \pm 250 \mu\text{m}$ , respectively.

The TOCNF samples contained entangled nanofibrils  $19 \pm 5 \text{ nm}$  diameter (Fig. 4a). Cellulose nanofibrils as well as dispersed spherical nanoparticles were observed in LCNF<sub>1</sub> and LCNF<sub>2</sub> samples (Figs. 4b and 4c). The spherical nanoparticles most likely consisted of lignin. Similar structures for lignin-containing cellulose nanofibrils obtained from various sources have been observed and described previously [16, 49, 50]. During TEMPO-mediated oxidation, lignin was oxidized and depolymerized to form small fragments of lignin. Due to its hydrophobic nature, lignin aggregated into spheres in order to minimize its contact surface with water [16]. The average diameter of the obtained LCNF  $14 \pm 5 \text{ nm}$  nanofibrils was slightly smaller than the diameter of TOCNF nanofibrils. This was probably due to the different sources used to obtain TOCNF and LCNF. The morphology of LCNF<sub>1</sub> was less uniform than that of LCNF<sub>2</sub>: lignin nanoparticles were located separately from cellulose nanofibrils and had a large size spread ( $14 \pm 8 \text{ nm}$ ). Possibly, this morphology of LCNF<sub>1</sub> was due to structural changes in lignin upon mild hydrolysis of TMP<sub>pr</sub> with dilute HCl. Longer LCNF<sub>2</sub> nanofibrils were uniformly coated with spherical lignin nanoparticles  $10 \pm 3 \text{ nm}$  in size. However, aggregation, lack of aligned fibrils, and overlap of individual LCNF<sub>2</sub> nanofibrils made it difficult to accurately determine the length of nanofibrils using AFM. Spherical lignin nanoparticles on the surface of LCNF<sub>2</sub> nanofibrils could be associated with lignin redeposition [22]. It is worth noting that the lignin nanoparticles appeared to be attached to the LCNF<sub>2</sub> rather than separated from fibrils as for LCNF<sub>1</sub> specimens.

The resulting LCNF<sub>1</sub> and LCNF<sub>2</sub> films can be considered as nanocomposites of two nanosized biomaterials, cellulose and lignin. In order to study the effect of hydrophobic lignin on the wettability of films, the water contact angles (WCA) of TOCNF, LCNF<sub>1</sub>, and LCNF<sub>2</sub> films were measured (Fig. 4g,h,i). TOCNF films were the most hydrophilic (WCA  $39^\circ$ ) compared to LCNF<sub>1</sub> (WCA  $75^\circ$ ) and LCNF<sub>2</sub> (WCA  $82^\circ$ ) films. This behavior of TOCNF films can be explained not only by the difference in chemical composition (the absence of lignin), but by a decrease in surface roughness [51]. The mean surface roughness value (Ra) for TOCNF, estimated by AFM, was 20 times lower than Ra for LCNF<sub>1</sub> and more than 12 times lower than Ra for LCNF<sub>2</sub> (Table 2). Despite the higher Ra values for LCNF<sub>1</sub> and their higher lignin content, WCA films of LCNF<sub>1</sub> were lower than for LCNF<sub>2</sub> films. Apparently, larger lignin particles, located separately from cellulose nanofibrils, increased the surface roughness of LCNF<sub>1</sub> films ( $61 \text{ nm}$  vs.  $37 \text{ nm}$  Ra for LCNF<sub>1</sub> films; Figs. 4e,f). However, a more uniform distribution of lignin nanoparticles over the surface of nanofibrils resulted in the greater hydrophobicity of LCNF<sub>2</sub> films compared to LCNF<sub>1</sub>.

### 3.3. Optical and thermal properties of LCNF<sub>1</sub>, LCNF<sub>2</sub> films

Translucent LCNF<sub>1</sub> and LCNF<sub>2</sub> films were obtained without cracks (Fig. 5). The LCNF<sub>2</sub> films were flexible (Figs. 5c,d) in contrast to the brittle LCNF<sub>1</sub> films (Figs. 5a,b). In the visible light region (400–800 nm), LCNF films showed optical transmission dependent on lignin content and film thickness. Comparison of the transmission spectra

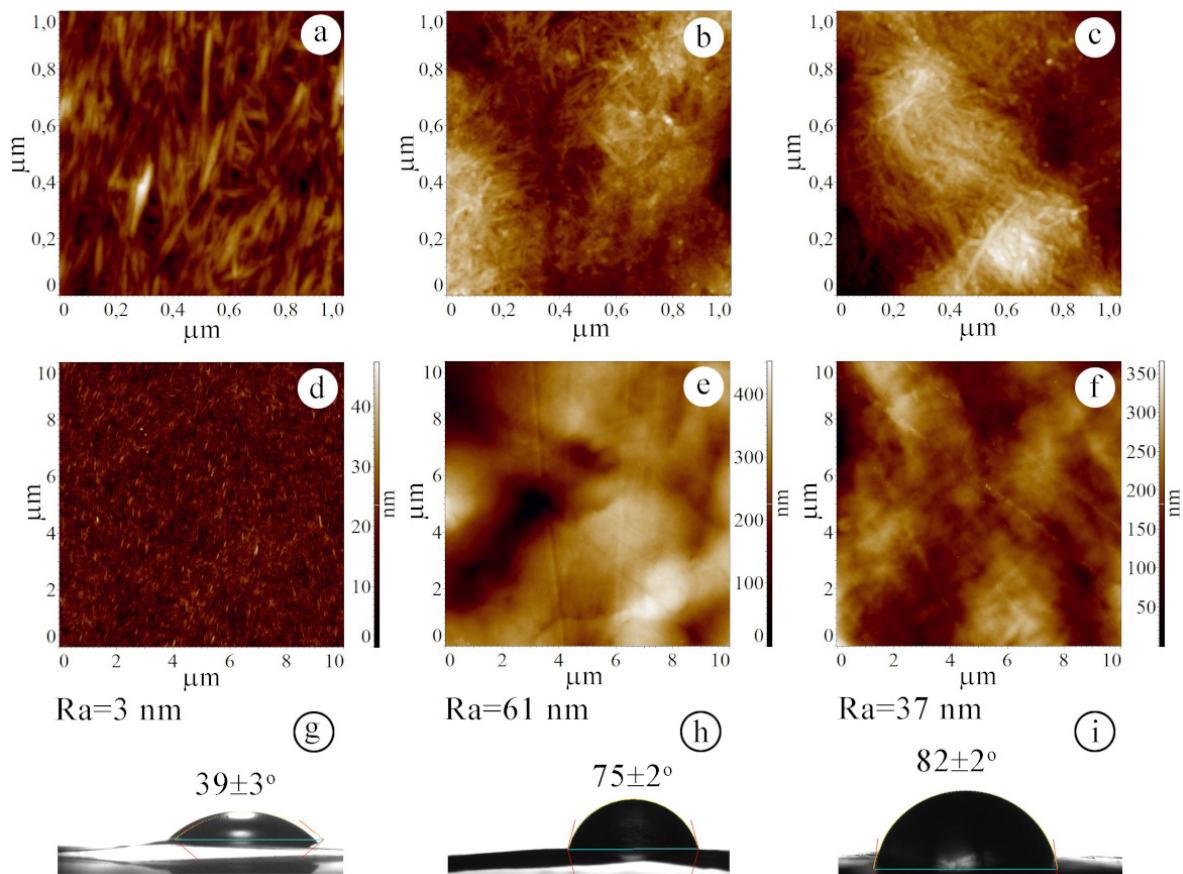


FIG. 4. AFM images of films: TOCNF (a,d), LCNF<sub>1</sub> (b,e), LCNF<sub>2</sub> (c,f). Images of a water droplet spreading over the films: TOCNF (g), LCNF<sub>1</sub> (h), LCNF<sub>2</sub> (i)

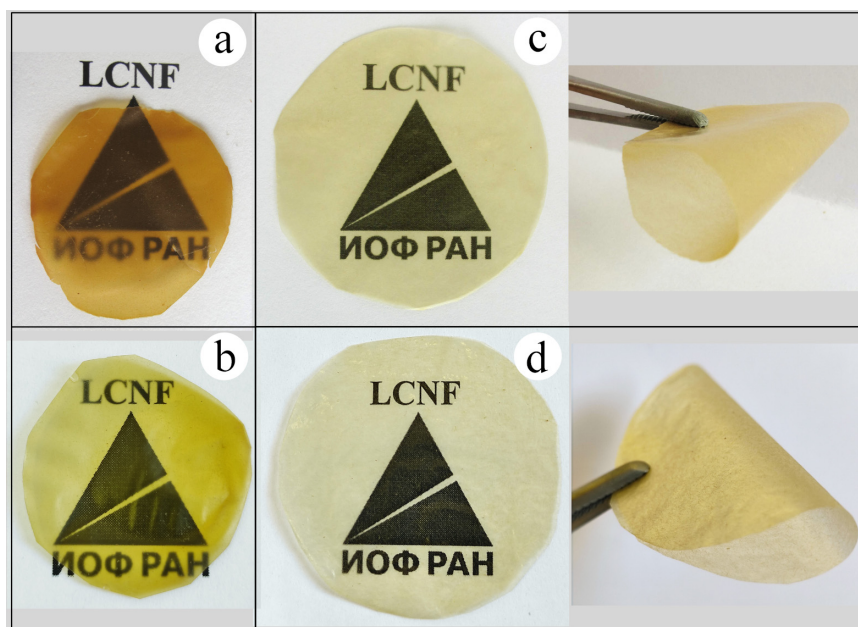


FIG. 5. Appearance of the films: LCNF<sub>1</sub> (a,b), LCNF<sub>2</sub> (c,d), obtained from suspensions of 2.2 wt.% and 1.1 wt.%, respectively. The logo is used with permission from Prokhorov General Physics Institute of the Russian Academy of Sciences

of LCNF films obtained from a dispersion with the same concentration showed that the lignin content makes the main contribution to the decrease in the transmission coefficient (Fig. 6, Table 3).

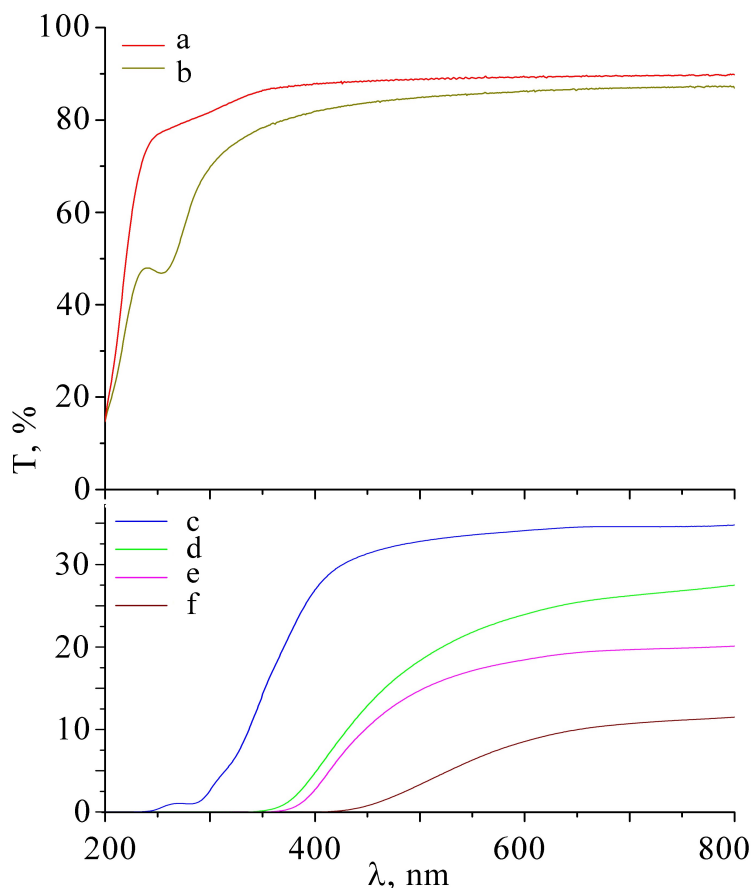


FIG. 6. Transmission spectra of the films: TOCNF (a,b), LCNF<sub>2</sub> (c,e), LCNF<sub>1</sub> (d,f), obtained from suspensions of 1.1 wt.% and 2.2 wt.%, respectively

TABLE 3. Optical properties of TOCNF, LCNF<sub>1</sub>, LCNF<sub>2</sub> films

Sample	Suspension concentration, wt.%	Film thickness, $\mu\text{m}$	Transmittance (T), %			UV blocking ratio (R), %	
			600 nm	275 nm	350 nm	275 nm	350 nm
LCNF <sub>1</sub>	1.1	20 $\pm$ 5	24.1	0	0	100	100
LCNF <sub>1</sub>	2.2	40 $\pm$ 5	8.8	0	0	100	100
LCNF <sub>2</sub>	1.1	20 $\pm$	33.7	0.9	13.1	98.9	84.8
LCNF <sub>2</sub>	2.2	40 $\pm$ 5	18.5	0	0.8	100	99.0
TOCNF	1.1	20 $\pm$ 5	89.4	80.0	86.2	0	0
TOCNF	2.2	35 $\pm$ 5	86.7	60.1	77.9	0	0

The LCNF<sub>1</sub> and LCNF<sub>2</sub> films showed strong absorption in both UVB (280–315 nm) and UVA (315–400 nm) compared to TOCNF films (Fig. 5). LCNF<sub>2</sub> films had a UV absorption band at 295–301 nm (Figs. 8b,c), due to the  $\pi$ – $\pi$  interaction between lignin molecules [52]. The transmittance coefficients (T) and UV blocking ratio (R) of these films at 275 and 350 nm, respectively, were summarized in Table 3. The UV blocking ratios (R, %) were evaluated using equation (1) [53]:

$$R = \frac{(T_0 - T) \cdot 100}{T_0}, \quad (1)$$

where the transmittance coefficients of TOCNF and LCNF films were defined as  $T_0$  and  $T$ , respectively.

The LCNF<sub>1</sub> films exhibited a pronounced UV blocking property in the wavelength range below 375 nm (Fig. 5c,e). LCNF<sub>2</sub> films showed high UV blocking effect in both UVB ( $R = 99\%$ – $100\%$ ) and UVA ( $R = 84.8\%$ – $99.0\%$ ) with a decrease in transmission at 600 nm ( $T = 33.7$ – $18.5\%$ ), depending on the film thickness (Table 3).

Thermal stability of LCNF and TOCNF films as well as  $TMP_{pr}$  was evaluated by thermogravimetric analysis (TG) under synthetic air flow (Fig. 7). The initial weight losses at 150°C for  $TMP_{pr}$ , TOCNF films, LCNF<sub>1</sub>, and LCNF<sub>2</sub> were 7.9%, 7.0%, 5.9%, and 6.7%, respectively; and they were attributed to the adsorbed water evaporation. The initial and final decomposition temperatures ( $T_{onset}$  and  $T_{endset}$ ) were defined as the temperatures at which the sample weight losses became more apparent, and at which the weight losses stopped, respectively.

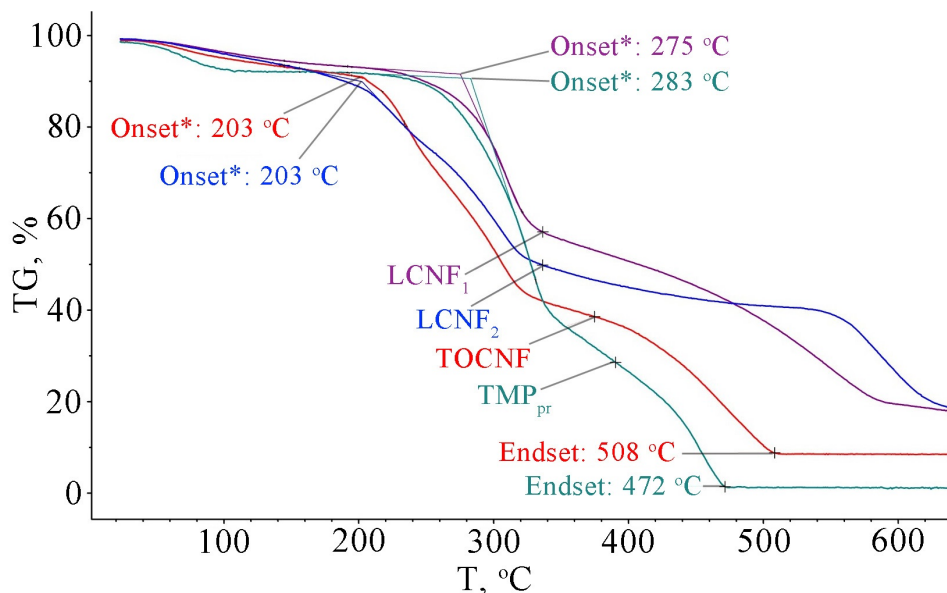


FIG. 7. TG curves for  $TMP_{pr}$  and films: TOCNF, LCNF<sub>1</sub>, LCNF<sub>2</sub>

The initial weight losses at 150°C for  $TMP_{pr}$ , TOCNF films, LCNF<sub>1</sub>, and LCNF<sub>2</sub> were 7.9%, 7.0%, 5.9%, and 6.7%, respectively; and they were attributed to the adsorbed water evaporation. The initial and final decomposition temperatures ( $T_{onset}$  and  $T_{endset}$ ) were defined as the temperatures at which the sample weight losses became more apparent, and at which the weight losses stopped, respectively.  $T_{onset}$  for  $TMP_{pr}$ , (283°C) and  $T_{onset}$  for LCNF<sub>1</sub> (275°C) differed insignificantly by 8°C due to the high content of lignin in them, Table 1. Lignin, composed of phenyl-propane units interconnecting via various ether and carbon-carbon bonds, is more thermally stable than cellulose and hemicelluloses [45]. The decrease of  $T_{onset}$  of LCNF<sub>1</sub> was probably associated with an increase in the heat exchange rate due to the surface area increase and decrease in the particle size to nanoscale. The decomposition proceeds of TOCNF and LCNF<sub>2</sub> films occurred at lower temperatures comparing to LCNF<sub>1</sub> film and  $TMP_{pr}$ , Fig. 7. The decrease in the TEMPO oxidation of lignocellulosic biomass thermal destruction temperature due to the influence of carboxylate groups has been thoroughly studied Rohaizu and Wanrosli [45]. We believe that the lower temperatures ( $T_{onset}$ ) for thermal decomposition (203°C) of TOCNF and LCNF<sub>2</sub> films are due to the higher content of carboxyl groups, Table 1. The TG curves of all samples showed three stages of degradation with overlapping stages of degradation of various components. The first stage was associated with the loss of moisture. The second stage of decomposition was associated with dehydration, depolymerization of hemicelluloses and cellulose. The third stage of sample decomposition can be explained by the oxidation of residual carbon [8] and the degradation of the complex structure of lignin [22]. For  $TMP_{pr}$  and TOCNF film, the final decomposition temperatures  $T_{endset}$  were determined to be 579°C and 508°C, respectively. The increased value of  $T_{endset}$   $TMP_{pr}$  was associated with the high thermal stability of the aromatic chain of lignin. For LCNF<sub>1</sub> and LCNF<sub>2</sub> films, the final decomposition temperature was not determined; the residue at 650°C was 17.5% and 18.1%, respectively, which significantly exceeds the residue for  $TMP_{pr}$  (1.1%). This indicates that the incorporation of carboxylate functional groups into LCNF<sub>1</sub> and LCNF<sub>2</sub> as a result of TEMPO oxidation had a flame retardant effect. The high content of lignin at a low content of carboxyl groups led to an increase in the thermal stability of LCNF<sub>1</sub> films. The high content of carboxyl groups with a simultaneous decrease in the content of lignin contributed to a decrease  $T_{onset}$  of LCNF<sub>2</sub> films to 203°C. The LCNF<sub>1</sub> and LCNF<sub>2</sub> films exhibited flame retardant properties.

#### 4. Conclusions

We developed the efficient process for the isolation of  $14 \pm 5$  nm diameter lignin-containing cellulose nanofibrils from  $TMP$  using TEMPO oxidation followed by sonication. The 23.8 wt% lignin content in LCNF<sub>1</sub>, isolated with the use of dilute HCl prehydrolysis and a low dose of NaClO (5 mmol/g), was much higher than the same ingredient content reported in any previously published studies. The lignin content decreased to 14.1% in LCNF<sub>2</sub> with the increase of NaClO load to 10 mmol/g, while the content of carboxyl groups in LCNF<sub>2</sub> increased to 1.24 mmol/g (vs. 0.70 mmol/g for LCNF<sub>1</sub>).

Thin (20–40  $\mu\text{m}$ ), translucent, and flexible LCNF<sub>2</sub> films with a uniform distribution of  $10 \pm 3$  nm spherical lignin nanoparticles and more brittle LCNF<sub>1</sub> films with less uniform distribution of larger ( $14 \pm 8$  nm) lignin nanoparticles were obtained by a solution casting technique. LCNF films showed excellent UV-blocking ability in a wide spectrum range from 200 to 375 nm, and much less hydrophilicity (WCA = 75–82°) compared to TOCNF films (WCA = 39°). The thermal stability of LCNF films increased with an increase in the lignin content and a decrease in the content of carboxyl groups up to 275 °C compared to 203 °C TOCNF films.

Overall, LCNF can be considered as nanocomposite. The presence of nanolignin on the surface of LCNF resulted in a UV blocking effect, an increase in thermal stability, and increase of hydrophobicity of obtained films. The developed process has provided LCNFs with high yield and superior properties for making the packaging materials and/or biopolymer composites.

## References

- [1] Ahankari S.S., Subhedar A.R., Bhadauria S.S., Dufresne A. Nanocellulose in food packaging: a review. *Carbohydr. Polym.*, 2020, **255**, P. 117479.
- [2] Liu Z., Zhang S., He B., et al. Synthesis of cellulose aerogels as promising carriers for drug delivery: a review. *Cellulose*, 2021, **28**, P. 2697–2714.
- [3] De Amorim J.D.P., de Souza K.C., Duarte C.R., et al. Plant and bacterial nanocellulose: production, properties and applications in medicine, food, cosmetics, electronics and engineering: a review. *Environ. Chem. Lett.*, 2021, **18**, P. 851–869.
- [4] Fedorov P.P., Luginina A.A., Kuznetsov S.V., et al. Composite up-conversion luminescent films containing a nanocellulose and SrF<sub>2</sub>:Ho particle. *Cellulose*, 2019, **26**, P. 2403–2423.
- [5] De France K., Zeng Z., Wu T., Nyström G. Functional Materials from Nanocellulose: Utilizing Structure-Property Relationships in Bottom-Up Fabrication. *Advanced Materials*, 2021, **33**(28), P. 2000657.
- [6] Dias O.A.T., Konar S., Leão A.L., et al. Current State of Applications of Nanocellulose in Flexible Energy and Electronic Devices. *Frontiers in Chemistry*, 2020, **8**, P. 420.
- [7] Nie S., Hao N., Zhang K., et al. Cellulose nanofibrils-based thermally conductive composites for flexible electronics: a mini review. *Cellulose*, 2020, **27**, P. 4173–4187.
- [8] Fedorov P.P., Luginina A.A., Kuznetsov S.V., et al. Hydrophobic up-conversion carboxylated nanocellulose/fluoride phosphor composite films modified with alkyl ketene dimer. *Carbohydr. Polym.*, 2020, **250**, P. 116866.
- [9] Luginina A.A., Kuznetsov S.V., Ivanov, V.K. et al. Laser damage threshold of hydrophobic up-conversion carboxylated nanocellulose/SrF<sub>2</sub>:Ho composite films functionalized with 3-aminopropyltriethoxysilane. *Cellulose*, 2021, **28**, P. 10841–10862.
- [10] Guan Q.F., Yang H.B., Han Z.M., et al. An all-natural bioinspired structural material for plastic replacement. *Nat. Commun.*, 2020, **11**(1), P. 1–7.
- [11] Turbak A.F., Snyder F.W., Sandberg K.R. Microfibrillated cellulose, a new cellulose product: properties, uses and commercial potential. *J. Appl. Polym. Sci., Appl. Polym. Symp.*, 1983, **37**, P. 815–827.
- [12] Herrick F.W., Casebier R.L., Hamilton J.K., Sandberg K.R. Microfibrillated cellulose: morphology and accessibility. *J. Appl. Polym. Sci., Appl. Polym. Symp.*, 1983, **37**, P. 797–813.
- [13] Klemm D., Kramer F., Moritz S., et al. Nanocelluloses: a new family of nature-based materials. *Angew. Chem. Int. Ed.*, 2011, **50**, P. 5438–5466.
- [14] Klemm D., Cranston E., Fischer D., et al. Nanocellulose as a natural source for groundbreaking applications in materials science: today's state. *Mater. Today*, 2018, **21**, P. 720–748.
- [15] Park C.W., Han S.Y., Namgung H.W., et al. Preparation and characterization of cellulose nanofibrils with varying chemical compositions. *BioResources*, 2017, **12**(3), P. 5031–5044.
- [16] Nader S., Brosse N., Khadraoui M., et al. A low-cost environmentally friendly approach to isolate lignin containing micro and microfibrillated cellulose from Eucalyptus globulus bark by steam explosion. *Cellulose*, 2022, **29**, P. 5593–5607.
- [17] Oliaei E., Lindén P.A., Wu Q. et al. Microfibrillated lignocellulose (MFLC) and nanopaper films from unbleached kraft softwood pulp. *Cellulose*, 2020, **27**, P. 2325–2341.
- [18] Diop C.I.K., Tajvidi M., Bilodeau M. A., et al. Evaluation of the incorporation of lignocellulose nanofibrils as sustainable adhesive replacement in medium density fiberboards. *Industrial Crops and Products*, 2017, **109**, P. 27–36.
- [19] Khadraoui M., Khiari R., Bergaoui L., Mauret E. Production of lignin-containing cellulose nanofibrils by the combination of different mechanical processes. *Industrial Crops and Products*, 2022, **183**, P. 114991.
- [20] Espinosa E., Domínguez-Robles J., Sánchez R., et al. The effect of pre-treatment on the production of lignocellulosic nanofibers and their application as a reinforcing agent in paper. *Cellulose*, 2017, **24**, P. 2605–2618.
- [21] Terrett O.M., Lyczakowski J.J., et al. Molecular architecture of softwood revealed by solid-state NMR. *Nat. Commun.*, 2019, **10**, P. 4978.
- [22] Liao J., Latif N.H.A., Trache D., et al. Current advancement on the isolation, characterization and application of lignin. *Int. J. Biol. Macromol.*, 2020, **162**, P. 985–1024.
- [23] Solala I., Iglesias M.C., Peresin M.S. On the potential of lignin-containing cellulose nanofibrils (LCNFs): a review on properties and applications. *Cellulose*, 2020, **27**, P. 1853–1877.
- [24] Sadeghifar H., Venditti R., et al. Cellulose-lignin biodegradable and flexible UV protection film. *ACS Sustain Chem. Eng.*, 2017, **5**, P. 625–631.
- [25] Farooq M., Zou T., Riviere G., et al. Strong ductile and waterproof cellulose nanofibril composite films with colloidal lignin particles. *Biomacromolecules*, 2018, **20**, P. 693–704.
- [26] Huang C., Dong H., Zhang Z. et al. Procuring the nano-scale lignin in prehydrolyzate as ingredient to prepare cellulose nanofibril composite film with multiple functions. *Cellulose*, 2020, **27**, P. 9355–9370.
- [27] Chen Y., Fan D., Han Y. et al. Effect of high residual lignin on the properties of cellulose nanofibrils/films. *Cellulose*, 2018, **25**, P. 6421–6431.
- [28] Lê H.Q., Dimic-Misic K., Johansson L., et al. Effect of lignin on the morphology and rheological properties of microfibrillated cellulose produced from  $\gamma$ -valerolactone/water fractionation process. *Cellulose*, 2018, **25**, P. 179–194.
- [29] Liu K., Du H., Zheng T., et al. Lignin-containing cellulose nanomaterials: preparation and applications. *Green. Chem.*, 2021, **23**(24), P. 9723–9746.
- [30] Ferrer A., Hoeger I.C., et al. Reinforcement of polypropylene with lignocellulose nanofibrils and compatibilization with biobased polymers. *J. Appl. Polym. Sci.*, 2016, **133**, P. 43854.
- [31] Visanko M., Sirviö J.A., Piltanen P., et al. Castor oil-based biopolyurethane reinforced with wood microfibers derived from mechanical pulp. *Cellulose*, 2017, **24**, P. 2531–2543.
- [32] Herzele S., Veigel S., Liebner F., et al. Reinforcement of polycaprolactone with microfibrillated lignocellulose. *Ind. Crops. Prod.*, 2016, **93**, P. 302–308.

- [33] Ballner D., Herzele S., Keckes J., et al. Lignocellulose nanofiber-reinforced polystyrene produced from composite microspheres obtained in suspension polymerization shows superior mechanical performance. *ACS Appl. Mater. Interfaces*, 2016, **8**, P. 13520–13525.
- [34] Isogai A., Kato Y., Preparation of polyuronic acid from cellulose by TEMPO-mediated oxidation. *Cellulose*, 1998, **5**, P. 153–164.
- [35] Isogai T., Saito T., Isogai A. Wood cellulose nanofibrils prepared by TEMPO electro-mediated oxidatin. *Cellulose*, 2011, **18**, P. 421–431.
- [36] Saito T., Kimura S., et al. Cellulose nanofibers prepared by TEMPO-mediated oxidation of native cellulose. *Biomacromolecules*, 2007, **8**, P. 2485–2491.
- [37] Luginina A.A., Kuznetsov S.V., Ivanov V.K., et al. Dispersibility of freeze-drying unmodified and modified TEMPO-oxidized cellulose nanofibrils in organic solvents. *Nanosystems: Phys., Chem., Math.*, 2021, **12**(6), P. 763–772.
- [38] Jiang F., Han S., Hsieh Y.L. Controlled defibrillation of rice straw cellulose and selfassembly of cellulose nanofibrils into highly crystalline fibrous materials. *RSC Advances*, 2013, **3**(30), P. 12366–12375.
- [39] Chen Y.W., Lee H.V., Juan J.C., Phang S.M. Production of new cellulose nanomaterial from red algae marine biomass *Gelidium elegans*. *Carbohydr. Polym.*, 2016, **151**, P. 1210–1219.
- [40] Sluiter J.B., Ruiz R.O., Scarlata C.J., Sluiter A.D., Wolfrum E.J. Compositional Analysis of Lignocellulosic Feedstocks. 1. Review and Description of Methods. *Agric. Food Chem.*, 2010, **58**(16), P. 9043–9053.
- [41] Nikitin V.M., Obolenskaya A.V., Schegolev V.P. *Chemistry of wood and cellulose*. M.: Lesnaya promyshlennost, 1978, 368 p. (in Russian)
- [42] Brännvall E., Aulin C. CNFs from softwood pulp fibers containing hemicellulose and lignin. *Cellulose*, 2022, **29**, P. 4961–4976.
- [43] Bikales N.M., Segal L. *Cellulose and cellulose derivatives*, Part 2, M.: Mir, 1974, 510 p. (in Russian)
- [44] Zhao C., Zhang H., Li, Z. et al. Further understanding the influence of fiber surface and internal charges on the interfiber bonding capability and resulting paper strength. *Cellulose*, 2017, **24**, P. 2977–2986.
- [45] Rohaizu R., Wanrosli W.D. Sono-assisted TEMPO oxidation of oil palm lignocellulosic biomass for isolation of nanocrystalline cellulose. *Ultrason. Sonochem.*, 2017, **34**, P. 631–639.
- [46] Deepa B., Abraham E., Cordeiro N. et al. Utilization of various lignocellulosic biomass for the production of nanocellulose: a comparative study. *Cellulose*, 2015, **22**, P. 1075–1090.
- [47] Yao J., Odelius K., Hakkarainen M. Microwave Hydrophobized Lignin with Antioxidant Activity for Fused Filament Fabrication. *ACS Appl. Polym. Mater.*, 2021, **3**(7), P. 3538–3548.
- [48] Sun X.F., Xu F., Sun R.C., et al. Characteristics of degraded cellulose obtained from steamexploded wheat straw. *Carbohydr Res.*, 2005, **340**, P. 97–106.
- [49] Yang M., Zhang X., Guan S., et al. Preparation of lignin containing cellulose nanofibers and its application in PVA nanocomposite films. *Int. J. Biol. Macromol.*, 2020, **158**, P. 1259–1267.
- [50] Jiang Y., Wang Z., Liu X., et al. Highly Transparent, UV-Shielding, and Water-Resistant Lignocellulose Nanopaper from Agro-Industrial Waste for Green Optoelectronics. *ACS Sustain. Chem. Eng.*, 2020, **8**(47), P. 17508–17519.
- [51] Wenzel R.N. Resistance of Solid Surfaces to Wetting by Water. *Ind. Eng. Chem.*, 1936, **28**(8), P. 988–994.
- [52] Fu H., Li Y., Wang B., et al. Structural change and redispersion characteristic of dried lignin-containing cellulose nanofibril and its reinforcement in PVA nanocomposite film. *Cellulose*, 2021, **28**, P. 7749–7764.
- [53] Li Y., Zou Y., Hou Y. Fabrication and UV-blocking property of nano-ZnO assembled cotton fibers via a two-step hydrothermal method. *Cellulose*, 2011, **18**, P. 1643–1649.

---

Submitted 7 September 2022; accepted 10 November 2022

*Information about the authors:*

*Anna A. Luginina* – Prokhorov General Physics Institute of the Russian Academy of Sciences, 38 Vavilov str., Moscow 119991, Russia; ORCID 0000-0002-6564-5729; ana@lst.gpi.ru

*Sergey V. Kuznetsov* – Prokhorov General Physics Institute of the Russian Academy of Sciences, 38 Vavilov str., Moscow 119991, Russia; ORCID 0000-0002-7669-1106; kouznetzovsv@gmail.com

*Alexander A. Alexandrov* – Prokhorov General Physics Institute of the Russian Academy of Sciences, 38 Vavilov str., Moscow 119991, Russia; ORCID 0000-0001-7874-7284; alexandrov1996@yandex.ru

*Radmir V. Gainutdinov* – Shubnikov Institute of Crystallography of Federal Scientific Research Centre Crystallography and Photonics of Russian Academy of Sciences, 59 Leninsky Pr., Moscow, 119333, Russia; ORCID 0000-0002-5384-4026; rgaynutdinov@gmail.com

*Dmitrii I. Petukhov* – Lomonosov Moscow State University, Chemical department, 1 Leninskie Gory, Moscow, 119991, Russia; ORCID 0000-0002-0956-5820; di.petukhov@gmail.com

*Valery V. Voronov* – Prokhorov General Physics Institute of the Russian Academy of Sciences, 38 Vavilov str., Moscow 119991, Russia; ORCID 0000-0001-5029-8560; voronov@lst.gpi.ru

*Elena V. Chernova* – Prokhorov General Physics Institute of the Russian Academy of Sciences, 38 Vavilov str., Moscow 119991, Russia; ORCID 0000-0001-7401-5019; e-chernova@yandex.ru

*Pavel P. Fedorov* – Prokhorov General Physics Institute of the Russian Academy of Sciences, 38 Vavilov str., Moscow 119991, Russia; ORCID 0000-0002-2918-3926; ppfedorov@yandex.ru

*Conflict of interest:* the authors declare no conflict of interest.



# NANOSYSTEMS:

**PHYSICS, CHEMISTRY, MATHEMATICS**

## INFORMATION FOR AUTHORS

The journal publishes research articles and reviews, and also short scientific papers (letters) which are unpublished and have not been accepted for publication in other magazines. Articles should be submitted in English. All articles are reviewed, then if necessary come back to the author to completion.

The journal is indexed in Web of Science Core Collection (Emerging Sources Citation Index), Chemical Abstract Service of the American Chemical Society, Zentralblatt MATH and in Russian Scientific Citation Index.

### Author should submit the following materials:

1. Article file in English, containing article title, the initials and the surname of the authors, Institute (University), postal address, the electronic address, the summary, keywords, MSC or PACS index, article text, the list of references.
2. Files with illustrations, files with tables.
3. The covering letter in English containing the article information (article name, MSC or PACS index, keywords, the summary, the literature) and about all authors (the surname, names, the full name of places of work, the mailing address with the postal code, contact phone number with a city code, the electronic address).
4. The expert judgement on possibility of publication of the article in open press (for authors from Russia).

Authors can submit a paper and the corresponding files to the following addresses: [nanojournal.ifmo@gmail.com](mailto:nanojournal.ifmo@gmail.com), [popov1955@gmail.com](mailto:popov1955@gmail.com).

### Text requirements

Articles should be prepared with using of text editors MS Word or LaTeX (preferable). It is necessary to submit source file (LaTeX) and a pdf copy. In the name of files the English alphabet is used. The recommended size of short communications (letters) is 4-6 pages, research articles– 6-15 pages, reviews – 30 pages.

#### Recommendations for text in MS Word:

Formulas should be written using Math Type. Figures and tables with captions should be inserted in the text. Additionally, authors present separate files for all figures and Word files of tables.

### Recommendations for text in LaTeX:

Please, use standard LaTeX without macros and additional style files. The list of references should be included in the main LaTeX file. Source LaTeX file of the paper with the corresponding pdf file and files of figures should be submitted.

References in the article text are given in square brackets. The list of references should be prepared in accordance with the following samples:

- [1] Surname N. *Book Title*. Nauka Publishing House, Saint Petersburg, 2000, 281 pp.
- [2] Surname N., Surname N. Paper title. *Journal Name*, 2010, 1 (5), P. 17-23.
- [3] Surname N., Surname N. Lecture title. In: Abstracts/Proceedings of the Conference, Place and Date, 2000, P. 17-23.
- [4] Surname N., Surname N. Paper title, 2000, URL: <http://books.ifmo.ru/ntv>.
- [5] Surname N., Surname N. Patent Name. Patent No. 11111, 2010, Bul. No. 33, 5 pp.
- [6] Surname N., Surname N. Thesis Title. Thesis for full doctor degree in math. and physics, Saint Petersburg, 2000, 105 pp.

### **Requirements to illustrations**

Illustrations should be submitted as separate black-and-white files. Formats of files – jpeg, eps, tiff.



# **NANOSYSTEMS:**

**PHYSICS, CHEMISTRY, MATHEMATICS**

**Журнал зарегистрирован**

Федеральной службой по надзору в сфере связи, информационных технологий и массовых коммуникаций

(свидетельство ПИ № ФС 77 - 49048 от 22.03.2012 г.)

ISSN 2220-8054

**Учредитель:** федеральное государственное автономное образовательное учреждение высшего образования

«Национальный исследовательский университет ИТМО»

**Издатель:** федеральное государственное автономное образовательное учреждение высшего образования

«Национальный исследовательский университет ИТМО»

**Отпечатано** в Учреждении «Университетские телекоммуникации»

Адрес: 197101, Санкт-Петербург, Кронверкский пр., 49

**Подписка на журнал НФХМ**

На первое полугодие 2023 года подписка осуществляется через

ОАО «АРЗИ», подписной индекс Э57385